Title
Synthesis and Chemical Modification of Boron Nitride and Graphene Aerogels and Related Nanostructures

Author
DeMaio-Turner, Sally

Publication Date
2019

Peer reviewed|Thesis/dissertation

Synthesis and Chemical Modification of Boron Nitride and Graphene Aerogels and Related Nanostructures

By

Sally J DeMaio-Turner

A dissertation submitted in partial satisfaction of the

requirements for the degree of

Doctor of Philosophy

in

Chemistry

and a designated emphasis

in

Nanoscale Science and Engineering

in the

Graduate Division

of the

University of California, Berkeley

Committee in charge:

Professor Alex Zettl, Co-Chair
Professor A. Paul Alivisatos, Co-Chair
Professor Peidong Yang
Professor Mike Crommie

Spring 2019

Abstract

Synthesis and Chemical Modification of Boron Nitride and Graphene Aerogels and Related Nanostructures

By

Sally Josephine DeMaio-Turner

Doctor of Philosophy in Chemistry
with a Designated Emphasis in Nanoscale Science and Engineering

University of California, Berkeley

Professor Alex Zettl, Co-Chair Professor A. Paul Alivisatos, Co-Chair

Aerogels based on boron nitride and graphene can integrate macroscopic amounts of nanomaterial into a single, relatively open, multifunctional structure. Such aerogels possess the textural properties typical of aerogels including high surface area, high porosity, and low density. Most importantly, they are capable of retaining a number of the extraordinary properties of their nanomaterial building blocks. For example, boron nitride-based aerogels are electrically insulating while graphene aerogels are highly electrically conductive. These properties make the aerogels particularly promising for a variety of applications in supercapacitors, batteries, catalysis, gas sensing, gas storage, polymer composites, and water treatment. However, in order to optimize their performance in these applications, chemical modification is usually necessary.

This dissertation explores chemical modification of graphene and boron nitride aerogels with the goal of being able to introduce targeted chemical modifications in order to improve the performance of the aerogel for specific applications. Additionally, the synthesis of new classes of aerogels is investigated.

Examples of chemical modification of graphene aerogels are the introduction of chemical dopants like boron, or the controlled formation of defects, often called defect-engineering (**Chapter 3)**. These types of chemical modifications are particularly advantageous for highly sensitive and selective NO_2 detection. New compositions of aerogels with electronic properties predicted to be intermediate between graphene and BN are possible by synthesizing boron carbon nitride aerogels (**Chapter 4)**. Two chemically and electronically disparate materials can also be coupled to one another by the formation of multifunctional core-shell hybrids. **Chapter 5** discusses the synthesis of photocatalytic graphitic carbon nitride shells on top of graphene aerogels cores for photocatalytic applications. In addition to chemical modification, physical modification is an approach to control the macroscopic properties of graphene and boron nitride aerogels. **Chapter 6** explores density-tuning of graphene and boron nitride aerogels in order to tune the thermal conductivity for polymer composite applications.

In addition to aerogels based on 2D nanomaterials, 1D nanomaterials can also serve as aerogel building blocks. **Chapter 7** discusses a new approach to synthesize aerogels based on 1D nanofibers of an organic semiconductor, as well as a treatment method to convert them into carbon nanofiber aerogels. Lastly, **Chapter 8** discusses the functionalization of BN nanostructures including BN aerogels, BN nanotubes, and BN nanosheets in order to improve the interfacial interactions between BN nanofillers and host polymer matrices in polymer composites for thermal interface materials.

To my family for all your love and support from thousands of miles away,
Mom, Dad, Lucy, Kismet, Cem, Emma, and Sofia

And to my new family for being my biggest cheerleaders,
Max, Judah, and Vicente

Table of Contents

List of Figures

List of Tables

Acknowledgements

I'd like to thank my advisor Alex Zettl for being everything I could have asked for in an advisor. Your ability to give your graduate students freedom to explore their scientific curiosity and also provide support and guidance when needed has made graduate school such a pleasure. Thanks for taking a chance on a chemistry student and providing humor along the way.

I'd like to thank all of the Zettl group members for being such a fantastic group of people to share ideas, collaborate, and build friendship. A special thanks to Ashley for introducing me to the Zettl group and being my fellow chemistry member navigating a physics group. Aidin, thank you for being the first person to pull me into the lab. Your infectious energy and positivity made the lab such a fun place. Gabe, thanks for making our office so full of laughter and sharing your your wisdom through grad school and post-grad life. Thang, thank you for all of your guidance, friendship and boba over the years. You were such a fountain of knowledge for me in grad school. Matt, you are one of the most passionate scientists that I know and I am constantly learning from you. Thanks for being a good friend and my afternoon coffee buddy. Brian, my skeptic friend, thank you for being so willing to help over the years. Your collaboration has been so key to many of my projects. Hu Long, thank you for being such a wonderful teacher and labmate. You are an amazing scientist, incredibly knowledgeable, and willing to help others. Scott, my chemistry buddy, thanks for being an incredible friend. I have so enjoyed seeing you grow as a scientist and can't wait to see what you accomplish next. JDeasy, thanks for keeping the lab running smoothly and helping me with any task I send your way. Thank you to Zettl group all post-docs and graduate students. Getting to know all of you and being a part of such a collaborative group with different backgrounds has made me a better scientist.

This dissertation would not have been possible without Marcus Worsley. Thank you for being a wonderful collaborator and like a second advisor to me over the years. You played an important role from my first project to my last project.

I am so grateful for the support I have had from my family all the way back from my first move to the west coast many years ago. Mom and Dad, I suppose you are now forgiven for forcing me to go to science camp as a kid. It instilled in me the work ethic that was instrumental to getting me to Berkeley and through my PhD. Mom, thank you for being an excellent role model. Our phone calls to and from lab will be one of my most wonderful memories of graduate school. Dad, I have always wanted to make you proud and thanks for always pushing me to do my best. Lucy, thanks for always providing a good laugh (usually at Mom's expense) and being able to lift me up when I am down. Kismet, Cem, Emma, and Sofia I am so thankful to have you guys and going back east and spending time with you guys is always the much needed recharge I need.

Max, for all of the embraces we've sacrificed for FaceTime and phone calls over the last five years, I'm so grateful for every moment we have together. Those Sophie fees were rough. Thanks for being my biggest support system. You are my favorite. Judah and Vicente, thanks for being the most handsome, awesome, perfect cats in the whole wide world.

Lastly, a special thanks to Berkeley Humane for giving me kittens to raise in the office. You gave me something to care about outside of graduate school, challenged me in a completely different way, and have certainly changed my life. And most importantly, you brought me Judah and Vicente.

Chapter 1: Introduction to Graphene and Boron Nitride Nanostructures

Nano Fun Fact: For perspective on the scale of the nanomaterials discussed in this thesis, a human hair is approximately 80,000nm.

In this introduction, the reader will be given a foundation into the concept of scaling down from a bulk material to a single layer nanomaterial, as well as the nature of the chemical bonds that make up layered nanomaterials like graphene and hexagonal boron nitride (h-BN). The extraordinary electronic, thermal and mechanical properties of graphene and h-BN will also be introduced, as well as the variety of structural polymorphs that have been synthesized from these nanomaterials. All data reported in this thesis is produced by the author unless otherwise noted.

1.1 From Bulk to Single Layer Graphene and Boron Nitride

Graphite is one of the naturally occurring forms of carbon and is composed of individual layers of atoms that are non-covalently bonded to one another in the z direction. This is similar for example to sheets of paper stacked on top of one another. When one layer of graphite is exfoliated, it is called graphene and it extends in the *x* and *y* directions with confinement in the *z* direction giving rise to its designation as a two-dimensional (2D) material. Prior to isolation of graphene, Mermin predicted that an atomically thin 2D material would be not be thermodynamically stable and would decompose due to thermal fluctuations in the material[1]. Yet, in 1947 tight-binding calculations suggested that if it could exist, such a material would have unique properties as a result of the nanoscale dimensions including a zero eV band gap[2]. Repeated attempts throughout the late 1990s and early 2000s to synthesize graphene yielded graphite or samples too small for full analysis[3,4].

One of the greatest scientific advances of the 21th century was the isolation of graphene and exploration of its extraordinary properties which was awarded the Nobel Prize in Physics to Geim and Novoselov in 2010. Perhaps the greatest punchlines of this discovery was that it was isolated using simply graphite, the lead from a pencil, and Scotch tape from the drug store. In 2004, Geim and Novoselov isolated a layer of graphene from graphite using Scotch tape that was large enough for fundamental studied. This process of exfoliation from a bulk powder to a single layer material with one atom thickness is shown in **Figure 1.1a-b**. With this isolation, the arms race to

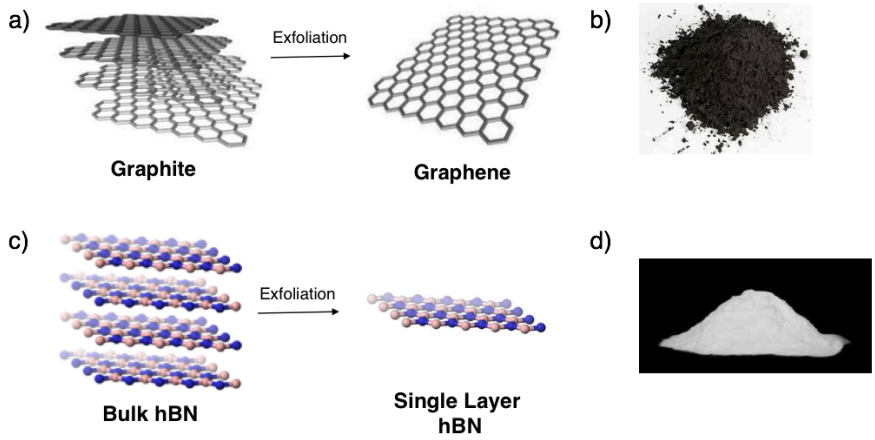

Figure 1.1 a) Exfoliation of the layered material graphite yields single layer graphene[253] b) Photograph of graphite powder c) Bulk h-BN is another layered material which can be exfoliates to yield single layer hBN d) Photograph of bulk h-BN.

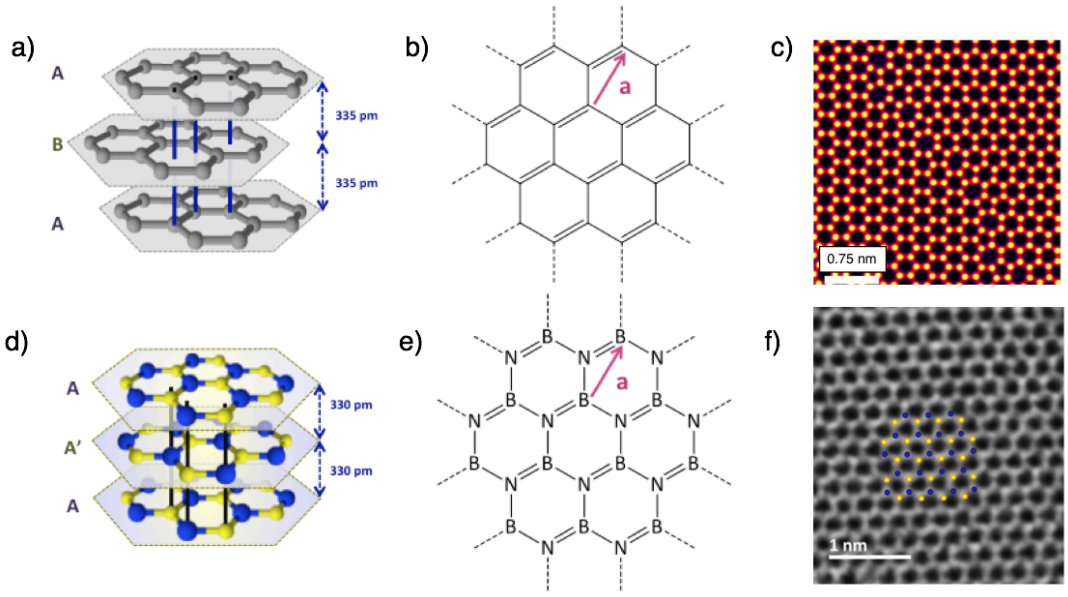

Figure 1.2 a.d) Stacking structure b,e) Hexagonal lattice and c,f) atomic resolution images of graphene and h-BN, respectively[251–253].

discover new physics in graphene and synthesize single layers of other layered materials began.

One other layered material that is widely studied is h-BN. Graphite and h-BN are isoelectronic with a C-C unit containing 8 valence electrons and a B-N unit also containing 8 valence electrons. Thus, boron nitrides can adopt similar structures to their isoelectronic carbon counterparts. Unlike graphite which is a black powder, bulk h-BN is a white powder which is indicative of the starkly different electronic properties of the two materials. However, h-BN possesses a layered structure like graphite and can be exfoliated down to the single layer using the Scotch tape method, also called mechanical exfoliation (**Figure1.1c-d)**.

As shown in **Figure 1.2**, graphene sheets stacked on top of one another have an interlayer distance of 0.335nm and stack in an ABAB configuration. The structure of a single layer of graphene and atomic resolution TEM image are shown in **Figure 1.2b,c** and indicate the sp^2 bonded, hexagonal material**.** H-BN possesses a similar structure but has a slightly smaller interlayer distance of 0.330nm due to additional interlayer interactions as a result of the polar B-N bonds (**Figure 1.2d)**. Its stacking is classically thought to be AA' with boron and nitrogen stacking on top of one another, but recently it has been discovered that the stacking sequence is dependent on synthesis method[5]. The hexagonal structure and atomic resolution TEM image are shown in **Figure 1.2e,f**.

Both graphene and h-BN can be isolated by exfoliation of a high quality bulk crystal through mechanical or liquid means[6–8] or synthesized directly. Graphene is also grown using chemical vapor deposition (CVD) by reaction of a carbon containing precursor gas such as methane on a metal substrate in a reducing hydrogen and nitrogen atmosphere[9,10]. Boron nitride is also synthesized using CVD using boron and nitrogen containing precursors like ammonia-borane or borazine[11,12].

When materials are exfoliated or synthesized at these dimensions, a number of intriguing phenomena occur including changes in the electronic, mechanical and thermal properties. In order to understand the origin of these changes, a deeper look into the chemical structures of graphene and h-BN is necessary.

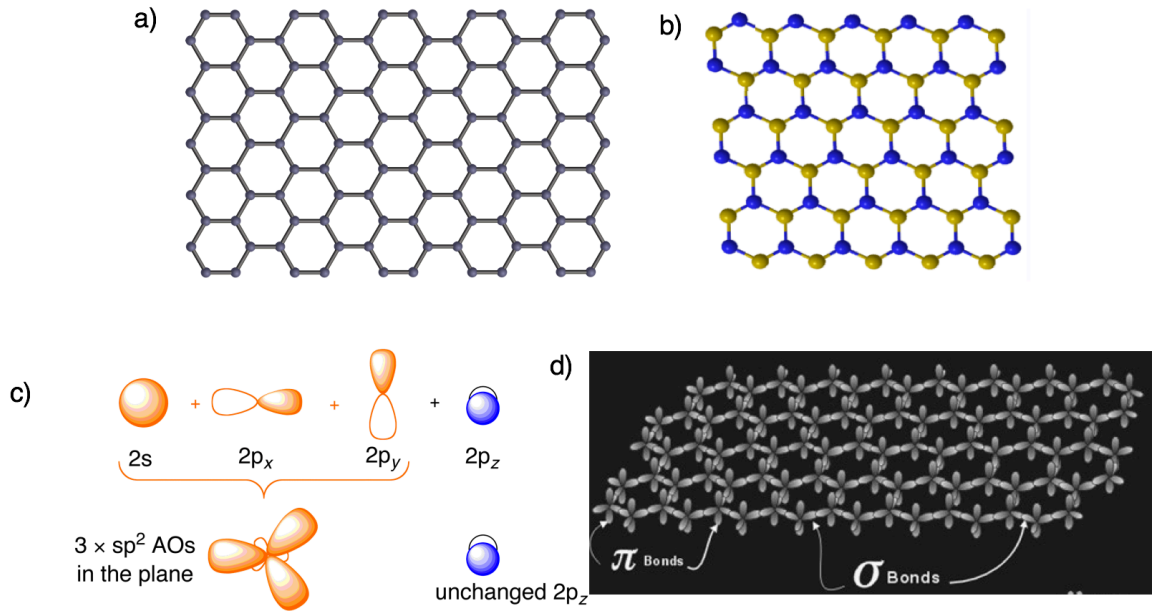

Figure 1.3 a,b) Hexagonal structures of graphene and boron nitride, respectively. Yellow atoms: nitrogen, Blue atoms: boron c) 2s, $2p_x$ and $2p_y$ orbitals hybridize to form the sp^2 orbitals that will overlap to form σ bonds and unchanged p_z orbitals for π bonds. D) Representative overlap of the sp^2 and p_z orbitals to form the π and σ bonds of graphene.

1.2 sp^2 Bonding and Hexagonal Structures

A number of the remarkable properties of graphene and h-BN are attributed to their bonding structure. Graphene and h-BN both have hexagonal lattices as shown in **Figure 1.3a,b** which are also referred to as honeycomb structures. In graphene, all atoms are carbon, and in h-BN, atoms alternate between boron and nitrogen making all boron atoms bonded to three nitrogen atoms and vice versa. In both materials, the bonds between C-C or B-N bonds are called sp^2 bonds.

When atoms are assembled into molecules, the most favorable configuration is the one that maximizes orbital overlap. A linear combination of s and p orbitals provides higher orbital overlap than that of two $2p$ orbitals making hybridization favorable in order to maximize overlap. In sp^2 hybridization, the $2s$ orbital is combined with the $2p_x$ and $2p_y$ orbitals to form 3 degenerate orbitals that can overlap to form σ bonds (**Figure 1.3c)**. These hybrid orbitals have $\frac{1}{3}s$ character and $\frac{2}{3}p$ character and lie in the same plane separated by 120º. The fourth p_z orbital contains pure p character and forms π bonds. **Figure 1.3d** shows how these orbitals overlap to form the hexagonal lattice with in-plane σ bonds between each atom and p_z orbitals above and below the bonding axis forming π bonds. The conjugated aromatic π system can lead to electron delocalization throughout the network as will be described in **Section 1.3.1** and the high strength of sp^2 bonds coupled with light elements results in the excellent mechanical and thermal properties, respectively as will be described in **Section 1.3.2 and 1.3.3**, respectively**.**

1.3 Properties of Graphene and Boron Nitride

Graphene and h-BN nanomaterials are renowned for their remarkable electronic, thermal, and mechanical properties. This dissertation will focus on using chemical modification of graphene and BN aerogels and other nanostructures as a means alter and tailor their properties for specific applications. In this section the intrinsic properties of 2D graphene and h-BN will be introduced, and **Section 1.4** will discuss the other nanomaterial structures that can be formed in the graphene and h-BN family and some of their properties.

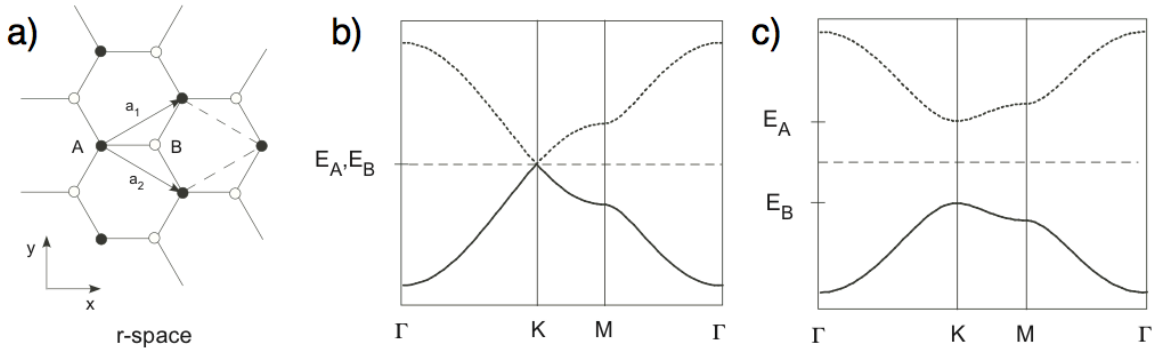

Figure 1.4 a) Real space structure of two interpenetrating sublattices, A and B. Band structure of lattice where b) sublattices A and B are the same atom as in graphene and c) sublattices A and B are not the same as in h-BN[250].

1.3.1 Electronic Properties of Graphene and Boron Nitride

The contrasting electronic properties of graphene and h-BN can be deduced simply from the distinct optical properties of their bulk component materials. Graphene is a 0eV band gap semimetal whose bulk is a black color, while h-BN has a wide band gap of approximately 5.8eV[13] and parent bulk material is a white color. A straight forward model predicts the remarkably different electronic properties between the two materials called the tight binding approximation.

The tight binding approximation solves the problem of non-interacting electrons in a periodic potential and approximates the wave functions of the electrons as superpositions of atomic p_z orbitals. In this case, the periodic potential is the honeycomb lattice of graphene or h-BN whose unit cell is constructed of atoms from two sublattices, A and B as shown in **Figure 1.4a**. In order to solve the Schrodinger equation, **Equation 1.1** must be solved.

$$\begin{vmatrix} H_{AA} - E & H_{AB} \\ H_{BA} & H_{BB} - E \end{vmatrix} = 0 \qquad \textbf{Equation 1.1}$$

where H_{AA} and H_{BB} are the energies on the sublattices and H_{AB}, H_{BA} are the hybridization energies due to π electron hopping between sublattices. The two solutions to this secular equation result in the E_- antibonding and E_+ bonding solutions depicted in **Equation 1.2**.

$$E_{\pm} = \frac{1}{2}\left(H_{AA} + H_{BB} \pm \sqrt{(H_{AA} - H_{BB})^2 + 4|H_{AB}|^2}\right) \qquad \textbf{Equation 1.2}$$

The key finding here is that when the onsite energies H_{AA} and H_{BB} are equal, such as when A and B are the same element, there is a degeneracy in E_- ad E_+ and there will be no band gap. This is the

case for graphene where both A and B are carbon atoms and the band diagram is shown in **Figure 1.4b** . When A and B are not the same element, H_{AA} does not equal H_{BB} and a band gap opens. For h-BN, the onsite energies are not the same, resulting in a band gap as shown in **Figure 1.4c**. These results are a consequence of the symmetry of the lattice and a fundamental property of honeycomb lattice materials.

Another way to understand the insulating character of h-BN is from a more chemistry perspective and taking into account the differences in electronegativities of boron and nitrogen. Boron's electronegativity on the Pauling scale is 2.0 and nitrogen has a 3.0 electronegativity. Due to this different in electronegativity, bonds between boron and nitrogen are polar and sharing of electrons between atoms is not equal. Approximately 0.56 electrons are transferred from boron to nitrogen making delocalization of electrons throughout the extended pi network impossible.

While h-BN's insulating electronic properties are quite straight forward, graphene has received extensive attention due to its intriguing electronic properties including conduction by massless electrons. This means that electrons in graphene are more easily described using the Dirac equation (**Equation 1.3**) as opposed to the Schrodinger equation[14].

$$E = \hbar v_f k \qquad \textbf{Equation 1.3}$$

Other notable electrical characteristics of graphene include its high charge carrier mobilities even at high carrier concentrations which translates to ballistic transport. Additionally, the Fermi level can be tuned to the conduction band for electron conduction, as well as into the valence band for hole conduction[15].

Graphene's large electrical conductivity coupled with its large theoretical surface area make it an excellent candidate for energy storage electrodes such as supercapacitors and battery anodes. Additionally, the single layer is a promising transparent conducting materials for flexible electronics[16–18]. H-BN's electronic structure limits its use to insulating applications[19–21].

1.3.2 Mechanical Properties of Graphene and Boron Nitride

Graphene and h-BN are among two of the strongest known materials due to the strong in-plane sp^2 bonds which make up their structures. Graphene and h-BN have experimentally measured Young's moduli of 1 and 0.87 TPa and tensile strengths of 125 and 70 GPa, respectively (**Table 1.1)**. To put this into perspective, steel typically has a Young's modulus of approximately 0.2 TPa and a tensile strength of 0.4GPa. Not only do they exhibit mechanical properties several orders of magnitude greater than steel, but graphene and h-BN are also extremely light materials

	Graphene	h-BN
Band Gap	0 eV	5.9 eV
Young's Modulus	1 TPa	0.87 TPa
Tensile Strength	125 GPa	70.5 GPa
Thermal Conductivity	4800 W/mK	400 W/mK
Oxidation Temperature	500°C	800°C

Table 1.1 Summary of thermal, mechanical, and electronic properties of graphene and h-BN[247–249].

making it possible to utilize them for mechanical reinforcement without incorporating large masses.

1.3.3 Thermal Properties of Graphene and Boron Nitride

Thermal conductivity is the ability for a material to conduct heat. Graphene and h-BN are both made up of light elements and conduct heat extremely well through phonon transport. The thermal conductivity of graphene has been measured to be 4800 W/mK and h-BN has a thermal conductivity of 400 W/mK. H-BN is unique because thermal conductivity and electrical conductivity are closely coupled due thermal transport via both phonons and electrons. It is rare for an electrically insulating material to exhibit such a high thermal conductivity as h-BN does with the exception of diamond. For comparison, a metal such as copper has a thermal conductivity of 400 W/mK, comparable with insulating h-BN. One cause of the lower thermal conductivity of h-BN compared to graphene is the isotope effect. In nature boron is 19.9% ^{10}B and 80.1% ^{11}B compared to 98.9% natural abundance of ^{12}C and 1.1% ^{13}C. Thermal conductivity is dramatically effected by isotopic disorder, leading h-BN to have hindered thermal conductivity without isotopic enrichment[22].

In addition to high thermal conductivities, graphene and h-BN also exhibit high resistance to oxidation. The highly stable sp^2 bonds that make up the materials prevent oxidation of graphene in an air atmosphere up to 500ºC. H-BN has even higher resistance to oxidation due to the presence of boron and is stable in air up to 800ºC.

Due to the high thermal conductivities, excellent mechanical properties, and resistance to oxidation BN nanomaterials make excellent candidates for polymer additives to form polymer

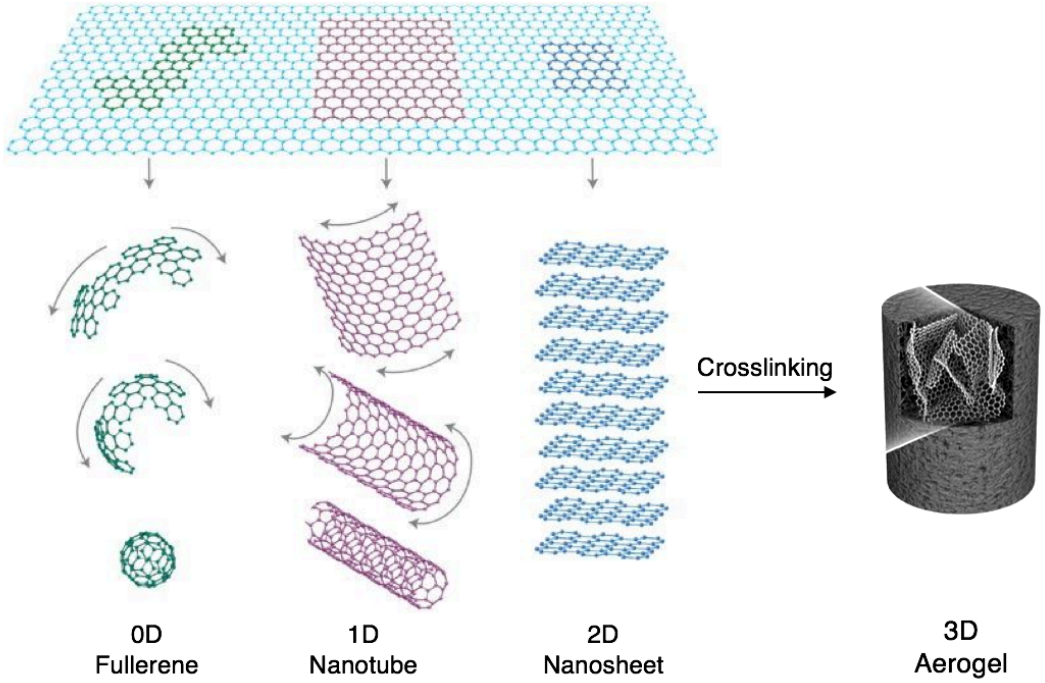

Figure 1.5 Graphene is the building block for other carbon nanomaterials. It can be rolled into a ball for a 0D fullerene, rolled into a cylinder for a 1D nanotube, or used as a 2D single layer of atoms. Additionally it can be crosslinked into a 3D morphology as an aerogel. Isoelectronic structures can also be synthesized of h-BN with the exception of BN fullerenes[246].

nanocomposites in order to increase the thermal and mechanical properties. Graphene materials are also good candidates but will impart some electrical conductivity to the polymers.

1.4 Structural Polymorphs: Fullerenes, Nanotubes, Nanosheets and Aerogels

Going from a bulk material to a single layer material is not the only manner of forming a nanomaterial. Other nanomaterials can be derived from the hexagonal structure of bulk graphite or h-BN as shown in **Figure 1.5** and include 0D fullerenes, 1D nanotubes and nanoribbons, and 3D aerogels.

1.4.1 0D Fullerenes

Beginning with the nanomaterial of the smallest dimension, zero dimensional fullerenes were the first nanoscale allotrope of carbon to be synthesized. Fullerenes, or C_{60}, were first isolated in 1986 by Richard Smalley who was awarded the 1996 Nobel Prize in Chemistry for his work[23]. C_{60} is an icosahedral cage with a similar structure to graphite, but contains both hexagons and pentagons. Other allotropes of C_{70} and C_{80} have also been synthesized. To date, true fullerenes of boron nitride have not been reported.

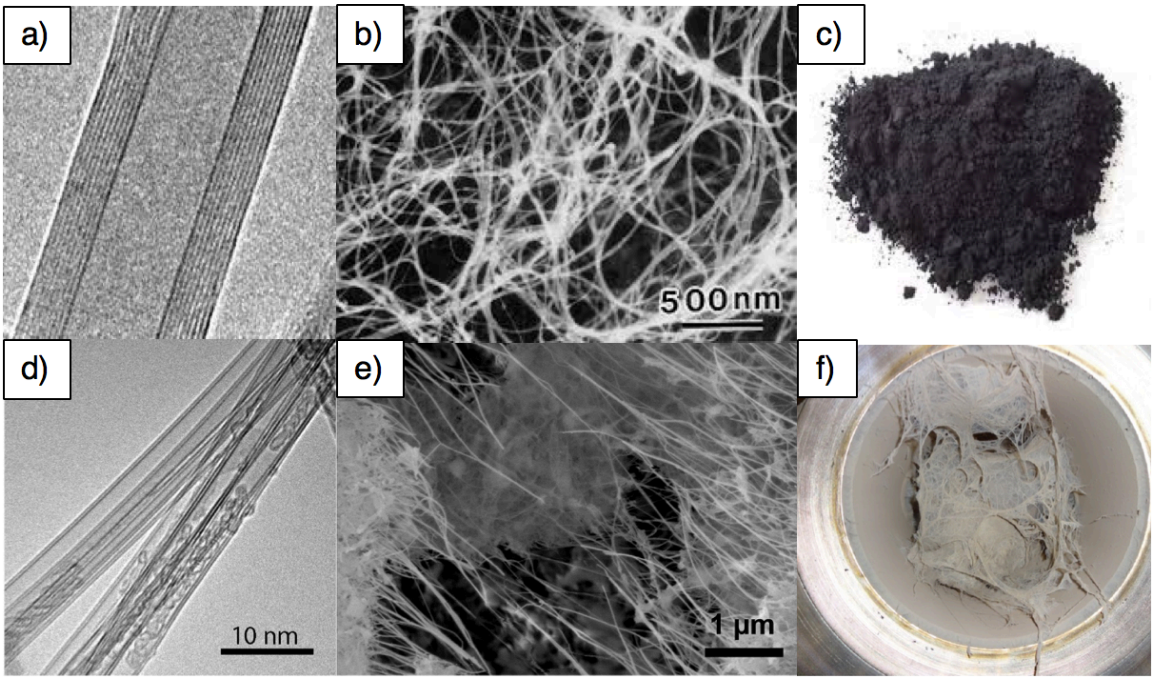

Figure 1.6 a-c) TEM, SEM, and photograph of CNTs, d-f) TEM, SEM, and photograph of BNNTs[32].

1.4.2 1D Nanotubes and Nanoribbons

One dimensional nanomaterials extend in only one direction and include nanotubes and nanoribbon structures. Carbon nanotubes (CNTs) were first studied by Iijima in 1991, and are sp^2 bonded graphene sheets that are wrapped into perfect cylinders as shown in **Figure 1.6a-c**[24,25]. They can be synthesized using chemical vapor deposition or arc-discharge methods as single

walled CNTs or multi-walled CNTs and their electronic properties are highly dependent on the chirality of the nanotube, as well as the number of walls[26,27]. The closely related family of graphene nanoribbons (GNRs), can be viewed as unrolled analogs of CNTs, or essentially thin strips of graphene a few nanometers wide. They are synthesized through both top-down methods by unzipping of CNTs, as well as bottom-up methods using molecular precursors[28,29]. CNTs and GNRs have captivated the fields of solid state physics and materials science due to their intriguing electronic properties, where the band structures of CNTs and GNRs are determined by their widths and chiralities.

Boron nitride nanotubes (BNNTs) were first predicted by the Cohen group in 1994 and synthesized in the Zettl group shortly thereafter and possess similar cylindrical structures to CNTs (**Figure 1.6d-f**)[30,31]. Research on these materials was hindered due to a lack of synthetic method capable of producing large quantities of materials. In 2014 scalable methods of producing BNNTs using inductively coupled plasmas were published making BNNT research more accessible[32,33]. Boron nitride nanoribbons are predicted to have unusual magnetic properties and have been synthesized by longitudinal unzipping of BNNTs[34]. Unlike CNTs and GNRs, the electronic properties of BNNTs and BNNRs are largely independent of chirality and width and have a constant band gap of ~5.8eV[13].

1.4.3 3D Aerogels

While 3D analogs of layered materials are classically considered bulk, a relatively new class of nanostructured 3D assemblies of nanomaterials have been studied called aerogels. Graphene or BN aerogels are three dimensional structures in which the nanosheets have been covalently crosslinked together. They are porous, low density materials with high surface areas and are of particular interest because they are capable of integrating macroscopic amounts of nanomaterial into a single structure. Graphene and boron nitride aerogel structures, properties and characterization techniques are extensively discussed in **Chapter 2.**

PART I: 3D Aerogels Based on 2D Building Blocks

Chapter 2: Introduction to 3D Aerogels

Nano Fun Fact: The first aerogel synthesized by Steven Samuel Kistler was the result of a bet with colleague Charles Learned to replace the liquid in strawberry jelly with gas without causing shrinkage.

2.1 Aerogel Background

Aerogels are a class of three-dimensional materials characterized by their high surface areas, low densities and hierarchical porosities. Hierarchical porosity is the presence of micropores with diameters below 2nm, mesopores with diameters between 2 and 50nm, and macropores with diameters greater than 50nm. Mesopores and micropores contribute to the large surface area of aerogels while macropores provide accessibility to the large active surface area.

The first documented aerogel synthesis was a silica aerogel by Steven Samuel Kistler in 1931, with an early application in aerospace[35]. Silica aerogels were incorporated into the Stardust mission in 1999 to capture matter from space and bring back to earth for study[36]. Since 1931, the field of aerogels and scope of study has expanded tremendously with new classes of aerogels being synthesized regularly and incorporated into new and exciting applications. Other classes of aerogels include carbon aerogels, polymer aerogels, metal oxide aerogels, quantum dot and metal aerogels[37–45] (**Figure 2.1)**. They have been integrated into a variety of applications in aerospace, catalysis, supercapacitors, hydrogen storage, water treatment, and sensors[46–51].

Due to the large amount of research studying the extraordinary properties of nanomaterials, aerogels that are composed of nanoscale building blocks have been a rapidly expanding area of research. They have the potential to incorporate macroscopic amounts of nanomaterials into a single structure, while maintaining the extraordinary properties of the nanomaterial building block. While **Chapter 1** discussed graphene and boron nitride (BN) nanomaterials and their remarkable properties, in this chapter aerogels based on graphene and BN building blocks will be introduced

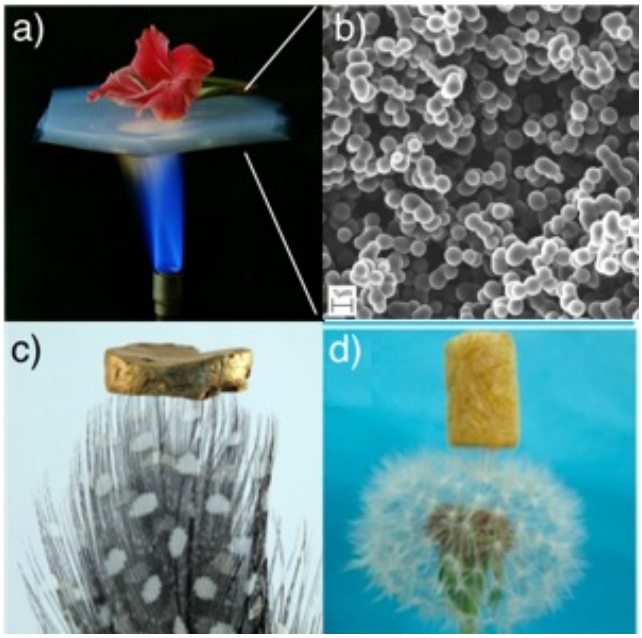

Figure 2.1 a) Image of silica aerogel protecting delicate flower from the hot blue flame due to low thermal conductivity b) SEM image of silica aerogel showing porous morphology c) Gold aerogel and d) polyimide aerogel with low densities sitting on top of flowers[44,254,255].

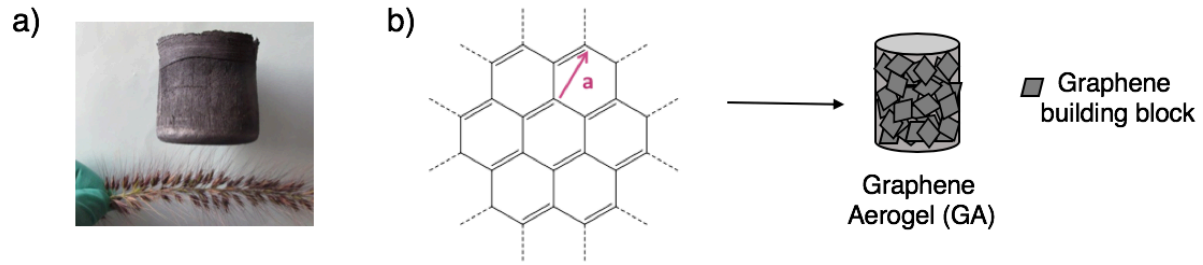

Figure 2.2 a) Image of GA not disturbing flower petal due to low density[256] b) Graphene building blocks incorporated into aerogel morphology.

including their synthesis, approaches for chemical modification, and the plethora of applications they can be integrated into. Additionally, readers will be given an introduction to the characterization methods used throughout this dissertation to study the structural and chemical composition of aerogels.

2.2 Graphene Aerogels

Graphene aerogels (GAs) are three-dimensional monoliths made up of graphene sheets which are chemically crosslinked into a high surface area, porous morphology with low density (**Figure 2.2)**. The allure of such a material lies in the combination of the intrinsic properties of the graphene building block, as described in **Chapter 1**, and the textural properties afforded by the aerogel morphology. While 2D graphene requires labor intensive nanofabrication steps for integration into many applications, GAs incorporate grams of graphene into a single multifunctional structure that retains many of graphene's exceptional properties[52,53]. For example, GAs are highly conductive and have excellent mechanical properties as a result of the graphene sheets making up the structure[54,55].

2.2.1 Graphene Aerogel Synthesis

The base-catalyzed synthesis of GAs, developed by Worsley et al., is summarized in **Figure 2.3** and begins with a 20 mg/mL graphene oxide (GO) precursor suspension in water[55]. GO is a graphitic material with a large number of oxygen containing functional groups on the surface, including carboxylic acids, hydroxyl groups and epoxides (**Figure 2.3a**)[56] . Ammonium hydroxide (1:6 by volume NH_4OH:H_2O) is added to the GO suspension in order to catalyze reactions between functional groups on GO sheets and leads to a process called gelation. Gelation takes place at 80°C over 3 days and covalently crosslinks the GO sheets together. The suspension undergoes a sol-gel transition to form a GO hydrogel which shrinks to about half the volume of the original GO suspension (**Figure 2.3c**). The resulting hydrogel is a porous material, with pores occupied by water.

To recover an aerogel, the solvent must be removed from the hydrogel and replaced with air. The drying method must not have surface tension; Simple evaporation of the solvent would lead to complete collapse of the pore structure and a dense, low surface area material[57]. Solvent removal without surface tension can be achieved using supercritical CO_2 or freeze-drying. For supercritical drying, the GO hydrogel is solvent exchanged into acetone, which is miscible with CO_2, followed by exchange with liquid CO_2 in a pressure vessel designed for supercritical drying. After full exchange of acetone for CO_2, the critical point of CO_2 is surpassed to form a supercritical fluid. Supercritical fluids have both liquid and gaseous properties, and an aerogel remains after

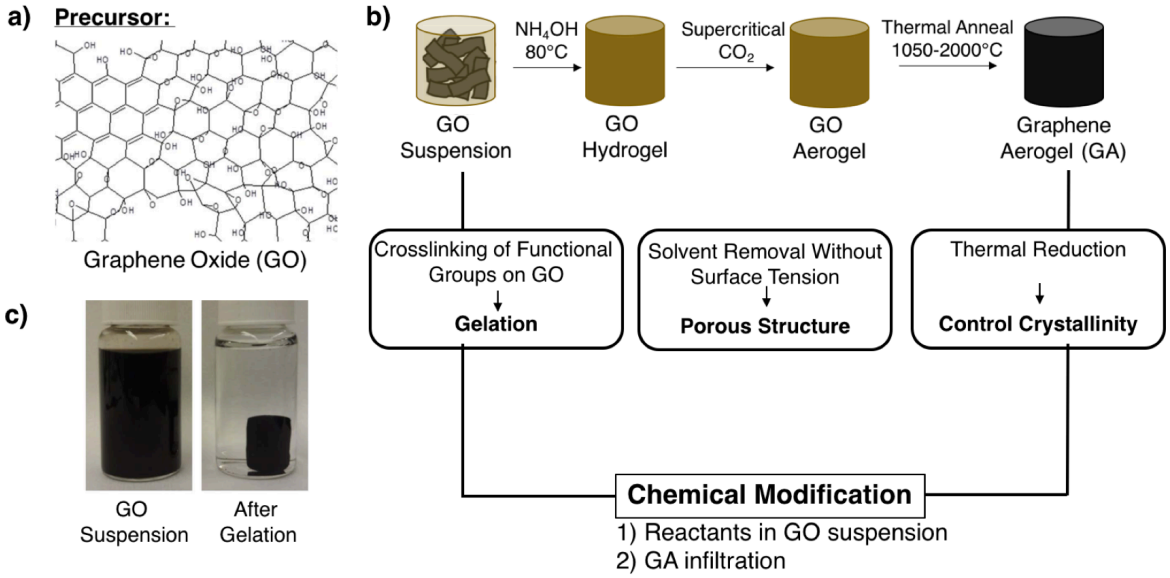

Figure 2.3 a) Chemical structure of GO used in aerogel synthesis b) Schematic of base-catalyzed synthesis of GAs using GO precursor, gelation, drying, and heat treatment c) Image of GO suspension before and after gelation[56,169].

evaporation of the supercritical fluid. In order for a hydrogel to be dried using supercritical drying it must be well formed and capable of withstanding solvent exchanges. The other solvent removal method is freeze-drying where the solvent, usually water, is frozen solid, and vacuum is applied to sublime the solvent. Both drying methods yield GO aerogels but they have differing textural properties, with supercritical drying resulting in higher surface areas than freeze-drying.

After drying, the GO aerogel still has a large oxygen content and many functional groups, resulting in a low conductivity mixture of sp^2 and sp^3 bonds. In order to fully graphitize the aerogel to a graphene aerogel, it is thermally reduced at 1050°C in argon to remove oxygen containing functionalities and anneal out defects. It can be further reduced by a subsequent treatment between 1500-2000°C. The firing temperature used for thermal reduction can be used to control the crystallinity of the graphene aerogel, with higher annealing temperatures resulting in highly crystalline graphene aerogels[58]. High temperature graphitization treatments of graphene aerogels are done in collaboration with Marcus Worsley and Lawrence Livermore National Lab.

2.2.2 Graphene Aerogel Structural Characterization

Electron microscopies are the predominant techniques used for structural characterization of aerogels including scanning electron microscopy (SEM) and transmission electron microscopy (TEM). They play vital roles in studying aerogels on the micro and nanoscale.

2.2.2.1 Scanning Electron Microscopy

SEM is a key tool in aerogel characterization to study their microscale morphology. It utilizes a focused beam of electrons with energies from 1kV-30kV in order to image the sample. In this technique, electrons can interact with the sample in a number of ways, but SEM images shown in this dissertation are generated from electrons inelastically interacting with the sample and emitting a secondary electron which is detected and used to construct an image. A simplified

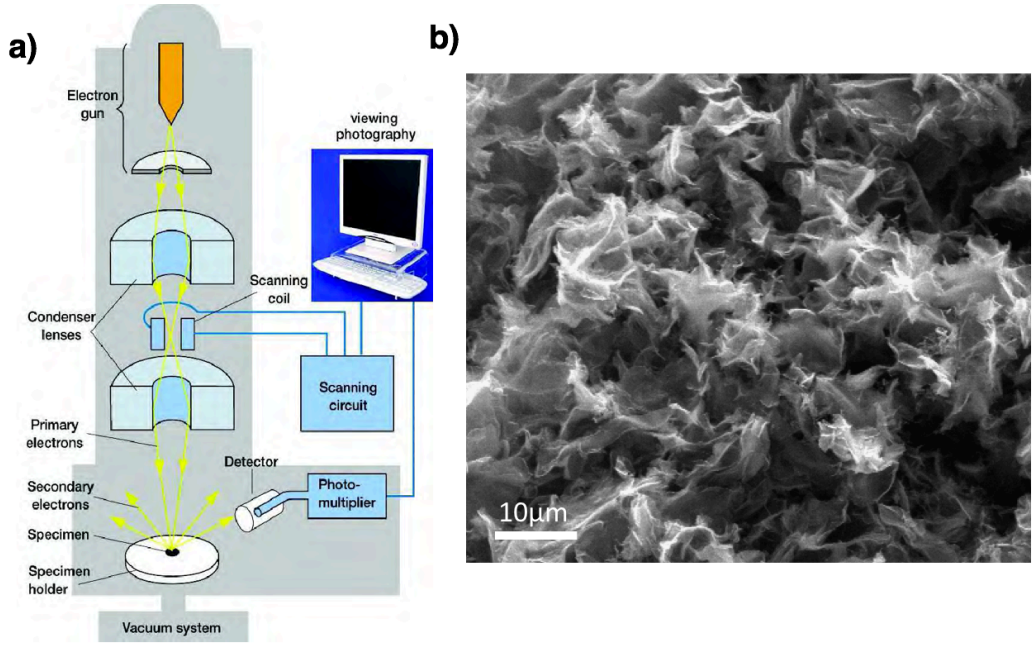

Figure 2.4 a) Schematic for a scanning electron microscope showing electron paths[257] b) Representative SEM image of GA.

diagram is shown in **Figure 2.4a**. As implied by the name, SEM images are generated by scanning of the electron beam and detecting secondary electrons at points throughout the sample to construct an image of the surface.

A representative SEM image of a GA is shown in **Figure 2.4b**. The image displays the three dimensional nature of the sample made up of graphene sheets. The crosslinking of the sheets leads to the open structure of the aerogel and contributes to its high surface area. Additionally, free-space between graphene sheets makes up the pore structure characteristic of aerogels.

2.2.2.2 Transmission Electron Microscopy

TEM is a powerful technique to study nanomaterials and gives information on the nanoscale morphology of aerogels. TEM uses a beam of electrons accelerated at high voltage (80keV unless otherwise noted) that pass through a thin sample. Electrons transmitted through the

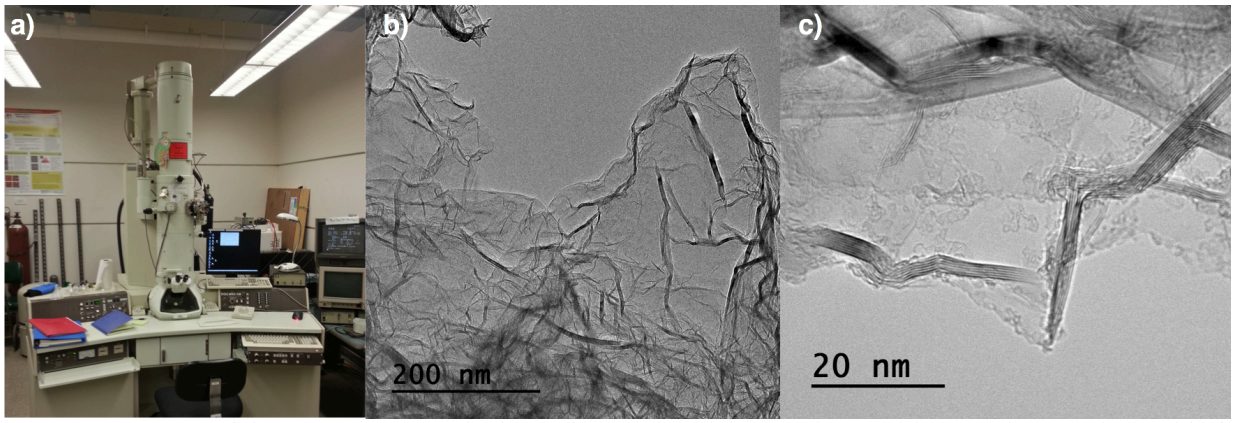

Figure 2.5 a) Image of the JEOL 2010 TEM in the Zettl Group b,c) Representative TEM images of GAs at low and high magnification, respectively.

sample are transferred to a florescent screen or CCD for image capture. The JEOL 2010 TEM in the Zettl Group is shown in **Figure 2.5a** and has a resolution of approximately 1nm.

With regards to utilizing TEM as a characterization tool for GAs, it is important for studying the morphology of the individual graphene sheets that make up the aerogel. Graphene sheets typically are full of wrinkles as opposed to lying flat. This is the characteristic, "tissue paper-like" morphology of graphene sheets as shown in **Figure 2.5b**. High magnification imaging can also be used to observe the presence of lattice fringes from layers of graphene stacked on top of one another and measure the 0.33nm interlayer space of the (002) plane (**Figure 2.5c)**.

2.2.3 Graphene Aerogel Chemical Characterization

Comprehensive chemical characterization of modified aerogels is necessary in order to fully understand the new chemistries introduced. Raman and infrared spectroscopy probe the vibrational properties of aerogels and are powerful tools for studying new chemical functionalities, defect concentration, and doping in aerogels. Additionally, x-ray photoelectron spectroscopy provides highly sensitive bonding information and x-ray diffraction reveals crystallographic information of the aerogels. These characterizations coupled with structural characterization are necessary in order to full study the aerogel.

2.2.3.1 Raman Spectroscopy

The principle of Raman spectroscopy depends on inelastic scattering of light when it interacts with a sample. Inelastic scattering occurs due to the characteristic vibrations in the material which can serve as a vibrational fingerprint. To characterize these vibrations, the energy shift between incident light and scattered light is measured and the shift is equal to the energy of the corresponding phonon. One selection rule for inelastic scattering is that there must be a change in polarizability due to the vibration. As such, most asymmetric vibrations cannot be detected using Raman spectroscopy. Raman spectroscopy is particularly useful for studying graphene materials and important information can be deduced from subtle changes to the Raman spectrum including layer number, crystallinity, chemical functionalization and doping.

The characteristic Raman spectrum of graphene is shown in **Figure 2.6a**. It contains a peak at 1590cm^{-1} due to the E_{2G}, in plane phonon. This peak is called the G peak. The D peak is

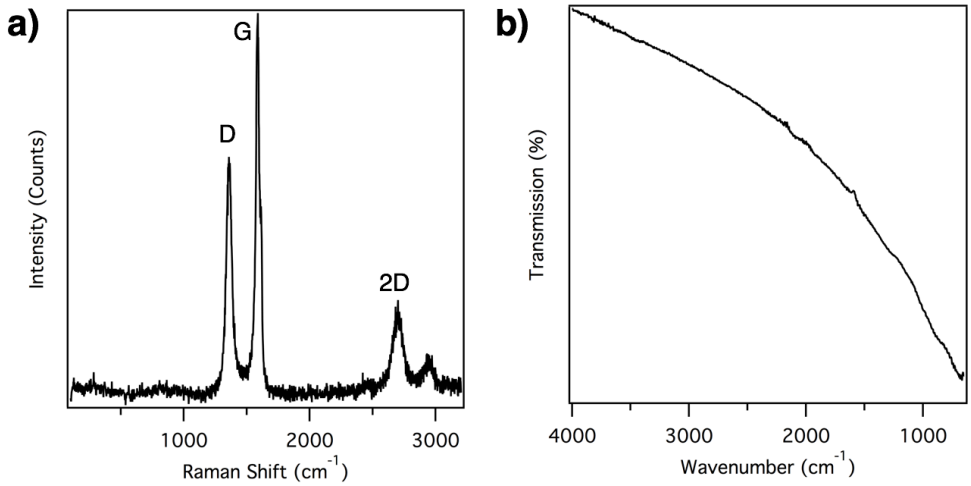

Figure 2.6 a) Raman spectrum and b) IR spectrum of GAs.

the breathing mode in the lattice. It occurs at 1360cm^{-1} and requires a defect in the material in order to activate. A peak at 2680cm^{-1} called the 2D peak is the overtone mode for the D peak and requires two phonons.

Due to the fact that the D peak requires a defect in order to activate, a large D peak is due to a large population of defects in the sample. The ratio of the intensity of the D peak to the G peak (I_D/I_G) is a quantitative metric for determining density of defects in the material and comparing between samples. An increased DtoG ratio in a chemically modified sample compared to a control GA sample indicates an increased defect density after chemical modification. Throughout this dissertation I_D/I_G will be used to study introduction of dopants, crystallinity, or other chemical functionalizations into GAs.

2.2.3.2 Infrared Spectroscopy

Similar to Raman spectroscopy, infrared spectroscopy (IR) probes the vibrational structure of aerogels. Due to graphene's extended C=C structure, the IR spectrum for all graphene materials including GAs is simply a drifting baseline and lack of noticeable peaks (**Figure 2.6b)**. After chemical modification, the introduction of new peaks in the IR spectrum can be used as indicators of successful modification.

2.2.3.3 X-Ray Photoelectron Spectroscopy

X-Ray photoelectron spectroscopy (XPS) is used to gain highly sensitive bonding information in the aerogels and is heavily utilized in order to understand the chemical modifications in graphene and BN aerogels. A schematic of the technique is shown in **Figure 2.7a** where monochromatic x-rays are used as a photon source. Due to their high energy, x-rays are capable of ionizing core energy levels of the material and an electron is ejected. This ionized

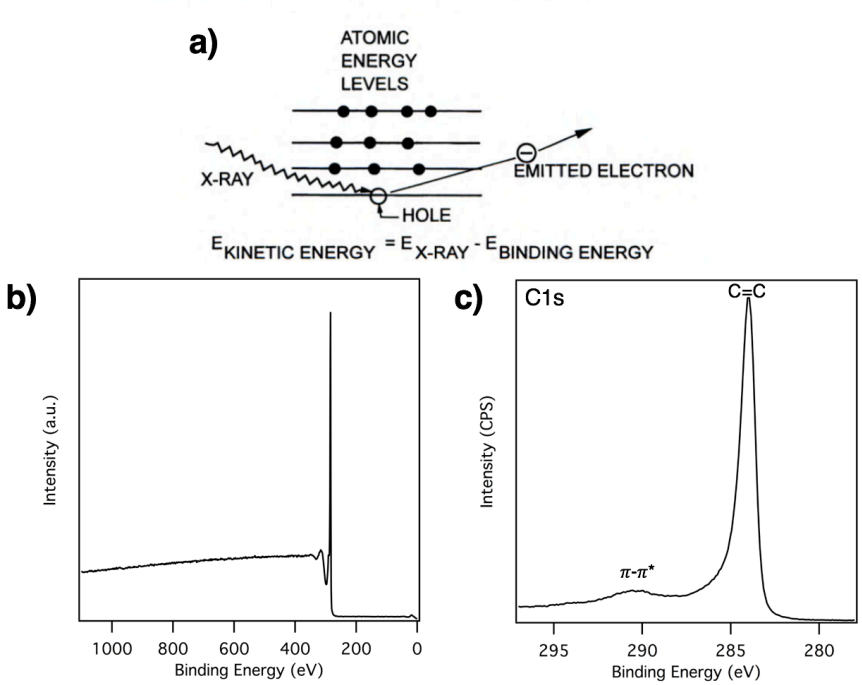

Figure 2.7 a) Diagram demonstrating electron transitions that occur for XPS b) Survey spectrum and c) C1s high-resolution scan of GA.

electron is detected and its energy is measured. The x-ray energy is known, the kinetic energy of the ionized electron is measured and due to the following relation,

$$E_{kinetic} = E_{x-ray} - E_{binding} \quad \textbf{Equation 2.1}$$

the binding energy of the electron can be calculated. Binding energies are highly dependent on the local bonding environments and can be assigned to specific bonding configurations, thus allowing researchers to thoroughly chemically characterize their material.

XPS analyses typically contain one survey spectrum, a low resolution scan over a large range of energies, and high resolution scans over a small energy range corresponding to electrons ejected from elements of interest. For example, a GA survey spectrum is shown in **Figure 2.7b**, with a large peak at 285eV, which corresponds to C1s electrons. A high resolution scan in the C1s spectrum reveals a spectrum with more features that can be deconvoluted to reveal the presence of electrons in difference chemical environments. **Figure 2.7c** shows the C1s spectrum of a GA, which has a large peak at 284eV, corresponding to C=C bonds. A small, broad peak at 290.7eV is a shake-up feature due to π-π* transitions in sp^2 bonded materials. The C1s spectrum can be used to study chemical modifications occurring with carbon, and high resolution scans in other energy ranges are also used to study chemical modifications using other elements, making XPS one of the most important techniques in this dissertation to study the introduction of new chemical species.

2.2.3.4 X-Ray Diffraction

X-Ray diffraction (XRD) is used to identify crystal phases present in aerogels and uses the condition for constructive interference of waves, Bragg's law, as described in **Equation 2.2**.

$$n\lambda = 2dsin\theta \quad \textbf{Equation 2.2}$$

where θ is the diffraction angle, λ is the x-ray wavelength and d is the distance between planes

The periodic arrangement of crystalline materials will meet this Bragg condition at specific values of θ, resulting in strong diffraction at these angles, corresponding to crystal planes. Thus, it is possible to construct a diffractogram to study the crystal structure of a material. This process is summarized in **Figure 2.8a**.

The typical diffractogram for a GA is shown in **Figure 2.8b**. It contains a strong peak around 29° which is due to diffraction from the (002) plane of graphene. This corresponds to a d spacing of around 0.33nm between (002) planes, which is the interlayer spacing of graphite. GAs have disordered packing of the (002) plane and low density, resulting in a broad (002) peak from d spacing differing from the expected value, and low overall signal, respectively. The other peak

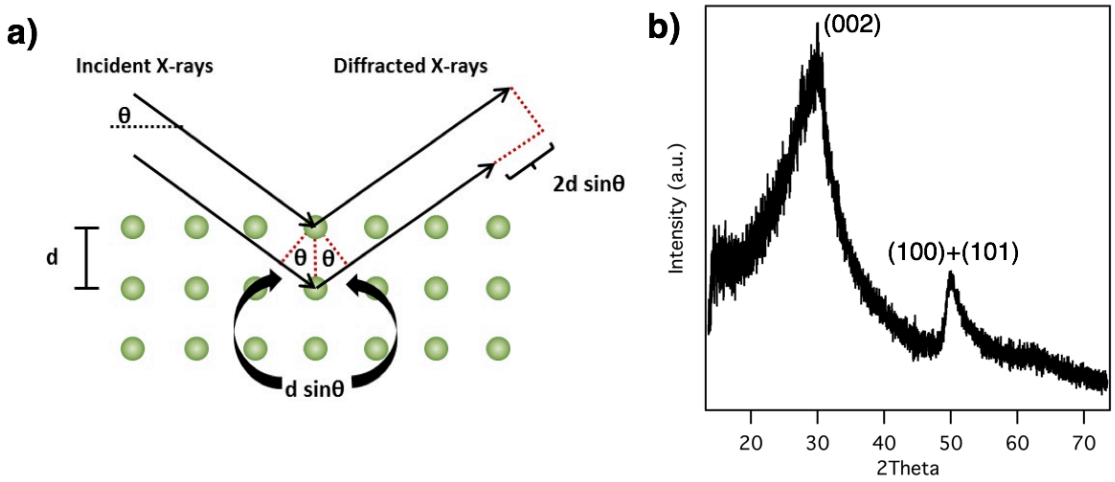

Figure 2.8 a) Diagram illustrating Bragg's law for constructive interference b) Representative diffractogram of a GA.

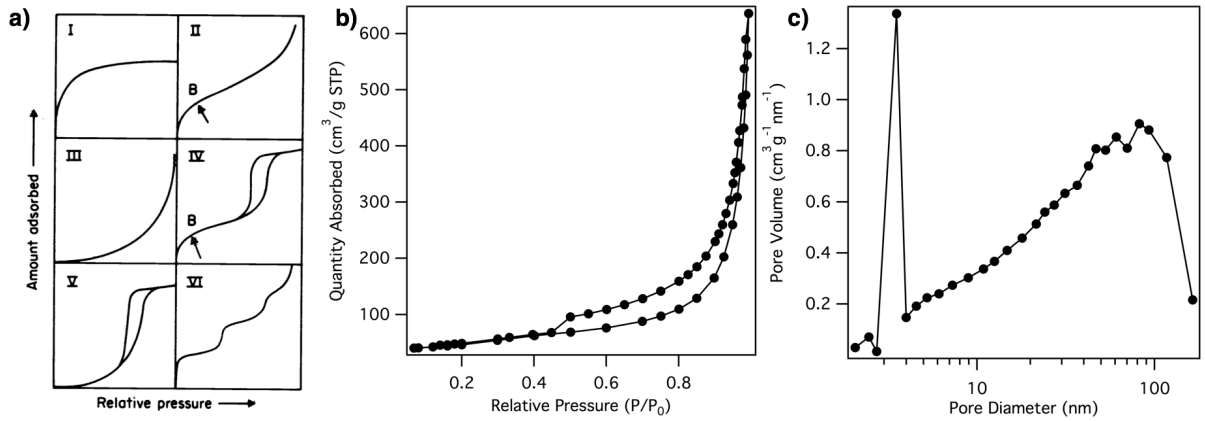

Figure 2.9 a) Nitrogen isotherms with IUPAC classifications Type I-VI[59] b) Nitrogen adsorption and desorption isotherm and c) Pore size distribution of GA.

occurs at 50° due to diffraction from the (100) and (101) planes. When introducing chemical modifications into graphene aerogels, these two peaks should continue to be present and additional peaks can emerge as a result of introducing additional crystal phases into the structure.

2.2.4 Graphene Aerogel Textural Characterization

Nitrogen porosimetry is a volumetric method used to study the textural properties of aerogels. Textural properties include surface area and pore size distribution and are part of the fundamental properties afforded by integrating nanomaterials into an aerogel morphology. In this method, over 50mg of sample is loaded into a porosimeter tube and evacuated. After immersing in liquid nitrogen, the sample is dosed with known volumes of nitrogen and the pressure measured. The relative pressure (P/P_0) is calculated by dividing the measured pressure by the saturation pressure of nitrogen and isotherms are plotted as the quantity adsorbed vs. the relative pressure.

The shape of the nitrogen isotherm can reveal information about the pore sizes present in the sample. There are six types of isotherms defined by IUPAC which are illustrated in **Figure 2.9a**[59]. Type I isotherms are indicative of microporous materials, Type II are macroporous or non-porous solids and Type IV are mesoporous materials. Type III and V are uncommon and governed by adsorbate-adsorbate interactions and Type VI is due to stepwise multilayer adsorption on non-porous materials. In addition to the Type of isotherm, IUPAC also defines the type of hysteresis loop. Hysteresis occurs due to capillary condensation in mesopores and the magnitude of the hysteresis loop can indicate pore volume in the sample. Graphene aerogels have an H3 hysteresis loop indicative of slit-like pores and a Type IV isotherm for mesoporous solids, shown in **Figure 2.9b**.

The isotherm is used to calculate the surface area of samples using Brunaer-Emmett-Teller (BET) theory[60]. BET is a simplified, yet widely used theory for adsorption and surface area determination. It assumes gas molecules can adsorb into an infinite number of layers, adsorbates only interact with adjacent neighbors and Languimir's theory for monolayer adsorption can be applied to each layer. The BET equation is shown in **Equation 2.3**:

$$\frac{p}{n^a \times (p^0 - p)} = \frac{1}{n_m^a \times C} + \frac{(C-1)p}{n_m^a \times C p^0} \qquad \textbf{Equation 2.3}$$

where n^a is the amount adsorbed at the relative pressure p/p^0, n_m^a is the monolayer capacity and C is the BET constant.

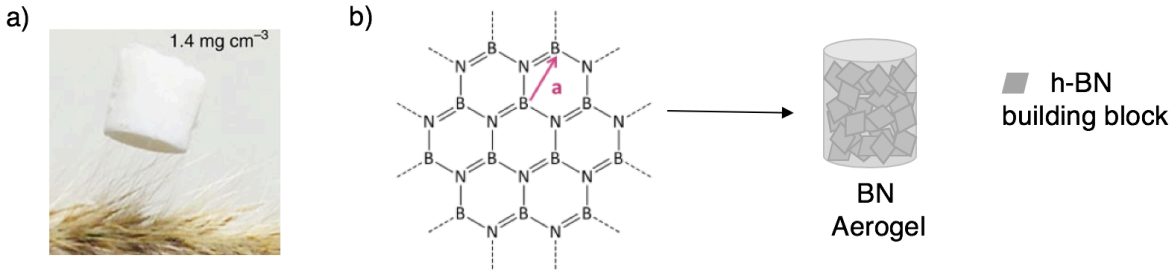

Figure 2.10 a) Image of BN aerogel resting on top of a flower without disturbing the pedal due to low density[258] b) Diagram showing h-BN sheets incorporated into aerogel morphology.

The BET equation can be reduced to a linear, y=mx+b form where y= $\frac{p}{n^a \times (p^0 - p)}$, m=$\frac{(C-1)}{n_m^a \times C}$ and b=$\frac{1}{n_m^a \times C}$ in order to calculate the surface area. Graphene aerogels typically have a BET surface area of 800-1000 m^2/g.

The pore-size distribution can also be determined using nitrogen porosimetry by applying Barrett-Joyner-Halenda (BJH) theory. This method uses the Kelvin model applied to meso and small macropore volumes to construct a pore size distribution. The pore size distribution plots the pore volume vs. pore width and can be used to confirm the hierarchical porosity of aerogels. Typically graphene aerogels have a peak in the mesopore region due to a large population of mesopores creating a large volume, and a gradual increase in volume in the macropore region (**Figure 2.9c)**.

2.3 Boron Nitride Aerogels

BN aerogels are composed of graphene's isoelectronic counterpart, h-BN and h-BN sheets are covalently cross-linked into a 3D, high surface area, and porous aerogel morphology (**Figure 2.10)**. While graphene aerogels are highly conductive, BN aerogels adopt the properties of the h-BN building block. The advantages of incorporating graphene into an aerogel morphology are mimicked in BN and given BN's drastically different electronic properties as discussed in **Chapter 1**, BN aerogels are well suited for insulating applications including polymer composites, water treatment, and gas storage applications[61–63].

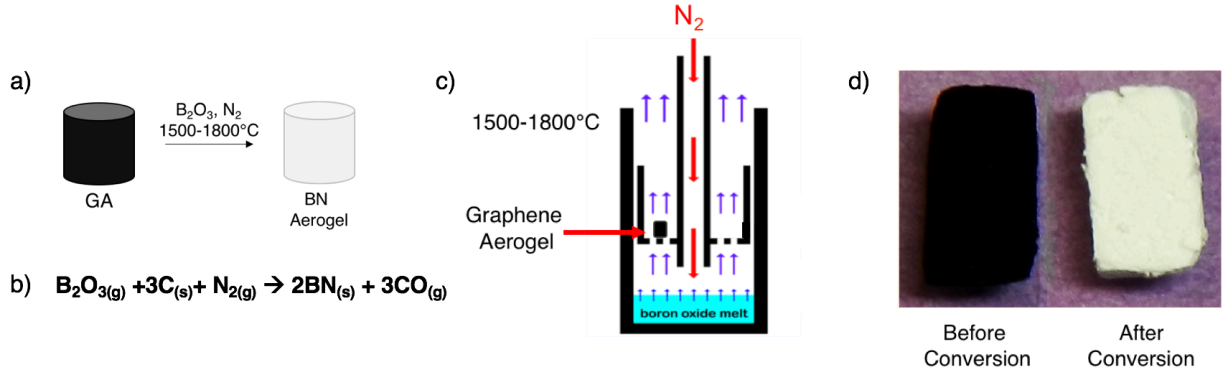

Figure 2.11 a) Reaction conditions and b) Reaction equation for conversion of GA to BN aerogels c) Schematic of the vertical induction furnace used for BN aerogel synthesis d) Image of black GA before conversion and white BN aerogel after conversion[64].

2.3.1 Boron Nitride Aerogel Synthesis

Highly crystalline BN aerogels were first synthesized in the Zettl group in 2013 utilizing a GA as a precursor and exploiting a carbothermal conversion process to BN (**Figure 2.11a**) [64]. In this process, boron oxide and nitrogen gas react with graphene to produce BN and carbon monoxide biproduct (**Figure 2.11b)**. This is experimentally realized using a vertical induction furnace as shown in **Figure 2.11c.** A graphite crucible is assembled with boron oxide in the bottom and graphene aerogels are placed into a separate holder within the crucible to suspend them in the center. The assembled graphite crucible is loaded into the vertical induction furnace for carbothermal reduction. At a temperature between 1500-1800°C, nitrogen is flowed at 75 sccm to the bottom of the crucible in order to sufficiently mix with boron oxide and react with the GA. After 40 minutes, GAs are fully converted to BN. The conversion process is evident even with the naked eye and shown in **Figure 2.11d.** Graphene aerogels are a black color as would be expected from its electronic properties, and after conversion the aerogel is converted to a fully white aerogel indicative of the wide band gap of BN.

2.3.2 Boron Nitride Aerogel Chemical Characterization

Characterization techniques discussed in **Sections 2.2.2-2.2.4** that are employed in order to fully study the structural and chemical properties of GAs are also utilized to characterize BN aerogels.

BN has strong IR active vibrational modes, making infrared spectroscopy particularly useful to analyze BN aerogels and their chemical modifications. The primary IR active modes in BN are the E_{2G}, in-plane vibration of lattice occurring at 1367cm^{-1} and the B-N-B bending mode

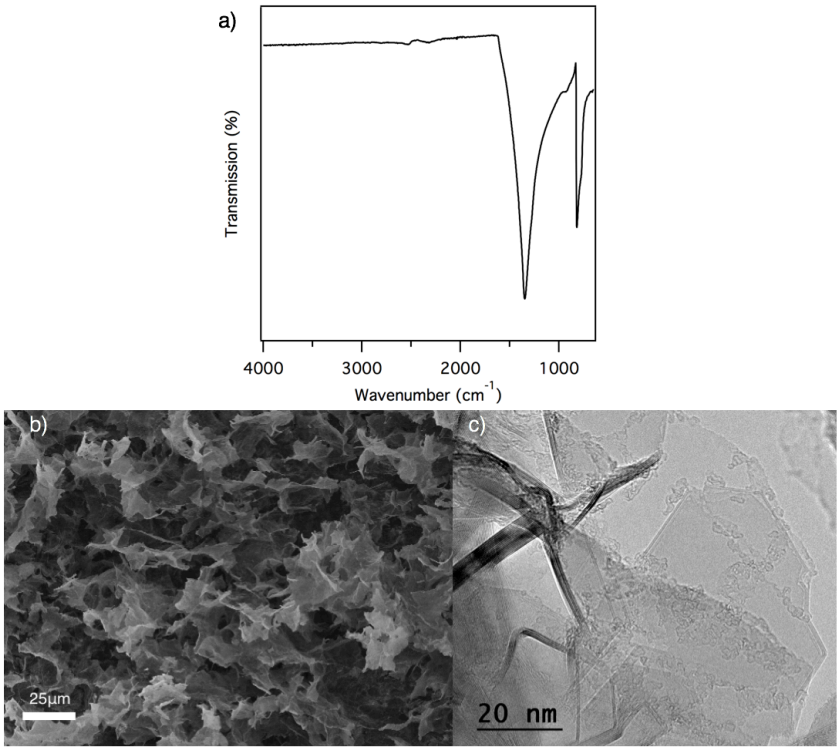

Figure 2.12 a) FTIR spectrum b) Representative SEM image and c) Representative TEM image of BN aerogels.

occurring at 810cm^{-1}. Both peaks are clearly visible in the BN aerogel IR spectrum shown in **Figure 2.12a**. The E_{2G} mode is also a Raman active mode and can be used for further diagnostic confirmation of a h-BN phase. However, due to the large fluorescence of BN, it can be challenging to decipher this peak over the background signal. For this reason, IR spectroscopy is predominantly used in this dissertation for probing the vibrational properties of BN aerogels.

2.3.3 Boron Nitride Aerogel Structural Characterization

As in **Section 2.2.2**, the structural properties of BN aerogels are studied using SEM and TEM. Due to BN's insulating nature, SEM imaging results in charging of BN aerogels. To prevent this, the sample is prepared for SEM by sputtering a thin layer of gold on the surface to dissipate the charge while maintaining the morphology of the sample. As shown in **Figure 2.12b**, BN aerogels have a highly irregular 3D structure that is made up of sheet morphologies crosslinked together. The open pore structure reflects the low density of BN aerogels and high porosity. TEM reveals the morphology of individual BN sheets (**Figure 2.12c)**. The sheets contain significantly less wrinkling on the nanoscale as compared to the precursor GAs, and are highly crystalline. The reduced wrinkling is likely due to the high temperatures used for the conversion. GAs annealed at high temperatures also undergo flattening[58]. The flat sheet morphology impacts the textural properties of BN aerogels, discussed below.

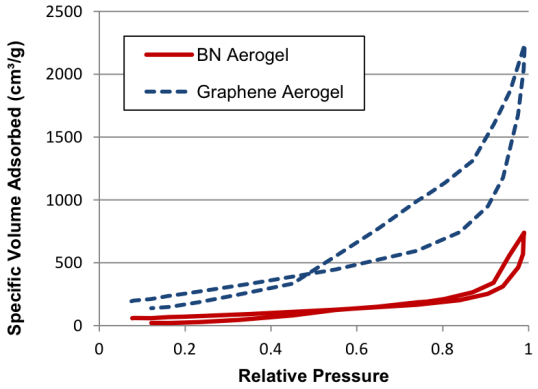

Figure 2.13 Nitrogen adsorption and desorption isotherms of GA and BN aerogels[64].

2.3.4 Boron Nitride Aerogel Textural Characterization

The textural properties of BN aerogels are studied using nitrogen porosimetry to determine the BET surface area and pore size distribution. The nitrogen adsorption and desorption isotherms of BN aerogels are shown in **Figure 2.13** along with the isotherms for a GA. The quantity of N_2 adsorbed is clearly lower in BN aerogels at all relative pressures, and the corresponding BET surface area is 431 m^2/g, which is reduced compared to the 1158 m^2/g BET surface area of the GA precursor, but still high enough for many applications.

2.4 Approaches to Chemical Modification

One of the paramount goals of this dissertation is to introduce chemical modifications into graphene and BN aerogels in order to improve and tailor their performance for specific applications. As such, there are two areas in the synthesis that can targeted in order to introduce new chemistries into graphene and BN aerogels. The first approach is during the synthesis of GAs

by selecting a precursor for modification and including it in the GO suspension (**Figure 2.14a)**. The precursor can react with the functional groups on the GO or with the NH_4OH to synthesize a modified GO hydrogel and aerogel. Additionally, the thermal annealing temperature is a parameter that can be carefully controlled to study the change in chemistry with temperature. This approach is utilized to synthesize boron carbon nitride aerogels (**Chapter 4)** and density tunable graphene aerogels and BN aerogels (**Chapter 6)**.

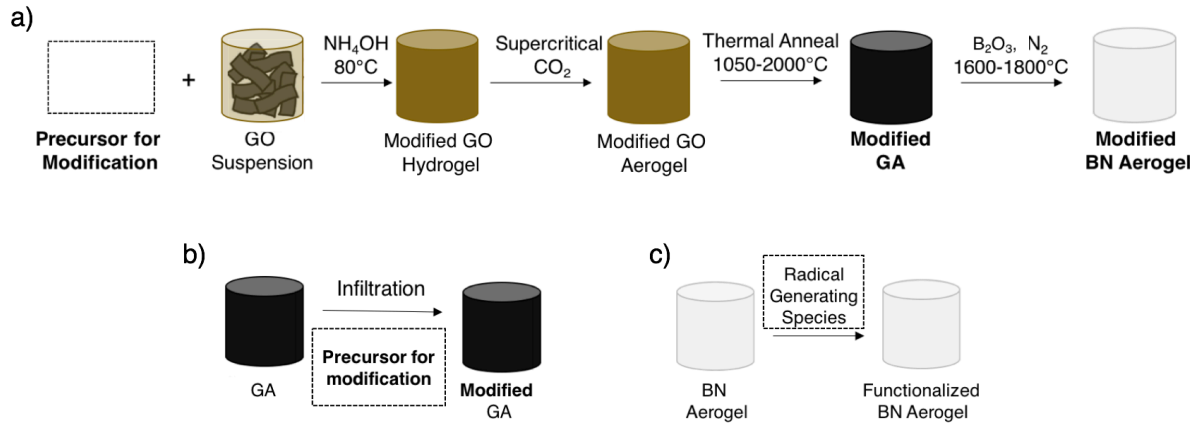

Figure 2.14 a) Approach for chemical modification during aerogel synthesis by incorporating a precursor for modification in the GO suspension b,c) Approach for post-synthetic modification by infiltrating aerogels with precursor for modification or radical generating species, respectively.

Another approach to modify aerogels is by making a control, non-modified GA or BN aerogel and modifying it post-synthesis. This can include infiltrating aerogels with a precursor for modification and additional heat treatment (**Figure 2.14b)** in order to introduce dopants or defects into the aerogel (**Chapter 3)** or synthesize core-shell structures (**Chapter 5)**. Post-synthetic modification can also be used to functionalize the surface of aerogels and other BN nanostructures by exposing them to radical generating species (**Figure 2.14c, Chapter 8).**

Chapter 3: Boron Doping and Defect-Engineering of Graphene Aerogels

Nano Fun Fact: Aerographite, a type of graphene aerogel, holds the Guinness World Record for lowest density material with a density 0.16 mg/cm^3, 6 times less dense than air.

3.1 Theoretical Motivation to Boron Doping and Defect-Engineering

While graphene itself and graphene aerogels (GAs) have been widely studied and integrated into a variety of applications, modification is necessary in order to improve their performance. Many approaches can be used to alter graphene's electronic structure, with doping being a popular strategy to enhance the electronic and catalytic properties of graphitic materials[65–69]. Two common dopants for graphene are boron and nitrogen due to their similar atomic radii to carbon and ease of substitution.

A large body of theoretical work has been done, predicting some of the promising properties of boron-doped graphene for various applications. Boron doped graphene is predicted to have enhanced Li storage capacity due to the increased binding energy and diffusion of Li ions leading to a theoretical capacity over twice that of graphite[70]. Additionally, DFT calculations indicate that polar B-C bonds improve the absorption kinetics of oxygen for the oxygen reduction reaction, drastically increasing the catalytic activity as a result of boron doping of graphene[71]. Lastly, enhanced gas sensing properties are predicted due to increased binding energies for certain gases and enhanced charge transfer between graphene and the analyte gas[72].

Despite the large amount of theoretical progress on boron-doped graphene indicating that it is a promising material, experimental progress has been much slower. While several studies have used boron and nitrogen incorporation in order to enhance the performance of graphene aerogels for various applications, low temperatures are employed resulting in boron containing functional groups and incomplete reduction of graphene oxide to graphene[66,73–77].

In addition to boron doping of graphene aerogels, this chapter will explore the controlled formation of defects in the graphene lattice, or defect-engineering. This is a relatively new field, where previously the presence of defects was considered to be undesirable. Currently the ability to control the formation and type of defects present in a material can have a profound influence of its properties. For example, the formation of sulfur vacancies in transition metal dichalcogenides is a new route to create active sites and enhance the catalytic properties of the material[78]. Additionally, defect sites in graphene can be active sites for hydrogen adsorption for enhanced hydrogen storage performance[79].

3.2 GAs in Gas Sensing Applications

Graphene has been studied as a potential candidate for high performance gas sensors due to its high conductivity and high surface area that facilitates the adsorption of a large quantity of gas molecules, resulting in a highly sensitive sensor. It has even been reported to detect as low as one molecule of analyte gas[80,81]. However, challenges that remain when considering graphene as a potential commercial gas sensor include:

1) High temperatures and thus high powers are necessary for gases to desorb and allow the sensor to recover
2) Lack of selectivity in its sensing response
3) Challenging and unscalable nanofabrication of graphene sensors

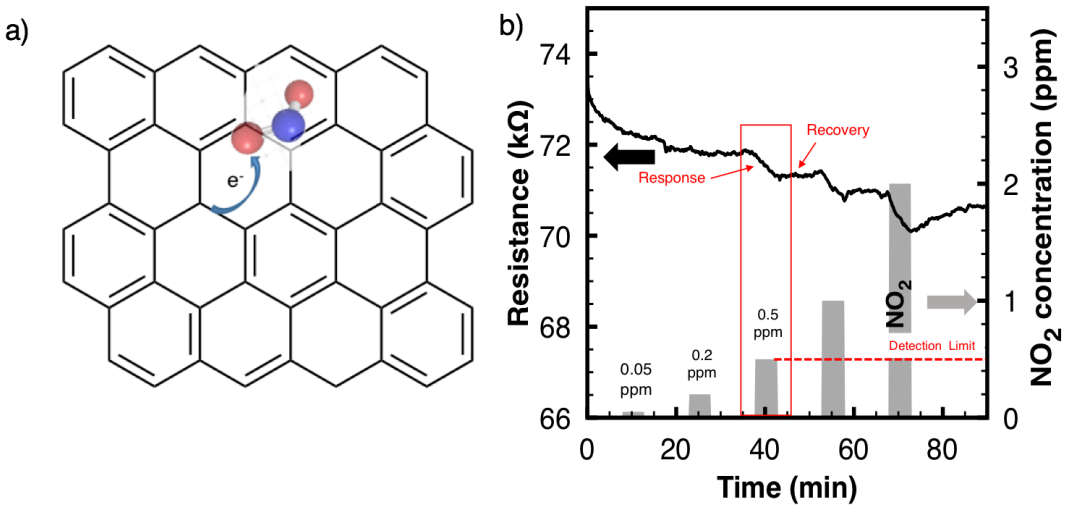

Figure 3.1 a) Illustration of conductometric sensing mechanism demonstrate NO_2 adsorption onto graphene surface and charge transfer from graphene to NO_2 b) Representative gas sensing experiment data set including important sensing parameters, response, recovery, and detection limit.

In order to combat the high temperatures and thus high power consumptions required for gas desorption, a low power microheater using microfabricated poly-silicon as a heater can be employed. This sensing platform was developed in the Maboudian group at UC Berkeley and allows high sensing temperatures to be achieved with minimal power consumption; a necessary characteristic in order to incorporate sensors into personal electronic devices.

GAs have key advantages over graphene as a sensing material. It can be incorporated into the low power microheater sensing platform as the active sensing material in place of graphene and eliminate the challenging fabrication. GAs are highly conductive, with large surface areas and can be simply sonicated and dropcast onto the microheater platform in order to fabricate the sensors.

One challenge that remains with GA gas sensors is that, like their graphene building block, they tend to have a large adsorption energy for a number of gases meaning that they will sense several gases and it is difficult to achieve a selective sensor; Chemical modification is a method that could improve the sensitivity and selectivity of the response by altering the binding energy and charge transfer for certain gases[72,82]. Modifications to GAs for sensing have been largely limited to the introduction of active sensing materials into the high surface area structure of the aerogel, such as nanoparticles or other 2D materials and modifications to pure GAs have not been widely pursued to improve GA sensing capabilities[80,83,84].

3.3 Principles of Conductometric Gas Sensing

This chapter will explore the synthesis and characterization of boron doped and defect-engineered GAs and the effect of the evolving boron chemistries on the gas sensing properties are investigated in order to fabricate an optimized NO_2 gas sensor using only graphene aerogels as a sensing material[85].

Conductometric GA gas sensors are fabricated on a low-power microheater. In conductometric gas sensing the resistance in the sensing material is monitored. When the sensing material is exposed to an analyte gas, the gas will adsorb onto the surface of the material and charge transfer will occur **(Figure 3.1a)** leading to a change in resistance in the material. In the

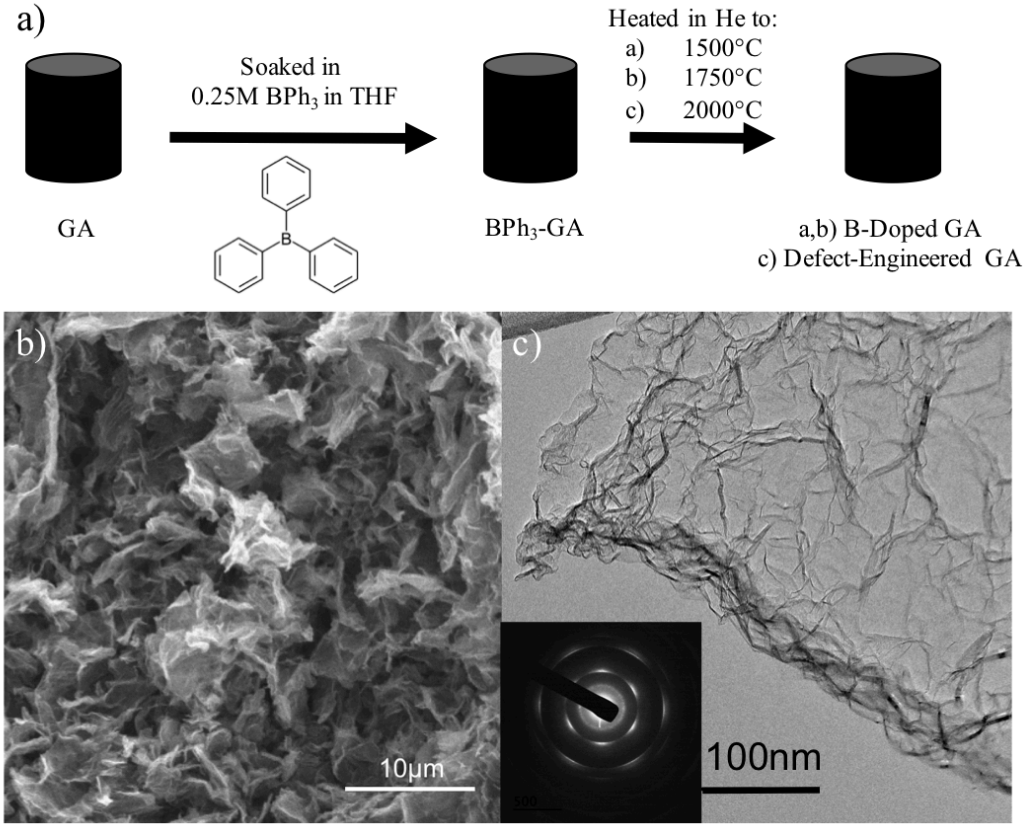

Figure 3.2 a) Synthesis of BPh3-GA's using infiltration and heat treatment. (b,c) SEM and TEM images of BPh_3-GA heated to 2000°C, respectively.

case of graphene and the analyte gas, NO_2, NO_2 adsorbs onto the high surface area of the GA and charge transfer from the adsorbed NO_2 to the graphene occurs, leading to a decrease in the resistance of the material. This is a p-type sensing response.

A typical room temperature sensing experiment is shown in **Figure 3.1b** using a control GA sensor. After deposition of the GA on the microheater sensing platform, changes in the resistance are monitored as the sensor is exposed to different concentrations of NO_2. In the control GA sensor, exposure to low concentrations of NO_2 result in no change in the resistance of the material. However, at 0.5ppm NO_2 there is a decrease in the resistance. This lowest concentration that results in a response in the material is called the *detection limit*, and is a key sensing characteristic. Other key sensing characteristics that are marked in **Figure 3.1** are:

Response: Percent change in resistance when analyte gas is exposed to sensor
Recovery: Percent change in resistance back to baseline when analyte gas is removed
Sensing Temperature: Temperature used for experiment

The sensing temperature is used to improve the response and recovery characteristics. At room temperature, there is not enough thermal energy to desorb all of the adsorbed analyte molecules and some will remain on the sensing material and continue to contribute the resistance. This leads to incomplete recovery of the material when analyte gas is no longer present. As seen in **Figure 3.1b**, the resistance does not return to baseline when NO_2 is not present. Incomplete recovery makes continuous sensing impossible due to the changing baseline. To improve recovery, elevated sensing temperatures are used to increase the desorption kinetics and allow continuous

sensing. Increasing the sensing temperature also increases the adsorption kinetics and can impact the detection limit and response. For full sensor optimization, the response and recovery characteristics are studied at a variety of temperatures to determine the optimized temperature.

3.4 Synthesis of B Doped and Defect-Engineered GA

A post-synthetic modification approach is used in order to synthesize boron doped and defect-engineered GAs. A control GA is first synthesized as described in **Chapter 2**. Briefly, a 20 mg/mL solution of graphene oxide (GO) in water is sonicated and a 1:6 by volume NH_4OH:H_2O is added to catalyze the gelation. Gelation is carried out over 3 days at 80°C. After gelation, the solvent in the hydrogel is removed using supercritical carbon dioxide to yield a graphene oxide aerogel. Thermal reduction is achieved by treatment at 1050°C in Ar and subsequent treatment at either 1500, 1750, or 2000°C to yield control GAs.

As shown in **Figure 3.2a**, after synthesis of a GA, it is submerged in a solution of 0.25M triphenyl borane (BPh_3) in THF and allowed to dry. The infiltrated aerogel is then fired at 1500, 1750, or 2000°C to provide enough thermal energy to drive boron into the graphene lattice. The resulting changes in morphology, boron chemistries, concentrations, and sensing performance to NO_2 are monitored.

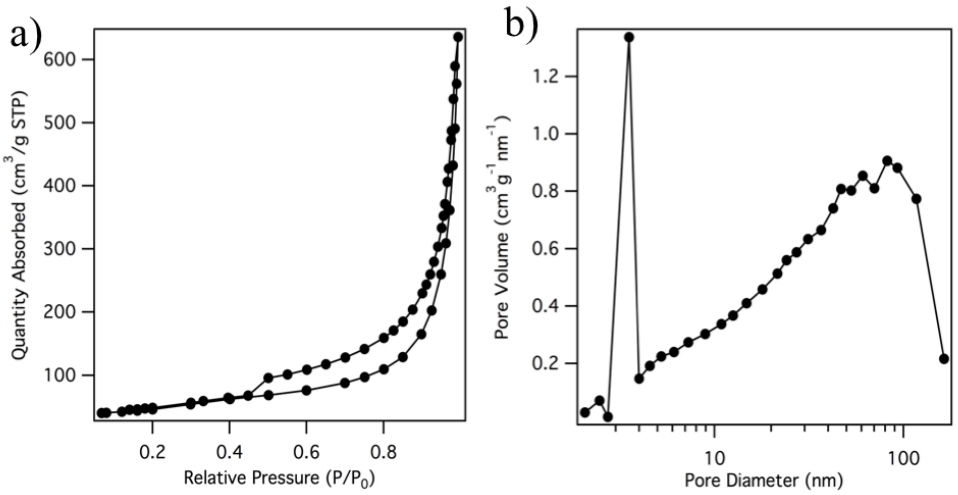

Figure 3.3 (a,b) N_2 adsorption-desorption isotherms and pore size distribution for BPh_3-GA heated to 2000°C, respectively.

3.5 Structural and Textural Characterization of B Doped and Defect-Engineered GA

The morphology of BPh_3-GA is characterized using scanning electron microscopy (SEM) and transmission electron microscopy (TEM) to probe possible structural changes at the micro- and nanoscale. In **Figure 3.2b**, a representative SEM image of a BPh_3-GA fired at 2000°C is shown. The morphology after infiltration is unchanged and the open porous structure is maintained. This retention of morphology is independent of temperature used for firing. TEM analysis shows the traditional wrinkled structure characteristic of GAs (**Figure 3.2c**) with a hexagonal diffraction pattern and lattice spacing of 0.39 nm, close to the ideal spacing for graphene (0.33 nm). The BPh_3-GA samples fired at 1500, 1750 and 2000°C have similar 3D, wrinkled

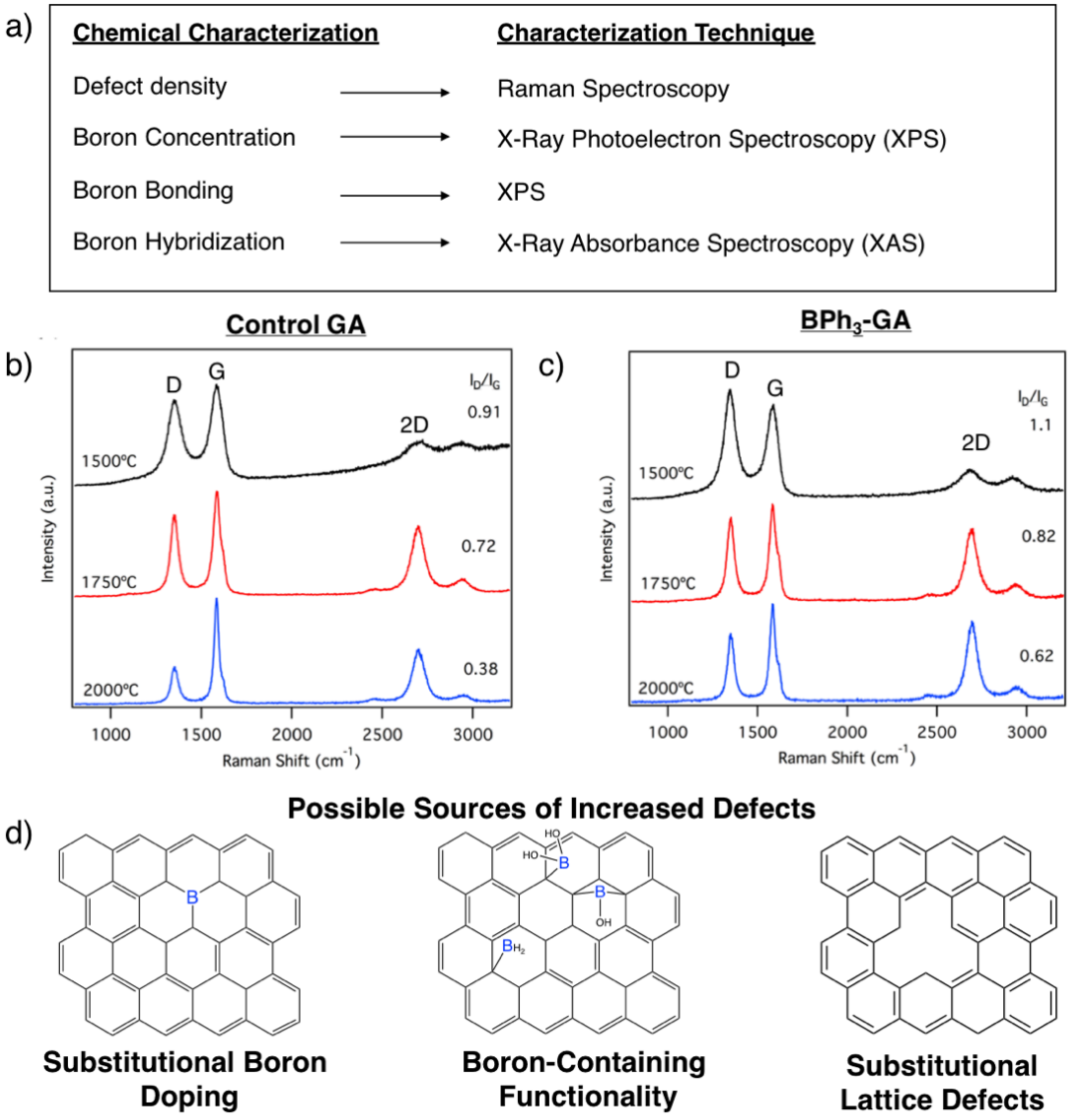

Figure 3.4 a) Summary of chemical characterizations necessary for comprehensive analysis of BPh_3-GAs and techniques used to obtain chemical information b,c) Raman spectra of BPh_3-GAs and control GAs fired at various temperatures, respectively d) Structures of various bonding configurations that could lead to increased densities of defects.

morphology, and no flattening on the scale of around 20 nm is observed with increasing annealing temperature, consistent with previous reports[58]. Overall, no change in morphology at the nanoscale or microscale is observed as a function of annealing temperature.

High surface area and porosity are important properties of graphene aerogels and vital to many of their functionalities. The nitrogen adsorption/desorption isotherm for a 2000°C fired BPh_3-GA is shown in **Figure 3.3a** displaying a Type-IV and H3 hysteresis loop (IUPAC definition) typical of mesoporous materials. The calculated BET surface area for BPh_3-GA fired at 2000°C is about 160 m^2/g, which is smaller than control graphene aerogels (~1000 m^2/g). The reduced surface area is likely due to surface tension effects during THF evaporation after infiltration of BPh_3. In the future, one way to avoid this is to use a solvent that is both compatible with BPh_3 and capable of being freeze-dried, such as benzene. While there is a decrease in the

surface area as a result of the BPh_3-GA, the resulting aerogel still possesses a high surface area and pore volume sufficient for many applications. The pore size distribution shown in **Figure 3.3b** has a strong peak at about 3.5 nm and a tail into the larger pore regime reflecting the large surface area of the BPh_3-GA.

3.6 Chemical Characterization of B Doped and Defect-Engineered GA

In order to study boron content and the evolution of boron chemistry with temperature, the material must be extensively chemically characterized. Important chemical characterizations to fully study the boron chemistry include studying the defect density, boron bonding and boron concentration and importantly, boron hybridization. The chemical information necessary for comprehensive understanding of boron chemistry and the characterization technique used to obtain that information is summarized in **Figure 3.4a.** Boron dopants would be considered defects in the graphene lattice and can be studied using Raman spectroscopy. The boron bonding and concentration within the lattice can be characterized using x-ray photoelectron spectroscopy (XPS). However, XPS does not give information on the hybridization of the boron in the aerogel, so it is possible that boron could reside as sp^3 boron containing functionalities on the graphene or it could be sp^2 bonded substitutional boron doping. The hybridization and location of boron significantly impacts the properties of boron containing materials and sp^2, substitutionally doped boron is required for improved properties in boron doped graphene.

3.6.1 Raman Spectroscopy

Raman spectroscopy is a powerful tool to study graphene and gives insight into the crystallinity and defect concentration in the material. The Raman spectrum of graphene has a G peak corresponding to the in-plane E_{2g} phonon around 1590 cm^{-1}, a second-order two-phonon mode identified as the 2D peak at 2700 cm^{-1}, and a D peak due to defects in the material at 1350 cm^{-1}. The ratio of the intensity of the D peak to the G peak (I_D/I_G) is a common metric for evaluating the quality of graphene. Introduction of a heteroatom into the lattice would increase the D to G ratio

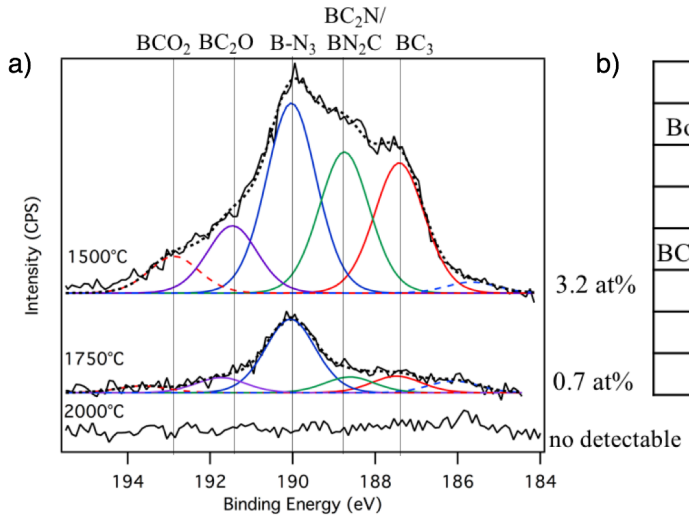

b)

Bonding Abundance (%)			
Bond Type	1500°C	1750°C	2000°C
$B\text{-}C_3$	22.6	11.8	N/A
$B\text{-}N_3$	33.0	52.9	N/A
BC_2N/BN_2C	24.5	11.3	N/A
BC_2O	11.7	10.8	N/A
B_2O_3	6.3	4.8	N/A
B-B	1.8	8.4	N/A

Figure 3.5 a)B1s XPS spectra of BPh3-GA's fired at increasing temperatures b) Summary table of boron bonding configurations present in BPh_3-GAs at increasing temperatures. In collaboration with Art Nelson provided courtesy of LLNL.

and it has been used as an indicator of doping levels[86]. **Figures 3.4 b,c** contain the Raman spectra of BPh_3-GA, and control GAs, fired at various temperatures. For control GA samples, a decrease in I_D/I_G and sharpening of the G peak is observed with increased firing temperature. These trends and I_D/I_G values measured are in agreement with previous work[58]. This behavior is mirrored in BPh_3-GA samples, but the I_D/I_G is increased at all heat treatments when compared to control GA samples. At 1500 and 1750°C firing temperatures, I_D/I_G in BPh_3-GA increases by 21% and 14% relative to the control, respectively. The largest increase occurs at 2000°C for which the BPh_3-GA has a I_D/I_G 58% larger than the control, indicating that there is an increased number of defects after BPh_3 treatment.

While Raman spectroscopy results confirm the presence of additional defects in the GA in comparison to the control GA, there are a number of possible bonding configurations that could result in an increased I_D/I_G ratio. As illustrated in **Figure 3.4d**, in addition to substitutional boron doping, other possible sources of increased defects include sp^3 boron containing functionalities or substitutional lattice defects.

3.6.2 X-Ray Photoelectron Spectroscopy

In order to determine if the increased defects in the BPh_3-GA samples are due to substitutional boron doping, XPS and XAS are performed. Boron 1s XPS spectra for aerogels fired at 1500, 1750, and 2000°C are shown in **Figure 3.5a**. A clear trend is present in the atomic concentration of boron incorporated. At 1500°C, boron is incorporated at 3.2 at%; after firing at 1750°C the boron level drops to 0.7%; and after the 2000°C treatment no detectable boron remains in the lattice. Importantly, bonds that incorporate boron into the material vary with temperature. After firing at 1500°C, boron is incorporated through B_2O_3, BC_2O, BN, BC_2N/BN_2C, BC_3, and B-B bonds indicated by peaks at 192.9, 191.5, 190.1, 188.8, 187.4, and 185.6 eV, respectively. Given that graphene oxide is used as a precursor, the presence of boron and oxygen bonding is not surprising. However, no nitrogen source is used in the BPh_3-GA samples that is not present in the control, making B-N bonding unexpected. BN is known to be a thermodynamically favorable phase and the source of nitrogen in this case is likely due to nitrogen in the air present in the aerogel

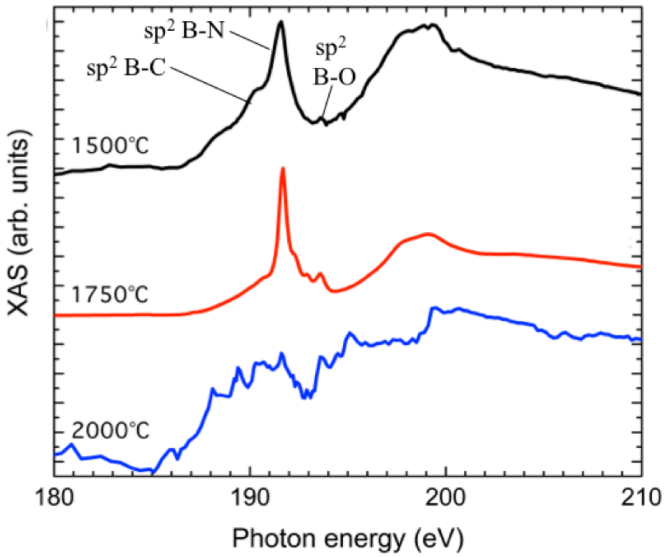

Figure 3.6 XAS spectra for BPh_3-GA's fired at increased temperature. Spectra normalized and offset for clarity. In collaboration with Alex Baker and Jon Lee of LLNL.

pores[87]. At 1750°C there is a change in the boron chemistry and B-N is the predominant source of boron incorporation. Aerogels fired at 2000°C have no detectable boron which we attribute to boron being annealed out and expelled from the lattice at such high temperatures through a self-healing mechanism[88,89]. Changes in boron chemistries are summarized in **Figure 3.5b**. Additionally, at such low doping levels no change in the carbon spectrum is visible.

3.6.3 X-Ray Absorption Spectroscopy

As a highly sensitive tool to characterize the element-specific local bonding environment, XAS is used to determine if boron is incorporated into the lattice of the BPh_3-GA samples through sp^2 bonds, or simply resides within a functional group on the surface through sp^3 bonds. The boron XAS spectrum is shown in **Figure 3.6**. Two important features appear at 191.7 and 193.6 eV; these arise from sp^2-hybridized boron bonded to nitrogen and oxygen, respectively. Comparison of the B, C, and N spectra against previous studies confirms the incorporation of B and N as dopants, rather than forming isolated regions of B_4C or hBN[90,91]. At 1500°C, the B-N π* peak at 191.7 eV dominates, but a smaller feature is also observed at 190.5 eV, which is attributed to substitutional doping of boron in an sp^2 hybridized, B-C_3 environment[91] . Additionally, a small peak at 193.6 eV is present due to the oxidized species on the surface. Aerogels fired at 1750°C have a similar dominant peak at 191.7 eV, but there is a decrease in the relative intensity of the B-C_3 features, in agreement with XPS data. There is also an increase in surface oxide species, as the oxidized boron peak increases in prominence. The BPh_3-GA sample fired at 2000°C displays dramatically reduced signal strength, and consequently no clear structure can be resolved.

Each method provides complementary information in providing a clear picture of the evolution of boron incorporation with annealing temperature as shown in **Figure 3.7**. The BPh_3-GA samples fired at 1500°C have boron incorporation through similar levels of B-N and B-C bonding, with additional oxidized boron. They are referred to as Boron-Doped GAs. Aerogels fired at 1750°C have an overall decreased level of boron incorporated and the incorporation is predominantly through B-N bonds. Importantly, boron is bound in the material through substitutional doping via sp^2 bonds as opposed to boron functional groups on the surface. They are referred to as BN-Doped GAs. Finally, the BPh_3-GA samples treated at 2000°C contain no

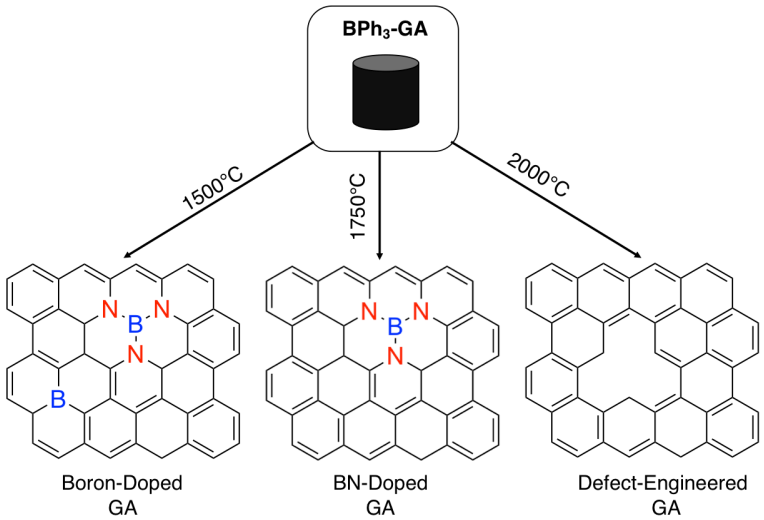

Figure 3.7 Structures of BPh_3-GAs fired at various temperatures leading to boron doping after 1500°C treatment, BN doping after 1750°C treatment and defect-engineering after treatment at 2000°C.

detectable boron. However, Raman spectroscopy indicates that this material has an increased density of defects and are called Defect-Engineered GAs. These defects can serve as active sites for catalysis and gas sensing and provide a route towards defect-engineering of graphene aerogels.

3.7 NO_2 Detection of B-Doped and Defect-Engineered GAs

After comprehensive characterization of BPh_3-GAs, the gas sensing properties of aerogels with different boron chemistries are explored in collaboration with Wenjun Yan in the Maboudian Group at UC Berkeley. The boron doping, BN doping, and defect engineering are chemical modifications that can be particularly advantageous to the performance for molecular gas detection. Theoretical work indicates that boron-doped graphene and defective graphene have superior potential for NO_2 detection due to enhanced adsorption energies and charge transfer from the graphene to NO_2[72]. Experimental work on single layer boron-doped graphene supports these predictions[92].

NO_2 is a toxic gas that is a main component in smog and is a major health concern in cities like Beijing and Mumbai which have notoriously poor air quality as a result of smog. The most prominent source of NO_2 is the burning of fossil fuels and the harmful effect of NO_2 can be felt as low as 50ppb, making detecting NO_2 particularly important[93].

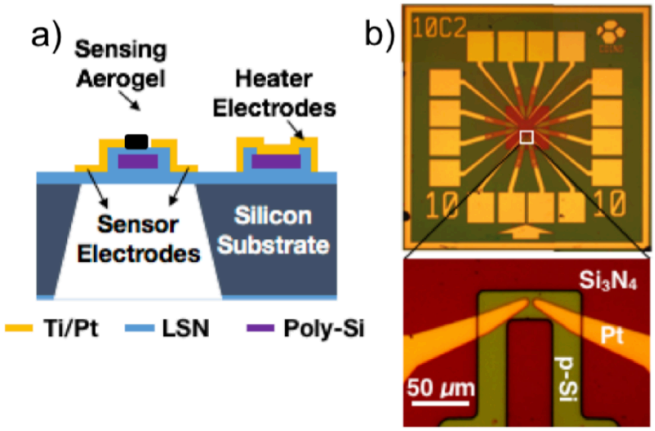

Figure 3.8 a) Schematic diagram of the sensor cross-section. b) Optical image of a 3.5×3.5 mm2 chip containing four microheaters, and zoom-in of one microheater with sensing electrodes on top. In collaboration with Wenjun Yan of the Maboudian group.

3.7.1 Low-Power Microheater Fabrication

In order to study the NO_2 detection properties of GAs with different boron chemistries, a specially designed microheater is fabricated. The low-power microheater is vital in order to achieve elevated sensing temperatures while consuming minimal power. The microheater is fabricated according to a process developed in the Maboudian group[94]. A silicon substrate is coated with silicon-rich, low-stress silicon nitride (100 nm) followed by the deposition of phosphorus-doped polysilicon (100 nm), which is patterned using photolithography to form the microheater. Another silicon nitride layer (100 nm) is deposited and patterned for the microheater contacts, which are electron-beam evaporated Ti/Pt (10/90 nm). The back side of the wafer is patterned and etched using KOH to release the silicon nitride membrane. The Ti/Pt electrodes overlaid on the silicon nitride membrane are used as electrodes for conductometric sensing. The chip is wire bonded into a 14-pin ceramic dual inline package for electrical characterization and sensor testing. A schematic of the microheater and optical images of the fabricated chip are shown in **Figure 3.8a&b.** Conductometric gas sensors are prepared by integrating a BPh_3-GA onto a low-power

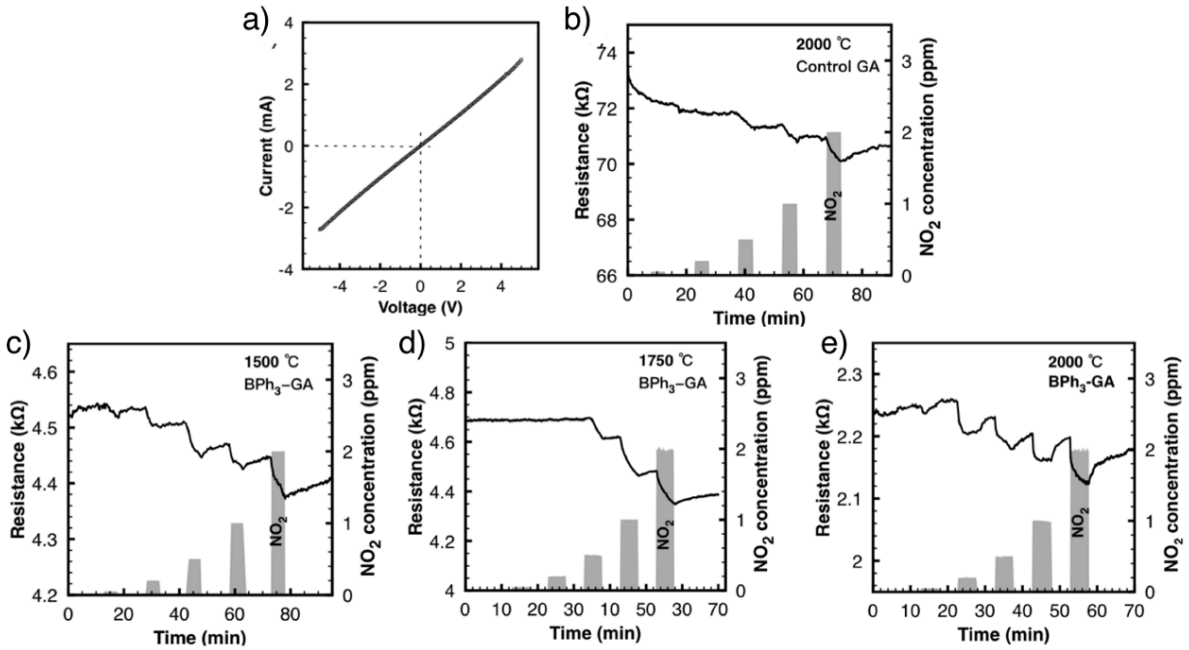

f)

Annealing Temperature (°C)	Sensitivity 2 ppm NO_2 (%)	Detection Limit to NO_2 (ppm)
Control	2.6	0.5
1500	2.6	0.05
1750	4.8	0.5
2000	**8.0**	**0.05**

Figure 3.9 a) I-V characteristics of the BPh3-GA (heated to 2000°C) sensor at RT. Resistance versus time to NO2 (0.05 – 2 ppm range) at RT of the sensors based on b) control GA, c) BPh_3-GA heated at 1500°C, d) BPh_3-GA heated at 1750°C, and e) BPh_3-GA heated at 2000°C, f) Summary of sensitivity to 2ppm of NO_2 and detection limit of BPh_3-GA treated at increasing temperatures. In collaboration with Wenjun Yan of the Maboudian group.

microfabricated heater platform. The aerogel is sonicated into suspension in isopropyl alcohol (0.5 mg/mL). A 1 µL drop (five drops of 0.2 µL each) is placed onto the microheater chip, while the microheater is heated to 100 °C and maintained there for 3 hours to promote solvent evaporation and material deposition at the center of the microheater.

3.7.2 Room Temperature Sensing of BPh_3-GAs

The microheater chip (3.5 ×3.5 mm^2) contains four microheater sensors, with each sensor having four electrical contacts, two for the microheater leads and two for electrical probing of the sensing layer **(Figure 3.8b)**. Taking the 2000°C BPh_3-GA sample as an example, nearly linear current vs. voltage behavior of the BPh_3-GA sensor suggests an Ohmic contact between the aerogel and sensor electrode (**Figure 3.9a)**.

Sensors of BPh_3-GAs treated at 1500, 1750 and 2000°C are prepared and the room temperature sensing performance for NO_2 is compared to that of the control GA. The two important criteria for comparison are the detection limit and the response of the material to 2ppm of NO_2. **Figure 3.9(b-e)** show the responses of control GA and BPh_3-GA sensors to different concentrations of NO_2 at room temperature (20 °C) for 5 min duration pulses and the table in

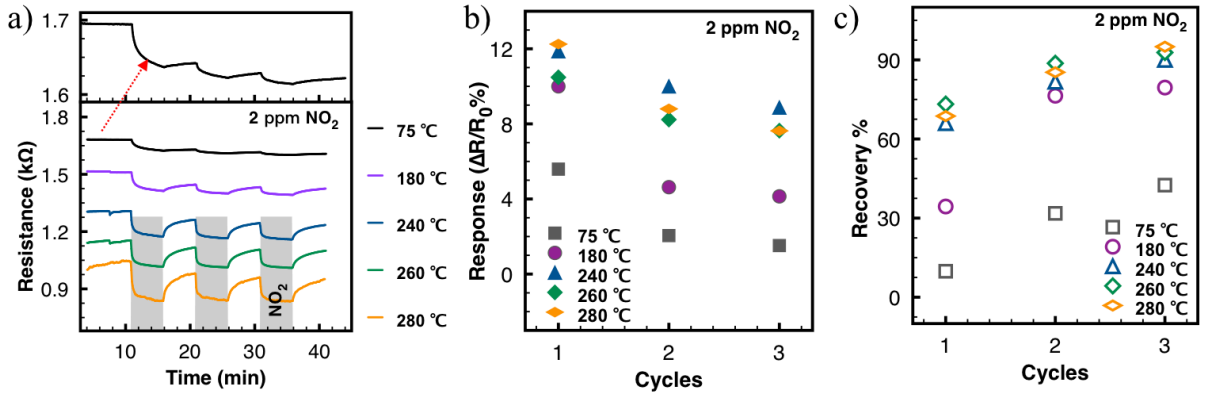

Figure 3.10 a) Resistance change of the 2000°C BPh_3-GA sensor, b) % response change, and c) % recovery change during 3 cyclic exposures to 2 ppm NO_2 at different microheater temp. In collaboration with Wenjun Yan of the Maboudian group.

Figure 3.9f summarized the results. There is a clear change in the sensing performance for BPh_3-GA materials fired at different temperatures. The resistance of all sensors decreases upon exposure to NO_2 gas, demonstrating a p-type behavior, in agreement with experimental and theoretical findings of NO_2 on graphene[80,81]. Notably, the control GA is unable to detect NO_2 concentrations below 0.5 ppm and has a response of 2.6% to 2ppm NO_2. The sensors based on BPh_3-GA annealed at 1500°C have an enhanced detection limit and respond to concentrations as low as 0.05 ppm of NO_2 with the same signal response to 2ppm of NO_2 as the control. The sensors based on 1750°C BPh_3-GA have a detection limit the same as the control, but have an enhanced response to 2ppm of NO_2 with a 4.6% change in resistance. Lastly, the sensors based on BPh_3-GA annealed at 2000°C detect NO_2 concentrations of 0.05 ppm, a factor of 10 enhancement with respect to the control. Additionally, the response of the material is improved threefold and has an 8% change in resistance to 2ppm of NO_2. The changes in sensing performance may be attributed to the distinct boron chemistries or defects left behind as a result of BPh_3 treatment. Boron incorporated through substitutional doping via B-C_3 bonds yields active sites for NO_2 adsorption[72]. Thus, the 1500°C BPh_3-GA, which contains 23% B incorporation through B-C_3 bonds and 33% through B-N_3, has an improved detection limit. Boron incorporation through B-N bonds is not thought to be beneficial to sensing performance and the effect of BC_2N/BN_2C is unknown. Therefore the predominant B incorporation through 53% B-N bonds in the 1750°C BPh_3-GA is not contributing to sensing and the detection limit is not enhanced. The BPh_3-GA treated at 2000°C has no detectable boron, but rather an increased density of defects left behind due to boron expulsion from the lattice. These defects are active sites for NO_2 adsorption and contribute to the sensing behavior of the material, making defect-engineered aerogels excellent NO_2 sensors. Due to the enhanced detection limit and sensitivity of defect-engineered BPh_3-GA, the sensors based on 2000°C BPh_3-GA are further characterized and optimized.

3.7.3 Sensing Temperature Optimization of Defect-Engineered GAs

The effect of heater temperature on the 2000°C BPh_3-GA sensor is reported in **Figure 3.10**. **Figure 3.10a** displays the response of the sensor during exposure to 2 ppm NO_2 for 3 cycles, with the temperature of the chip ranging from 70 to 280°C. When exposed to 2 ppm NO_2 flow, the percentage response decreases after repeating the 3 sensing cycles, for all temperatures, while the percentage recovery increases with increased temperature (**Figure 3.10b,c**). Due to the high binding energy of NO_2 on the defect-engineered GA, the binding sites become tightly occupied by NO_2 molecules after adsorption. At lower temperatures, the thermal energy is insufficient to

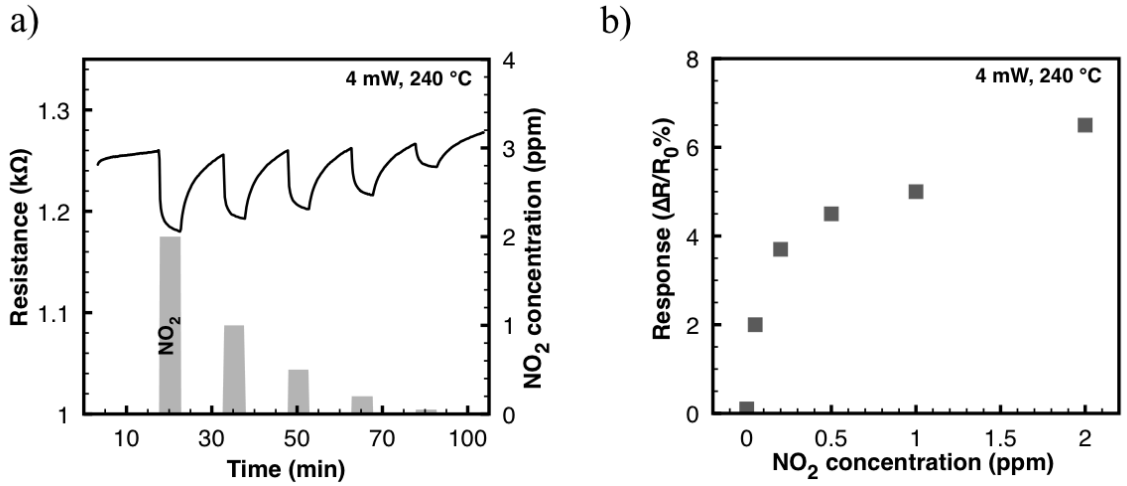

Figure 3.11 a) Resistance versus time, and b) % response of the 2000°C BPh_3-GA sensor to NO_2 at 240°C. The NO_2 concentration was modulated decreasing from 2 ppm to 0.05 ppm. c,d) Selectivity of the 2000°C BPh_3-GA sensor and control GA sensor at 240°C, respectively. In collaboration with Wenjun Yan of the Maboudian group.

overcome the activation energy for NO_2 desorption. Therefore, as the adsorption/desorption cycles are repeated, the initial resistance is reduced as a result of non-recoverable response. Additionally, as the temperature increases from 70 to 240°C, the percentage response of the sensor increases, and the recovery characteristics improve. This is due to the high temperature accelerating the adsorption and desorption of NO_2 gas molecules on the aerogel surface. However, in the temperature range of 240 – 280°C, both the response and recovery changes are slight, with response time around 100s and recovery time around 300s. Considering the response and recovery characteristics to NO_2 and the power consumption of the device, a sensor temperature of 240°C is considered the optimum operating temperature and further tests are taken at this sensing temperature.

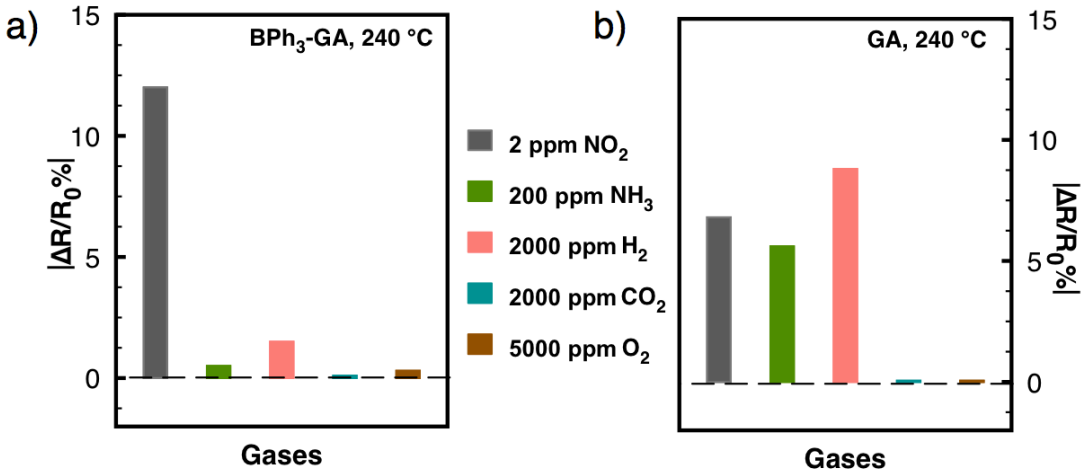

Figure 3.12 a,b) Selectivity of the 2000°C BPh3-GA sensor and control GA sensor at 240°C, respectively. In collaboration with Wenjun Yan of the Maboudian group.

3.7.4 Sensitivity of Defect-Engineered GAs for NO_2

The 2000°C BPh_3-GA sensor response to varied concentrations of NO_2 from 0.05 to 2 ppm at 240 °C is shown in **Figures 3.11a and b**. The sensor response is clearly detectable at extremely low concentrations of 50 ppb and exhibits minimal noise. Although the minimum NO_2 delivery concentration is 50ppb due to limitations with the experimental setup, the detection limit of the BPh_3-GA sensor based on the signal-to-noise ratio of 3 is estimated at 7 ppb[95]. Additionally, the sensor has fast response and recovery times for all NO_2 concentrations between 90-120s and 300s, respectively.

3.7.5 Selectivity of Defect-Engineered GAs

The most remarkable benefit of defect-engineering is the improved selectivity to NO_2, compared to the control GA. As shown in **Figure 3.12a**, the 2000°C BPh_3-GA sensor shows excellent selectivity to NO_2 at a much lower concentration (2 ppm), with a weak response to higher concentrations of NH_3 and H_2. In contrast, the control GA sensor does not exhibit such high selectivity as it responds to H_2, NH_3 and NO_2, with the highest response percentage to 2000 ppm H_2 at 240 °C (**Figure 3.12b**).

The origin of the improved selectivity can be explained based on first-principles calculations reported by Zhang et al. as summarized in the table in **Figure 3.13**[72]. Pristine graphene has a binding energy of -0.48 for NO_2 which increases by a factor of 6 to -3.04 as a result of defect-engineering. The charge transfer also increases from -0.19 to -0.34. Meanwhile, the binding energy for NH_3 has a very modest increase from -0.11 to -0.24 as a result of defect-engineering. This discrepancy results in more favorable NO_2 adsorption and defect-engineered GAs having a high selectivity for NO_2[72,79].

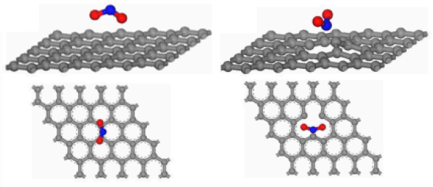

Analyte Gas	Graphene E_{ad}	Defect-Engineered E_{ad}
NO_2	-0.48	-3.04
NH_3	-0.11	-0.24

Charge Transfer to NO_2	-0.19	-0.34

Figure 3.13 Table summarizing the adsorption energies of analyte gases NO_2 and NH_3 in pristine graphene and defect-engineered graphene, and charge transfer from graphene to NO_2 [72].

3.8 Principles of Supercapacitors

Due to theoretical and experimental work indicating that introducing boron into graphene materials can improve its energy storage capacity, boron doped graphene aerogels are explored for supercapacitor applications[96].

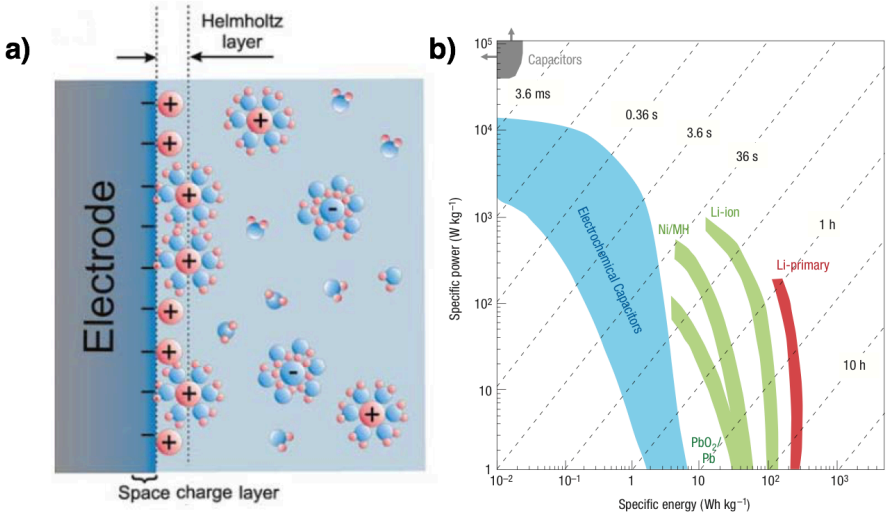

Figure 3.14 a) Diagram illustrating supercapacitor storage mechanism through reversible adsorption of electrolyte ions b) Ragone plot demonstrating differences in energy density and power density for different classes of energy storage devices[48].

Supercapacitors are energy storage materials that are capable of being charged and discharged to deliver energy on demand and are constructed of two electrodes and electrolyte between them. The electrodes reversibly store charge through ion adsorption from the surrounding electrolyte and form an electrochemical double layer. Charge storage in the electrochemical double layer makes supercapacitors also be referred to as electrochemical double layer capacitors (EDLCs). Charge separation occurs on the polarization at the electrode-electrolyte interface as illustrated in **Figure 3.14a**. This separation is reversible and fast, due to not being diffusion controlled, making supercapacitors capable of storing high power densities. However, due to charge storage confined to the surface, they have low energy densities. The discrepancy between the high power densities and low energy densities in supercapacitors contrasted with the low power densities and high energy densities in batteries is illustrated in the Ragone plot shown in **Figure 3.14b**. Additionally, supercapacitors are renowned for their high cyclability due to lack of swelling or mechanical stress as a result of the ion adsorption storage mechanism. They can withstand millions of cycles as opposed to the thousands of cycles in batteries.

The ideal properties of a supercapacitor are high conductivity, large surface area, a pore size distribution to complement ion size, highly interconnected pores, and a wettable surface[97,98]. Graphene aerogels fit into this description due to the intrinsic conductivity of the graphene building block and the textural properties afforded by the aerogel morphology. This has led them to be extensively explored as supercapacitor electrodes, and researchers have also coupled the electrochemical double larger capacitance (EDLC) of GAs with pseudocapacitive materials that undergo redox reactions[99–101]. Additionally, graphene aerogels can be used to make symmetric supercapacitors where the aerogels make up the two working electrodes and a solid electrolyte is used[102,103]. This is integral for developing state of the art, commercially viable supercapacitor materials.

The equation used to describe double layer capacitance is shown in **Equation 3.1**.

$$C = \frac{\varepsilon_0 \varepsilon_r A}{d} \qquad \textbf{Equation 3.1}$$

where C is the double layer capacitance, $\varepsilon_0$is the dielectric constant of vacuum, ε_r is the dielectric constant of the electrolyte, A is the surface area of the electrode, and d is the thickness of the double layer

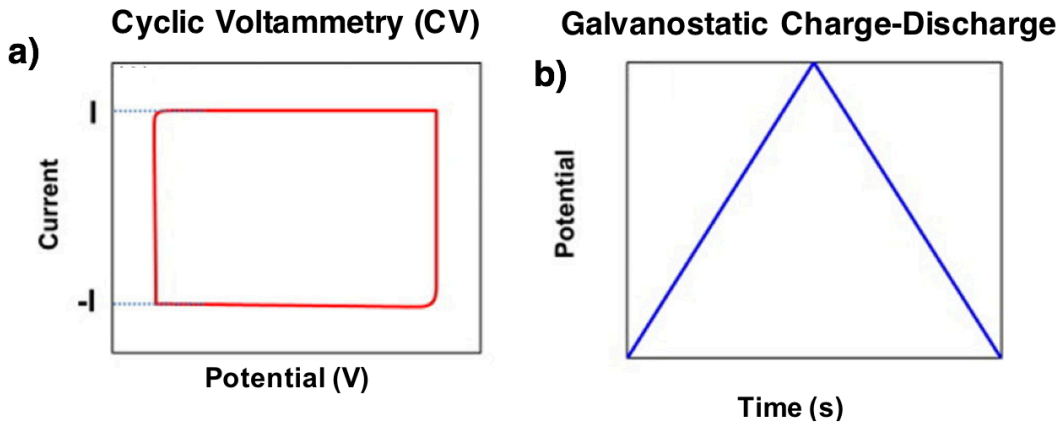

Figure 3.15 a) CV curve and b) galvanostatic charge-discharge curves of an ideal supercapacitor.

Due to the high surface area of supercapacitors, and the small thickness of the double layers, supercapacitors can achieve high capacitances. Experimentally, capacitance is measured using cyclic voltammetry (CV) and galvanostatic charge-discharge measurements. In CV, the voltage is swept between two specific values and changes to the current are monitored. Double layer capacitance is characterized by a classical rectangular shape in the CV curve as seen in **Figure 3.15a**. This rectangular shape can be explained using **Equation 3.2**

$$I = C \times \frac{dV}{dt} \qquad \textbf{Equation 3.2}$$

where I is the current, C is the capacitance, and dV/dt is the potential scan rate

The constant current of the rectangle and scan rate can be used to calculate the capacitance. The more common method for calculating the capacitance is from a galvanostatic charge discharge experiment. In this experiment a constant current is applied and the change in voltage is measured. Double layer capacitance is characterized by a straight line in voltage change with time when operated at constant current (**Figure 3.15b)**. The discharge curve can be used to calculate the capacitance of the electrode. Galvanostatic charge discharge experiments are also useful to measure the operating limits and tolerance of the electrode for being operated at a variety of current

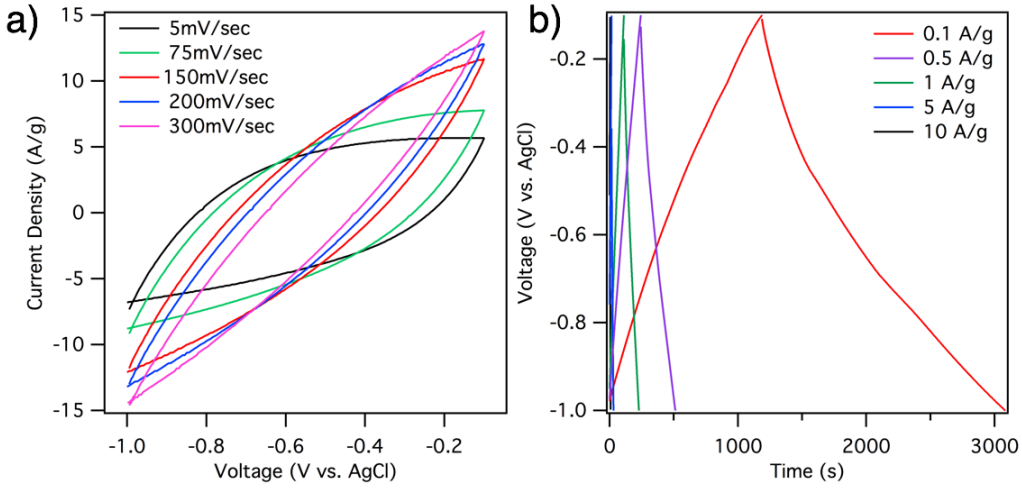

Figure 3.16 a) CV curve and b) Galvanostatic charge-discharge curves of boron doped GAs.

densities. To test the cyclability of the electrode, the supercapacitor is cycled thousands of time and the capacitance calculated for each cycle.

3.9 Supercapacitor Properties of B-Doped GAs

BPh_3-GAs treated at 1500°C leading to boron doping are incorporated as supercapacitor electrodes. Wires are inserted into the aerogel cylinders and sealed with silver paint. The electrochemical properties of the aerogel electrode are tested with 6M KOH electrolyte in a three electrode configuration with a platinum foil counter electrode, and an AgCl reference electrode.

The CV curves for the boron doped GA are shown in **Figure 3.16a**. At low scan rates, the curve resembles the rectangular ideal supercapacitor behavior. However, at high scan rates the shape becomes more oblong, a sign that there is a large amount of resistance in the system. It is hypothesized that there is poor contact between the wire and the aerogel, resulting in these changes. Further study is necessary in order to optimize the sample preparation and prevent this resistive behavior.

Galvanostatic charge discharge experiments operating at current densities between 0.1A/g and 10 A/g show largely linear behavior at all current densities (**Figure 3.16b**). The calculated gravimetric capacitance at 0.1A/g is 190F/g and 117F/g at 1A/g. This is comparable to other values reported for graphene aerogels and is a promising result for an unoptimized system[104–106]. In order to fully understand the role of boron chemistry on the supercapacitive behavior, the sample preparation must be optimized and compared with the performance of a control GA. In the future, this study should be further expanded to include the BN-doped GA and defect-engineered GAs as well.

Chapter 4: Synthesis of Boron Carbon Nitride Aerogels with Tunable BN Content

Nano Fun-Fact: The ancient Romans used nanoparticles in the 4th century AD the Lycurgus Cup of height 16.5 cm and diameter 13.2 cm changes its color from green to red depending on illumination due to colloid particles of gold and silver of size approximately 90 nm.

4.1 Introduction to BCN Materials

Layered materials like graphene and h-BN have made huge impacts to the field of materials science, physics, and chemistry. The extraordinary properties of each material have enabled their integration into a number of exciting applications including sensors, catalysis, energy storage, gas separation, and protective coatings[81,107,108]. Following seminal studies by Novoselov and Geim revealing graphene's high electrical conductivity and carrier mobility, graphene was declared the future of electronics and capable of taking us "beyond the silicon age". Fifteen years after these initial studies, graphene has yet to make a large impact in commercial electronics. One major cause of this is the fact that graphene is a zero band gap semimetal, and a band gap is necessary for many roles in electronics. Contrary to graphene's electronic structure, it's other 2D counterpart, h-BN, has a large band gap (~5.8eV), limiting its use to insulating applications, making it necessary to find an approach to open a small gap in graphene without detriment to carrier mobility and conductivity. Some approaches to achieve this goal include introducing strain, patterning defects, or reducing the dimensionality[109–111]. Another approach is to alter the chemistry of the material through the formation of a ternary boron carbon nitride (BCN) layered structure; the synthesis of an aerogel based on BCN nanosheets in order to tune the electronic properties of the material will be explored in this chapter.

4.1.1 Electronic Structure of BCN Materials

In order to consider prospects for a semiconducting graphene analog, it is important to consider the phase diagram between boron carbon and nitrogen as shown in **Figure 4.1**. An interesting relationship exists between the three elements. Graphene exists at the top of the triangle, composed of purely carbon atoms. P and n-type doping with boron or nitrogen as expressed on the triangle edges is used as an approach to increase the conductivity of the material or improve its performance in certain applications as described in **Chapter 3**. Binary B-C and C-N compounds also exist along these triangle edges such as B_4C and C_3N_4. At the base, binary BN compounds exist like h-BN described in **Chapter 1**. Within the center of the triangle, ternary B-C-N phases are located such as BCN, BC_2N, and BC_4N. These ternary phases are a long sought after group of materials which have been extensively explored theoretically and have the potential to achieve intermediate band gaps between graphene and h-BN[112].

Theoretical work has focused on a solid solution of $B_xC_yN_z$ compounds that are anticipated to have a range of electronic structures with dependence on the concentrations of each element in the material as well as the atomic arrangement[27,113]. Thus a material with a tunable band gap as small as a few meV up to 6eV could be achievable by changing the B:C:N atomic ratios.

Among one of the factors impacting the electronic structure of BCN materials is the crystal structure. In order to alter the electronic properties in the manner predicted by theoretical calculations, the materials must be two dimensional layered BCN crystals with a hexagonal lattice and boron, nitrogen and carbon atoms bonded to one another. A graphitic material with boron and nitrogen functional groups on the surface will not result in the desired electrical properties of a BCN material, nor will cubic BCN crystals or BN-graphene in-plane heterostructures. Synthesis

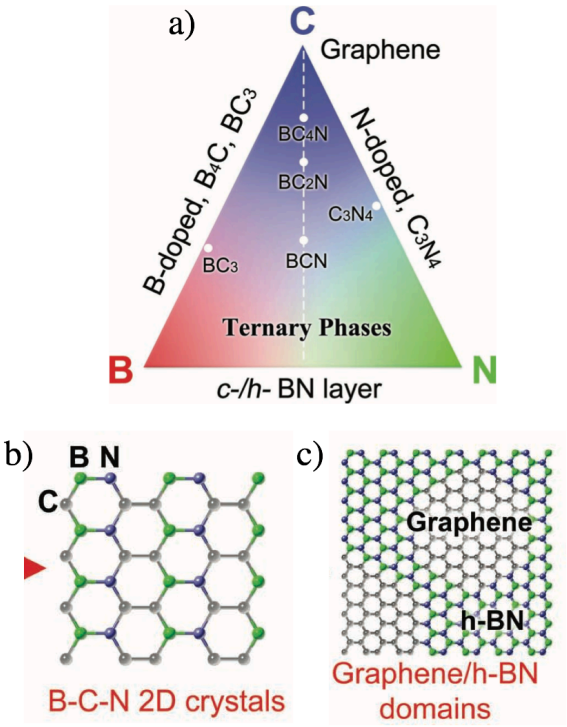

Figure 4.1 a) Phase diagram depicting the binary and ternary phases composed of boron carbon and nitrogen b) Hexagonal crystal structure of a ternary BCN leading to altered electronic properties c) Crystal structure of a phase segregated graphene and h-BN material[259].

and characterization of such a material is extremely challenging, with most reports containing polycrystalline BCN samples or carbon and BN phase segregation[114].

4.1.2 Phase Segregation and Synthesis Challenges of BCN Materials

One of the major challenges in synthesizing BCN materials is preventing phase segregation into graphene and BN phases. The two materials have high thermodynamic stability which are easily segregated into domains of BN and graphene. Theoretical calculations indicate that at high temperatures, it is favorable for a solid solution of BCN to separate into domains of graphene and hBN[115]. Researchers have even exploited this phase segregation in order to synthesize atomic layers of hybridized graphene and BN domains and study their electronic properties as well as applications in field-effect transistors[116,117]. Given the propensity of the system to phase segregate, it is important that BCN materials be studied using chemical characterization techniques that also possess spatial resolution to confirm that the product is truly a ternary BCN alloy.

Methods explored in order to synthesize BCN include chemical vapor deposition using boron, nitrogen, and carbon containing precursors, high temperature and pressure treatments, thermal substitution of graphene and BN nanosheets, as well as other higher throughput methods including a salt melt synthesis[118–123]. However, until recently a ternary BCN alloy had yet to be synthesized. In 2017, Benwal et al., reported a synthesis of graphene-like BCN monolayers by chemical vapor deposition using a precursor, bis-BN cyclohexane, which contains boron, carbon, and nitrogen bonded to one another[124]. However, the substrate plays a key catalytic role in the synthesis and transport measurements have yet to be completed to determine the band gap and electronic properties of the material.

4.1.3 Potential Applications of BCN Aerogels

BCN materials have a number of potential applications due to their intermediate electronic properties between graphene and hBN and altered chemical properties. Additionally, coupling the properties of BCN nanosheets with the textural properties of the aerogel morphology can provide additional functionality to the material. BCN materials containing low concentrations of B and N have been explored for metal-free electrocatalysis and yielded impressive results approaching the industry standard platinum electrode[66,125,126]. Other applications in non-linear optics, hydrogen storage and water treatment have also been reported and one of the ultimate goals of BCN materials is their integration into electronics [127–129].

With these goals in mind, a synthesis of BCN aerogels is developed and the material is extensively characterized for structural and chemical compositions as well as spatially resolved chemical analysis to fully study the system. The results are presented here in **Sections 4.2-4.8.**

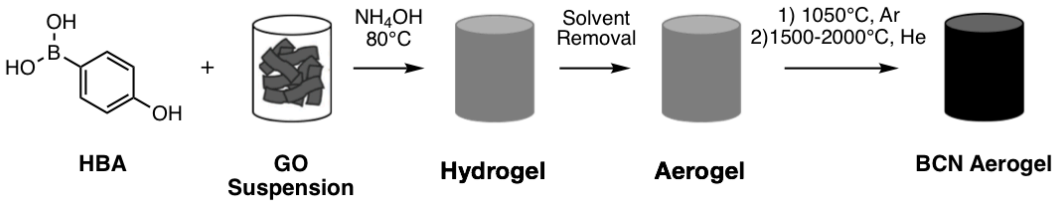

Figure 4.2 Schematic of the synthesis of BCN aerogels using an HBA precursor and ammonium hydroxide with subsequent heat treatment after forming an aerogel.

4.2 Synthesis of BCN Aerogels

BCN aerogels are synthesized by incorporating 4-hydroxyphenyl boronic acid (HBA) into the graphene oxide (GO) suspension during aerogel synthesis as outlined in **Figure 4.2**. A 40 mg/mL solution of HBA in water is prepared by heating in order to fully dissolve HBA. GO (20 mg/mL) is added into the solution and shaken to form a homogenous and very viscous suspension, which is lightly sonicated overnight in order to exfoliate GO sheets. Ammonium hydroxide (1:6 by volume NH_4OH:H_2O) is added and gelation takes place at 80°C for 3 days to form a hydrogel. The solvent is removed either through freeze-drying of critical point drying to yield an aerogel which is thermally annealed to reduce GO to graphene and thermally incorporate boron and nitrogen chemistries into the aerogel. Further treatment at either 1500, 1750 or 2000°C is used to both increase crystallinity of the sp^2 bonded network and provide enough thermal energy to add boron and nitrogen into the graphitic network. In this chapter, BCN-1500 will be used to describe BCN aerogels treated at 1500°C, BCN-1750 will be used to describe BCN aerogels treated at 1750°C, and BCN-2000 will be used to describe BCN aerogels treated at 2000°C.

There are a number of important benefits to incorporating HBA at the very beginning stage of the aerogel synthesis. Firstly, HBA can be effectively dispersed within the GO suspension by π stacking with GO. Secondly, incorporating HBA into the GO suspension allows it to react with the functional groups on the surface of GO and be covalently incorporated into the aerogel. Infiltrating a pre-synthesized aerogel with HBA, would only allow it to reside within the pores and not in the crosslinks. Perhaps the most important benefit of adding HBA into the GO suspension is that HBA can react with the ammonium hydroxide used in the synthesis. Ammonium hydroxide serves two functions in this approach: 1) It catalyzes the crosslinking of GO sheets to drive gelation, as described in **Chapter 2** and 2) In this case it also serves as a reactant in the reaction

with HBA which incorporates nitrogen into the product. The product of this *in-situ* reaction will be studied in **Section 4.6**. Lastly, by adding HBA into the GO suspension, it is possible to alter this parameter and integrate different concentrations of HBA to tune the B:C:N content in the final aerogel. This parameter will be explored in **Section 4.7**.

4.3 Structural Characterization of BCN Aerogels

Scanning electron microscopy (SEM) is used to study the microscale morphology of BCN aerogels after high temperature firing. Given that GO is used as the building block, a sheet-like morphology is expected to make up the aerogel. As shown in **Figure 4.3a-c**, BCN-1500, BCN-1750 and BCN-2000 aerogels are all made up of sheets crosslinked together in a 3D morphology with a large volume occupied by air. No changes in morphology are observed as a result of increasing the firing temperature from 1500 to 2000°C, and the large macropores that are clearly visible in SEM are a result of the freeze-drying method used to remove the solvent without surface tension.

Freeze-drying is used in this study unless otherwise noted in order to preserve the HBA and ammonium hydroxide reaction product that is located within the crosslinks and in the pores after gelation. Critical point drying requires solvent exchanges which can wash away the molecules that lead to boron and nitrogen incorporation after high temperature treatment. Thus, freeze-dried aerogels are extensively characterized and presented here. **Section 4.8** will study critical point dried aerogels in order to achieve higher surface area BCN aerogels which may come at a cost to B and N incorporation.

The morphology of the individual sheets making up the BCN aerogel is studied using transmission electron microscopy (TEM). **Figure 4.3d-f**, shows low magnification images of

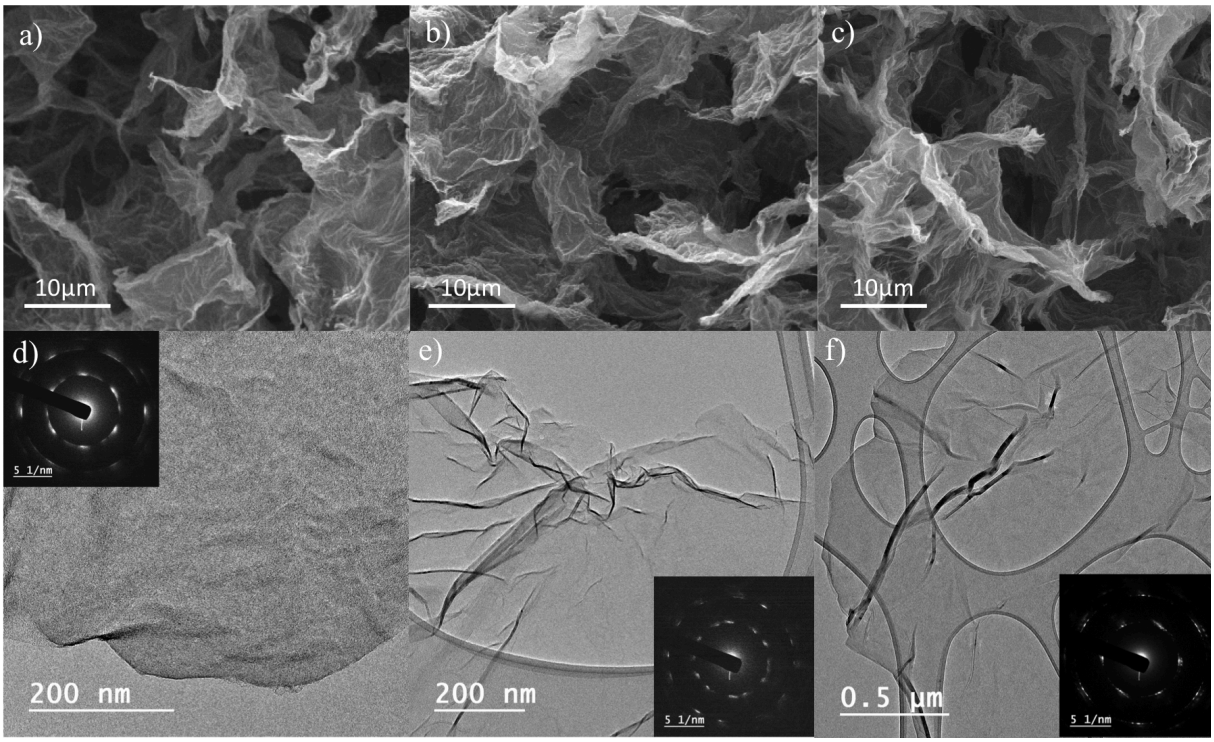

Figure 4.3 a-c) SEM and d-f) TEM images (inset: selected area electron diffraction patterns) of BCN-1500, BCN-1750, and BCN-2000 aerogels, respectively.

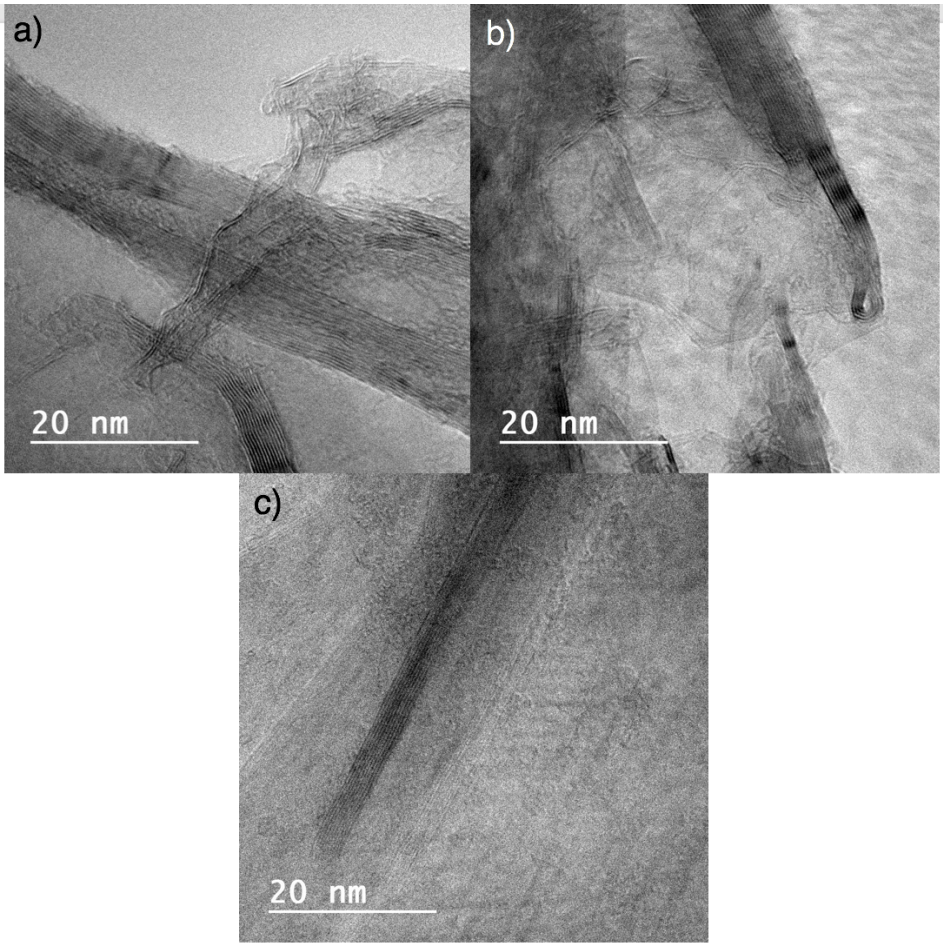

Figure 4.4 a-c) High magnification images of BCN-1500, BCN-1750, and BCN-2000 aerogels showing the lattice fringes.

BCN-1500, BCN-1750, and BCN-2000 aerogels, respectively. The individual sheets have a very flat morphology. This is typical of aerogels which have been freeze-dried, where templating from the solvent occurs. It is also accompanied by a restacking of graphene sheets making multilayer graphene as opposed to single or few layer seen in critical point dried samples. Selected area electron diffraction shown in the insets reveals the hexagonal diffraction pattern that would be expected for a hexagonal crystal structure, confirming that few layer or multilayers of the hexagonal lattice is present. The individual diffraction spots as opposed to rings are indicative of a highly crystalline material being obtained after high temperature treatment. A highly crystalline and hexagonal lattice is necessary in order to gain the electronic properties desired in a BCN aerogel as opposed to synthesizing other phases without a well-developed π electron network or with many defects.

Despite the flattened sheet morphology, wrinkles are still present within the sheets which are studied with higher magnification (**Figure 4.4)**. At this magnification, the lattice fringes are visible with a measured interlayer space of 0.33nm. The interlayer spacing of graphite is 0.335nm and h-BN has an interlayer spacing of 0.330nm. BCN would have an interlayer spacing similar to these values, but measuring changes this small is beyond what is achievable at this resolution.

While surveying each sample, the presence of several particles with diameters around 50nm was observed in BCN-1500, BCN-1750 and BCN-2000 aerogels. These nanoparticles are shown in **Figure 4.5a,c** and are circled in order to guide the reader's eye. They contain a very similar contrast to BCN sheets, but higher magnifications show an entirely different morphology

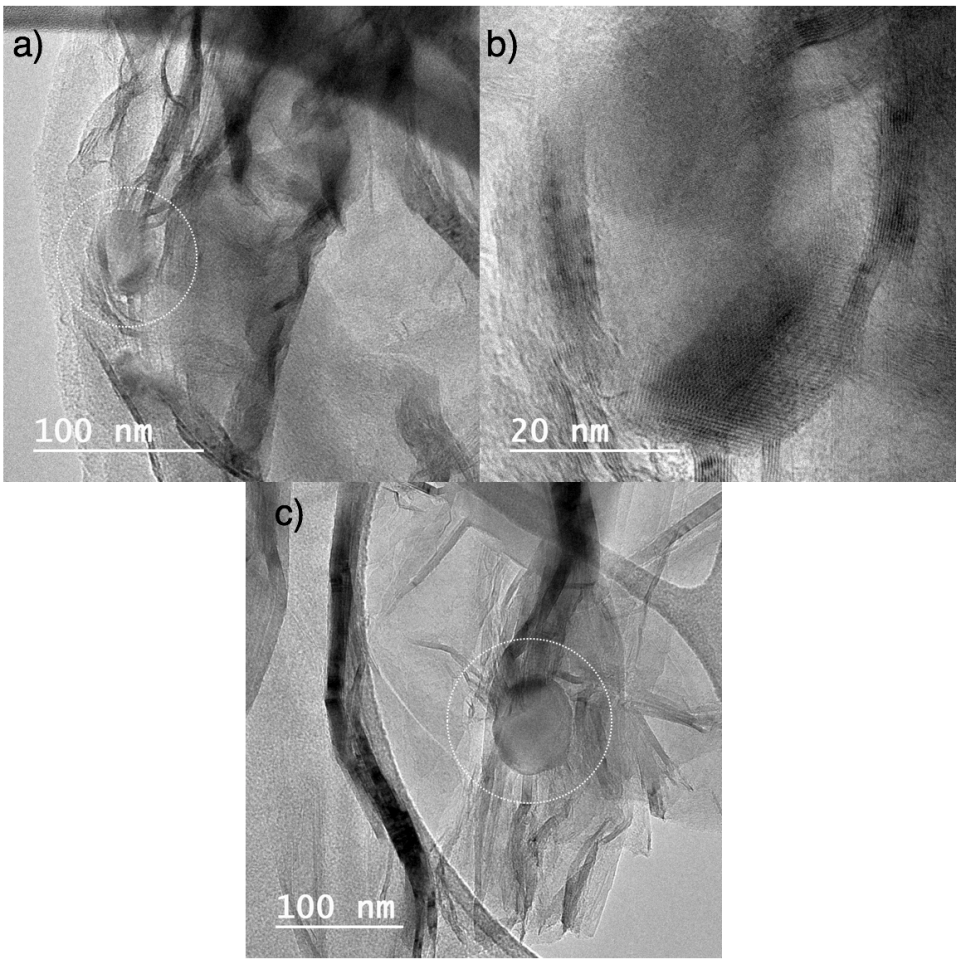

Figure 4.5 a) TEM image of BCN-1500 aerogel region containing a nanoparticle (outlined in white) b) High magnification image nanoparticle showing lattice fringes that are not graphitic c) TEM image of BCN-2000 aerogel region with outlined nanoparticle.

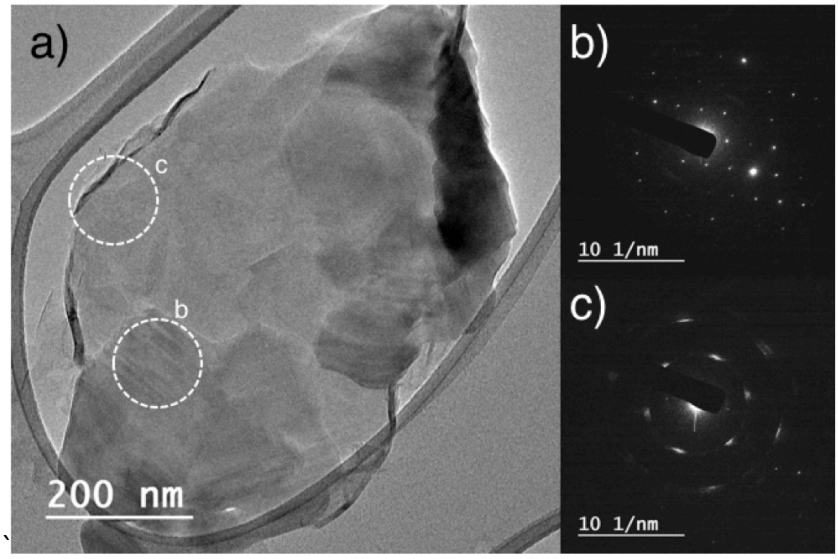

Figure 4.6 a) TEM image of region of BCN-1750 aerogel showing areas of altered contrast and interference. Selected area diffraction is performed in areas outlined with corresponding diffraction patens (b,c) showing a graphitic crystal structure and a cubic structure.

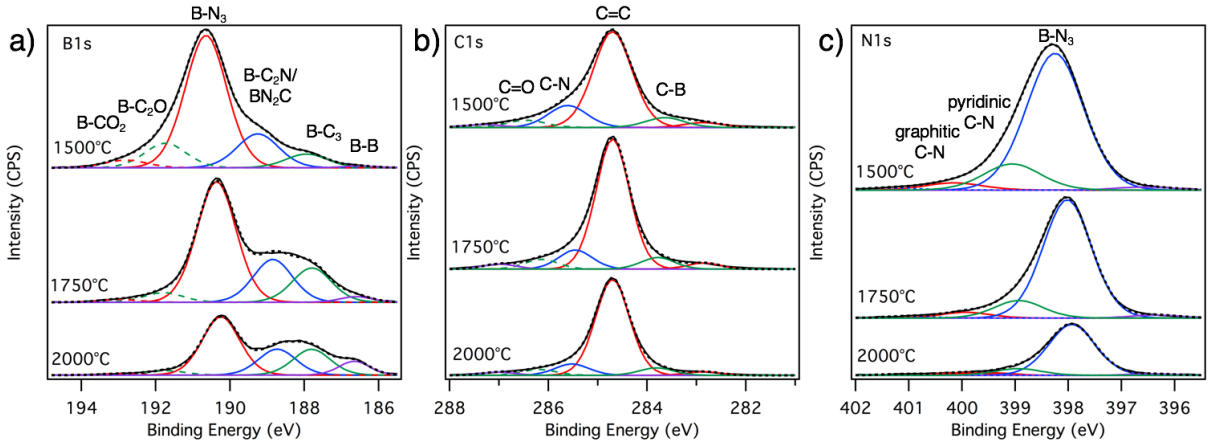

Figure 4.7 XPS analysis of BCN aerogels. a) B1s spectra, b) C1s spectra, and c) N1s spectra of BCN-1500, BCN-1750, and BCN-2000 aerogels.

Sample	Carbon (at%)	Boron (at%)	Nitrogen (at%)	Oxygen (at%)
BCN-1500	68	17	12	3.7
BCN-1750	78	13	7.0	1.9
BCN-2000	92	5.1	2.1	1.2

Table 4.1 Summary of carbon, boron, nitrogen and oxygen atomic concentrations in BCN-1500, BCN-1750 and BCN-2000 aerogels.

than would be expected from graphene. **Figure 4.5b** shows lattice fringes from a phase that is slightly off of a zone axis as opposed to classical graphene lattice fringes.

Crystallographic differences between the two phases in the BCN-1750 aerogel are shown in **Figure 4.6**. A circle is drawn around two regions that were selected for electron diffraction in **Figure 4.6a**, and the corresponding diffraction patterns are shown in **Figure 4.6b,c**. The region selected for **Figure4.6c** has a hexagonal diffraction pattern corresponding to the hexagonal structure which makes up the nanosheets. However, **Figure 4.6b** contains a completely different diffraction pattern of a cubic crystal. These two phases are worth noting and using spatially resolved chemical characterization techniques in **Section 4.6**, they will be proven to be boron nanoparticles. Their presence is a significant minority phase within the aerogels, but important to note.

4.4 Chemical Characterization of BCN Aerogels

Structural characterization indicates that 2D nanosheets make up BCN aerogels at all temperatures and the structure maintains a low density and porous morphology. Chemical characterization provides complementary information to structural studies of BCN aerogels and is important to understand the chemistries introduced and confirm the hexagonal BCN phase. In this section the chemical composition will be extensively probed using x-ray photoelectron spectroscopy (XPS), x-ray absorption spectroscopy (XAS), solid state ^{11}B NMR, Raman Spectroscopy, and x-ray diffraction (XRD).

4.4.1 X-Ray Photoelectron Spectroscopy

XPS is the most important tool for chemical characterization in order to confirm the presence of boron, carbon, and nitrogen within the aerogel as well as study the bonding configurations that form the BCN material. XPS samples are prepared by mounting silver tape on a silicon substrate and a piece of aerogel is broken off and pressed onto the silver tape, ensuring full contact with the tape and a tight connection. To be sure no aerogel will be lost into the XPS chamber, samples are blown off with gentle stream of nitrogen. The XPS used in the study is a K Alpha Plus XPS accessed through a user proposal at the Molecular Foundry at Lawrence Berkeley National Lab, and XPS work was done in collaboration with Dr. Virginia Altoe.

High resolution scans in the B1s region (194-184eV), C1s region (288-278eV), and N1s region (402-392 eV) are collected. The number of scans collected for each sample is decided with the anticipation that higher annealing temperatures will reduce boron and nitrogen concentrations and thus a high number of scans are necessary to acquire enough signal for analysis.

The B1s, C1s, and N1s spectra for BCN-1500, BCN-1750, and BCN-2000 are shown in **Figure 4.7** with corresponding boron, nitrogen, and carbon atomic concentrations in **Table 4.1**. BCN-1500 aerogels are composed of 68% carbon, 17% boron and 12% nitrogen. Higher temperature treatment decreases the boron and nitrogen incorporation to 13% and 7% in the BCN-1750 aerogel, and 5.1 and 2.1% in the BCN-2000 aerogel, respectively. The decreased boron and nitrogen content with increased firing temperature is consistent with the findings in **Chapter 3**, where boron content decreases with increased firing temperature. However, unlike BPh_3-GAs which undergo full expulsion of boron from the lattice leading to defect-engineering, boron and nitrogen content is retained in BCN aerogels as high as 2000°C. It is also important to note that boron is in excess of nitrogen at each firing temperature.

The B1s spectrum for BCN-1500 aerogels is deconvolved into six distinct bonding environments (**Figure 4.7a)**. Oxidized boron species including B-C_2O and B-CO_2 are found at the highest binding energies of 191.8 and 192.8 eV, respectively. Peaks corresponding to B-N_3 and B-C_3 bonding environments are found at 190.6 and 188.0 eV, respectively. An intermediate peak is found at 189.3eV, which is assigned to BC_2N and BN_2C bonding environments. The two would be expected to occur at very similar binding energies between the values B-N_3 and B-C_3 due to the differences in electronegativites, so we assign one peak which likely contains both environments. Lastly, an extremely low binding energy peak is found at 186.6 eV which can only be assigned to B-B bonding. The distribution of these bonding environments is highly dependent on the temperature used to activate boron and nitrogen into the lattice. Peaks from oxidized environments are expected due to the GO precursor used, and are decreased from 1500°C to 1750°C, reflecting oxygen annealing out of the lattice at these high temperatures. Additionally, B-B bonds significantly increase from BCN-1500 to BCN-1750 and increased more dramatically from BCN-1750 to BCN-2000. At high temperatures, boron can readily diffuse throughout the material and reform bonds in more favorable configurations, such as B-B bonds. The largest change in bonding contributions is between B-N_3, B-C_3, and B-C_2N/B-NC_2. While BCN-1500 has a large peak for B-N_3 and a smaller contribution from other bonding configurations, BCN-1750 and BCN-2000 have significant contributions from B-C_3 and B-C_2N/B-CN_2 environments. It is believe that there is a decrease in B-N_3 bonds in the material and they may be selectively annealed out of the material when the temperature is increased from 1500°C to 1750°C.

The C1s spectrum shown in **Figure 4.7b**, has the largest contribution from C=C bonding environments at 284.7eV provided by the GO precursor. The C1s spectrum is also deconvoluted into individual peaks corresponding to C-B, C-N, C=O, and O-C-O bonding environments at 283.6, 285.6, 286.5 and 287.3 eV, respectively. Changes to the C1s spectrum with firing

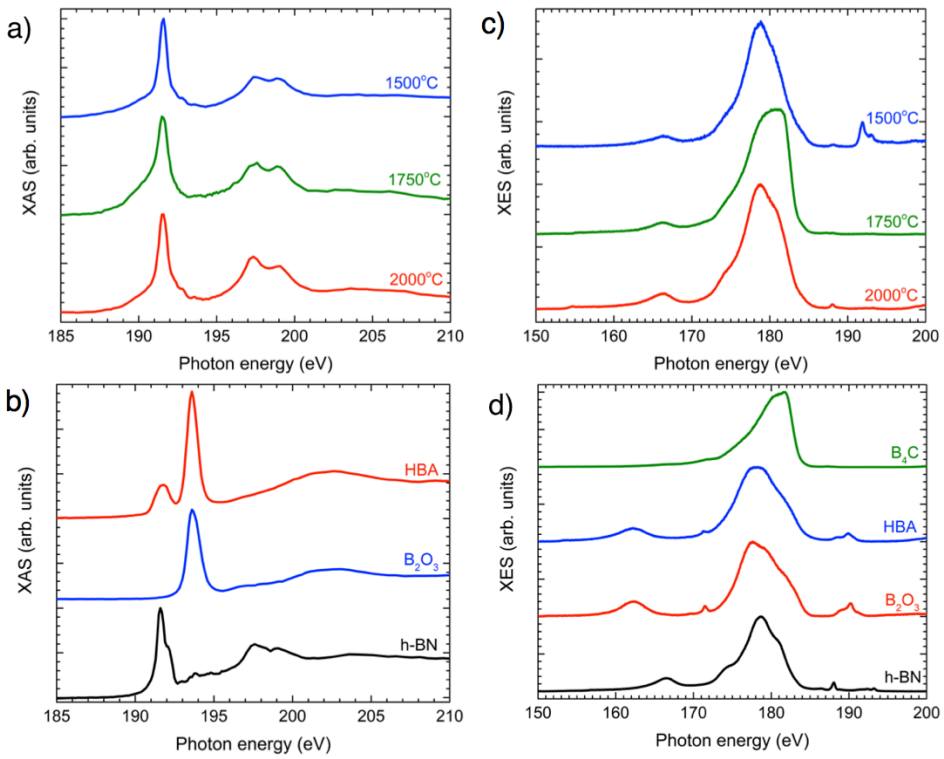

Figure 4.8 XAS and XES analysis of BCN aerogels. B-K edge a) absorbance and b) emission spectra of BCN-1500, BCN-1750, and BCN-2000 aerogels as well as c) B-Kedge absorbance spectra of HBA, boron oxide and h-BN standards and d) emission spectra of boron carbide, HBA, and boron oxide standards for comparison. In collaboration with Alex Baker and Jon Lee provided courtesy of LLNL.

temperature are subtle due to the dominant presence of C=C bonds. However, as firing temperature increases from 1500 to 2000°C there is a slight decrease in C-N and C-B bonding configurations, which is consistent with the decreased atomic concentration of these two elements.

The N1s spectrum shown in **Figure 4.7c**, shows the large contribution from an N-B bonding environment. We take a more general approach to assigning the nitrogen bonding configurations due to the less extensive literature assigning values for N-B_2C and N-BC_2. Three peaks are deconvoluted at 398.3, 399.1, and 400.2eV corresponding to B-N, pyridinic C-N, and graphitic C-N bonding environments, respectively. Similar relative levels of each bonding environment are found in BCN-1500, BCN-1750 and BCN-2000 aerogels.

The XPS results from high resolution scans of each element confirms the presence of boron, nitrogen, and carbon as well as bonding between the three. Additionally, boron is the element whose chemistry is most sensitive to the treatment temperature with B-N_3 bonds decreasing relative to B-C_3 and B-C_2N/B-CN_2 bonding environments.

4.4.2 X-Ray Absorption and Emission Spectroscopies

While XPS supports the incorporation of boron, carbon and nitrogen to make a BCN aerogel, the hybridization of the elements is vital for the electronic performance of the aerogel. Sp^2 bonded BCN is necessary as opposed to sp^3 hybridized functional groups on the surface. X-Ray absorbance spectroscopy (XAS) is performed to probe the electronic environment of BCN aerogels and the firing temperature dependence is investigated. XAS probes the unoccupied density of states in the material and gives sensitive information on the local bonding environment in the material.

The B K-edge XAS spectra for BCN-1500, BCN-1750, and BCN-2000 aerogels are shown in **Figure 4.8a,b** along with standards used for comparison including HBA, h-BN, and boron oxide. The spectra of all BCN aerogels contain large similarities to the features present in the h-BN standard with a sharp π^* resonance peak corresponding to sp^2 hybridized BN at 191.7eV and two broad σ^* resonances at 197.7 eV and 199.2 eV corresponding to core level electron transitions to unoccupied anti-bonding π^* and σ^* orbitals, respectively. A smaller feature at 190.5 eV is not present in the h-BN standard and is attributed to substitutional incorporation of boron in an sp^2-hybridized environment. This could be through either B-C_3 bonding, B-C_2N bonds, or B-CN_2 incorporation or a combination of the three. The feature at 190.5eV is observed in BCN-1500 and is enlarged in BCN-1750, indicating additional incorporation of B-C or B-C-N environments into the aerogel. This feature is slightly reduced in BCN-2000, but is still more prominent than in the BCN-1500 aerogel. Features present at 197.7 and 199.2 eV indicate an sp^2 h-BN-like environment and their line shapes sharpen with increased firing temperature indicating an increased crystallinity in the material with temperature. Additionally, no oxidation is present in the XAS spectra at any firing temperature.

Figure 4.8c,d show the XES B K-edge spectra of BCN-1500, BCN-1750, and BCN-2000 as well as the standards: B_4C, HBA, boron oxide, and h-BN , respectively. BCN aerogels contain a number of peaks present in the hBN standard at 166.5, 174.5, 178.6, 180.5, and 188eV. As the firing temperature is increased from 1500 to 1750°C, the asymmetry in the large peak is enhanced due to an increased contribution from the boron carbide transition at 181.6 eV. This is consistent with the more prominent 190.6 feature observed in XAS in BCN-1750 aerogels.

These results indicate that boron is incorporated into B-C and B-N bonding configurations through sp^2 bonds. Aerogels increase in crystallinity with higher temperature firing and BCN-1750 has the strongest components of boron incorporated into sp^2 B-C and B-C-N environments. These findings are largely in agreement with the XPS results showing a combination of B-N bonds as

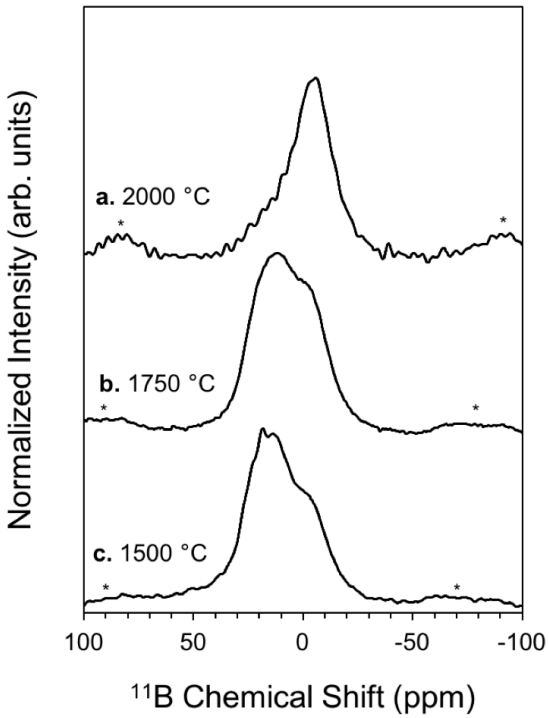

Figure 4.9 ^{11}B (SP/MAS) NMR spectra of BCN-1500, BCN-1750 and BCN-2000 aerogels. In collaboration with Harris Mason provided courtesy of LLNL.

well as B-C, C-N and B-C_2N/B-CN_2 bonds making up the material, with a more B-C-N environment moving from 1500 to 1750°C annealing temperature. This confirmation of sp^2 boron incorporation as opposed to functional groups is vital for the intriguing electronic properties that BCN materials offer.

4.4.3 Solid State ^{11}B NMR

In order to further comprehensively study boron chemistries present, ^{11}B single pulse magic angle spinning (SP/MAS) NMR is used to study BCN aerogels. ^{11}B (SP/MAS) NMR spectra are collected on a 400 MHz Bruker Avance Spectrometer. Samples are loaded into 4 mm (o.d.) rotors and spun at 11 kHz and data are collected using a Revolution NMR HX probe. Spectra are collected using a 1 μs pulse (ν_{rf} = 45 kHz) and a 0.5 s pulse delay. All spectra are referenced with respect to an external solution of 0.1 M boric acid (δ_B = 19.7 ppm). This characterization is done in collaboration is Dr. Harris Mason at Lawrence Livermore National Lab.

The ^{11}B SP/MAS spectra of the annealed aerogel samples are shown in **Figure 4.9**, and produce spectra containing a broad envelop of overlapping peaks that are not easily deconvolved. Attempts to perform ^{11}B MQ/MAS experiments to identify distinct sites were unsuccessful. Broadly, as the annealing temperature is increased a loss in intensity is observed in the spectral region of 40 to 0 ppm relative to the spectral region below 0 ppm. In BCN-2000, the peak is centered at about -4.9 ppm. The location and more isotropic peak shape suggest that BC_4 domains dominate in this sample (Kirpatrick et al, 1991). The gradual shift to lower chemical shifts would suggest that as the samples are annealed, the C:B ratio is increasing with increased annealing temperature, and that the BCN environments present in the precursor phase is being lost. Unfortunately, ^{11}B (SP/MAS) NMR yielded ambiguous results which will require further experiments in order to fully interpret to assign each peak to a bonding configuration.

4.4.4 Raman Spectroscopy

Raman spectroscopy is used to further characterize BCN aerogels and their Raman spectra are compared with those of a pure graphene aerogel (GA) treated at the same temperature. A similar naming convention is used as with BCN aerogels, with GAs treated at 1500°C called GA-1500 and GAs treated at 1750°C named GA-1750 etc.. There no current consensus in the literature regarding the Raman spectrum of a BCN material. Certain studies report a material with a classical graphene spectrum and an additional peak at 1367 cm^{-1} for BN, some report BCN containing solely graphene peaks, while others do not report the Raman spectrum[124,127,130]. As shown in **Figure 4.10a,b**, the Raman spectrum of graphene is obtained for BCN aerogels treated at all temperatures. Each aerogel contains a D peak at 1355cm^{-1}, a G peak at 1584cm^{-1}, and a 2D peak at 2695$cm^{-1.}$ As described in **Chapter 2,** the ratio of the intensities of the D peak to the G peak (I_D/I_G) is used to evaluate the quality of the material and information regarding heteroatoms in the lattice can be deduced with larger I_D/I_G indicating an increased number of heteroatoms in the material. The I_D/I_G of the BCN-1500 is 0.97 while that of the control graphene aerogel is 0.91, indicating that there is an increase in the number of defects in the material, most likely due to the incorporation of B and N heteroatoms into the lattice. The same trend occurs in BCN-1750 with the I_D/I_G of 0.82 relative to 0.74 in GA-1750, as well as in BCN-2000 containing I_D/I_G of 0.7 relative to 0.39.

Another significant difference between the GA Raman spectrum and that of all BCN aerogels is the reduced signal to noise ratios in BCN aerogels. Both sets of data are collected at the same laser power, thus the diminished signal to noise of the BCN aerogel is intrinsic to the

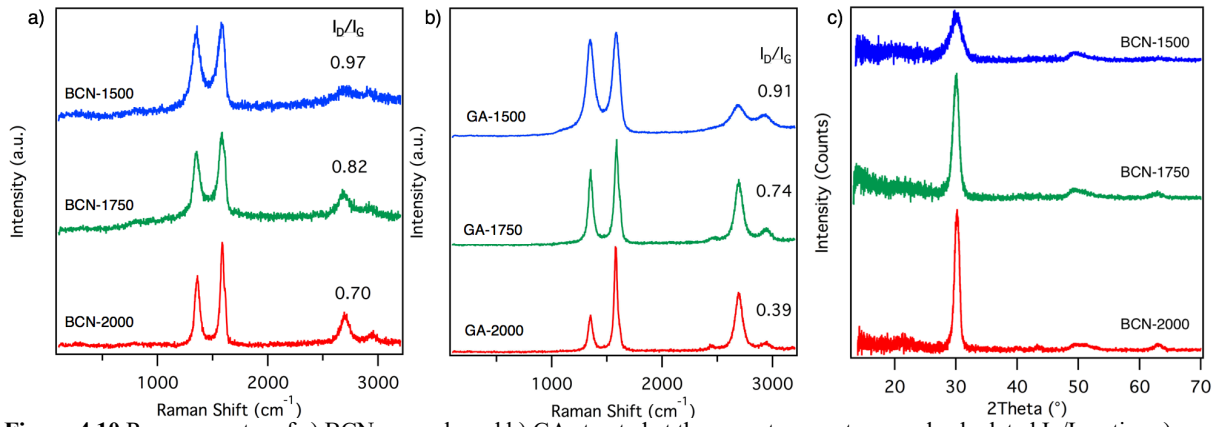

Figure 4.10 Raman spectra of a) BCN aerogels and b) GAs treated at the same temperatures and calculated I_D/I_G ratios c) XRD diffractograms of BCN-1500, BCN-1750, and BCN-2000 aerogels.

sample. While boron and nitrogen heteroatoms contribute to the increased D to G ratios, the decrease in the abundance of graphene domains and formation of a BCN phase is believed to be responsible for the decreased signal to noise in BCN aerogels.

4.4.5 X-Ray Diffraction

X-ray diffraction (XRD) is used to study the crystal structure of BCN materials and confirm that they contain a hexagonal structure. As described in **Chapter 2**, hexagonal materials like graphene and h-BN have a dominant peak around 30° (for a 1.79Å x-ray source) from the (002) plane corresponding to an interlayer spacing of 0.33nm. The diffractograms are shown in **Figure 4.10c** for BCN aerogels. At each temperature there is a dominant peak at 30° due to diffraction of the (002) plane with an interlayer distance of 0.336 nm. This is in agreement with the expected interlayer distance. Additional peaks corresponding to the (100)+(101) planes as well as the (004) are located at 49° and 63°, respectively. BCN-1750 and BCN-2000 exhibit more prominent and narrower (002) peaks than BCN-1500 due to the increased crystallinity afforded by the high temperature treatment, as previously reported in GAs[131]. The presence of a large (002) peak and absence of other prominent peaks from a cubic or wurtzite phase confirms the hexagonal nature of the BCN aerogels.

4.5 Spatially Resolved Chemical Characterization of BCN Aerogels

Sections 4.3 and 4.4 individually studied the spatial and chemical composition of BCN aerogels, respectively. These thorough analyses determined that the material is composed of crosslinked nanosheets, and that the aerogel as a whole contains bonds between boron carbon and nitrogen. However, simultaneous characterization of the spatial orientation of the sample and the chemistries present are necessary to correlate the two. Using electron energy loss spectroscopy (EELS) mapping and scanning transmission electron microscopy (STEM), the chemical composition of BCN aerogels with nanometer spatial resolution is accomplished. This work is done in collaboration with Brian Shevitski and Dr. Shaul Aloni at the Molecular Foundry.

EELS is a widely used technique to study the atomic composition of nanomaterials. It is coupled to a TEM, giving researchers the capability to study the chemical composition and structure of samples. Electrons are transmitted through the sample and undergo inelastic scattering before detection. The predominant origin of inelastic scattering is called “core loss EELS” and is due to ionization of an inner electron shell, giving the technique atomic sensitivity. The fine

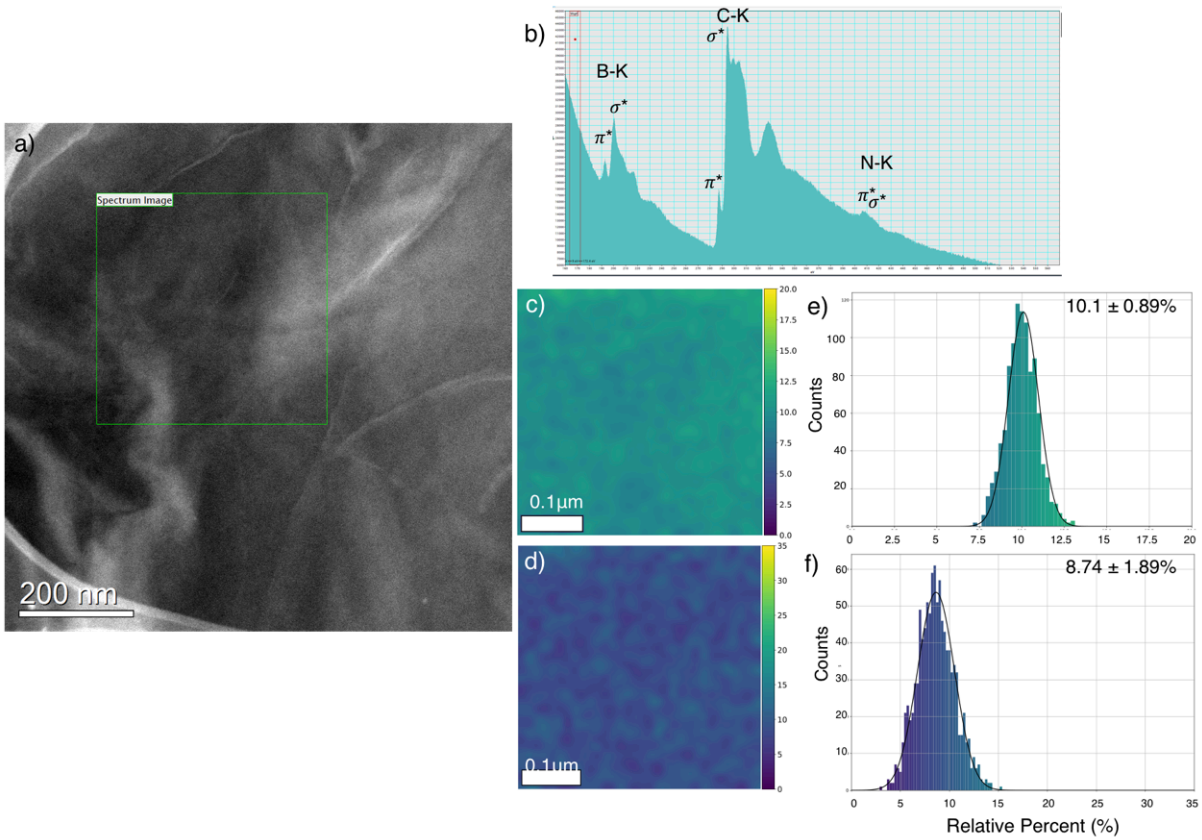

Figure 4.11 a) STEM image of BCN-1500 aerogel and b) representative EELS spectrum. EELS maps of c) B/C and d) N/C atomic concentrations collected from square region in (a) and e,f) corresponding histograms of B/C and N/C , respectively. In collaboration with Brian Shevitski.

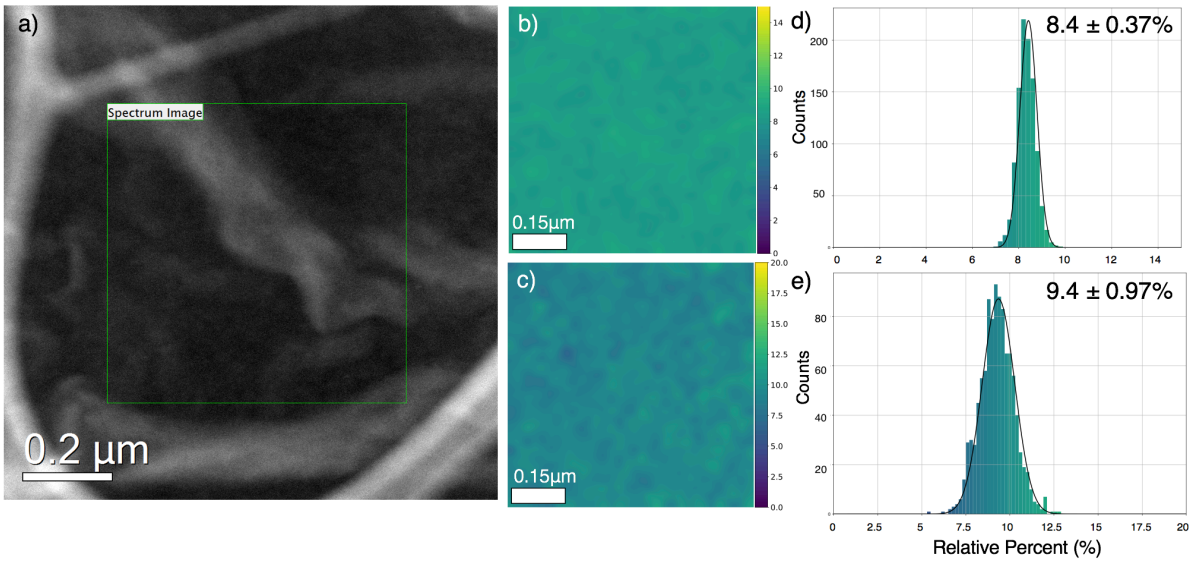

Figure 4.12 a) STEM image of BCN-1750 aerogel and EELS maps of b) B/C and c) N/C atomic concentrations collected from square region in (a) with d,e) corresponding histograms of B/C and N/C , respectively. In collaboration with Brian Shevitski.

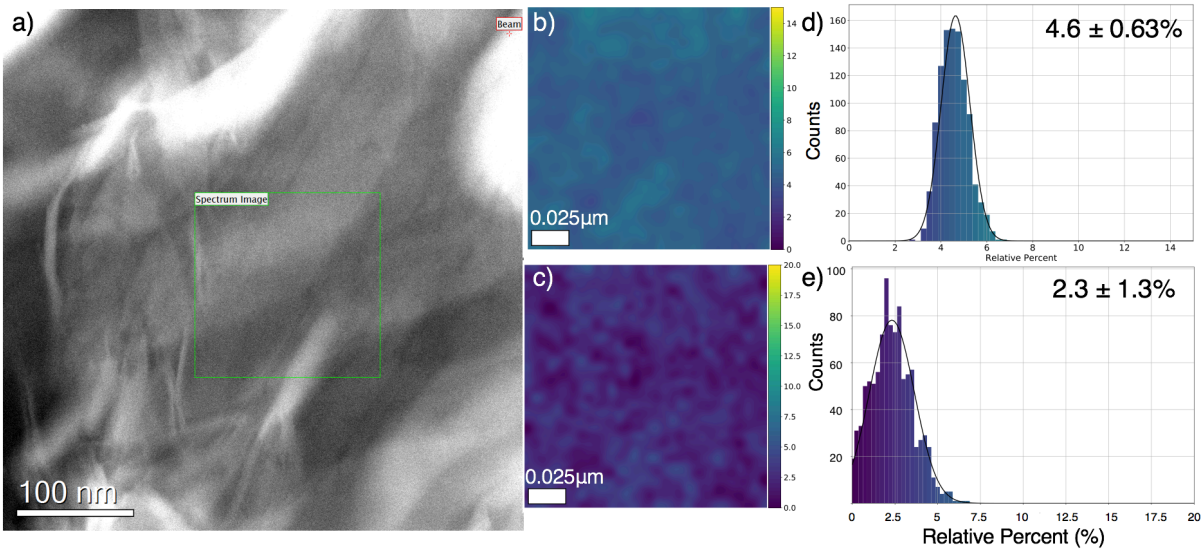

Figure 4.13 a) STEM image of BCN-2000 aerogel and EELS maps of b) B/C and c) N/C atomic concentrations collected from square region in (a) with d,e) corresponding histograms of B/C and N/C , respectively. In collaboration with Brian Shevitski.

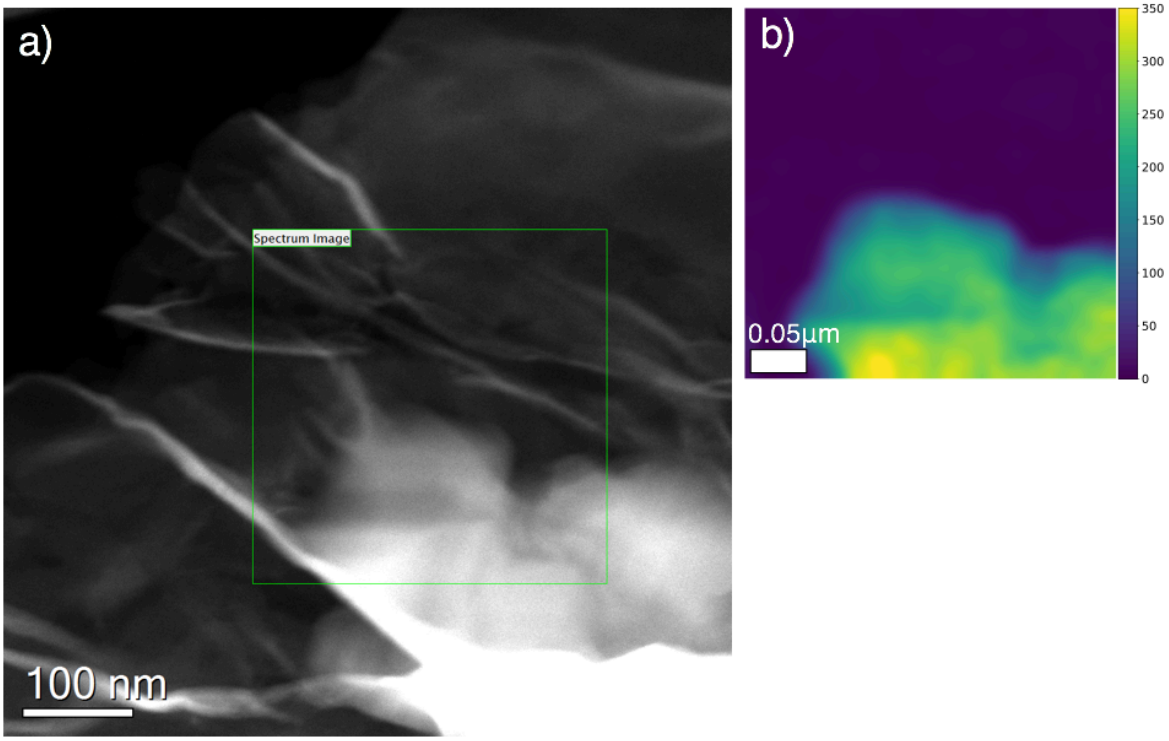

Figure 4.14 a) STEM image of BCN-1750 aerogel in area with nanoparticle present b) EELS map of B/C in region showing high concentration of B in nanoparticle. In collaboration with Brian Shevitski.

structure and shape of peaks can also be used to determine the types of bonds present. Other mechanisms for inelastic scattering include phonon excitations, inter- and intra-band transitions, and plasmon excitations and are detected using "low loss EELS". While core loss EELS is used to determining atomic composition and chemical bonding, low loss EELS is capable of determining valence and conduction band energies and electronic properties. In this section, core loss EELS is used for identification and spatial distribution of boron, carbon, and nitrogen by constructing EELS maps over a specified region of a STEM image.

For spatially resolved EELS, a STEM image is taken of the sample to determine the morphology of the area and part of the region is selected for EELS mapping. A 32x32 pixel map is constructed where an EELS spectrum is collected at each pixel and an elemental map can be constructed by plotting the signal of each element at each pixel. EELS maps of BCN aerogels will be expressed as the ratio of atomic concentration of B:C (%) and N:C (%). Uniform contrast is indicative of a homogenous material, where areas with enriched signal would imply phase segregation of a graphene phase and another phase such as h-BN or crystalline boron.

Figure 4.11a shows the STEM image of a BCN-1500 aerogel. The source of image contrast in STEM is Z contrast, thus a BCN aerogel with low Z elements has low contrast and consequently many features are not observable. The region outlined in the center is chosen for EELS mapping and a representative EELS spectrum is shown in **Figure 4.11b**. Peaks corresponding to boron, carbon, and nitrogen are present, and the fine structure of these peaks indicates that all three are in an sp^2 environment. A spectrum is taken at each pixel and the B/C and N/C maps are shown in **Figure 4.11c,d**, respectively, with the corresponding histograms shown in **Figure 4.11e,f**. Both B/C and N/C maps show a highly homogenous material with even contrast and no evidence of phase segregation. This also evident in the histograms plotting the distribution of B/C values from each pixel, which can be fitted to a tight gaussian distribution with low standard deviation. The average B/C concentration is 10.1% and N/C concentration is 8.7%. EELS maps and histograms of BCN-1750 and BCN-2000 aerogels are shown in **Figure 4.12 and 4.13** which also maintain excellent homogeneity in the sample. A phase segregated material would show areas of high contrast and low contrast and the histogram would contain two peaks. Thus the only possibility of phase segregation would be if it occurred on a scale less than the size of a pixel, or approximately 21nm. The narrow and large (002) peak observed in XRD as well as single crystal hexagonal electron diffraction patterns of regions larger than this do not agree with phase segregation on this scale and the synthesis of a ternary BCN phase is confirmed. Lastly, the boron and nitrogen concentrations decrease with increasing firing temperature, and are in good agreement with the XPS analysis.

EELS mapping also has the capability to determine the composition of the nanoparticles observed using TEM as mentioned in **Section 4.4**. A STEM image of BCN-1750 containing a nanoparticle is shown in **Figure 4.14**. The EELS map clearly shows that two phases are present; One contains a large concentration of boron and another contains a much lower boron concentration. The nanoparticle has about 300% B/C, confirming that the nanoparticles are likely composed of crystalline boron with some detection of the underlying BCN nanosheet beneath it.

Integrating the conclusions drawn from each characterization method gives a clear picture of the composition of each sample. Electron microscopies indicate that BCN aerogels are made up of crosslinked nanosheets yielding a porous and low density material. Electron diffraction on individual nanosheets and XRD on the bulk material confirm the hexagonal crystal structure of the material. XPS and XAS show boron, carbon, and nitrogen are incorporated into the aerogel through sp^2 B-N, B-C, and N-C. Finally, chemical analysis with spatial resolution using EELS mapping confirms that a homogenous ternary BCN phase is synthesized without phase segregation.

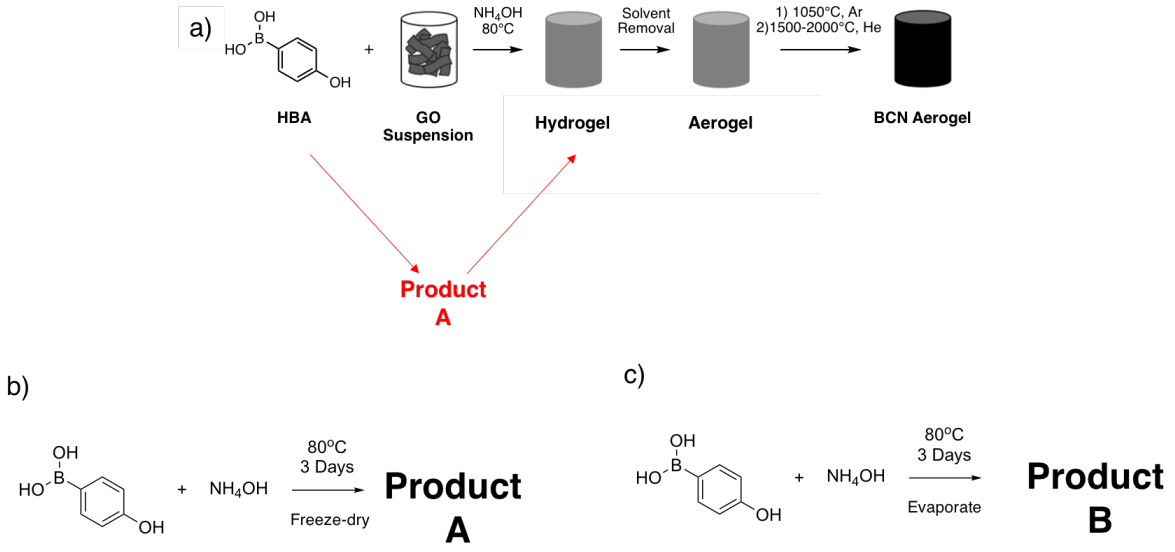

Figure 4.15 a) Schematic of BCN aerogel synthesis highlighting the production of **Product A** in the gelation step which continues to be present through heat treatment b,c) Control reactions between HBA and ammonium hydroxide yield **Product A** if freeze-dried, and **Product B** if solvent is evaporated.

4.6 Origin of BCN Chemistries

Sections 4.3-4.5 used extensive structural and chemical diagnostic tools in order to confirm the synthesis of a homogenous BCN aerogel. In this section the origin of the boron carbon and nitrogen chemistries will be explored.

As previously mentioned, both HBA and ammonium hydroxide play vital roles in the formation of the BCN aerogels. HBA can react with the functional groups on GO in order to be added into the crosslinks, as well as react with ammonium hydroxide as illustrated in **Figure 4.15a**. Due to the many competing reactions taking place, the analyses and determination of the precise compounds presents after gelation that lead to BCN chemistries is quite complex. Through a series of control reactions, it is possible to gain insight into these compounds to better understand the intermediate species leading to bonding between boron, carbon, and nitrogen.

In order to determine the product of the reaction between HBA and ammonium hydroxide, a control reaction mimicking the BCN aerogel synthesis conditions without GO is completed (**Figure 4.15b,c)**. Briefly, 40 mg/mL HBA and ammonium hydroxide (1:6 vol:vol NH_4OH:H_2O) are reacted at 80°C for 3 days without stirring. The products are either recovered through freeze-drying or solvent evaporation, and their products are called **Products A** and **B**, respectively. The IR spectra of **Products A** and **B** are shown in **Figure 4.16** along with the HBA starting material.

Both HBA and **Product B** have peaks corresponding to C=C stretches around 1600cm^{-1}, and in-plane C-H bends at 1080 and 1030cm^{-1} indicating that the phenyl group is still present in **Product B**. However, peaks corresponding to any aromatic compound are notably absent in the freeze-dried **Product A** meaning that the aromatic is lost during the freeze-drying process. A large peak is present at 1370cm^{-1} which is also present in **product B** and HBA. This peak is assigned to the B-O stretching mode. Additionally the broad peak in HBA at 3200cm^{-1} due to -OH stretch is present in **Product A** and diminished in **Product B**. Other peaks in **Product A** are present at 1600,1310,1050,990,780, and 692cm^{-1}.

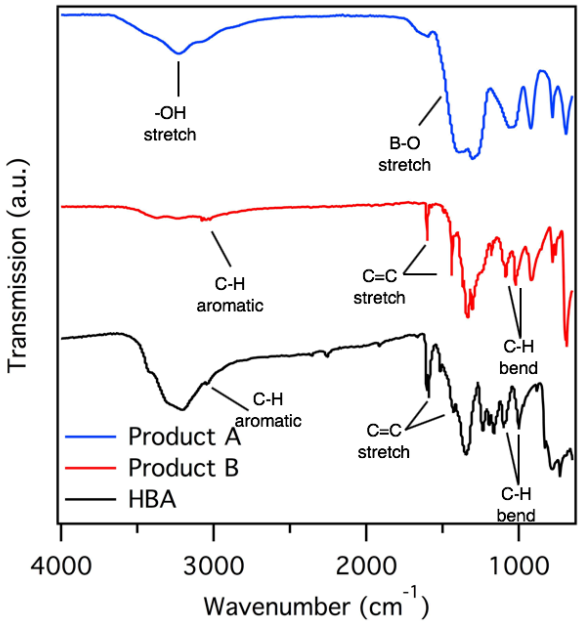

Figure 4.16 FTIR spectra of **Product A**, **Product B**, and HBA.

Due to the complex nature of the reactions taking place and sensitivity to drying method, we currently are only able to hypothesize the products present which lead to the chemistries observed. Due to the basic conditions, it is believed that HBA undergoes protodeboronation as described in **Figure 4.17.** In basic media, a hydroxyl will add onto the boron causing it to have a negative charge. This intermediate undergoes deborylation, resulting in a $B(OH)_4^-$ product. This complex can then react with ammonium hydroxide as described in **Figure 4.17b**.

To test this hypothesis, control reactions between boric acid, $B(OH)_3$, the closest readily available compound to $B(OH)_4^-$, and ammonium hydroxide at 80°C for 3 days are completed and the product is called **product C**. The IR spectra of **Product C**, as well as **Product A** and the boric acid starting material are shown in **Figure 4.18**. Boric acid contains peaks for a -OH stretch at 3190cm^{-1}, asymmetric B- O stretch at 1410cm^{-1}, and B-OH peaks at 1190, 883, and 774cm^{-1}. Peaks

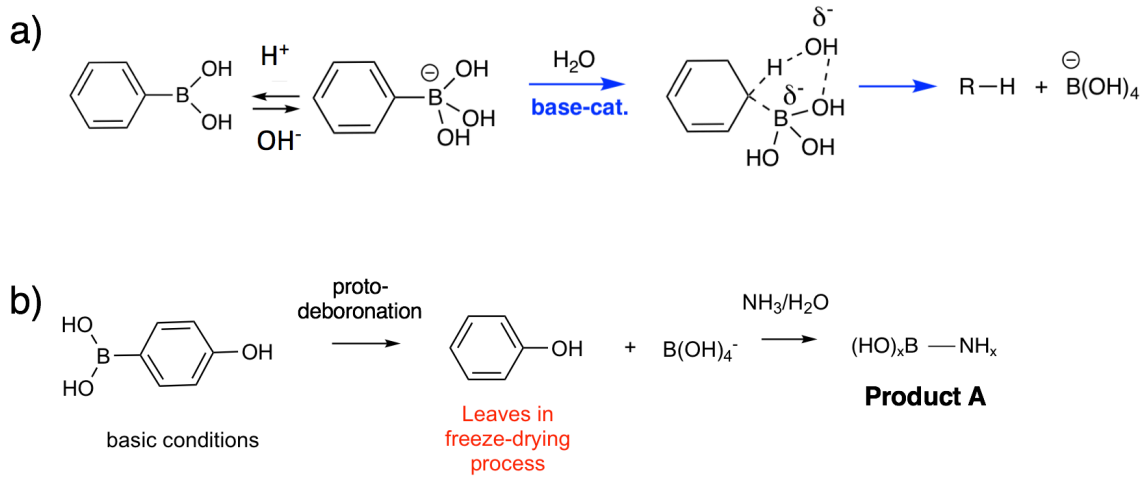

Figure 4.17 a) General mechanism or protodebornation[260] b) Proposed scheme for formation and identification of **Product A.**

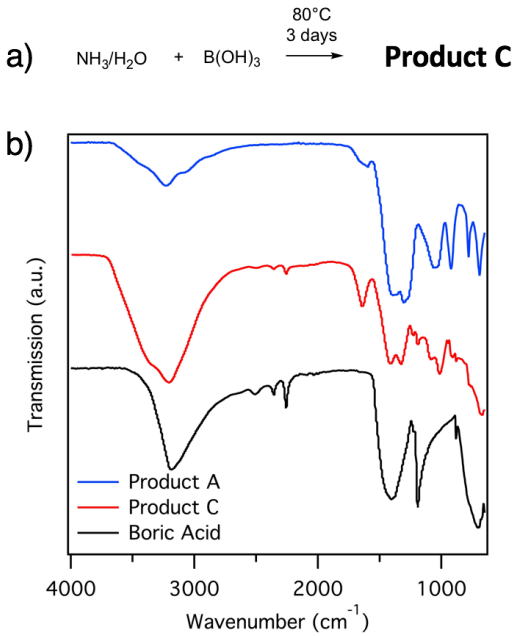

Figure 4.18 a) Control reaction between ammonium hydroxide and boric acid yielding **Product C** b) IR spectra of **Product A**, **Product C**, and boric acid.

due to unreacted boric acid are still present after reaction with ammonium hydroxide indicating that boric acid was not fully consumed. However, a number of new peaks emerge which are also present in **Product A,** supporting a reaction between the two reactants takes place. A peak at 1640cm^{-1} from -NH_2 vibrations emerges along with a feature for N-H stretch at 3380cm^{-1}. Additionally B-N stretches are present 1130 and 780cm^{-1}. These results indicate that a B-N complex is formed in both **Product A** and **Product C**.

Further experiments are necessary in order to precisely determine the compounds that lead to boron, nitrogen, and carbon chemistries. However, current evidence indicates that:

1) Deborylation occurs due to basic conditions
2) The phenyl product is lost during freeze drying
3) The resulting $B(OH)_4^-$ complex reacts with ammonium hydroxide to form a $B(OH)_x$-NH_x complex,
4) The presence of the $B(OH)_x$-NH_x complex leads to boron and nitrogen incorporation.

This process is also further complicated by the fact that both HBA and **Product A** can react with GO functional groups and add into the crosslinks of the aerogel while also being capable of physisorbing to the nanosheets as free compounds.

4.7 Attempts to Increase Boron and Nitrogen Incorporation

In an attempt to increase the boron and nitrogen incorporation, be capable of synthesizing aerogels of controllable B:C:N concentrations, and hopefully synthesize a 1:1:1 B:C:N material, the amount of HBA added into the precursor GO suspension is altered. Previous analyses studied BCN aerogels that used 40 mg/ml HBA in water in the precursor GO suspension. In this section, 80 mg/mL and 120 mg/mL concentrations of HBA are added into the suspension, and will be referred to as 80-BCN-1500 or 120-BCN-1500 for aerogels synthesized using 80 mg/mL or 120 mg/mL HBA and heat treated at 1500°C, respectively. No other factors in the synthesis are altered.

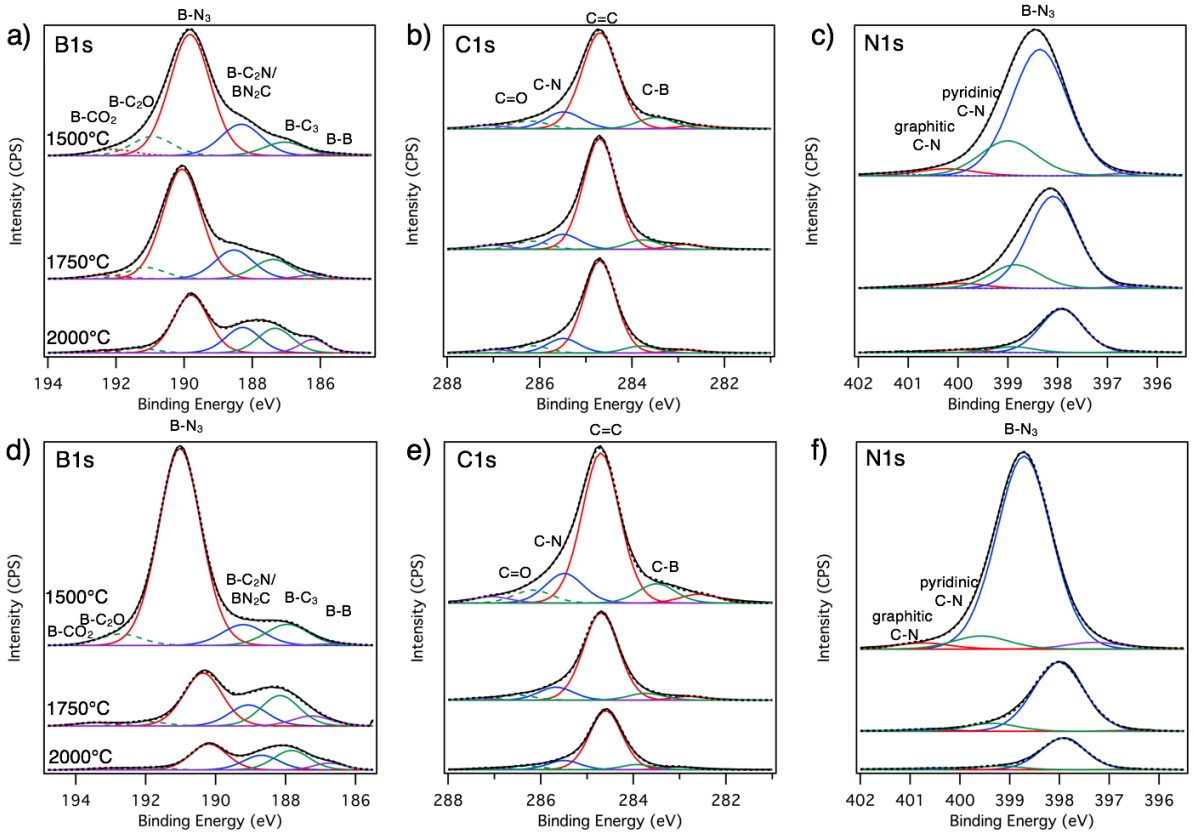

Figure 4.19 a-c) B1s, C1s, and N1s spectra of 60-BCN aerogels and d-f) B1s, C1s, and N1s spectra of 80-BCN aerogels.

a)

Sample	Carbon (at%)	Boron (at%)	Nitrogen (at%)	Oxygen (at%)
80-BCN-1500	65	20	13	2.6
80-BCN-1750	77	13	8.2	1.6
80-BCN-2000	92	4.5	1.8	2

b)

Sample	Carbon (at%)	Boron (at%)	Nitrogen (at%)	Oxygen (at%)
120-BCN-1500	34	37	26	2.8
120-BCN-1750	79	13	5.4	2.4
120-BCN-2000	89	6.5	2.0	2.2

Table 4.2 a,b) Summary of carbon, boron, nitrogen and oxygen atomic concentrations in 80-BCN and 120-BCN aerogels, respectively.

XPS is once again used as the primary diagnostic tool for chemical analysis. The B1s, C1s, and N1s of 80-BCN and 120-BCN aerogels treated between 1500-2000°C are shown in **Figure 4.19**. The C1s and N1s spectra contain the same bonding configurations as described in **Section 4.4.1** that do not undergo large changes depending on high temperature treatment.

The B1s spectrum contains the same trends described in **Section 4.4.1**; The 80-BCN-1500 and 120-BCN-1500 samples have the largest contribution from a B-N_3 environment at 190.6eV. Higher temperatures result in decreased B-N_3 and larger contributions from B-C_3 and B-C_2N/B-N_2C bonding environments at 188.0 and 189.3eV, respectively. Oxidized boron species also decrease above 1500°C with corresponding increase in B-B bonds at 186.6eV.

Table 4.2 summarizes the atomic concentrations of boron carbon and nitrogen in 80-BCN and 120-BCN samples. The concentrations of each chemical species in BCN aerogels treated at 1500°C are extremely dependent on the concentration of HBA incorporated into the GO suspension. While 40-BCN-1500 aerogels have 17% B, 68% C, and 12% N as reported in **Section 4.4.1**, 80-BCN-1500 contains 20% B, 65% C, and 13% N and 120-BCN-1500 is made up of 34%

B, 37% C, and 26% N. Treatment at 1750°C results in all aerogels containing approximately 13% B, 78% C, and 7% N regardless of the concentration of HBA included in the GO suspension. Furthermore, 2000°C conditions result in all BCN aerogels composed of approximately 5% B, 92% C, and 2% N. Thus, there may be a thermodynamic criteria limiting the incorporation of B and N into the material at high temperatures.

Using SEM and TEM, the microscale and nanoscale morphologies are studied. SEM images of 80-BCN and 120-BCN aerogel samples treated at 1500, 1750 and 2000°C are shown in **Figure 4.20**. All aerogels are made up of nanosheet morphologies, nearly identical to the microscale structure of 40-BCN aerogels characterized in **Section 4.4**. However, the 120-BCN-2000 aerogel also contains a spinel-like morphology indicating a recrystallization process is likely occurring at such high concentrations of HBA. Notably, these structures are stable at incredibly high temperatures.

The sheet morphologies of each aerogel are studied using TEM as shown in **Figure 4.21**. At this low magnification, the full sheets are clearly visible, as well as the presence of boron nanoparticles as noted in **Section 4.4**. It is also noted that all samples contain much more jagged and uneven edges and more textured sheet surfaces than are present in 40-BCN aerogels, and is likely due to the growth of new phases. Further analysis is necessary in order to determine if the textured areas are BCN materials or possible grains of another material.

Using spatially resolved EELS, 120-BCN-1500 is studied to correlate the different nanoscale morphologies observed under TEM with their chemical composition (**Figure 4.22**). 120-BCN-1500 is chosen for this analysis due to its composition being nearly 1:1:1 B:C:N. A uniform B/C distribution in the selected region with an average relative concentration of about 13%. Even distribution of N/C is also confirmed with an average relative concentration of 9.5%. These boron and carbon values highly deviate from the concentrations calculated using XPS which would be expected around 100% for B/C and N/C. XPS collects data from a region of the sample on the

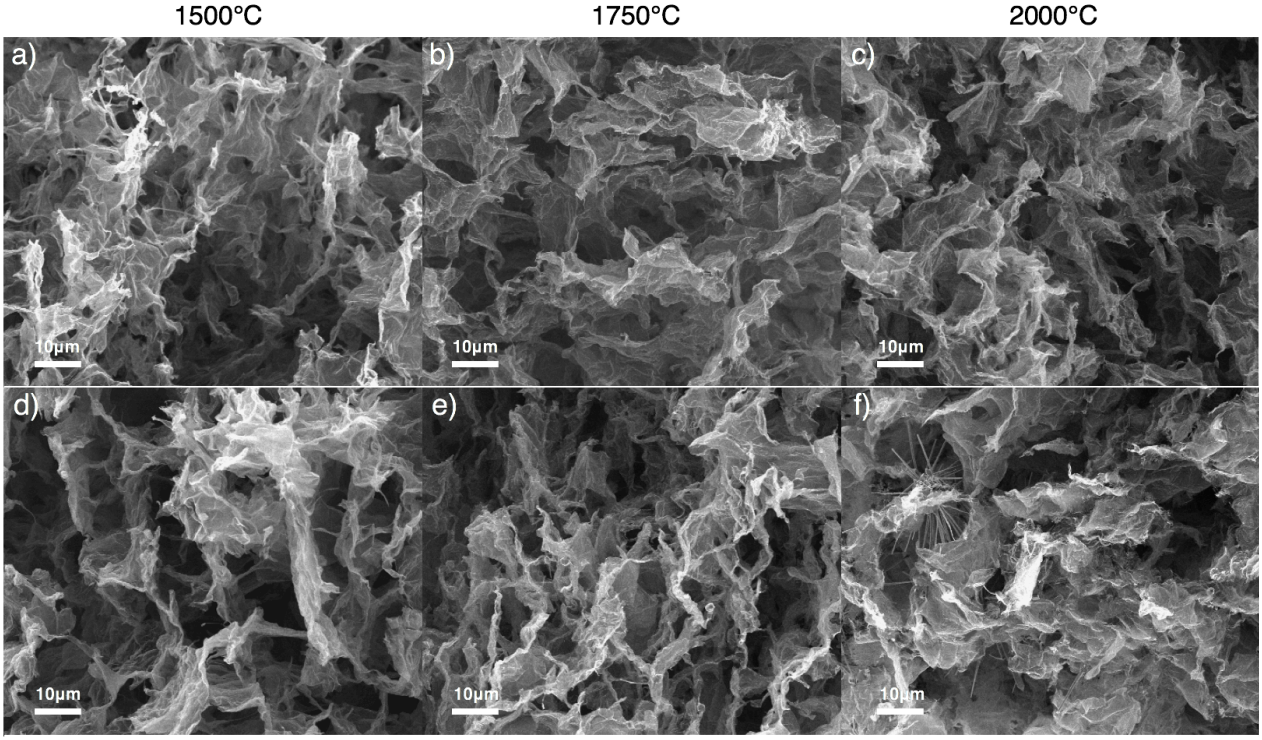

Figure 4.20 SEM images of a-c) 80-BCN-1500, 80-BCN-1750, and 80-BCN-2000 aerogels and d-f) 120-BCN-1500, 120-BCN-1750, and 120-BCN-2000 aerogels, respectively.

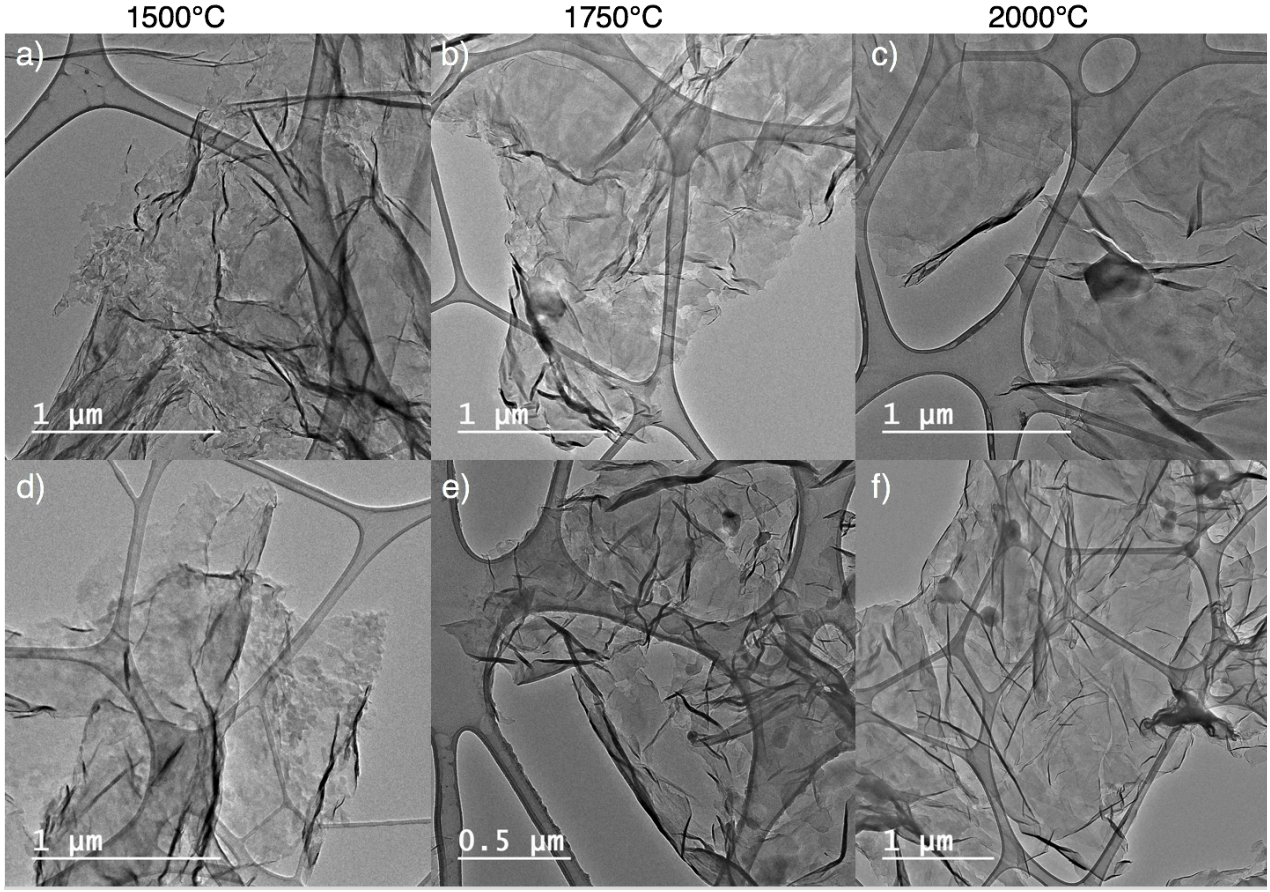

Figure 4.21 TEM images of a-c) 80-BCN-1500, 80-BCN-1750, and 80-BCN-2000 aerogels and d-f) 120-BCN-1500, 120-BCN-1750, and 120-BCN-2000 aerogels, respectively.

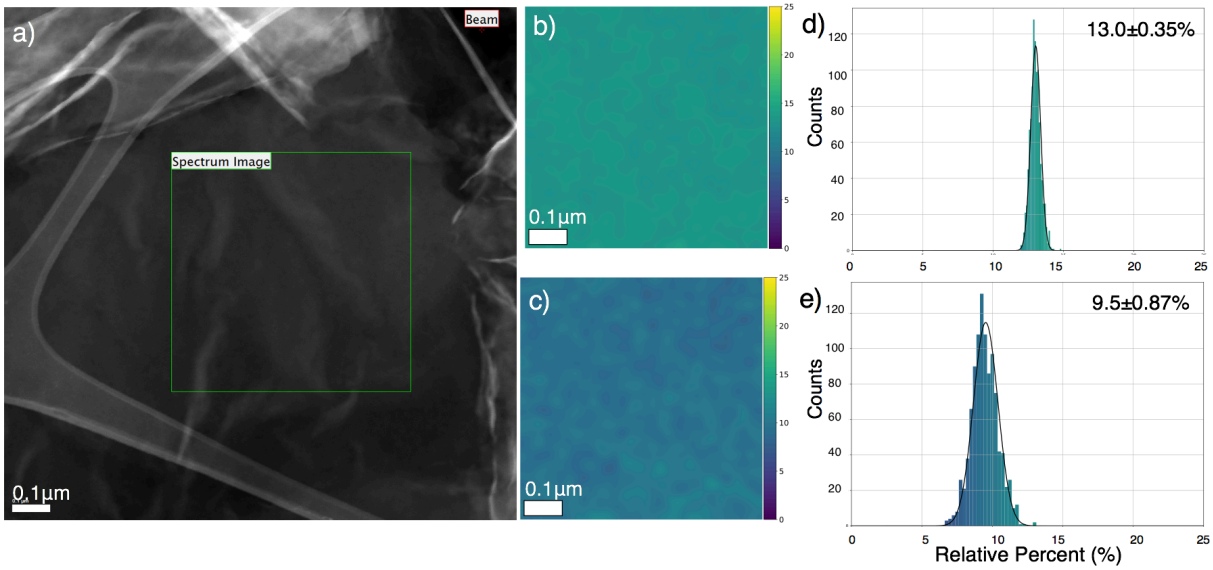

Figure 4.22 a) STEM image of 120-BCN-1500 aerogel and EELS maps of b) B/C and c) N/C atomic concentrations collected from square region in (a) with d,e) corresponding histograms of B/C and N/C , respectively. In collaboration with Brian Shevitski.

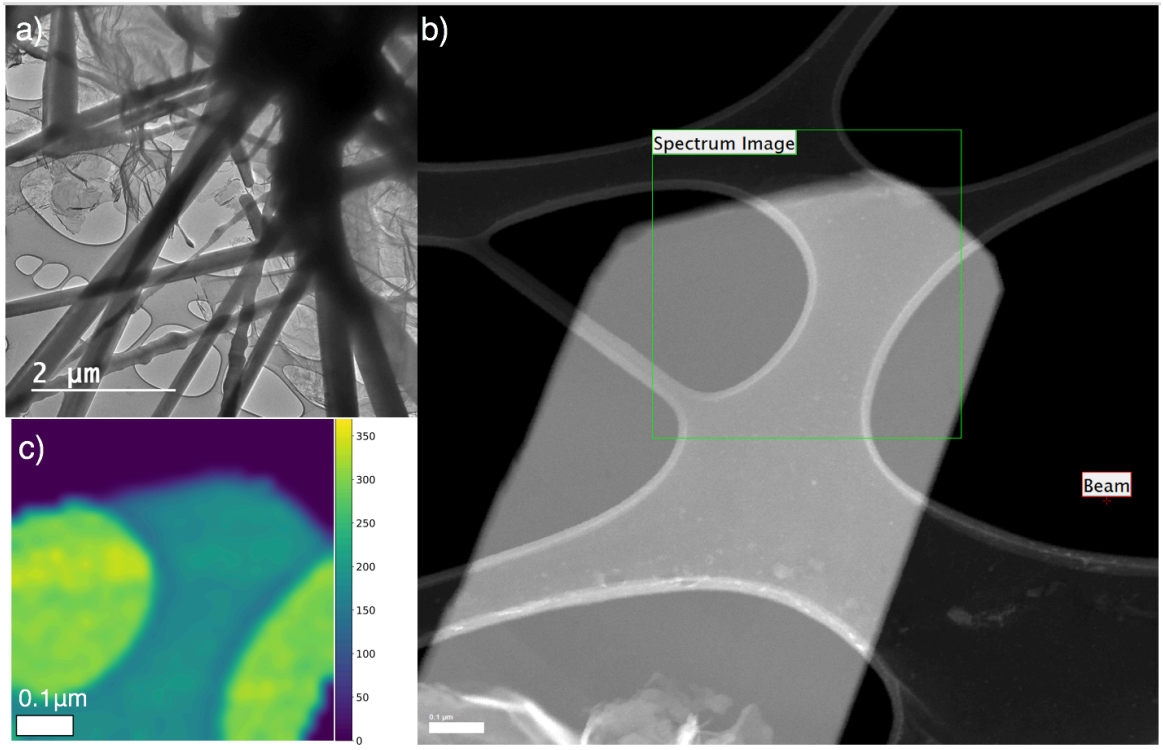

Figure 4.23 a) TEM image of 120-BCN-1500 sample in a region with spinel structures b) STEM image of spinel structure and c) EELS map of B/C concentration in enclosed square region from (b). In collaboration with Brian Shevitski.

order of millimeters. Thus the 1:1:1 B:C:N ratios calculated indicate that there is likely another phase leading to this value. The spinel structures observed under SEM in 120-BCN-2000 are also observed under TEM in 120-BCN-1500 (**Figure 4.23a)**. The EELS map of these structures show an extremely high concentration of boron in the spinel and is likely composed of boron carbide (B_4C, **Figure 4.23b,c**). In order to determine the location of the remaining nitrogen in this sample, further studies are necessary.

These results indicate that while increasing the concentration of HBA in the GO suspension during synthesis can incorporate additional boron and nitrogen into aerogels treated at 1500°C, there is not a change in the composition of the individual nanosheets and results in the synthesis of additional morphologies making an inhomogeneous material. It is possible that the additional boron and nitrogen chemistries could be beneficial for catalytic applications and further studies are necessary to more comprehensively examine the nitrogen and boron chemistry of the 80-BCN and 120-BCN aerogels.

4.8 Critical Point Drying of BCN Aerogels for Enhanced Surface Area

The textural properties of aerogels are studied using nitrogen porosimetry as described in **Chapter 2**. The nitrogen adsorption and desorption isotherms of BCN-1500, BCN-1750, and BCN-2000 aerogels are shown in **Figure 4.24.** The low surface areas typical of freeze-dried aerogels are found in BET surface areas of BCN aerogels at all firing temperatures as described in **Table 4.3**. BCN-1500 aerogels have a surface area of 20.6 m^2/g, BCN-1750 have surface areas of 23.9 m^2/g and BCN-2000 aerogels possess surface areas of 23.5 m^2/g. These low surface areas could be increased using post-processing techniques such as CO_2 or KOH activation[132,133]. Another approach to improve the textural properties of BCN aerogels is to change the method of solvent removal.

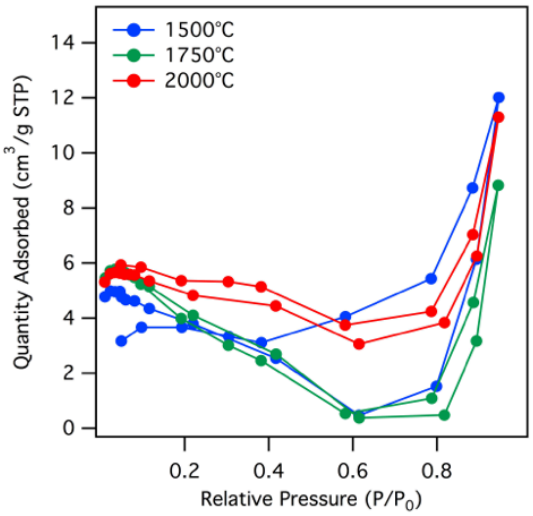

Figure 4.24 Nitrogen adsorption and desorption isotherms of freeze-dried BCN-1500, BCN-1750, and BCN-2000 aerogels.

	BET Surface Area (m^2/g)	Pore Volume (cm^3/g)
BCN-1500	20.6	0.0125
BCN-1750	23.9	0.0071
BCN-2000	23.5	0.0068

Table 4.3 Calculated BET surface areas and pore volumes of freeze-dried BCN-1500, BCN-1750, and BCN-2000 aerogels.

It is well documented that the conditions for solvent removal can lead to changes in the surface area and pore structure of graphene aerogels[100]. Freeze-drying with flash freezing of the hydrogel at -77°C leads to larger pores and lower surface areas and an ultra-low density material, while critical point drying leads to a larger density and larger surface area with a higher population of mesopores. In order to enhance the surface area of BCN aerogels, they are exchanged into acetone and critical point dried. These critical point dried samples are referred to as BCN-CPD. It is important to note that the solvent exchanges necessary for critical point drying come at a cost to the boron and nitrogen incorporation into the aerogel due to washing away of **Product A** within the pores of the aerogel prior to drying.

Figure 4.25 shows the B1s, N1s, and C1s XPS spectra of BCN-CPD aerogel and **Table 4.4** contains the atomic composition of each sample. As expected, the amounts of B and N incorporated into the sample are reduced compared to the freeze-dried aerogels. Additionally, there is a slight change in the bonding configurations. The B1s spectrum shows that at BCN-CPD-1500 has larger contributions from B-C_3 and B-C_2N/B-CN_2 than the freeze-dried sample. Freeze-dried samples were predominantly composed of B-N_3 incorporation after 1500°C firing. **Section 4.6** determined that the *in-situ* generated compound, **Product A**, is likely a B-N complex. Thus, **Product A**, is washed away during solvent exchanges leading to less incorporation of B-N and overall lower boron and nitrogen incorporation. Additionally, with increased firing temperature, there is drastically more B-B incorporation in BCN-CPD aerogels.

The goal of altering the drying method is to increase the surface area. While there are some changes in the chemistries incorporated, boron, nitrogen and carbon are present in the material.

SEM is used to study the morphology of the material and is shown in **Figure 4.26**. The aerogels possess a more closely packed aerogel structure with a morphology very similar to a critical point

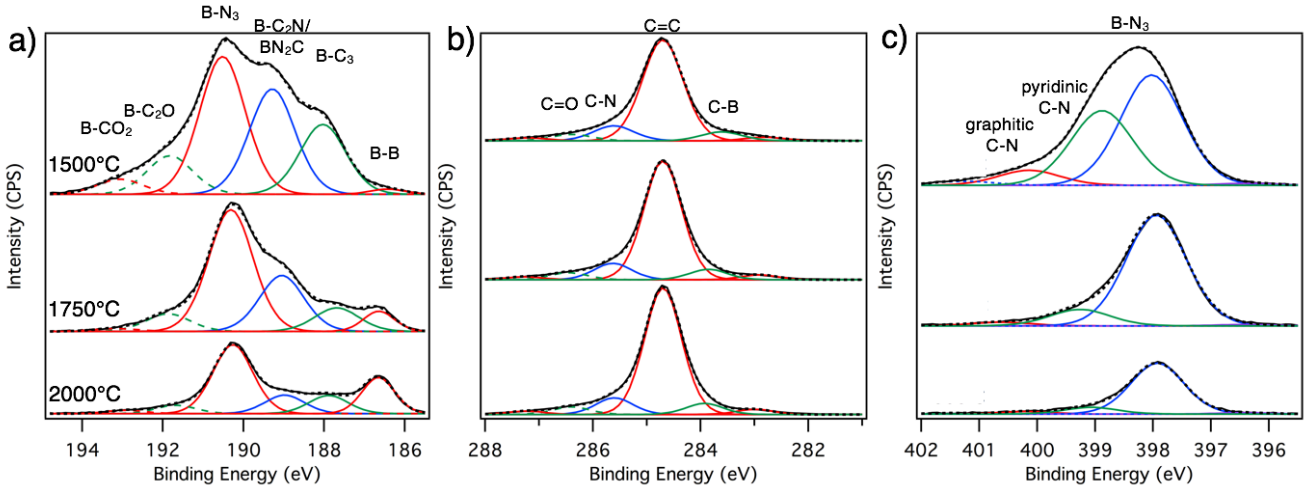

Figure 4.25 a-c) B1s, C1s, and N1s spectra of BCN-CPD aerogels, respectively.

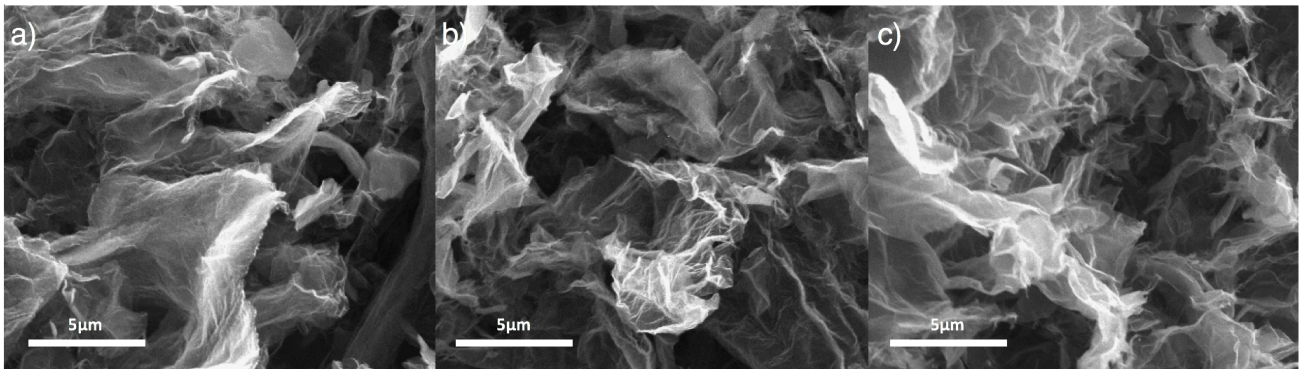

Figure 4.26 a-c) SEM images of BCN-CPD-1500, BCN-CPD-1750, and BCN-CPD-2000, respectively.

Sample	Carbon (at%)	Boron (at%)	Nitrogen (at%)	Oxygen (at%)
BCN-CPD-1500	87	6.9	4.1	2.5
BCN-CPD-1750	91	4.3	3.5	1.9
BCN-CPD-2000	95	2.3	1.0	1.7

Table 4.4 Summary of carbon, boron, nitrogen and oxygen atomic concentrations in BCN-CPD aerogels.

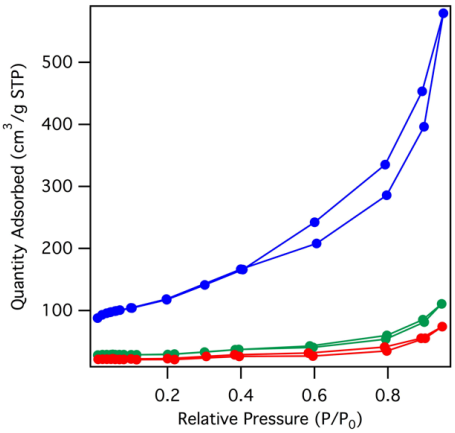

Figure 4.27 Nitrogen adsorption and desorption isotherm of BCN-CPD-1500, BCN-CPD-1750, and BCN-CPD-2000 aerogels.

	BET Surface Area (m^2/g)	Pore Volume (cm^3/g)
BCN-CPD-1500	412	0.716
BCN-CPD-1750	120	0.122
BCN-CPD-2000	88.6	0.075

Table 4.5 Calculated BET surface areas and pore volumes of BCN-CPD-1500, BCN-CPD-1750, and BCN-CPD-2000 aerogels.

dried graphene aerogel that contains a high surface area.

The textural properties of BCN-CPD aerogels are studied using nitrogen porosimetry. **Figure 4.27** shows the nitrogen adsorption/desorption isotherms and **Table 4.5** summarizes their BET surface areas and pore volumes. At each firing temperature BCN-CPD aerogels have higher surface areas than BCN aerogels flash frozen at -77°C and freeze-dried. BCN-CPD-1500, BCN-CPD-1750, and BCN-CPD-2000 aerogels have a surface areas of 412, 120, and 88.6 m^2/g, respectively. While these surface areas are still lower than graphene aerogels, they are many times greater than the surface areas recovered by freeze-drying and still sufficiently high for many applications.

4.9 Future Work

One of the most remarkable differences between BCN and graphene is the difference in electronic properties. As mentioned in the introduction, BCN with a hexagonal crystal structure can have electronic properties intermediate between graphene and boron nitride. Future work should focus on electrical characterization of BCN aerogels in order to determine changes that arise as a result temperature used to activate B and N into the lattice, as well as the concentration of HBA incorporated into the GO suspension.

Secondly, future work should focus on integrating BCN aerogels into catalytic applications. Early studies have noted the enhanced electrocatalytic behavior of boron and nitrogen doped graphene as well as BCN materials. However, previous studies have not had a thorough characterization of the structural and chemical compositions of the BCN materials. Due to the extensive analysis of these compositions in this study, important connections between chemistry and catalytic performance can be made and make large advancements to the field.

Chapter 5: Core-Shell Hybrid Aerogels for Photocatalytic Applications

Nano Fun-Fact: A hypothetical single sheet of monolayer graphene large enough to cover the city of San Francisco would only weigh approximately 57 grams, or an eighth of a pound. The flexibility of graphene would also allow it to easily contour to the many hills in the city.

5.1 Background

Graphitic carbon nitride (g-C_3N_4) is an emerging 2D material known for its promising photocatalytic performance and has been studied extensively for water splitting, CO_2 reduction, pollutant degradation, organic syntheses, and bacterial disinfection[134–141]. The variety of reactions that g-C_3N_4 is capable of catalyzing using light as the sole energy source has the capacity to have a huge impact on both global environmental and energy crises by making clean hydrogen energy more reasonable, as well as artificial photosynthesis, and light-driven environmental remediation.

G-C_3N_4 is made up of tri-s-triazine units connected through secondary nitrogens, as shown in **Figure 5.1a**. It can be easily synthesized through thermal condensation of nitrogen rich organic precursors including urea, melamine, and dicyandiamide (DCDA). During the thermal condensation process, all three precursors produce the g-C_3N_4 building unit, melam (**Figure 5.1b**), which undergoes full condensation to produce bulk g-C_3N_4. Analogous to graphite and its single layer graphene component, bulk g-C_3N_4 must be thermally, chemically, or liquid exfoliated in order to produce few layer g-C_3N_4 [142].

While other widely studied photocatalysts like TiO_2 have band gaps in the ultraviolet region, g-C_3N_4 has a 2.7eV band gap with valence band and conduction bands at -1.1eV and 1.6eV, respectively[134]. These properties make it possible for g-C_3N_4 to catalyze a range of reactions in the visible light range.

In addition to g-C_3N_4's well suited electronic properties for photocatalysis, its thermal and chemical stability make it particularly attractive. The aromatic C-N heterocycles impart remarkable thermal stability to the material, making it stable in air up to 600°C. Photocatalysts must be compatible with electrolytes and thus must be capable of withstanding alkaline and/or acidic pH conditions. G-C_3N_4 has high chemical stability and does not degrade in alkaline, acidic conditions, or in organic solvents facilitating its use in a variety of electrolytes[143]. Furthermore, it is entirely composed of carbon and nitrogen, two of earth's most abundant elements making the possibility of a synthesis that is both low cost and environmentally friendly feasible.

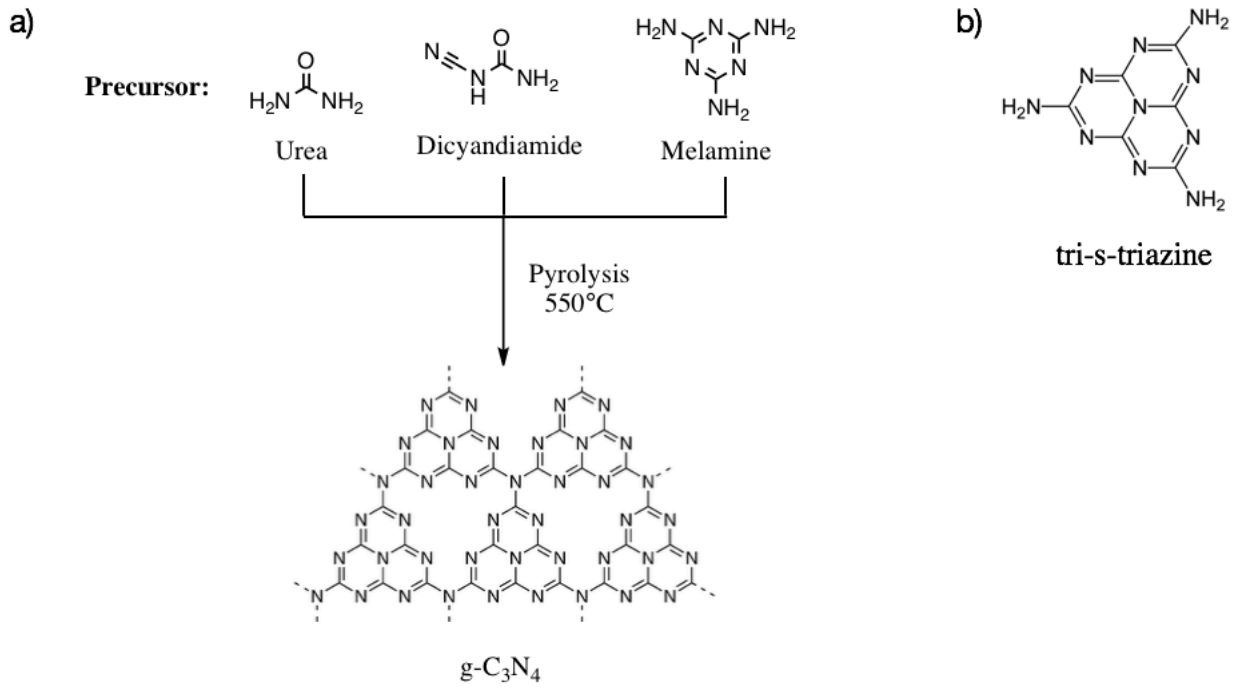

Figure 5.1 a) Synthesis of g-C_3N_4 from nitrogen rich organic precursors urea, dicyandiamide, melamine by pyrolysis at 550°C b) Structure of tri-s-triazine, the g-C_3N_4 building block.

5.2 Motivation of GA-gC_3N_4 Core-Shell Hybrid Structure

From a theoretical perspective, g-C_3N_4 should be capable of photocatalysis at high efficiency, including both photocatalytic water reduction and oxidation reactions. However, experimental photocatalytic performances universally fall short with overall watersplitting scarcely reported[144].

The flawed catalytic performance can be understood after first considering the generalized steps for photocatalytic reactions in semiconductors:

1) Photon Absorption
2) Charge Carrier Transfer
3) Catalytic Surface Reactions

In Step One, the semiconductor will absorb a photon with energy greater than or equal to the band gap to produce an electron in the conduction band and a hole in the valence band. These photogenerated charge carriers are transferred to the surface of the semiconductor in Step Two, and in Step Three the charge carrier and reactants will react in photoreduction or photoxidation processes.

For optimized performance, a photocatalyst should efficiently absorb light through a narrow bandgap and large absorption coefficient, effectively separate charges to prevent recombination before transfer to the surface and participation in surface reactions, as well as be stable over a long period of time. While g-C_3N_4 can efficiently absorb light, catalytic performance of bulk g-C_3N_4 is greatly hindered due to its low intrinsic conductivity resulting in high rates of carrier recombination and low catalytic efficiency. Additionally, bulk g-C_3N_4 also suffers from low surface area necessary to support catalytic reactions.

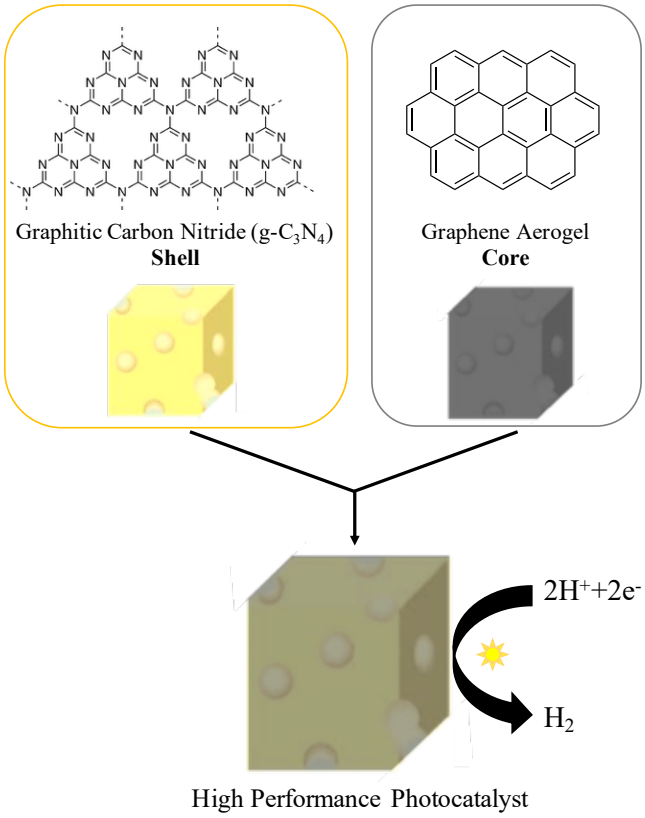

Figure 5.2 Representative structure of g-C_3N_4-GA hybrid. Conductive porous GA core covered with photocatalytic g-C_3N_4 shell for high performance photocatalyst.

A number of approaches to modify the chemical structure of g-C_3N_4 in order to improve charge separation have been explored including band-gap engineering through elemental or molecular doping, and the formation of heterojunctions, with many approaches requiring expensive transition metals and rare noble metals as co-catalysts[145–149].

As an alternative to integrating inorganic materials into g-C_3N_4, it can also be coupled with graphitic nanostructures to form photocatalytic composites. Graphene is an excellent coupling material due to its high conductivity and excellent electron mobility making it capable of promoting charge transfer and separation, thereby reducing rates of carrier recombination[141,150,151]. Graphene aerogels (GAs) in particular are ideal candidates due to their high surface area and porosity and well developed π network, capable of effectively interacting with g-C_3N_4. The sp^2 hybridization throughout graphene can increase the contact with g-C_3N_4 when the 2D materials stack on top of one another, as well as enhance the charge transfer rate from g-C_3N_4 to graphene.

Researchers have previously integrated GAs and g-C_3N_4 into composites by adding bulk g-C_3N_4 into the GO suspension before gelation or by incorporating nitrogen rich g-C_3N_4 precursors into the GO suspension and heat treating the aerogel for thermal condensation[152,153]. While both methods are effective at coupling the two functional materials and result in enhancement in photocatalytic dye degradation and electrocatalytic activity for HER, these approaches do not maximally expose graphitic carbon nitride for light absorption. Additionally, due to g-C_3N_4's 600°C decomposition temperature, high temperatures for thermal reduction of graphene cannot be employed, resulting in low quality graphene used in these studies.

In this chapter, the synthesis of core-shell hybrid aerogels consisting of a conductive graphene core and photocatalytic g-C_3N_4 shell will be presented (**Figure 5.2**). This configuration is rationally designed to be a high performance photocatalyst capable of overcoming the limitation of bulk g-C_3N_4. A thin g-C_3N_4 shell is maximally exposed for light absorption and photogenerated charge carriers can be transferred to the conductive GA core to facilitate charge separation. The non-random placement of g-C_3N_4 within the structure and exclusive orientation on the surface ensures that all g-C_3N_4 is available for photon absorption as opposed to embedded within the aerogel. Additionally, the GA core is highly crystalline and used as a template for the synthesis of g-C_3N_4. The direct growth of g-C_3N_4 on top of graphene layers ensures intimate contact between the 2D materials for maximal performance enhancement and the surface area and pore structure present in the GA is imparted onto to the hybrid structure after growth of g-C_3N_4.

5.3 Synthesis of g-C_3N_4-GA Hybrids

The synthesis of bulk graphitic carbon nitride is widely reported in the literature and is prepared by heating a nitrogen rich hydrocarbon precursor, such as DCDA, melamine or urea, in air or inert atmosphere to induce thermal condensation of the precursor into g-C_3N_4[154]. Here, DCDA is used as a precursor and a highly crystalline GA is used as a conductive core to grow g-C_3N_4-GA core shell structures. The crystallinity of the GA is not only important for the performance of the material, but is vital for the successful synthesis. Highly crystalline GAs are resistant against oxidation up to 700°C, whereas lower quality GAs oxidize at 500°C and would not survive the conditions necessary for g-C_3N_4 growth. GAs infiltrated with DCDA are heated to 550°C to thermally condense DCDA into g-C_3N_4 on the surface of the GA, yielding a g-C_3N_4 shell on a GA core as shown in **Figure 5.3a**.

GAs are synthesized as described in **Chapter 2.** A 20 mg/mL suspension of GO in water is prepared followed by light sonication overnight. Ammonium hydroxide (1:6 by volume NH_4OH:H_2O) is added to catalyze the gelation at 80°C for 3 days. The solvent is removed by solvent exchange into a water bath followed by two solvent exchanges into acetone and supercritical drying with carbon dioxide. The GO aerogels are reduced to highly crystalline GAs by a low temperature annealing step at 1050°C for two hours in argon to remove most oxygen containing species and prevent contamination of the high temperature graphite furnace. The subsequent high temperature treatment at 2000°C in helium is performed on a graphite furnace at Lawrence Livermore National Lab in order to anneal out defects in the graphene lattice.

Core shell structures of g-C_3N_4 grown on top of GAs are synthesized by an infiltration and heat treatment method. GAs are submerged in ethanol under vacuum to wet the pores, followed by a solvent exchange with 0.5M DCDA in water overnight at 80°C. The infiltrated GA and DCDA solution are loaded into an alumina crucible and box furnace and treated at 550°C for 4 hrs with a ramp rate of 2°C/min to yield the core shell g-C_3N_4-GAs. It is worth noting that the presence of aqueous DCDA is necessary for g-C_3N_4 growth. Attempts to freeze-dry the solvent prior to thermal condensation resulted in no growth.

5.4 Chemical Characterization of g-C_3N_4-GA Hybrids

After thermal condensation of DCDA, the GAs remain black/grey and a small amount of yellow bulk can be seen grown on the walls of the alumina crucible (**Figure 5.3b)**. Importantly,

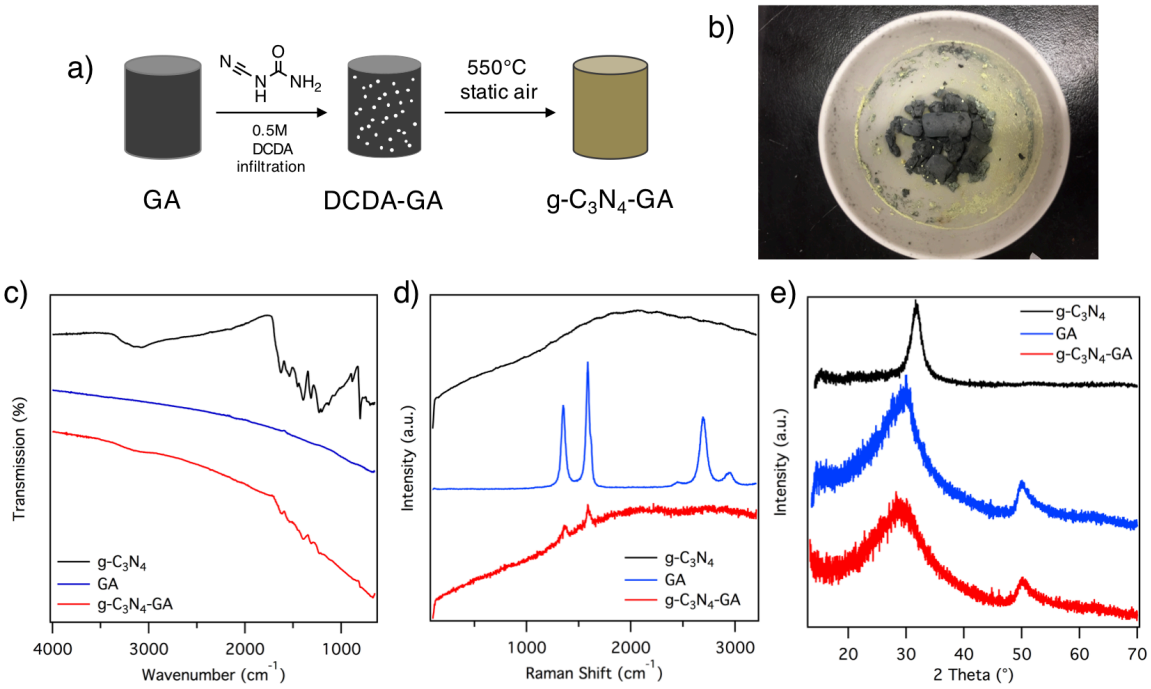

Figure 5.3 a) Scheme for synthesis of g-C_3N_4-GA hybrids b) Photo of alumina crucible after synthesis c-e) FTIR, Raman, and XRD of bulk g-C_3N_4, GA, and g-C_3N_4-GA, respectively.

the retention of GAs black color indicates that a large amount of bulk g-C_3N_4 is not synthesized. After g-C_3N_4 growth, on average aerogels are 3.7 times as heavy as prior to growth. This mass increase coupled with the lack of color change imply that a thin layer of g-C_3N_4 is grown on the surface.

In order to further characterize g-C_3N_4 growth FTIR, Raman and XRD are performed. **Figure 5.3c** shows the FTIR spectra of bulk g-C_3N_4, a highly crystalline GA, and g-C_3N_4-GA. The spectrum of bulk g-C_3N_4 contains several peaks between 1600-1200cm^{-1} due to C-N stretches in the heterocycle. Additionally, the peak located at 803cm^{-1} corresponds to a breathing mode of triazine units and the broad peak at 3110cm^{-1} is an amine stretch due to incomplete condensation of the precursor resulting in amine edge terminations. The typical FTIR spectrum of a GA contains no dominant peaks and is simply a drifting baseline. The spectrum of g-C_3N_4-GA hybrids contains the features of both the bulk g-C_3N_4 and GA spectra. Peaks between 1200-1600, 803 and 3100cm^{-1} are weak yet clearly discernable. Additionally, the drifting baseline feature from the GA core is present indicating the successful synthesis of a thin layer of g-C_3N_4 on the GAs.

As outlined in **Chapter 2**, Raman spectroscopy is extensively used to characterize graphene materials. Here, a 514nm is used as an excitation wavelength, and **Figure 5.3d** shows the Raman spectrum of GAs that includes the three characteristic graphene peaks: the G peak corresponding to the in-plane E_{2g} phonon around 1590 cm^{-1}, a two-phonon mode called 2D peak at 2700 cm^{-1}, and a D peak due to the number of defects in the material at 1350 cm^{-1}. With a 514nm excitation wavelength, the bulk g-C_3N_4 is dominated by luminescence in the visible, with no discernable peaks. The g-C_3N_4-GA core shell hybrid contains features from both the GA core and the g-C_3N_4 shell in the Raman spectrum. The D and G graphene peaks are prominent and the luminescence from the g-C_3N_4 shell is also found in the hybrid; Again, indicating that the g-C_3N_4 is present as a thin layer.

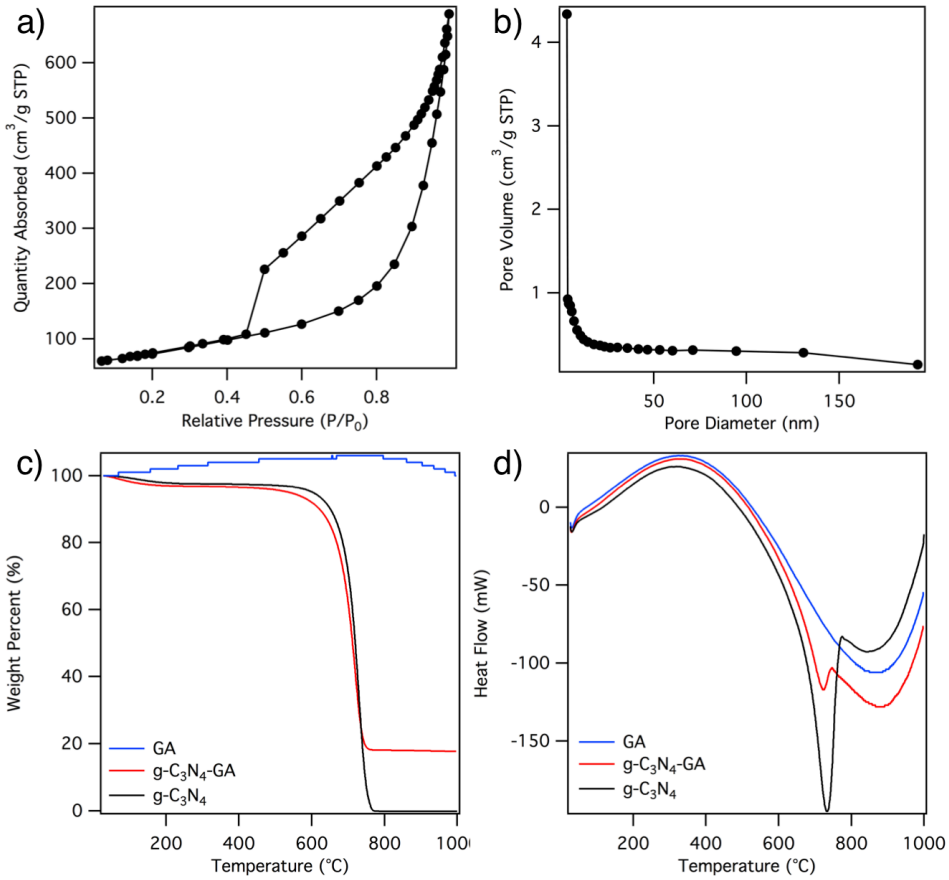

Figure 5.4 a,b) Nitrogen adsorption desorption isotherm and pore size distribution of g-C_3N_4-GA, respectively. c,d) TGA and DSC curves of bulk g-C_3N_4, GA, and g-C_3N_4-GA, respectively.

The XRD diffractograms of GAs before and after growth of the layer of g-C_3N_4 are nearly identical (**Figure 5.3e**). Two peaks are present at 30° and 50° due to (002) and (101)+(100) lattice planes, corresponding to a graphitic interlayer spacing of 0.339nm. Low diffraction signal intensity and broad peak width are due to the thin and wrinkled graphene sheets present in the GA. The bulk g-C_3N_4 diffractogram contains one strong peak at 31.9° corresponding to the (002) lattice plane with an interlayer spacing of 0.317nm. The absence of any detectable contribution from g-C_3N_4 is due to the small thickness of the layer, diffracting few X-rays and resulting in signal below the detection limit of the instrument.

A high specific surface area is crucial to the photocatalytic performance of g-C_3N_4 and many reports work to increase the surface area in order to enhance its photocatalytic performance by utilizing sacrificial templates, copolymerization, and nanofiber morphologies[136,155,156]. The nitrogen adsorption/desorption isotherm of g-C_3N_4-GA hybrids is shown in the **Figure 5.4a**. The isotherm is Type IV (IUPAC definition) indicative of a mesoporous material and contains a Type III hysteresis loop at high pressures as observed in other graphitic materials. The magnitude of the hysteresis loop is indicative of the pore volume in the material[53]. The calculated BET surface areas for the g-C_3N_4-GA is 255 m^2/g. Bulk g-C_3N_4 typically has a surface area less than 20 m^2/g[157] , thus

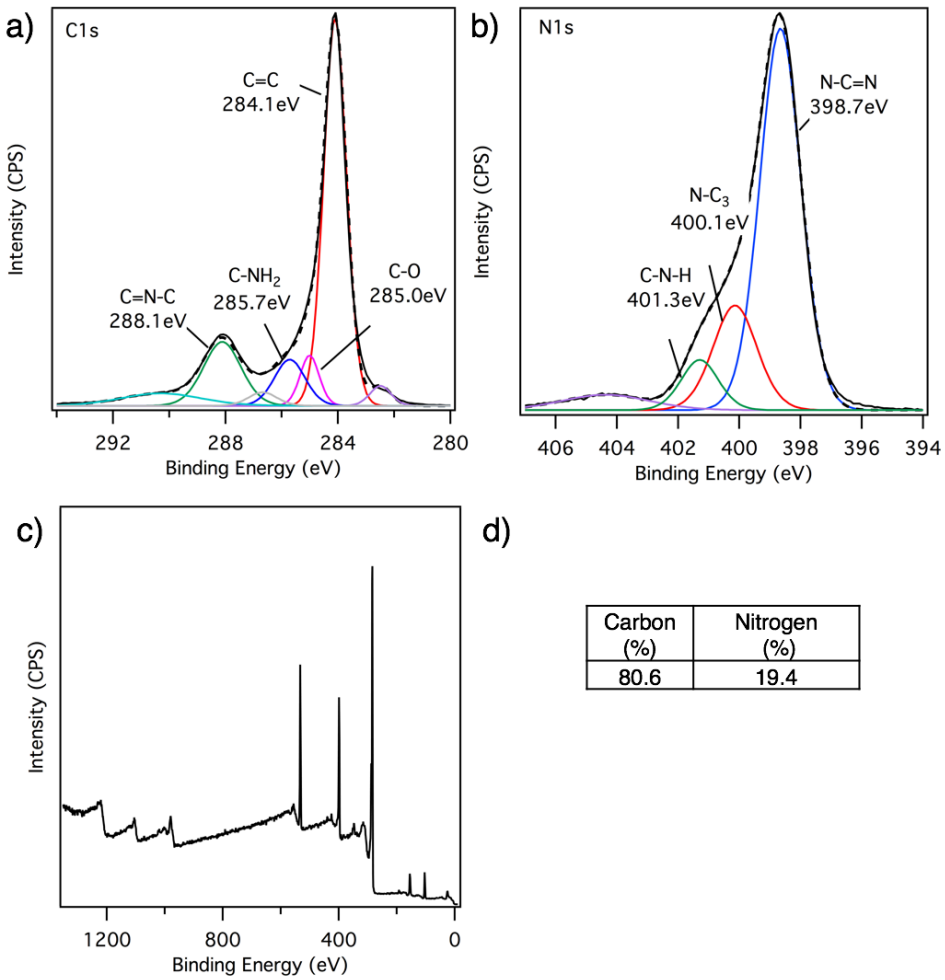

Figure 5.5 a) C1s, b) N1s and c) Survey XPS spectra and d) calculated atomic composition of bulk g-C_3N_4, GA, and g-C_3N_4-GA.

using GA cores as a template can result in a large surface area enhancement. GAs typically have a surface area between 800-1000m^2/g meaning that a decrease in the surface area occurs in the formation of the hybrid. This decrease is attributed to two factors; The first being that the resulting aerogels become more dense after growth of the g-C_3N_4 shell, meaning that more mass is included in the same unit of volume and the specific surface area will decrease. The second factor is the presence of surface tension in the growth process. DCDA is dissolved in water and the entire aerogel is submerged during the thermal condensation step. Thus when water is evaporated during temperature ramping, there could be some pore collapse due to surface tension leading to a decrease in surface area. Despite this decrease, the hybrid still maintains comparable surface areas to methods using less crystalline graphene[153] and has the added benefit of all g-C_3N_4 being entirely exposed on the surface.

The g-C_3N_4-GA hybrid possesses a large pore volume of 1.1 cm^3/g. The pore size distribution is plotted in **Figure 5.4b**, indicating an enormous contribution from mesopores with widths around 3Å. Such small pores are extremely beneficial for reversible adsorption of ions for supercapacitor applications[97].

The thermal stability of the hybrid structure is studied using thermogravimetric analysis (TGA) coupled with differential scanning calorimetry (DSC). TGA heats the sample in a nitrogen

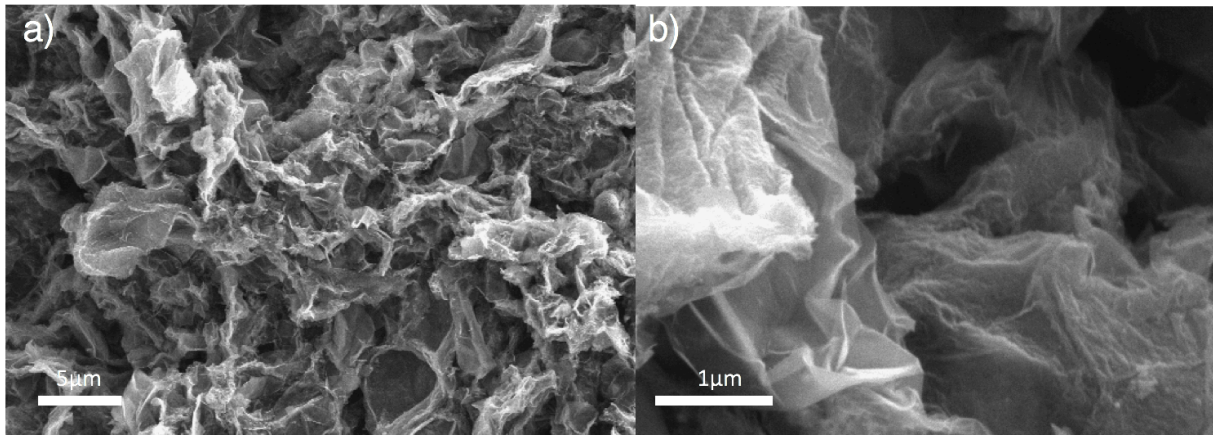

Figure 5.6 SEM images of g-C_3N_4-GA at low and high magnification.

atmosphere and the change in the mass is monitored to determine decomposition temperature and distinguish between two phases with different thermal stabilities. DSC is coupled with TGA and monitors the heat flow of the samples to analyze the chemical processes taking place during decomposition. As seen in **Figure 5.4c**, the highly crystalline GAs do not lose mass even up to 1050°C, the high temperature limit. Bulk g-C_3N_4 has an onset decomposition temperature of about 600°C and the mass is fully lost upon further heating to 1050°C. G-C_3N_4-GAs also have an onset of decomposition at 600°C, but 18% of mass remains up to 1050°C, indicating the presence of two phases with differing thermal stability.

The decomposition is also reflected in the DSC curve (**Figure 5.4d**). The GA, which undergoes no decomposition, serves as a baseline of the heat flow that is measured in the system regardless of sample type. Peaks that emerge on this baseline curve are a result of reactions in the sample. A strong peak at 734°C is present in bulk g-C_3N_4, reflecting the endothermic decomposition of g-C_3N_4[158]. A peak at the same temperature is present in the g-C_3N_4-GA hybrid, reflecting the presence of g-C_3N_4 in the material.

X-Ray Photoelectron Spectroscopy (XPS) is used to probe the chemical composition of the hybrid. As a surface sensitive technique, the predominant phase detected is expected to be carbon nitride due to the core shell morphology of the structure. As shown in the deconvoluted C1s XPS spectrum in **Figure 5.5a**, the presence of graphene is confirmed due to the strong peak at 284.1eV corresponding to C=C and an sp^2 overtone peak at 291eV. Peaks at 288.1 and 285.7eV are due to the g-C_3N_4 coating from C=N-C and C-NH_2 bonds, respectively. A C-O peak is also present at 285.0eV which is not unexpected due to thermal condensation occurring in air which can lead to a small degree of oxygen functionalization in the material. The origin of the peak at 286.7eV is still under investigation and may be indicative of covalent bonding formed between the g-C_3N_4 layer and the graphene core. In the N1s spectrum, peaks at 398.7, 400.1, and 401.3eV are due to N-C=N, N-C_3 and C-N-H bonds, respectively. An sp^2 overtone peak at 404eV is also present, indicative of the sp^2 hybridization of nitrogen, which is expected based on the structure of g-C_3N_4. The atomic composition from XPS is 80.6% carbon and 19.4% nitrogen. This is higher than the stoichiometric 0.75 C/N ratio and is due to the underlying graphene signal being detected. The depth of the XPS probe is around 2nm leading to additional C1s electrons detected from the graphene and enriching the C/N ratio with carbon. The occurrence of carbon signal enrichment indicates that g-C_3N_4 coating is less than 2nm thick.

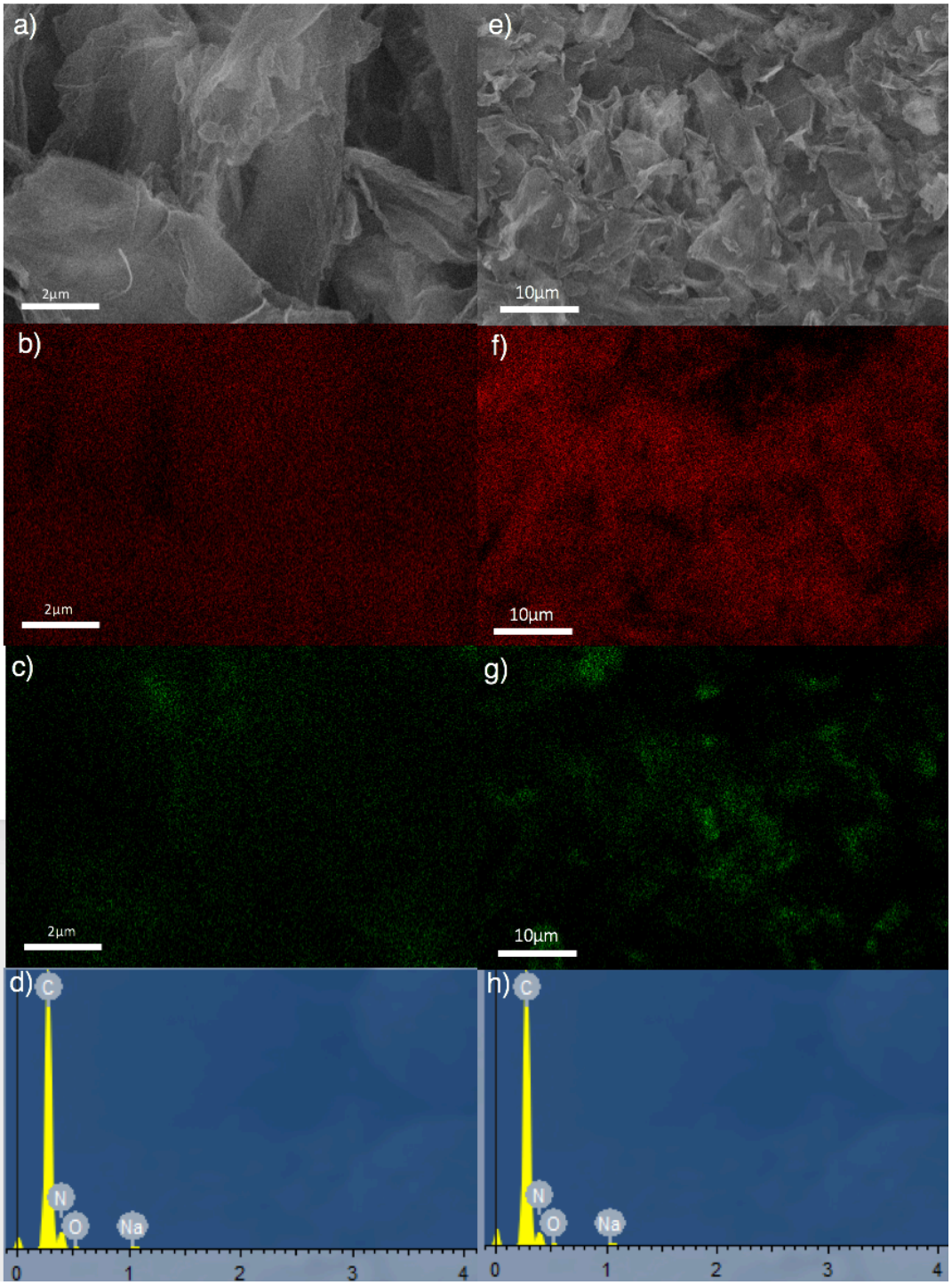

Figure 5.7 High magnification SEM image (a) with corresponding carbon EDS map (b), nitrogen EDS map (c) and EDS spectrum (d). Low magnification SEM image (e) with corresponding carbon EDS map (f), nitrogen EDS map (g) and EDS spectrum (h). In collaboration with Marcus Worsley provided courtesy of LLNL.

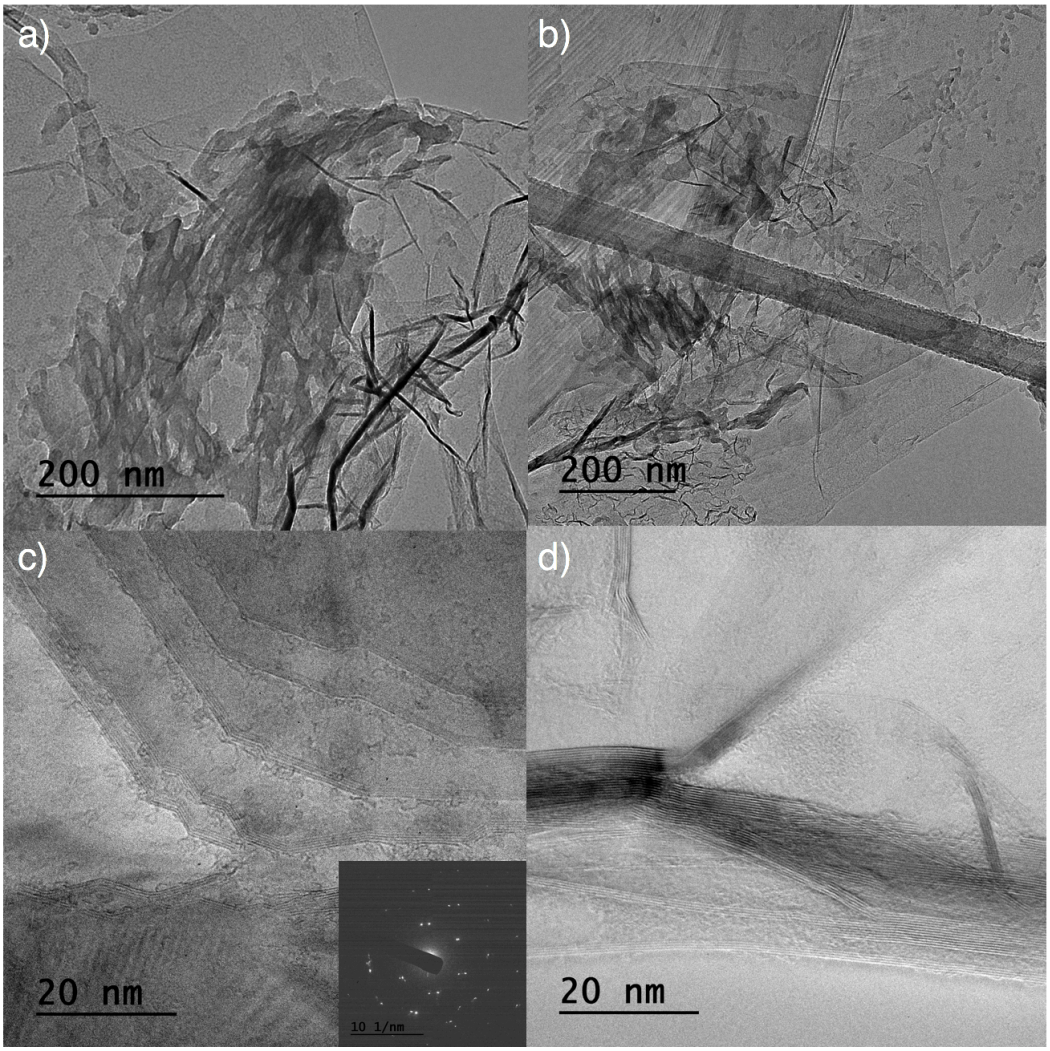

Figure 5.8 TEM images of g-C_3N_4-GA hybrid at various magnifications. Inset in c) Selected area diffraction pattern.

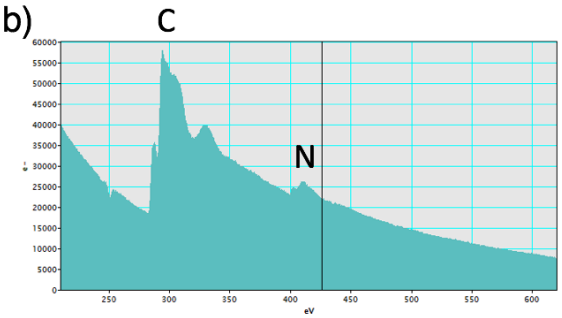

c)

Carbon (%)	Nitrogen (%)
83.3	16.7

Figure 5.9 a) Bright field TEM image b) EELS spectrum and c) EELS quantification of g-C_3N_4-GA Hybrid in collaboration with Brian Shevitski.

5.5 Structural Characterization of g-C_3N_4-GA Hybrids

Microscale and nanoscale morphologies of g-C_3N_4-GA hybrids are studied using electron microscopy. Scanning electron microscopy (SEM) probes the microstructure of the materials as shown in **Figure 5.6.** The g-C_3N_4-GA has a 3D, porous morphology which is expected based on surface area measurements. The material is made up of a nanosheets and possesses a microscale structure similar to that of GAs, but has a more tightly packed structure. Given the similar 2D morphology of g-C_3N_4 and graphene, the two phases are difficult to distinguish using SEM, so the chemical composition is spatially studied using energy dispersive spectroscopy (EDS) mapping in collaboration with Lawrence Livermore National Lab. **Figure 5.7** shows the SEM images of a g-C_3N_4-GA hybrid and corresponding carbon and nitrogen signal maps at low and high magnifications. In both magnifications, the nitrogen signal is significantly lower than the carbon signal, reflecting the thin coating of g-C_3N_4 on graphene and some areas where graphene may be bare. The spatial distribution of nitrogen is remarkably even with a small amount of signal throughout the hybrid and a few areas that are enriched with higher nitrogen content. Areas of higher nitrogen signal are due to thicker regions of g-C_3N_4 in those areas. EDS maps confirm that a uniform shell of a g-C_3N_4 is synthesized on top of GA cores.

Transmission electron microscopy (TEM) is used to study the nanoscale morphology of the core-shell structures. At the length scales achievable using TEM, the graphene and g-C_3N_4 phases are distinguishable. Graphene sheets are flat with even edges, while g-C_3N_4 is much more textured and mesh-like. This is due to the incomplete thermal condensation of DCDA into g-C_3N_4 and is the structure also observed in bulk g-C_3N_4[159] . As seen in **Figure 5.8**, the g-C_3N_4-GA hybrid is made up of two distinct structures. The graphene sheets are flat with wrinkles and a less ordered phase of mesh-like g-C_3N_4 is grown on top. Some domains are large while some are smaller, around 50nm. Interference patterns are visible in **Figure 5.8b** where g-C_3N_4 is found on top of graphene, indicating that the coating is thin. Any thick coating would be visible as simply dark regions due to few transmitted electrons detected.

GAs typically have a large degree of crumpling and wrinkling present within the individual sheets as shown in **Chapter 2**. However, after growth of the g-C_3N_4 layer, the graphene lies significantly more flat. This flattened graphene can maximize the contact with g-C_3N_4. Despite the

flattening of graphene during g-C_3N_4 growth, the crystal structure of graphene is left intact. As seen in **Figure 5.8c,d**, graphene still has a hexagonal diffraction pattern and lattice fringes are visible with an interlayer distance of 0.33 nm. G-C_3N_4 is highly sensitive to the electron beam and undergoes rapid decomposition, thus diffraction patterns on g-C_3N_4 layers are not possible.

In collaboration with Brian Shevitski and the Molecular Foundry, g-C_3N_4-GA hybrids are studied using election energy loss spectroscopy (EELS). **Figure 5.9a,b** shows the bright field image, and corresponding EELS spectrum of the g-C_3N_4-GA hybrid, respectively. The EELS spectrum shows that carbon and nitrogen make up the sample, and fine structure analysis indicate that both elements are sp^2 hybridized. Quantification of the EELS spectrum gives a carbon and nitrogen concentration of 83.3% and 16.7%, respectively (**Figure 5.9c)**. These values are in excellent agreement with XPS quantifications, and confirms the thin, functional g-C_3N_4 shell grown on a GA core.

The successful synthesis of GA-g-C_3N_4 core-shell hybrids is confirmed through extensive structural and chemical characterization. The composite is rationally designed in order to maximize exposure of the light absorption, photocatalytic layer while optimizing charge separation for improved performance. Additional studies are necessary to confirm this effect and future work should center around testing this material for photocatalytic water splitting. Additionally, a similar synthetic approach could be adopted to synthesize other functional core-shell aerogel structures by depositing precursors on the GA surface and thermal pyrolysis to grow the desired structure.

Chapter 6: Density-Tunable Graphene and Boron Nitride Aerogels

Nano Fun-Fact: The first naturally occurring boron nitride mineral was discovered in cubic form in Tibet in 2009 and given the name qingsongite.

Part I of this dissertation has focused on modification of aerogels that are based on 2D materials like graphene and boron nitride with modifications such as doping, defect-engineering, and formation of core-shell structures to improve their performance in gas sensing and catalysis. As opposed to chemical modification, this chapter will focus on physical modification of graphene and boron nitride aerogels in order to control their densities during synthesis and enhance the thermal conductivity for polymer composite applications[160].

6.1 Motivation

Many scalable syntheses of graphene aerogels (GAs) have been developed that can incorporate grams of graphene material into one single, multifunctional structure[52,55,161,162] and a large degree of progress has been made in controlling and optimizing the crystallinity of GAs[58]. However, there is still a need for synthetic control of their macroscopic, physical, properties.

Aerogel density, porosity, surface area and mechanical properties are essential for material performance but individual applications require specific and well-defined properties. For example, control of meso and macropore architectures in GAs used for supercapacitor electrodes allows multidimensional electron transport resulting in increased performance[100]. Furthermore, control over elasticity of GAs opens potential applications for energy dampening or biological applications[161].

Tuning the density of GAs can be a critical step towards the design of a truly optimized material. Decoupling properties such as density, mechanical strength and porosity of a material can allow researchers to study their individual impacts and advance the field to synthesize materials with enhanced performance. Moreover, many physical properties of aerogels scale with density including electrical and thermal conductivity[163,164]. Thus, the ability to tune the density of graphene and BN aerogels could open up the opportunity to have control over their electrical and thermal properties which is of particular importance for polymer composite applications.

Tunable densities and mechanical properties of carbon aerogels synthesized using organic sol-gel chemistry of resorcinol and formaldehyde have been achieved by controlling the sol-gel conditions[165]. However, tuning properties of GAs by altering gelation conditions has yet to be realized.

6.2 Role of Sacrificial Material in Density Tuning

In order to tune the density of both GAs and BN aerogels, the synthesis of a GA is targeted for modification. The density-tuned GAs can be carbothermally converted into a density-tuned BN aerogel, making this approach highly versatile.

GAs are synthesized using a base catalyzed gelation. During the gelation process, functional groups on graphene oxide (GO) chemically crosslink and deoxygenate to form a hydrogel. As a result, hydrogels undergo shrinkage and densification. In order to tune the density of GAs, control over this volume shrinkage is targeted by incorporating a sacrificial material into the GO suspension which can be removed after the aerogel is formed. The role of the sacrificial

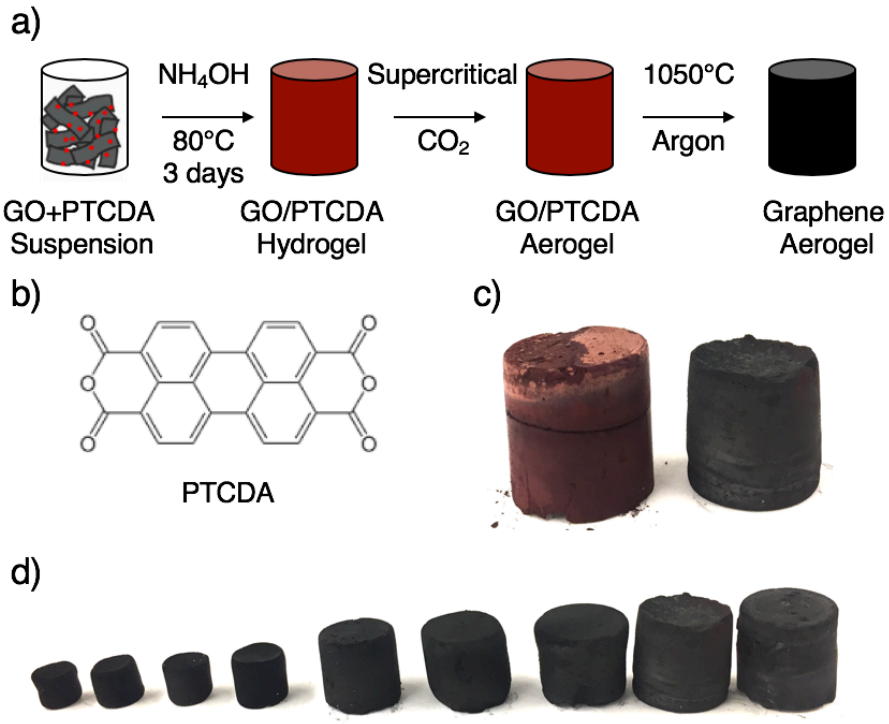

Figure 6.1 (a) Schematic of density tunable graphene aerogel synthesis. (b) Structure of PTCDA used as sacrificial PAH. (c) Samples containing 10:1 PTCDA: GO before thermal reduction and decomposition (left) and after heating to 1050°C (right). (d) Photograph of series of graphene aerogels with increasing PTCDA content.

material is to physically prevent the GO sheets from coming as close together during gelation, thus changing the volume of the aerogel. Due to the sacrificial nature of the additive, it can then be removed and not contribute to the mass of the aerogel making a lower density aerogel. Such a sacrificial material could include SiO_2 nanoparticles which could be removed using a KOH treatment, or an organic molecule which will thermally decompose. Some organic molecules with well-developed π electron networks have the added benefit of undergoing thermal decomposition and graphitization in an inert atmosphere making it possible to tune the density to lower and higher values. For this reason, a sacrificial polycyclic aromatic hydrocarbon (PAH) is chosen for incorporation into the GO suspension.

In this study, the PAH, perylenetetracarboxylic acid dianhydride (PTCDA), is used as the sacrificial molecule. PTCDA is a common red dye and n-type semiconductor which is used in optoelectronics and its structure is shown in **Figure 6.1b**[166]**.** PTCDA is commercially available, suspendable in water, and capable of π stacking with GO. Additionally, it reacts with amines to form the corresponding imide, which self-assemble into nanofibers[167,168].

6.3 Density Tunable GAs using PTCDA as a Sacrificial Molecule

The synthesis of GAs is extensively described in **Chapter 2** and incorporating a sacrificial molecule into the GO suspension is an example of a modification during GA synthesis. Following the synthesis, the volume change during gelation and mass are measured and the resulting aerogel densities are calculated. Further characterization including the morphology and chemical composition are performed.

6.3.1 Synthesis of Density Tunable GAs

The base-catalyzed synthesis of GAs is used as shown in Figure 6.1a. PTCDA is added into the GO suspension (20mg/mL in water) and gelation occurs following the addition of an ammonium hydroxide catalyst (1:6 by vol $NH_4OH:H_2O$). Over the course of this reaction, functional groups on graphene oxide chemically crosslink and deoxygenate to form a hydrogel [55,169]. GO content is kept constant in all samples and PTCDA content is altered to prepare aerogels of specific PTCDA:GO ratios by mass. For example, a 15:1 PTCDA:GO aerogel is synthesized using 15 times the mass of PTCDA to GO. After gelation, the graphene oxide hydrogels undergo solvent exchanges into acetone and are dried using supercritical CO_2 to yield GO/PTCDA aerogels. They are thermally treated at 1050°C in Ar atmosphere for 3 hours in order to decompose the PTCDA and reduce GO, yielding GAs with controlled density.

Due to the optical properties of the PTCDA, the GO/PTCDA aerogels have a red color (Figure 6.1c). After reduction, they turn the characteristic black color of GAs. A photograph of the series of aerogels varying from no PTCDA to 15 times the mass of PTCDA to GO is shown in Figure 6.1d. All aerogels contain the same amount of GO, and it is clear that the degree of aerogel shrinkage during gelation is significantly reduced with increased PTCDA content.

6.3.2 Characterization of Nanofibers

The morphologies of PTCDA/GO aerogels and GAs are characterized using SEM and TEM. As shown in the SEM images in Figure 6.2a, nanofibers are formed within the GO aerogel that are not present in the control. They are present in the 1:1 (PTCDA:GO) graphene oxide aerogels and are the dominant species in the 15:1 material (Figure 6.2c,d). These fibers are the result of a reaction between the PTCDA and the ammonium hydroxide catalyst and GO does not play a role in their formation.

In order to characterize the formation of nanofibers, the system is studied in the absence of GO. Figure 6.3a shows the IR spectra of PTCDA, GO aerogels with nanofibers, and nanofibers synthesized without GO. In PTCDA, peaks corresponding to the anhydride at 1775 and 1765 cm^{-1} due to the asymmetric and symmetric C=O stretches are present. After ammonium hydroxide treatment they disappear and are replaced with imide peaks from C=O, C-N, and N-H stretches at 1650, 1275, and 3130cm^{-1}, respectively in the PTCDA/GO aerogels and the no GO sample. This indicates that PTCDA reacts with ammonium hydroxide to form perylene tetracarboxylic diimide (PTCDI) whose structure is shown in Figure 6.3c. PTCDI is well known to self-assemble into one dimensional nanostructures due to π-π interactions between aromatic rings[170–172]. Thus, the formation of nanofibers is not unexpected and they play a key role in controlling the volume of the aerogel during gelation. Figure 6.3b shows an SEM image of the nanofibers formed in the absence of GO. In fact, it is also possible to make an aerogel purely of PTCDI nanofibers as will be discussed in Chapter 7.

Nanofibers visible under SEM are 100-200 nm in diameter and are not found under TEM likely due to the π stacking not withstanding sonication during sample preparation. Smaller nanofibers around 10 nm assembled directly on GO are observed under TEM (Figure 6.2e). After thermal reduction at 1050°C, nanofibers are no longer present and the GA has a porous structure composed of wrinkled graphene sheets indicative of a typical graphene aerogel (Figure 6.2b,d,f). This indicates that the reaction between ammonium hydroxide and PTCDA does not interfere with gelation in the formation of a hydrogel and the aerogel morphology is maintained.

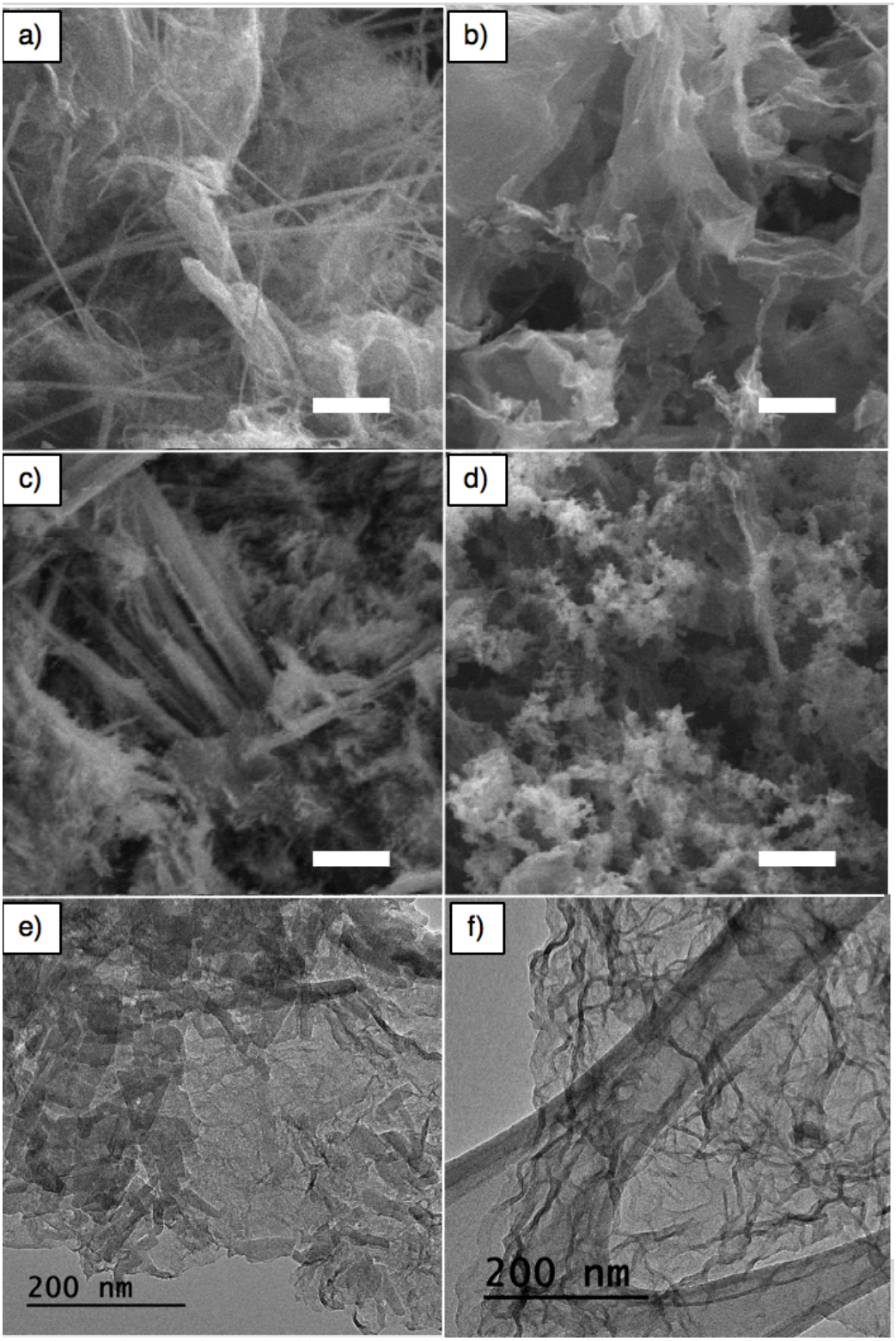

Figure 6.2 (a-b) SEM images of aerogels with 1:1 before after thermal reduction, respectively. (c-d) 15:1 PTCDA:GO before thermal reduction and after, respectively. Scale bars in a-d are 2µm. (e) TEM images of 1:1 PTCDA:GO aerogels before reduction and (f) after thermal reduction and decomposition of nanofibers.

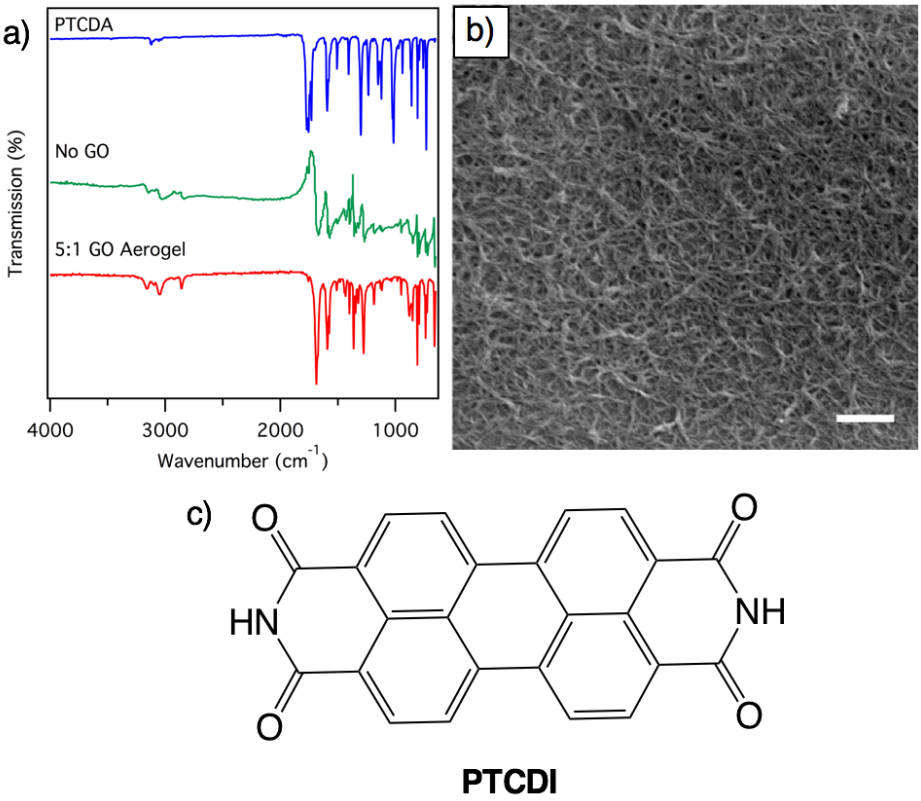

Figure 6.3 (a) FTIR spectra of PTCDA, nanorods synthesized with no GO, and 5:1 (PTCDA:GO) GO aerogel. (b) SEM image of nanorods synthesized with no GO. Scale bar 500nm.

6.3.3 Volume, Mass and Density Dependence of GAs with PTCDA Concentration

Gelation is performed in a vial resulting in graphene aerogel cylinders and the shrinkage during gelation is calculated by taking the fraction of the graphene aerogel diameter to the diameter of the gelation vial. The percent shrinkage during gelation as a function of PTCDA:GO shows two clear regimes (Figure 6.4a). At PTCDA:GO less than 1:1, there is a decreasing shrinkage with increased PTCDA content, meaning that the aerogel volume is larger. However, a minimum shrinkage of around 10% is reached when PTCDA:GO is 2.5:1 and additional PTCDA does not affect shrinkage during gelation. A control graphene aerogel shrinks around 50% during gelation, so an aerogel with the same mass and 10% shrinkage would have a density 80% smaller than the control.

The other contributor to aerogel density is the mass. Incomplete decomposition of nanofibers can affect the density and even lead to densities higher than the control without destroying the porous structure. If decomposition of PTCDI nanofibers were complete, all aerogels would have the same mass due to the normalized GO content across samples. However, a fraction of the mass from PTCDI nanofibers is retained inside the aerogel, resulting in increasing mass with increased PTCDA content (Figure 6.4a). The additional mass has likely graphitized and been incorporated into the aerogel. However, at higher PTCDA content, some nanofibers are still observed under SEM. Partial decomposition amd incorporation into graphene enables the synthesis of higher density aerogels.

The mass of aerogels and the volume shrinkage with increasing PTCDA content are competing terms. At low PTCDA content, the increased volume dominates compared to the small increase in mass, resulting in decreased aerogel density (Figure 6.4b). A maximum density

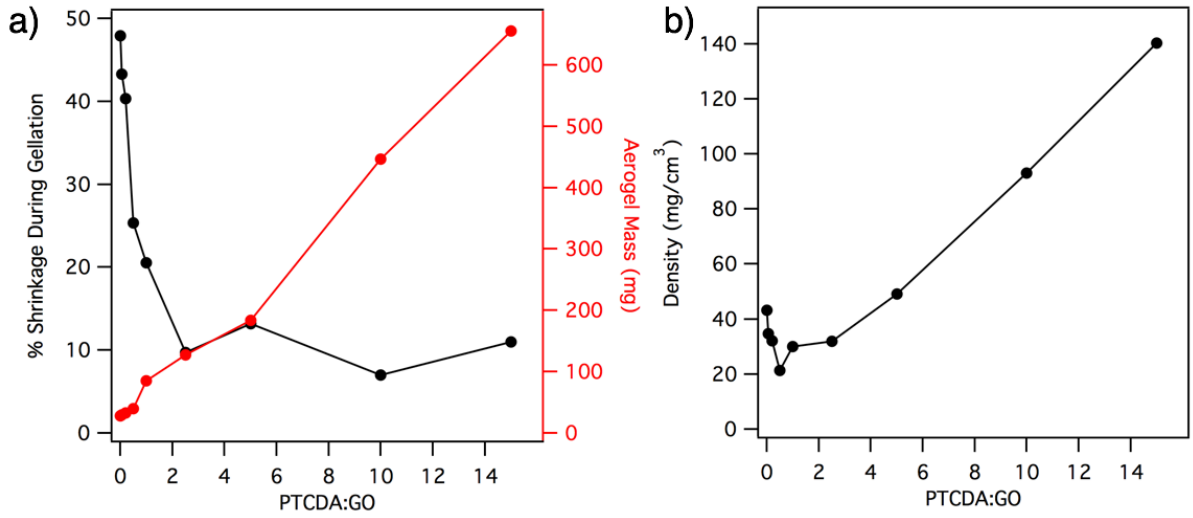

Figure 6.4 (a) Shrinkage of graphene aerogels with increasing PTCDA content during gelation on left axis, with 0:1 aerogel being the control. Mass of aerogels with increasing PTCDA content on right axis. (b) Density of graphene aerogels showing a minimum at 0.5:1 PTCDA:GO and increasing density with increased PTCDA between 1:1 and 15:1. All aerogels have been heat treated at 1050°C.

reduction of 50% is achieved when PTCDA:GO is 1:2. PTCDA:GO ratios larger than 1:2 result in a higher density due to both the increasing mass and having reached the minimum volume shrinkage. Drastic density increases are observed at large PTCDA content and a three-fold densification is achieved at 15:1 (PTCDA:GO). Xerogels, hydrogels dried under ambient conditions, have completely collapsed pore structures due to solvent evaporation with surface tension. This typically leads to densities 10 times that of the control[57]. Thus a three-fold densification while retaining a porous material is a significant achievement.

6.3.4 Chemical Characterization of Density-Tunable GAs

Further characterization of the material is performed to study the composition of the GAs. Before thermal reduction and decomposition of the nanofibers, the Raman spectrum is dominated by the modes of the PTCDI nanofibers at 1302, 1378 and 1572 cm^{-1} due to C-H and C-C vibrations and the characteristic graphitic peaks from the graphene oxide are not visible (Figure 6.5a). It is noted that the nanofibers have a large background fluorescence at large wavenumbers. After thermal reduction, the signature Raman spectrum of graphene is obtained. The graphene G peak due to the E_{2g} in plane phonon is observed at 1588 cm^{-1}, and the D peak which arises due to defects or scattering sites in the material is found at 1355 cm^{-1}. The 2D peak at 2705 cm^{-1} is a 2 phonon mode indicative of a graphitic material.

With increasing PTCDA content, the material exhibits an increase in the height and width of the D peak (Figure 6.5b). Typically, the ratio of the intensity of the D peak to the G peak is used to assess the quality of graphene. Peaks from residual nanofibers would overlap with the D and G peaks of the GAs, so this analysis is not valid. The increased width of the D peak is attributed to the presence of the overlapping peaks, but an increase in the number of defects due to graphitization of nanofibers cannot be ruled out. While nanofibers have a strong background signal at large Raman shifts, no strong background signal is present after thermal reduction. This, in combination with the fact that overlapping peaks are so small that the characteristic graphene spectrum is recovered, indicates that some nanofibers may still exist, but only a small fraction. Thus, the predominant species in the reduced aerogel is graphene.

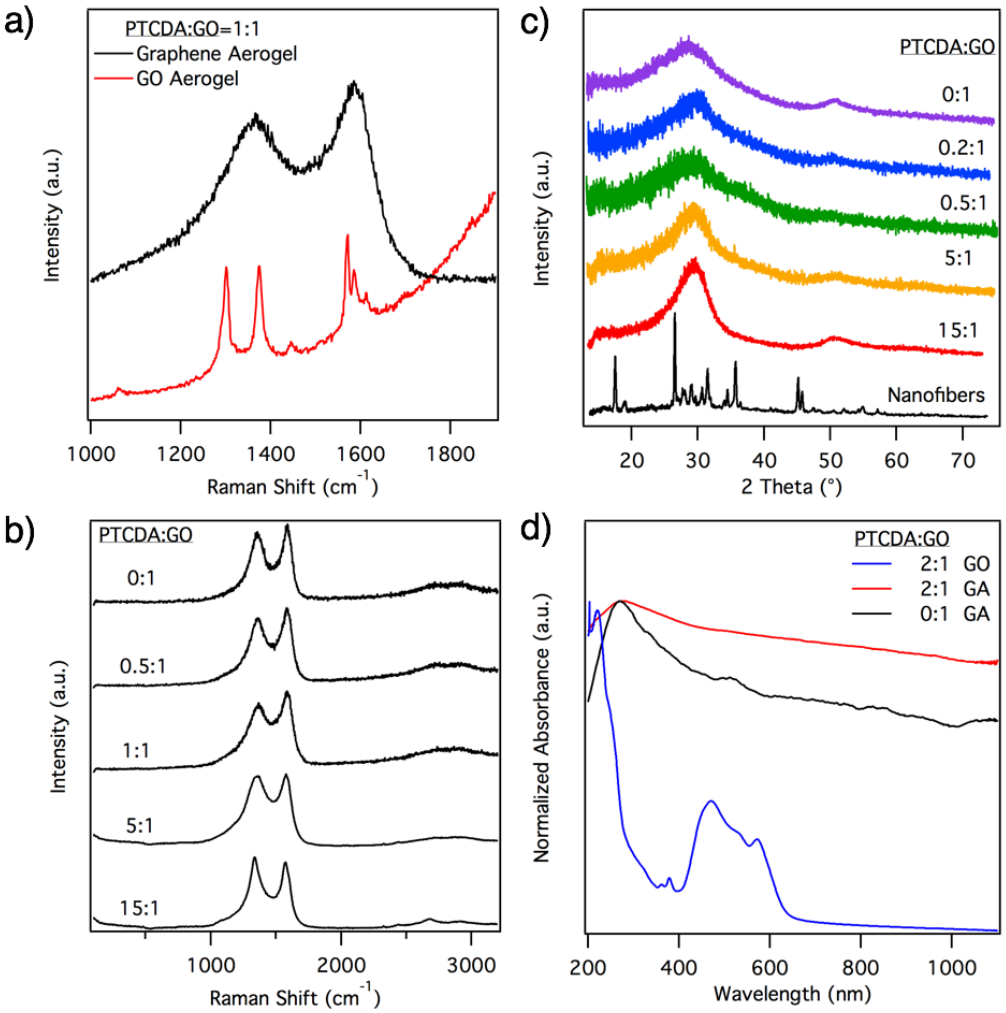

Figure 6.5 (a) Raman spectrum of 1:1 (PTCDA:GO) aerogels before and after thermal reduction. (b) Raman spectra of thermally reduced GAs with increasing PTCDA content. (c) XRD patterns of PAH nanofibers and GAs with increasing PTCDA content. (d) UV-Vis absorbance spectra of 2:1 (PTCDA:GO) aerogel before and after thermal reduction compared with control GA.

X-ray diffraction is performed to evaluate the crystal structure of the GAs (Figure 6.5C). The diffractogram shows two peaks in GAs at 29° corresponding to the (002) plane of graphene (d=3.47Å). Additionally, there is a weak peak at 50° due to the (100) and (101) planes[58,131]. The crystalline nanofibers contain many diffraction peaks, some of which are overlapping with the (002) peak in GAs. With increased PTCDA content, the 29° peak becomes more prominent. While some increase in the (002) peak could be attributed to underlying peaks from the nanofibers, it is most likely caused by the increased abundance of this plane due to incorporation of additional mass into the graphene. Additionally, there is no direct observation of any nanofiber peaks even at PTCDA:GO ratio of 15:1. This further supports that graphene is the dominant structure in the reduced product, but some undecomposed nanofibers likely remain.

Using UV-Vis absorbance spectroscopy, the 2:1 PTCDA:GO aerogel spectrum is dominated by the absorbance of the PAH nanofibers at 220nm and 400-600nm (Figure 6.5d). The UV-Vis absorption spectra of both control GAs and 2:1 (PTCDA:GO) GAs show a strong peak at 275nm due to π to π^* transitions indicative of the π conjugation in the graphene systems.

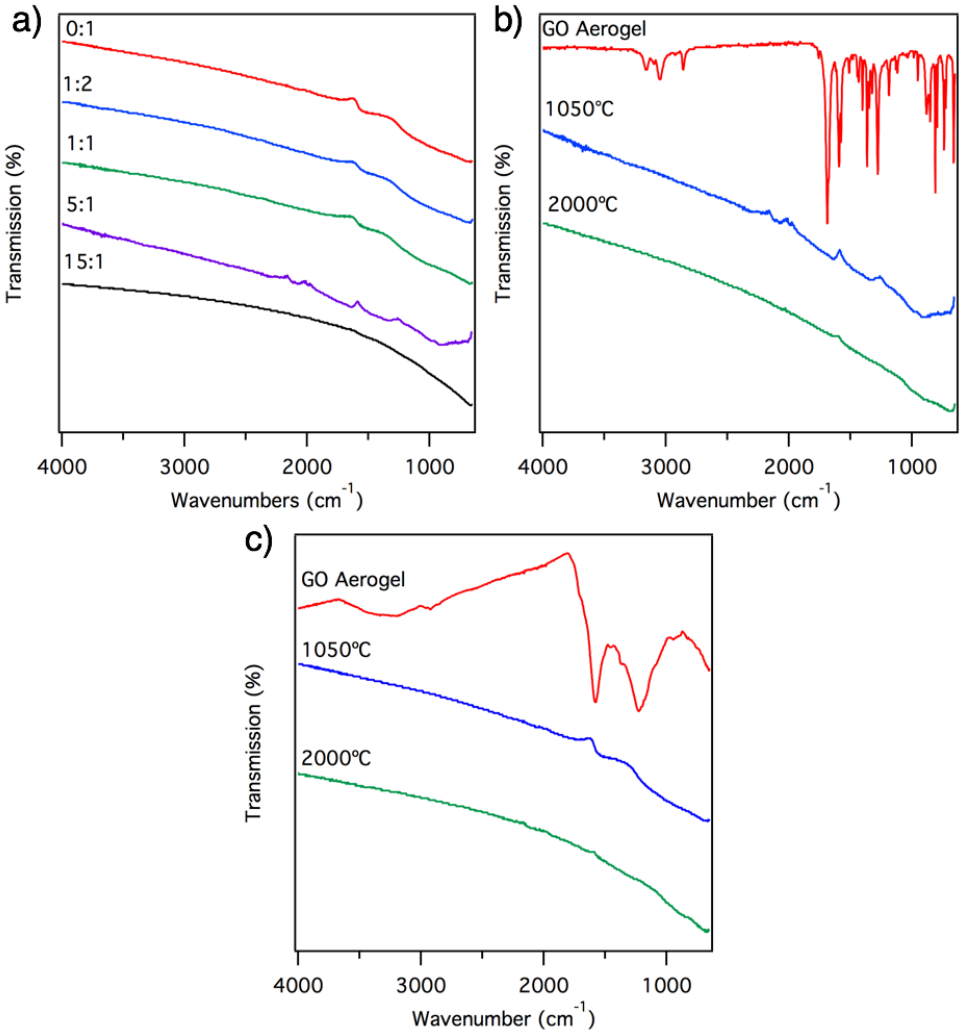

Figure 6.6 (a) FTIR spectra of graphene aerogels with increasing PTCDA concentration (PTCDA:GO). (b) FTIR spectra of 5:1 (PTCDA:GO) aerogel before thermal reduction and after firing at 1050°C and 2000°C. (c) FTIR spectra of control, 0:1 (PTCDA:GO) aerogel, before thermal reduction and after firing at 1050°C and 2000°C.

Absorbance across the entire UV-Visible spectrum is decreased upon graphitization, in agreement with reports in the literature[169]. Peaks present in the 2:1 (PTCDA:GO) sample disappear after treatment at 1050°C, confirming that most PAH nanofibers are decomposed after thermal treatment.

FTIR studies are completed to further study the aerogel composition after thermal reduction. Graphene materials show no distinct FTIR peaks, while PTCDI nanofibers have a strong IR signal. With increasing PTCDA content, no features from PTCDI emerge (Figure 6.6a). Furthermore, the peaks due to PTCDI nanofibers in 2:1 (PTCDA:GO) aerogels before reduction disappear after heating to 1050°C and are similar to the control (Figure 6.6b,c) further indicating that graphene is the predominant species in the reduced aerogels.

6.3.5 High Temperature Annealing of Density-Tunable GAs

To eliminate the potential interference from remaining nanofibers, an aerogel with PTCDA:GO of 5:1 is thermally treated to 2000°C. At this temperature no PTCDI should remain

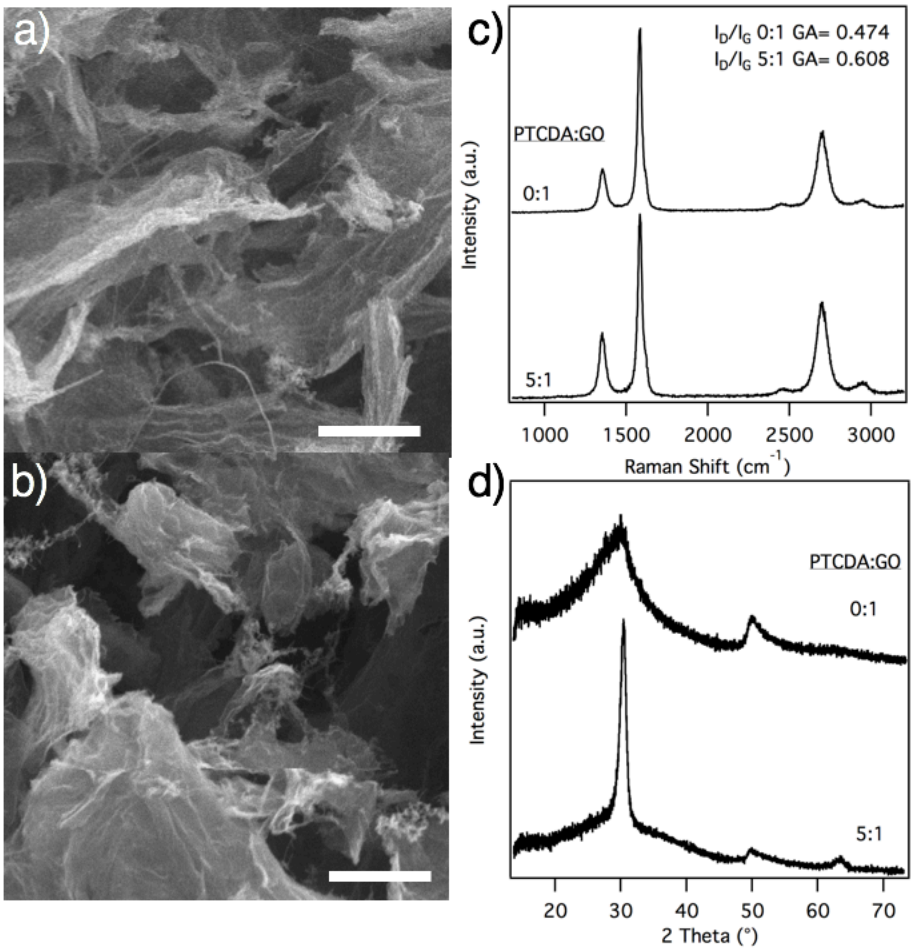

Figure 6.7 (a-b) SEM image of 5:1 (PTCDA:GO) aerogel treated at 1050°C and 2000°C, respectively. Scales bar are 2 μm. (c) Raman spectra of control graphene aerogel and 5:1 (PTCDA:GO) aerogel both treated at 2000°C and (d) XRD patterns of 2000°C control and 5:1 graphene aerogels**.**

and additional mass would be lost or graphitized and incorporated into the graphene lattice. The aerogel mass decreases 3% after treatment indicating that additional mass is likely incorporated into the graphene.

As seen in Figure 6.7a,b after treatment at 2000°C, the graphene aerogel morphology is maintained and nanofibers that were present in the 5:1 (PTCDA:GO) aerogel fired at 1050°C are no longer observed.

Treatment at such a high temperature increases the crystallinity of the graphene, which is apparent in the Raman spectrum (Figure 6.7c) [58]. The D and G peaks are narrower and the 2D peak becomes more prominent. There are no peaks from the nanofibers and no increase in the width of the D peak, indicating complete decomposition of the nanofibers. The average D to G ratio of the 5:1 (PTCDA:GO) graphene aerogel is 0.608 and the control is 0.474. Incorporation of the PTCDI into graphene would result in an increased D peak due to additional grain boundaries, scattering sites and overall disorder in the graphene. Thus the increased ratio supports the incorporation of the PTCDI into the graphene.

The XRD diffractogram shows remarkable changes compared to the control aerogel thermally treated to 2000°C (Figure 6.7d). The (002) peak increases in intensity and has a decreased width, indicating enhanced stacking and less curvature of graphene sheets. There is a decrease in the intensity of the (100) and (101) peaks also indicating more stacking of graphene.

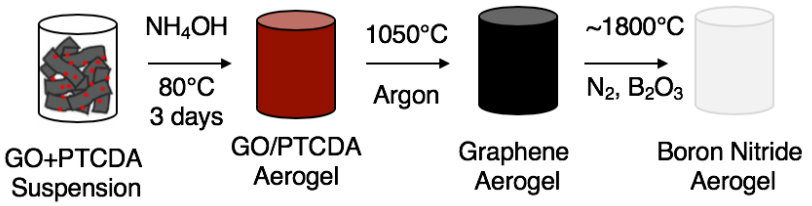

Figure 6.8 Schematic detailing the synthesis of density-tuned GA using PTCDA and subsequent carbothermal conversion to a density-tunable BN aerogel.

Lastly, a peak at 64° is present, corresponding to the (004) plane and is also due to the increasing layering in the material. Enhanced stacking of graphene sheets supports the incorporation of PTCDI nanofibers into the graphene lattice and no peaks from the PTCDI nanofibers are present.

Thus the entire series of aerogels with increasing PTCDA:GO can be fired at 2000°C to improve the crystallinity of the material and incorporate the PTCDI into the graphene without compromising the density.

6.4 Carbothermal Conversion to Density Tunable Boron Nitride Aerogels

One of the primary goals of tuning the aerogel density is to increase its thermal conductivity for polymer composite applications. In most polymer composites, maintaining the electrically insulating character is vital, thus GAs are not suitable. However, GAs have been widely studied as filling materials in polymer nanocomposites while BN aerogels have scarcely been utilized[173–177].

As discussed in Chapter 2, GAs can be carbothermally converted to BN aerogels. Therefore, density-tunable GAs can be converted to BN aerogels in order to synthesize density-tunable BN aerogels as shown in Figure 6.8. In the previous section, GA cylinders were synthesized for density tuning. In this section, GAs are cast into disk shape molds and converted to BN. The density of the control can be very sensitive to parameters such as the free headspace in the gelation vessel, making the density of GA disks and cylinders differ slightly. **Figure 6.9a**

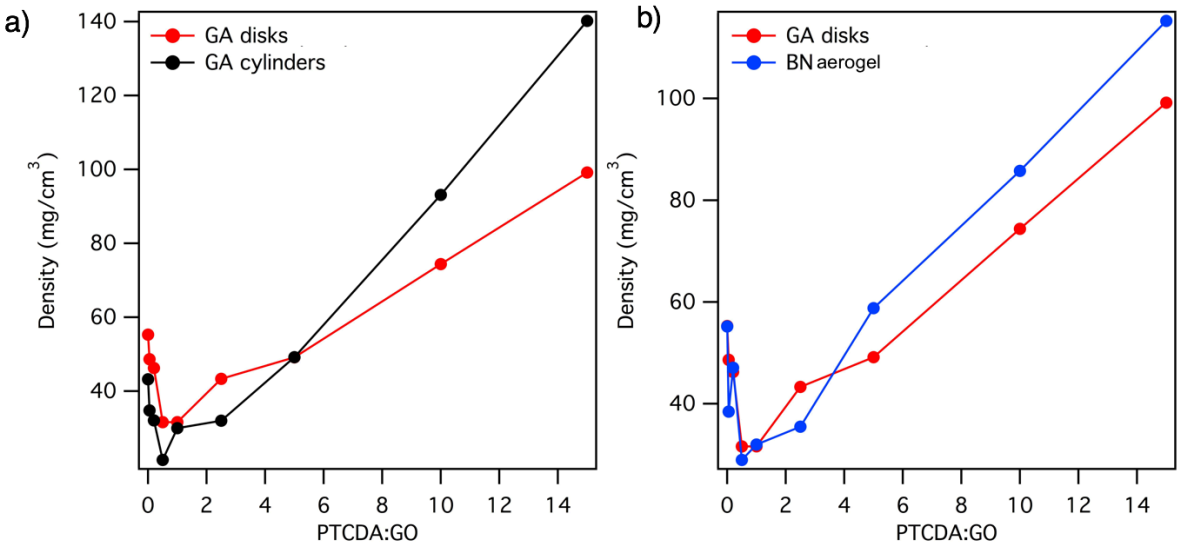

Figure 6.9 a) Comparison of densities of GA disks and GA cylinders and b) Comparison of densities of GA and BN aerogel disks.

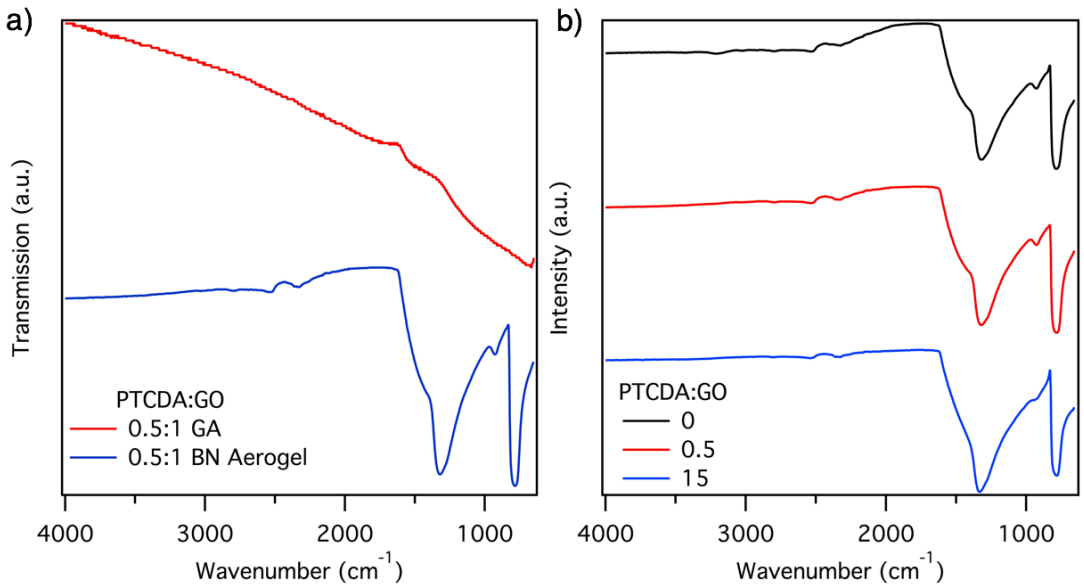

Figure 6.10 a) Comparison of FTIR spectra of a 0.5:1 PTCDA:GO aerogels as a GA and after conversion to BN aerogel b) IR spectra of control BN aerogels, 0.5, and 15 PTCDA:GO aerogels.

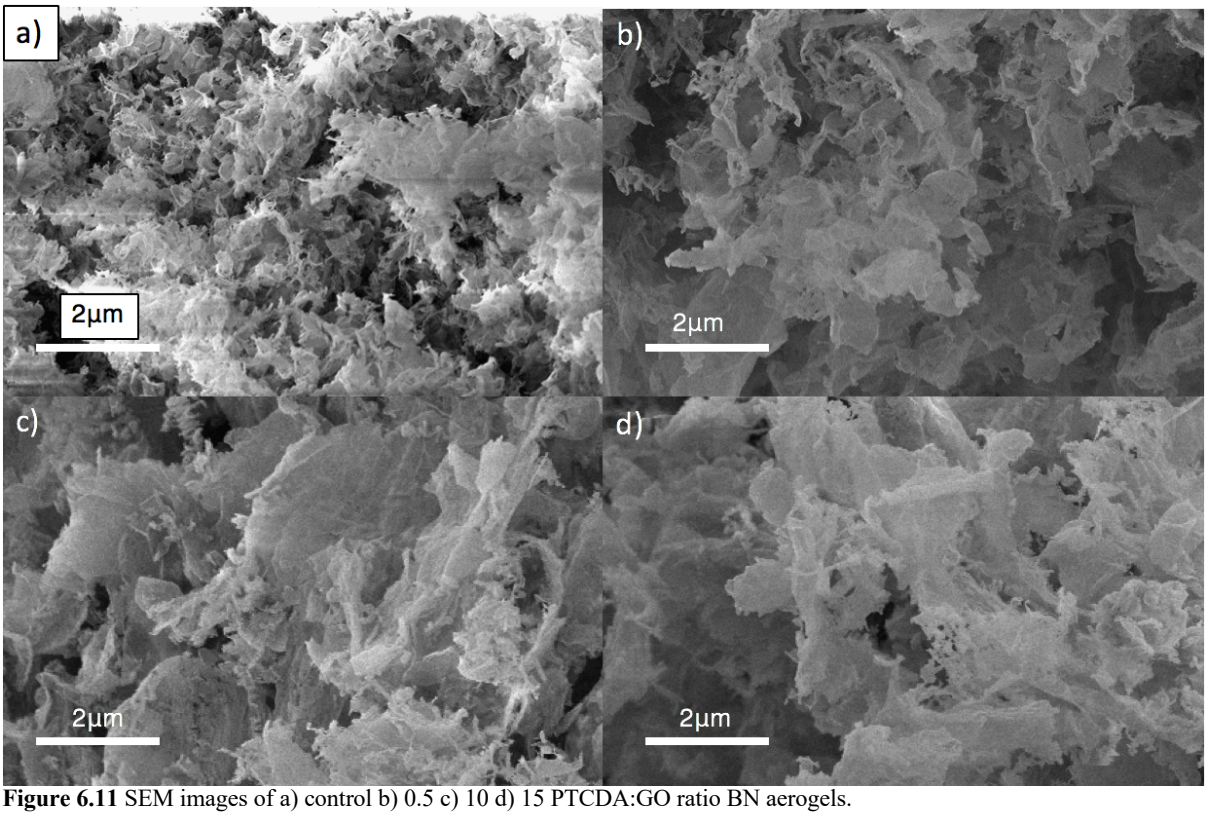

Figure 6.11 SEM images of a) control b) 0.5 c) 10 d) 15 PTCDA:GO ratio BN aerogels.

compares the densities of GA cylinders and GA disks made using sacrificial PTCDA. While there is a slight difference between the densities of GA cylinders and GA disks, both still maintain the same trend capable of accessing low and high densities of GAs.

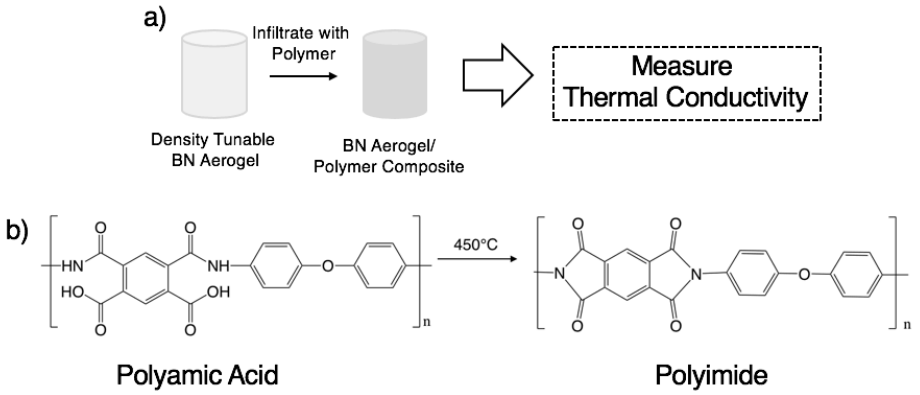

Figure 6.12 a) Proposal to infiltrate density tuned BN aerogels with polymers to enhance their thermal conductivity for thermal interface materials b) Proposed model polymer for infiltration is polyamic acid which can be heat treated to polyimide following annealing.

GAs are converted to BN aerogels using the carbothermal conversion method described in **Chapter 2** and their densities are plotted in **Figure 6.9b**. The control aerogel has a density of 55 mg/cm^3 and reaches a minimum density of 28 mg/cm^3 at a PTCDA:GO ratio of 1:2. Further increasing the PTCDA:GO ratio to 15:1 increases the density to a maximum of 115 g/cm^3. Thus, a density range from approximately half that of the control to over twice that of the control is achievable for BN aerogels.

Conversion from graphene to BN is verified using FTIR. Prior to conversion to BN, GAs have no notable peaks present in the IR spectrum as is typical of graphene materials (**Figure 6.10a**). Following conversion to BN, peaks at 1334 and 787 cm^{-1} emerge corresponding to the in-plane E_{2g} vibration and out of plane mode, respectively. A small peak at 925cm^{-1} is also present which is due to the B-OH stretch from residual boron oxide present on the surface which can be removed using hot water. These three peaks are present in aerogels across the entire spectrum of PTCDA:GO concentrations and verify a homogenous chemical composition between each set of BN aerogels (**Figure 6.10b**).

SEM characterization in **Figure 6.11** shows the pore structure of BN aerogels at increasing PTCDA:GO concentrations. All aerogels have a three-dimensional structure with a large amount of free space and a high porosity. The sheet structure is still present, but slightly less well defined at higher PTCDA:GO concentrations, likely due to the large incorporation of less crystalline graphitic species after annealing of PTCDI nanofibers. These results indicate that the porous aerogel morphology is maintained after BN conversion and BN aerogels with tunable density are successfully synthesized.

6.5 Future Direction

With the successful synthesis of density tunable BN aerogels, future work should focus on incorporating BN aerogels into polymer composites for thermal interface materials. A schematic of an effective potential approach is outlined in **Figure 6.12**. The porous BN aerogel structure should be infiltrated with a polymer and the solvent evaporated. This is the most effective way to maintain the aerogel morphology and take advantage of the increased density of the BN aerogel.

A potential model polymer with direct, real world applications is a polyimide. Polyimides are a class of polymers with a wide range of applications including in microelectronics, aerospace, and the military. Specifically they are used in electronic packaging but they have intrinsically low thermal conductivity and would benefit from a thermally conductive filler.

A precursor for polyimide, polyamic acid, is commercially available and can be diluted to a viscosity where it will infiltrate into the aerogel pores upon application of vacuum. Following infiltration, the solvent can be evaporated without compromising the pore structure of the aerogels. Subsequent treatment at 450°C will convert the amic acid group to an imide and the thermal conductivity of the polyimide composites over the tunable density range can be measured. Due to the relationship between density and thermal conductivity in aerogels, an enhanced thermal conductivity for a thermal interface material is expected.

PART II: 3D Aerogels Based on 1D Nanofiber Building Blocks

Chapter 7: Organic Semiconductor Aerogels and Conductive Carbon Nanofiber Aerogels with Controllable Nanoscale Morphologies

Nano Fun Fact: In 1872, Thomas Edison made the first carbon fiber by carbonizing cotton and bamboo for use as a filament in his light bulb.

7.1 Introduction and Motivation

In Part I, aerogels based on 2D nanomaterials which extend in the *x* and *y* directions with confinement in the *z* direction were explored; Part II will discuss the synthesis of aerogels based on 1D nanomaterials extending in only one direction. 1D nanomaterials based on inorganic constituents such as metal oxides and transition metal dichalcogenides, as well as organic semiconductor and conductive carbonaceous materials have been synthesized and a number of applications for these new classes of materials in electronics, photocatalysis, energy storage, and sensing have been explored, demonstrating their promising potential[170,176,178–183]. This chapter will focus on the synthesis of aerogels based on 1D carbon nanofibers and organic semiconductor nanofibers.

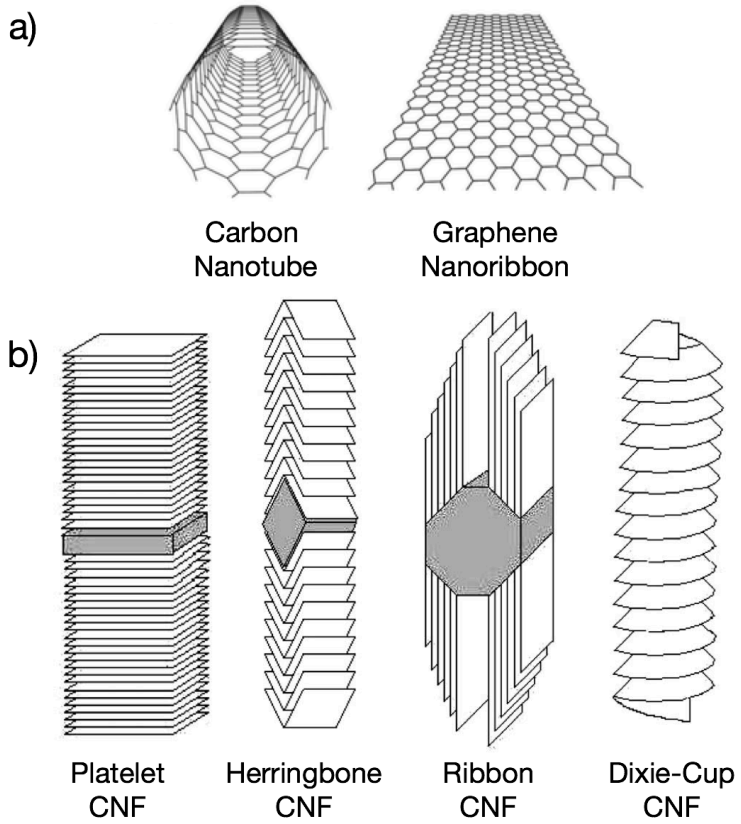

Figure 7.1 a) Structures of other 1D graphitic nanomorphologies, carbon nanotubes and graphene nanoribbons b) Structures of known CNF morphologies including platelet, herringbone, ribbon and Dixie cup types[187].

7.1.1 Carbon Nanofiber Background

There are three main types of 1D carbon nanomaterials: carbon nanotubes (CNTs), graphene nanoribbons (GNRs), and carbon nanofibers (CNFs) (**Figure 7.1a,b**). CNFs were first reported on record as far back at 1889 in the form of a patent, but were first studied in the 1970s[184,185]. They typically have diameters between 50-200nm, much larger than CNTs and GNRs. A large surge in interest in CNFs accompanied the synthesis of CNTs in the 1990s and many advancements in their synthesis were made[186]. CNFs are typically synthesized by catalytic chemical vapor deposition and the exploration of the relationship between catalyst used for synthesis as well as other growth parameters have resulted in the synthesis of fully graphitic CNFs with a variety of morphologies including platelet CNFs, herringbone CNFs, ribbon CNFs and Dixie-cup CNFs (**Figure 7.1b)** [187].

Conventional carbon fibers (CCFs) are a class of materials used for mechanical reinforcement and are synthesized by electrospinning of polyacrylonitrile (PAN) and heat treatment leading to a mixture of sp^3 and sp^2 bonds in the fibers. As synthetic developments of CCFs have allowed PAN fibers to be spun at smaller diameters, they too are referred to as CNFs despite lacking a fully sp^2 hybridized network. Mixing between the fields of CCFs and CNFs has blurred the lines between the two materials, but both types of CNFs produced through vapor processes and electrospinning have excellent thermal and mechanical properties, as well as high electrical conductivity. These outstanding properties make carbon-based 1D nanofibers promising materials for energy storage applications such as supercapacitor electrodes, lithium ion battery anodes, catalytic supports, and composite energy materials[188–191].

7.1.2 PTCDI Nanofiber Background

Another carbon-based family of 1D nanomaterials is made up of semiconducting organic nanofibers. The organic semiconductor perylene tetracarboxyldiimide (PTCDI) has attracted large attention due to its high electron affinity and ability to self-assemble into nanostructures[192,193]. The extended π electron network in PTCDI allows molecules to π stack with one another into nanofiber morphologies. Functionalization of PTCDI can lead to a variety of nanofiber diameters. Due to the semiconducting nature of PTCDI nanofibers, they have been integrated into field-effect transistors, photovoltaics, and other electronic applications[168,170,194–198].

7.1.3 Benefits of Incorporating 1D Nanomaterials into Aerogel Morphology

Despite their high aspect ratios, PTCDI nanofibers and CNFs synthesized through classical vapor or solution methods possess surface areas below 20 m^2/g and lack the high surface areas necessary for optimized performance in these applications[180]. As discussed in the **Chapter 2**, incorporating nanomaterials into aerogel morphologies results macroscopic amounts of material being integrated into a single, high surface area structure, while maintaining the extraordinary intrinsic properties of the building block and has the potential to significantly improve the performance of these materials in a variety of applications by exposing active sites and facilitating mass transfer in the solid-state[66,199,200].

This chapter will discuss the first synthesis of PTCDI nanofiber aerogels from inexpensive and commercially available perylene tetracarboxylic acid diianhydride. Additionally, the role of PTCDI nanofiber aerogels as precursors in the synthesis of CNF aerogels through a simple heat treatment approach will be presented. Lastly, the incorporation of metals into the synthesis in order to direct self-assembly into controllable nanostructures and provide a route to composite aerogel structures will be explored.

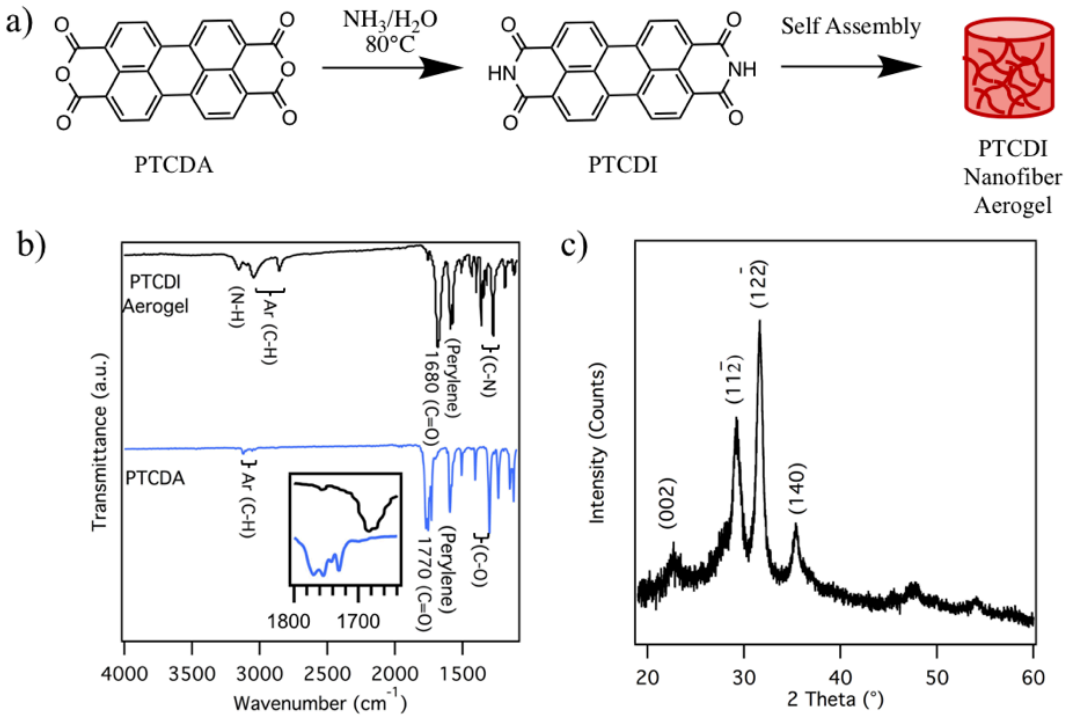

Figure 7.2 a) Synthesis of PTCDI nanofiber aerogels b) FTIR spectra of PTCDA and as-produced PTDI nanofiber aerogel c) XRD of PTCDI nanofiber aerogel.

7.2 Self-Assembly of PTCDI Nanofiber Aerogel

PTCDI nanofiber aerogels are synthesized using self-assembly principles and the resulting PTCDI nanofiber aerogels can be used as-synthesized as high surface area, organic semiconductors for photocatalysis and electronic applications or as precursors for CNF aerogels through a thermal graphitization process.

7.2.1 Synthesis of PTCDI Nanofiber Aerogel

Aerogels based on organic semiconducting nanofibers, PTCDI, are synthesized using perylene tetracarboxylic acid diianhydride (PTCDA) as a starting material. A 100 mg/mL suspension of PTCDA is prepared in water and ammonium hydroxide (1:6 by volume NH_4OH:H_2O) is added in order to convert the dianhydride to a diimide, as shown in **Figure 7.2a**. PTCDI is known to self-assemble into nanofibers due to strong π-π interactions between perylene cores[193]. At high concentrations of PTCDA, a large, entangled nanofiber network assembles and is capable of forming a freestanding hydrogel. In order to preserve the pore structure of the hydrogel during the drying process, solvent is removed using supercritical CO_2 or freeze-drying, yielding a PTCDI nanofiber aerogel.

7.2.2 Characterization of PTCDI Nanofiber Aerogel

The successful conversion of PTCDA to PTCDI is verified using FTIR (**Figure 7.2b**). Peaks corresponding to the anhydride at 1775 and 1765 cm^{-1} due to the asymmetric and symmetric

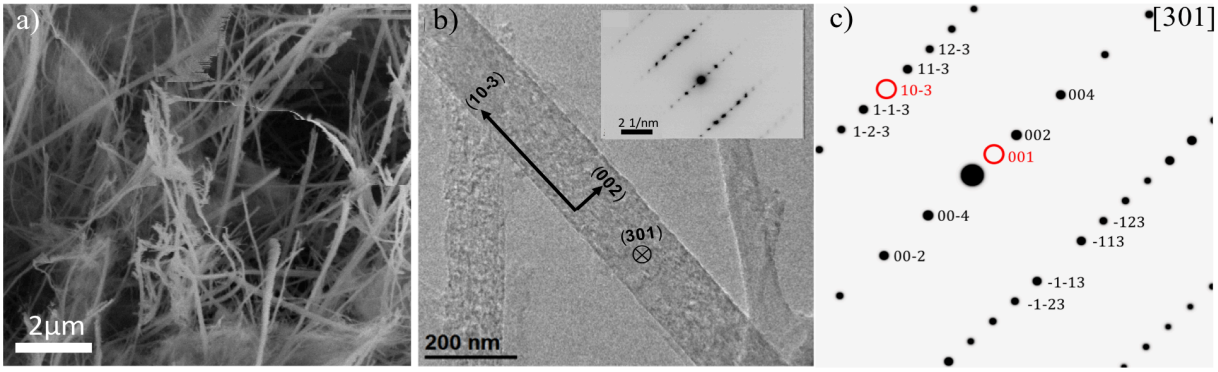

Figure 7.3 a-b) SEM and TEM images of PTCDI nanofiber aerogels and diffraction pattern (inset), respectively. c) Simulated diffraction pattern of PTCDI nanofiber on the [301] zone axis. The missing reflections (red circles) in (c) appear as weak spots in the experimental diffraction pattern due to double diffraction. The diffraction pattern shows that the fibers have the monoclinic P21/c crystal structure and the fibers are aligned in the 10-3 direction.

C=O stretches disappear and are replaced with imide peaks from C=O, C-N, and N-H stretches at 1650, 1275, and 3130cm^{-1}, respectively. Using XRD, the crystal structure of the nanofibers is studied (**Figure 7.2c)**. After the reaction, the product has prominent peaks at 22.6, 29.2, 31.6, and 35.4° corresponding to the (002), (11-2), (12-2), and (104) planes in PTCDI (monoclinic P21/n space group), respectively[201].

Formation of nanofibers is verified using SEM and TEM as shown in **Figure 7.3**. SEM reveals the three-dimensional (3D) nature of the aerogels which are composed of many micron long nanofibers with a clearly discernable porous structure (**Figure 7.3a)**. Using TEM, individual nanofibers with widths between 100 and 200nm are isolated and found to have a textured as opposed to smooth surface (**Figure 7.3b**). Selected area electron diffraction of isolated nanofibers is performed to determine PTCDI molecule orientation (**inset Figure 7.3b)**. The experimental

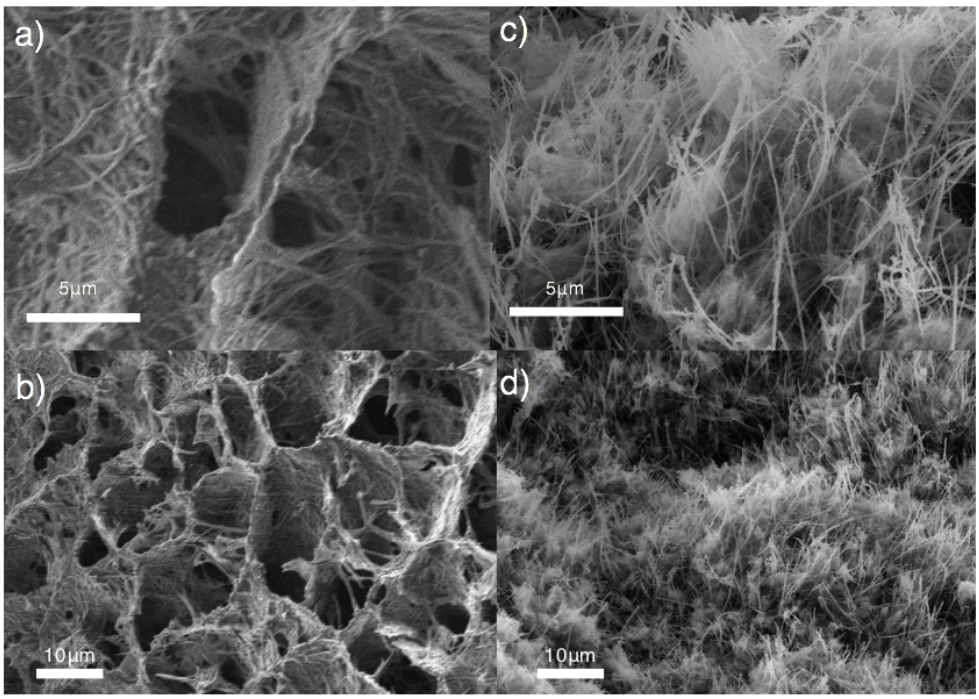

Figure 7.4 a,b) SEM images of freeze-dried PTCDI nanofiber aerogels c,d) SEM images of critical point dried PTCDI nanofiber aerogels

diffraction pattern matches that of a monoclinic p2c/1 (space group 14) crystal in the [301] orientation, shown in the indexed simulated diffraction pattern in **Figure 7.3c**. The crystal orientation is annotated on the fiber, indicating PTCDI assembly along the nanofiber axis in the (10-3) direction and in the (002) direction along the nanofiber width.

7.2.3 Tunable Parameters in PTCDI Nanofiber Aerogel Synthesis

Within the synthesis of PTCDI and CNF aerogels, there are a variety of parameters that can be altered, resulting in a highly tunable synthesis. As will be discussed in length in **Section 7.3**, the graphitization temperature of PTCDI aerogels plays an enormous role in the crystallinity and structure of the resulting CNF aerogel. Additionally, a number of parameters in the PTCDI synthesis can impact the final PTCDI aerogel, as well as the CNF aerogel.

Firstly, the method used for solvent removal has a large impact on the pore structure and surface area of the final aerogel. Freeze-drying is a technique in which a phase transition of the solvent from solid to gas (sublimation) takes place. This allows the solvent to be removed without surface tension, and thus preserves the pore structure of the hydrogel. In this process, the structure and orientation of the frozen solvent, typically water, will dictate the pore structure. Due to the phase diagram of water and expansion in its crystal structure upon freezing, freeze-dried samples typically have a large population of macropores many microns wide and an overall lower surface area. Critical point drying uses supercritical carbon dioxide in order to remove the solvent without surface tension due to the solid and liquid-like properties of supercritical fluids. Critical point dried

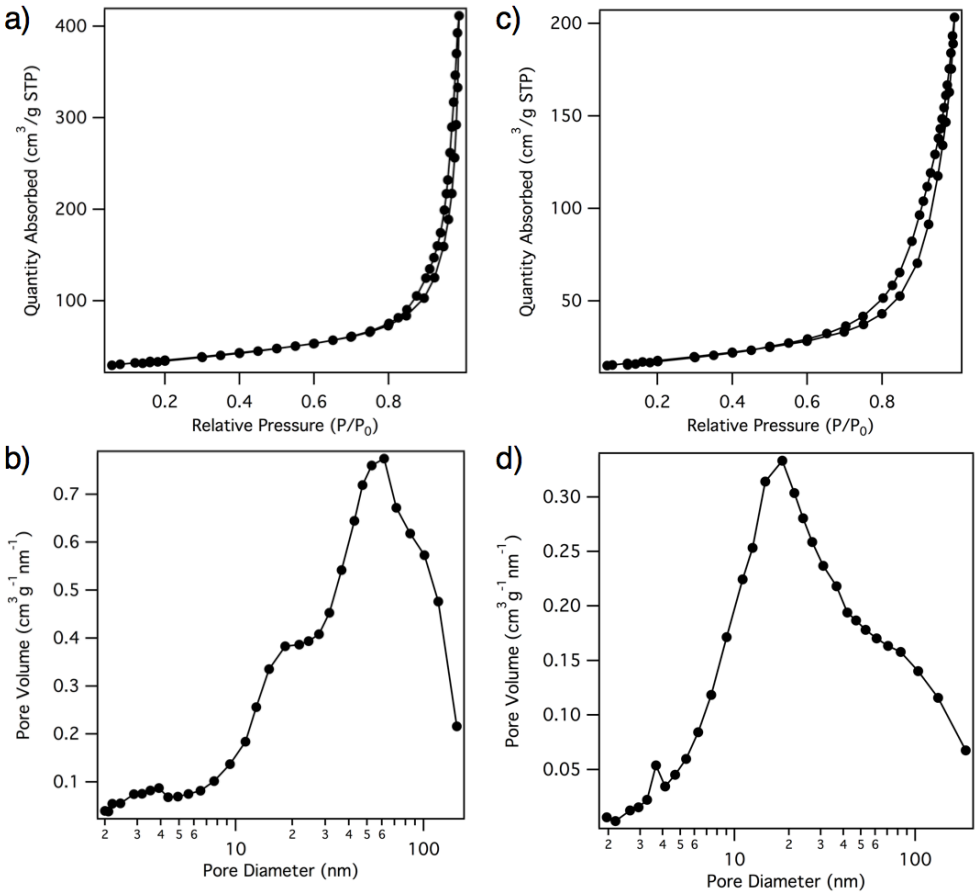

Figure 7.5 Nitrogen adsorption and desorption isotherms and pore size distribution of critical point dried (a.b) and freeze-dried (c,d) PTCDI nanofiber aerogels, respectively.

a)

Surface Area (m^2/g)	CPD	Freeze -Dry
PAH	123	62.3

b)

Pore Volume (cm^3/g)	CPD	Freeze -Dry
PAH	0.64	0.32

Table 7.1 a) Summary of surface areas of critical point dried and freeze-dried aerogels treated at various temperatures b) Summary of pore volume of critical point dried and freeze-dried aerogels treated at various temperatures

samples typically have larger surface areas and larger pore volumes of mesopores. However, critical point drying requires solvent exchange from water to a solvent that is miscible with CO_2, such as acetone. Given this requirement, only mechanically robust hydrogels are suitable for critical point drying. As shown in the SEM images in **Figure 7.4,** the changes in the microscale morphology are significant, with freeze-dried samples containing a network of macropores due to the ice templating, and critical point dried samples having a much closer-pack structure with less periodicity. The changes in the textural properties of the PTCDI nanofiber aerogels from these two drying methods are summarized in **Figure 7.5** and **Table 7.1**. The nitrogen adsorption and desorption isotherms of PTCDI nanofiber aerogels are shown in **Figure 7.5 a,c** and both drying methods form a Type IV (IUPAC definition) shape indicative of a mesoporous material. The calculated surface area for the critical point dried sample is 123 m^2/g, similar to other semiconducting aerogels in the literature[202]. This surface area is made up of predominantly meso and macropores, with a very small contribution of micropores, as indicated in the pore size distribution (**Figure 7.5b)**. On the other hand, freeze-dried PTCDI nanofiber aerogels have an overall reduced surface area and pore volume. Despite this, these samples do in fact have a large pore volume peak around 11nm, and the presence of periodic macropores with diameters of several microns could be useful for accessibility to meso and micropores in applications for energy storage to facilitate mass diffusion[102].

The density of resulting PTCDI nanofiber aerogels is also highly tunable during this synthesis by simply modifying the PTCDA concentration. The resulting PTCDI hydrogels undergo very little volume change during gelation due to the physical entanglement of nanofibers that holds the hydrogel together, as opposed to chemical bonds. As such, decreasing or increasing the PTCDA concentration simply alters the mass of PTCDI product without large change to the volume, resulting in modified densities. The density of PTCDI nanofiber aerogels using a PTCDA concentration of 100 mg/mL is 89.4 mg/cm^3, which is easily tuned in this manner by incorporating

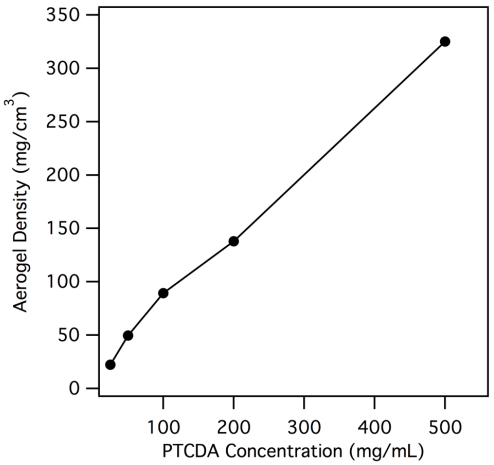

Figure 7.6 Density of PTCDI aerogels using different PTCDA concentrations.

PTCDA concentrations as low as 25 mg/mL up to 500 mg/mL into the suspension. The resulting densities range between 22 and 323 mg/cm^3 (**Figure 7.6)**. The minimum concentration of PTCDA required to reach a critical nanofiber entanglement to form a freestanding hydrogel cylinder is 25 mg/mL.

The final tunable parameter in the synthesis involves the addition of metal salts into the PTCDA suspension in order to coordinate to PTCDI and direct the self-assembly into a variety of nanostructures. This parameter is discussed in great detail in **Section 7.4**.

7.3 Graphitization of PTCDI Nanofiber Aerogels into CNF Aerogels

Polycyclic aromatic hydrocarbons (PAHs) like PTCDI lack temperature stability and at high temperatures will undergo decomposition or pyrolysis. This property has led them to be used as sacrificial materials[160]. While PAHs fully oxidize in the presence of oxygen, in an inert environment both thermal decomposition and graphitization occur. This property is exploited in order to graphitize PTCDI nanofibers into CNFs.

7.3.1 Synthesis of CNF Aerogels

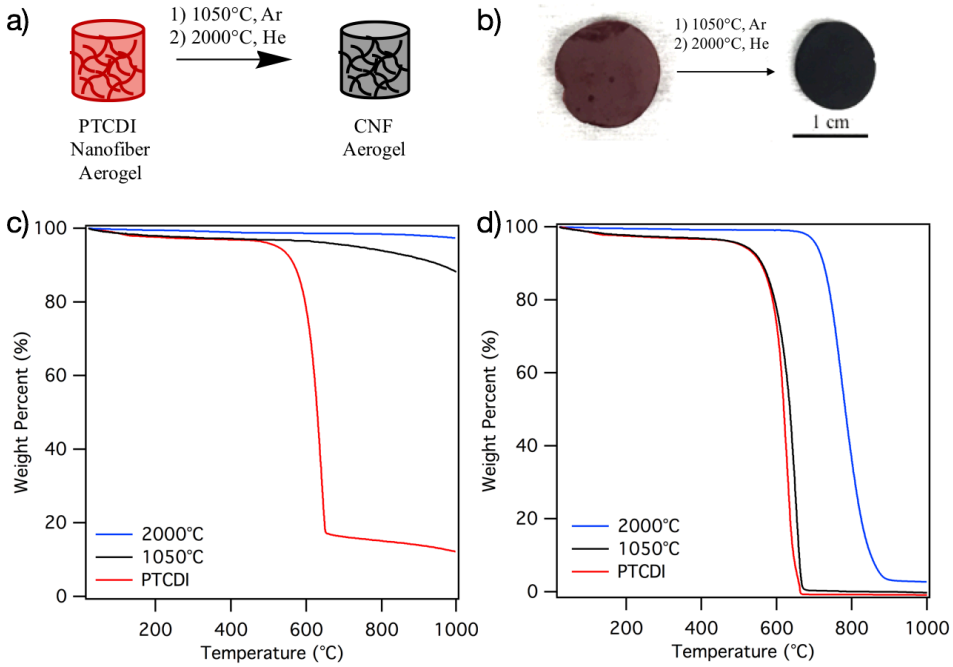

Figure 7.7 a) Graphitization process from PTCDI nanofiber aerogel to CNF aerogel. b) Photographs of PTCDI nanofiber aerogel (left) and CNF aerogel (right). c-d) TGA in inert atmosphere and air, respectively.

As outlined in **Figure 7.7a**, CNF aerogels are synthesized by thermal treatment of PTCDI nanofiber aerogels at 1050°C in Ar for 2 hours followed by an additional 2 hour treatment at 2000°C in He in order to increase crystallinity. TGA of PTCDI nanofiber aerogels conducted in an inert environment shows that a large mass change occurs between 400-600°C, followed by a relatively stable mass until the maximum temperature of 1000°C, indicating thermal decomposition and the formation of a more thermally stable phase (**Figure 7.7c)**. During this process there is a visible color change from dark-red to black, further implicating the reaction taking place (**Figure 7.7b**). Despite the clear chemical transformations, CNF aerogels treated at

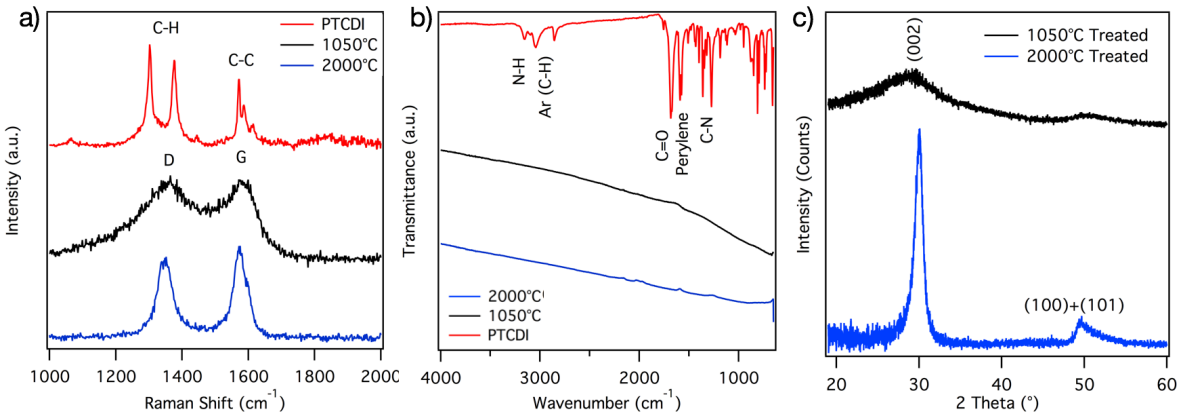

Figure 7.8 a,b) Raman and FTIR spectra of PTCDI nanofiber aerogel, and CNF aerogels treated at 1050°C and 2000°C, respectively. g) XRD of CNF aerogels treated at 1050°C and 2000°C.

1050 and 2000°C still possess modest surface areas of 46 and 43 m^2/g, respectively. This surface area is likely capable of increasing by post-synthesis activation using carbon dioxide or potassium hydroxide[132,133]. Additionally, after treatment at 2000°C, CNF aerogels are stable up to 750°C in air and above 1000 °C in an inert atmosphere, making them suitable for high temperature applications (**Figure 7.7d).**

7.3.2 Characterization of CNF Aerogels

Characterization of CNF aerogels treated at 1050 and 2000 °C is performed to study the chemical and structural transformations as a result of thermal annealing. Raman spectroscopy is a vital technique for characterization of graphitic materials and can be utilized to study crystallinity, defects, and conversion to graphitic phases[203]. Important Raman peaks in graphitic materials are the G peak due to the in-plane E_{2g} phonon at 1575 cm^{-1}, as well as the D peak at 1350 cm^{-1} which requires a defect in order to activate and is indicative of the density of defects in a graphitic material. Before carbonization, the Raman spectrum of the PTCDI nanofiber aerogel has peaks at 1302, 1378 and 1572 cm^{-1} due to C-H and C-C vibrations in the material (**Figure 7.8a)**. After treatment at 1050 °C, the spectrum becomes that of a graphitic material with wide D and G peaks at 1362 and 1582 cm^{-1}, indicating that graphitization occurs during the annealing step. However, the extremely broad D and G peaks indicate the low crystallinity of the material and the spectrum is similar to reduced graphene oxides lacking a fully sp^2 hybridized structure[204]. Subsequent treatment at 2000 °C results in extreme narrowing of the D and G peak consistent with enhancement in the crystallinity of CNF aerogels. Further chemical changes are probed using FTIR to verify loss of the vibrational structure of PTCDI nanofibers during thermal treatment. In the FTIR spectrum, peaks previously referenced for PTCDI are lost after treatment at 1050 and 2000°C and the classic IR spectrum for a graphitic structure is adopted which consists of a drifting baseline and lack of notable peaks (**Figure 7.8b)**.

After treatment at 1050 °C, XRD shows complete conversion of the PTCDI crystal structure to a graphitic structure with a dominant peak at 30° corresponding to the graphitic (002) lattice plane (**Figure 7.8c)**. The broad (002) peak is indicative of the low crystallinity in the material leading to a distribution of interlayer spacings. Subsequent treatment at 2000 °C results in a narrow (002) peak with significantly increased intensity due to enhanced crystallinity in the material, in agreement with Raman spectroscopy. Using the Scherrer equation, the crystallite size for aerogels treated at 1050 and 2000 °C are calculated to be 1.0 and 8.7 nm, respectively[205].

The chemical composition of CNF aerogels treated at 1050 and 2000 °C is studied using XPS (**Figure 7.9).** Treatment at 1050 °C results in a graphitic aerogel with 1.7% nitrogen remaining from the imide group. The C1s spectrum is made up of a dominant peak at 284.7 eV due to C=C bonding in the aerogels and minor peaks at 285.6, 286.3, and 287.2 eV due to C-O, C=O and O-C=O bonding, respectively. CNF aerogels treated at 2000 °C contain a similar C1s spectrum and no nitrogen is detected in the sample after treatment, suggesting a purely carbon composition.

CNF aerogels treated at 1050 and 2000 °C are structurally characterized using SEM and TEM (**Figure 7.10**). As seen in the SEM images in **Figure 7.10a**, after 1050 °C firing, the high surface area, 3D morphology, and nanofiber composition is largely maintained. CNFs have a range of widths predominantly between 100 and 200 nm and are several microns in length. After treatment at 2000 °C, the aerogel still maintains nanofiber morphologies, but they are more densely packed and have less free space. This is also reflected in the density increasing from 45.4 mg/cm^3 after 1050 °C treatment to 82.8 mg/cm^3 after 2000°C treatment.

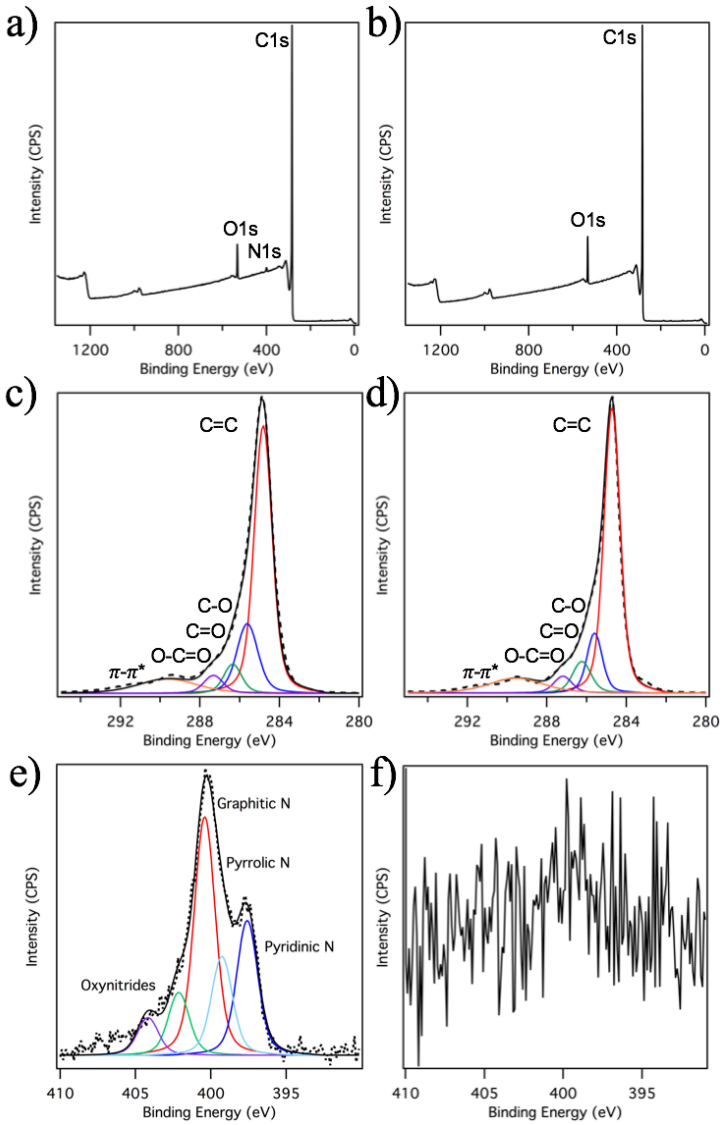

Figure 7.9 a-b) Survey spectra c-d) C1s spectra and e-f) N1s spectra of CNF nanofiber aerogels treated 1050 and 2000°C, respectively.

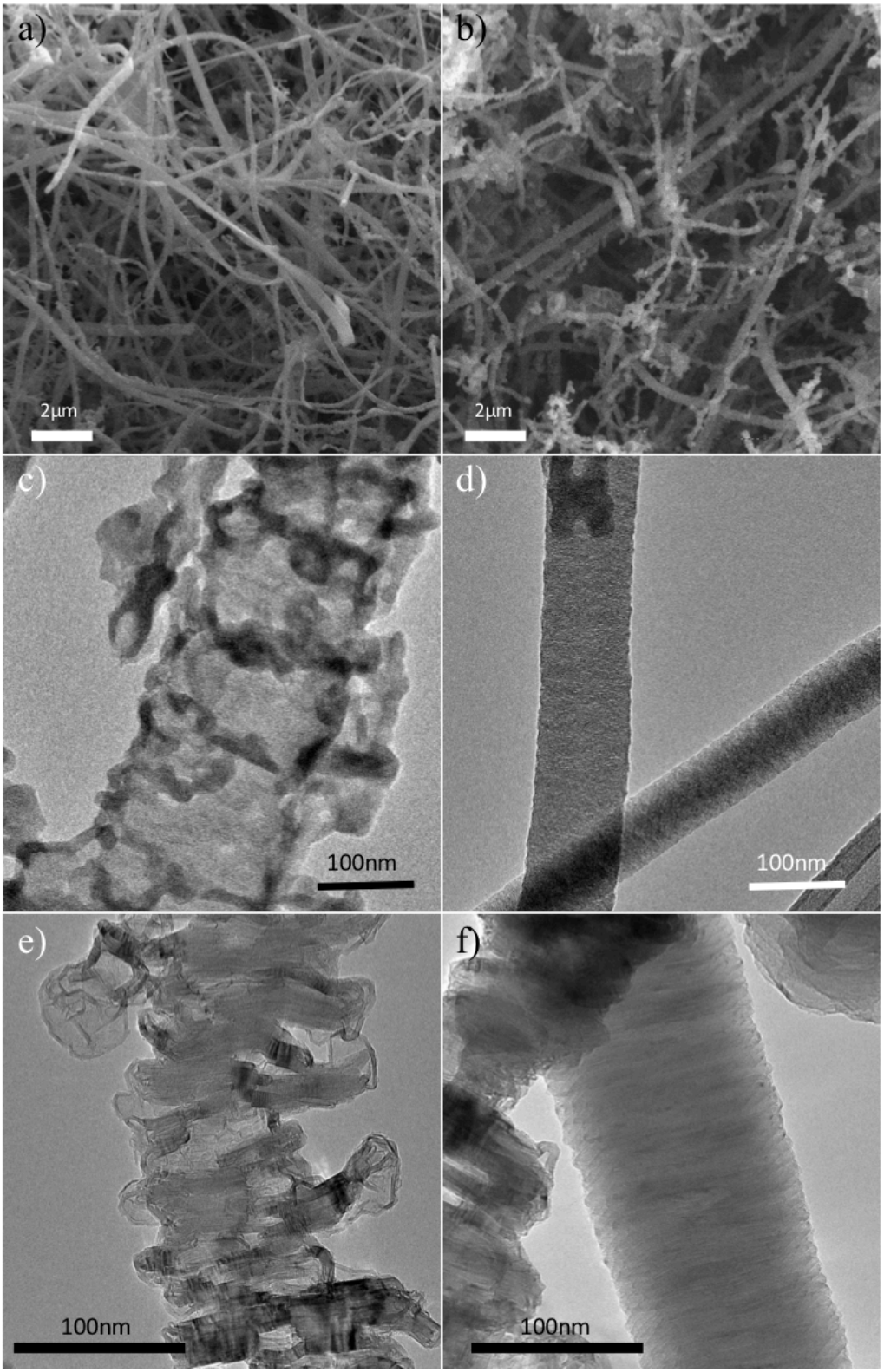

Figure 7.10 a-b) SEM images of CNF aerogel treated at 1050°C and 2000°C, respectively c,d) TEM images of CNF aerogels treated at 1050°C e,f) TEM images of accordion-type and platelet-type CNFs present after 2000°C treatment, respectively.

TEM of nanofibers treated at 1050 °C shows two distinct morphologies of nanofibers are present. As seen in **Figure 7.10c**, some nanofibers exhibit highly irregular structures that do not contain straight edges. This is likely due to the competing decomposition and graphitization processes taking place between 500-600 °C. The other type of nanofiber contains a much larger degree of ordering and quite smooth edges (**Figure 7.10d**). High magnification reveals that both types of nanofibers are made up of disordered graphitic layers with lattice fringes and a crystalline structure, in agreement with the broad (002) peak observed in XRD (**Figure 7.11a,b**).

High temperature treatment at 2000 °C results in remarkable graphitization and increased crystallinity of nanofibers, with the two distinct nanofiber morphologies present at 1050 °C persisting in the aerogel despite graphitization (**Figure 7.10e,f and 7.11c,d**). Nanofibers with smooth edges are a platelet-type carbon nanofiber and the irregular fibers have an accordion-type morphology. The aerogel is predominately composed of accordion-type morphology fibers, with fewer than one third of nanofibers being platelet type. Platelet-type fibers are composed of graphitic layers stacked perpendicular to the fiber axis. Such platelet fibers have previously been reported but only synthesized using vapor phase methods[206]. To our knowledge, this is the first documentation of the accordion-type morphology of CNFs. Accordion-type CNFs maintain ordering perpendicular to the fiber axis, but also feature irregular stacking approximately every 10-20nm along the nanofiber axis, leading to uneven nanofiber edges. Both platelet and accordion-type CNF morphologies have large domains composed of (002) planes, in agreement with the observation of an enhanced (002) diffraction peak in XRD.

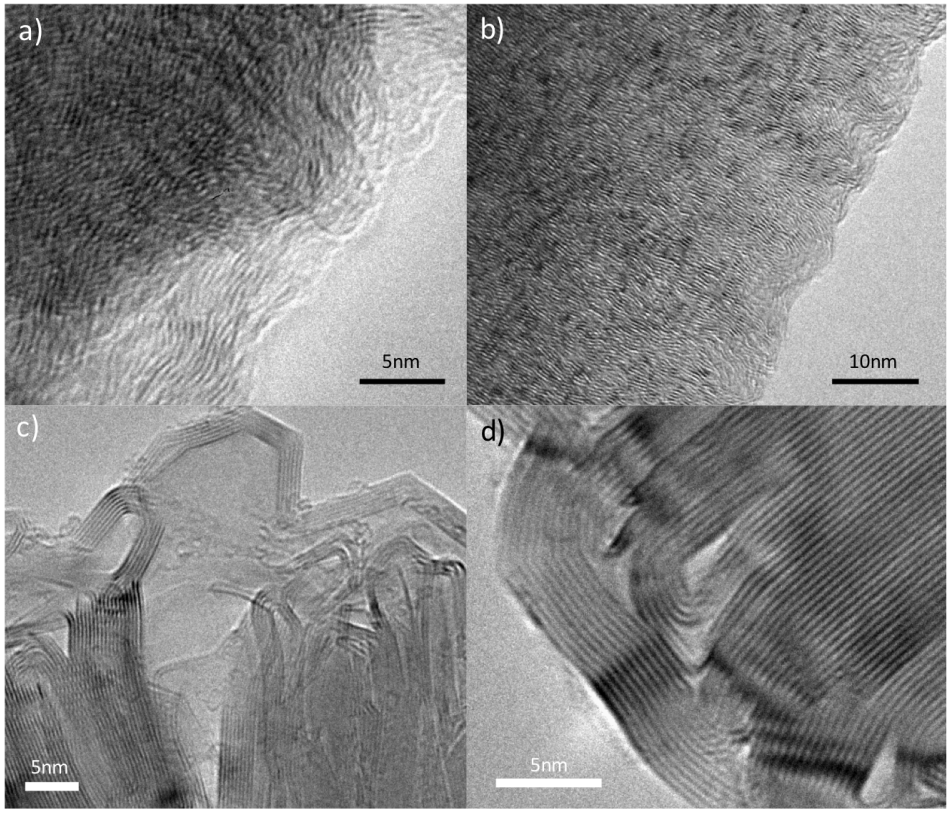

Figure 7.11 Higher magnification TEM images of (a) irregular nanofiber and (b) ordered nanofiber from CNF aerogel treated at 1050°C , (c) accordion-type nanofiber and (d) platelet-type nanofiber from CNF aerogel treated at 2000°C.

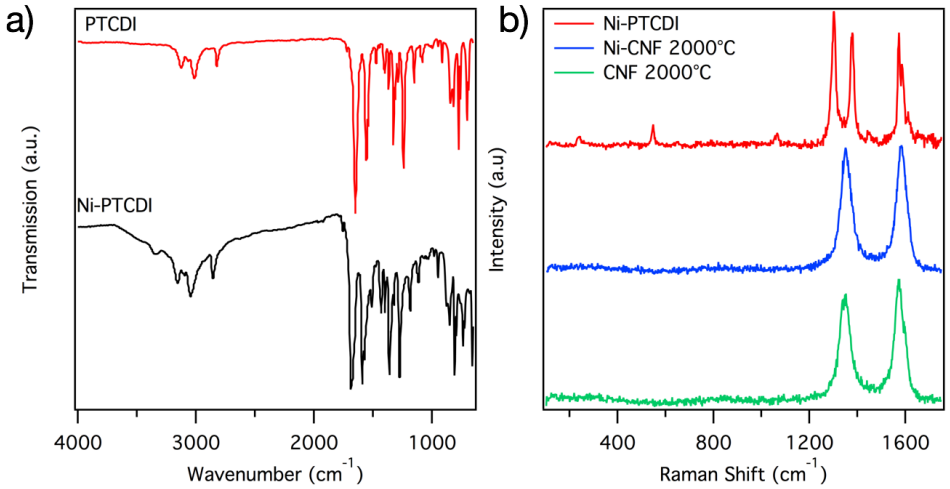

Figure 7.12 a) FTIR spectra of PTCDI and Ni-PTCDI aerogels b) Raman spectra of Ni-PTCDI as well as Ni-CNF and CNF aerogels treated at 2000°C.

This highly versatile synthesis yields carbon nanofiber aerogels of low crystallinity (1050 °C treated) and high crystallinity (2000 °C treated) and can easily be adapted to introduce additional active materials into the architecture, as described below.

7.4 Metal Directed Self-Assembly of Aerogels

In order to synthesize aerogels composed of controllable nanoscale morphologies, metal salts are incorporated into the PTCDA suspension during synthesis. The addition of a metal salt also serves to increase catalytic activity. Using this approach, metal ions can interact with PTCDA and lead to metal directed self-assembly of PTCDI (M-PTCDI aerogels). The annealing temperatures can be carefully selected in order to synthesize graphitized aerogels decorated with metal nanoparticles, as well as aerogels with no trace of metal (M-CNF). In this section, I describe the synthesis and characterization of nickel directed assembly of CNF aerogels (Ni-CNF aerogels) by incorporation of $NiCl_2$ into the PTCDA suspension as well as gold directed assembly of CNF (Au-CNF aerogels) using $HAuCl_4$. As a proof of concept, additional examples showing that cobalt, iron, and palladium can also be used for metal-directed assembly of PTCDI aerogels will also be presented.

7.4.1 Metal Directed Self-Assembly Synthesis

Metal directed assembly of aerogels is achieved by dissolving 1.5mM of metal salt ($NiCl_2$, $HAuCl_4$, $FeCl_2$, $PdCl_2$, $CoCl_2$) into the PTCDA suspension. A 1:6 by volume amount of NH_4OH:H_2O is added and the suspension is allowed to gel for 24hrs at 80 °C to yield metal directed assembled PTCDI hydrogels (M-PTCDI, M=Ni, Au, Fe, Pd, Co). Solvent is removed using supercritical CO_2 to yield M-PTCDI aerogels. M-PTCDI aerogels are annealed at 1050 °C in Ar followed by 2000 °C in He to yield M-CNF aerogels.

7.4.2 Characterization of PTCDI and CNF aerogels Synthesized through Metal Directed Assembly

As shown in the FTIR spectrum in **Figure 7.12a,** one additional peak at 3360 cm^{-1} emerges that is not present in PTCDI aerogels. This corresponds to Ni coordinated to the nitrogen in the

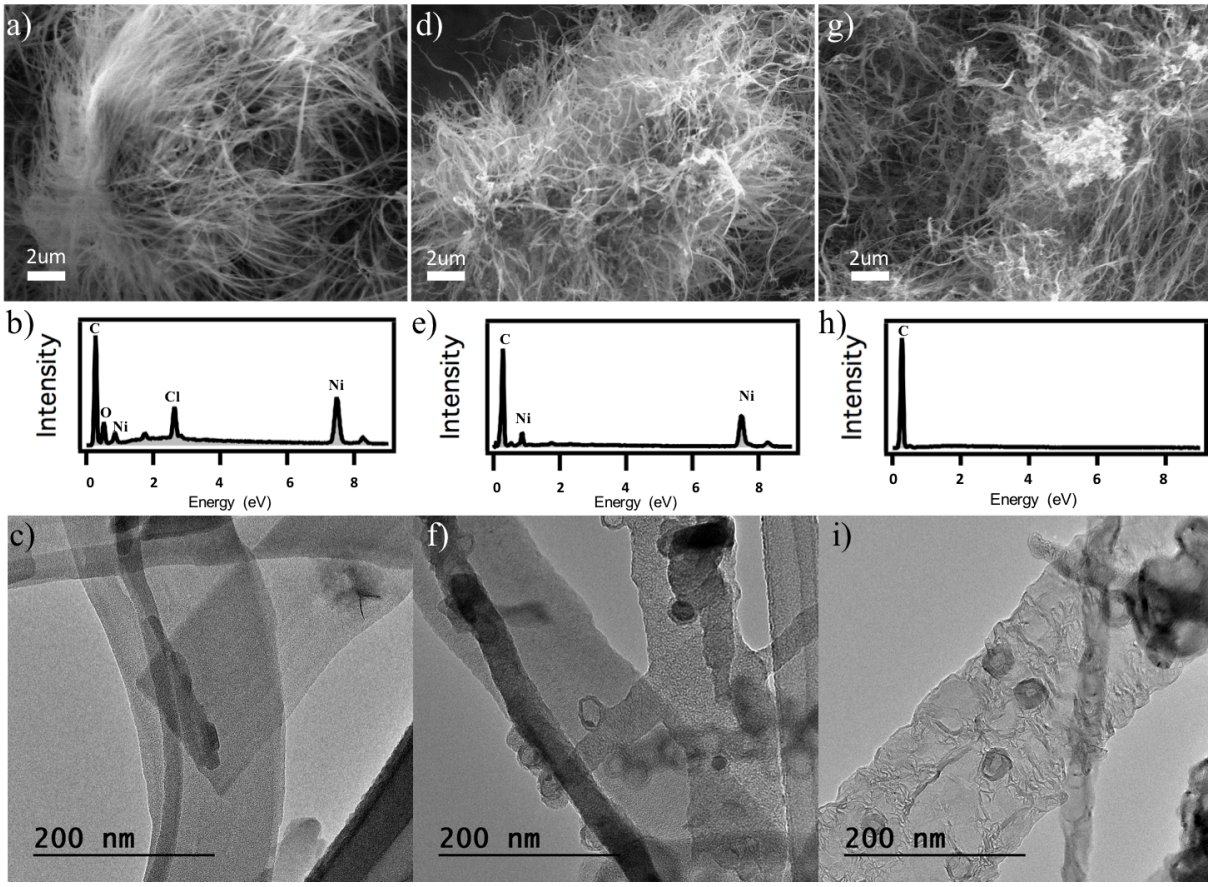

Figure 7.13 SEM image, EDS spectrum and TEM image of a-c) Ni-PTCDI aerogel, d-e) Ni-CNF aerogel treated at 1050°C, g-i) Ni-CNF aerogel treated at 2000°C, respectively.

imide. Additionally, shifting of peaks is observed as a result of Ni coordination resulting in the imide C=O shifting from 1650 cm^{-1} to 1690 cm^{-1}. After annealing at 1050°C and 2000°C, the expected graphene IR spectrum is obtained indicating loss of perylene cores and graphitization occurring during annealing. This is also supported by the recovery of the graphitic Raman spectrum after annealing (**Figure 7.12b**).

Using SEM, EDS and TEM, the 3D physical morphology and chemical composition of the Ni-PTCDI and Ni-CNF aerogels are studied (**Figure 7.13).** SEM shows that Ni directed assembly results in an extremely dense nanofiber network in which nanofibers are closely packed in a bush-like morphology and many nanofibers originate from the same point. Additionally, EDS confirms the presence of nickel and chlorine in the Ni-PTCDI aerogels after supercritical drying **(Figure 7.13b)**. Using TEM, Ni-PTCDI nanofibers are observed with widths around 100-200 nm and predominantly smooth edges (**Figure 7.13c).** After treatment at 1050°C, SEM indicates that the nanofibers are more irregular and have more curvature after annealing. The composition is studied using EDS, which shows the presence of nickel and the elimination of chlorine in the aerogel (**Figure 7.13d,e**). At high temperatures and under inert or reducing conditions, metal salts such as $NiCl_2$ will reduce and form metal nanoparticles, while chlorine is released as HCl gas[207]. TEM imaging confirms the formation of Ni nanoparticles with diameters around 20nm, and assembly directly on CNFs (**Figure 7.13f**). A portion of Ni nanoparticles contain carbon shells and some areas contain hollow onions, in which a graphitic shell catalytically grows and redeposits prior to nickel evaporation.

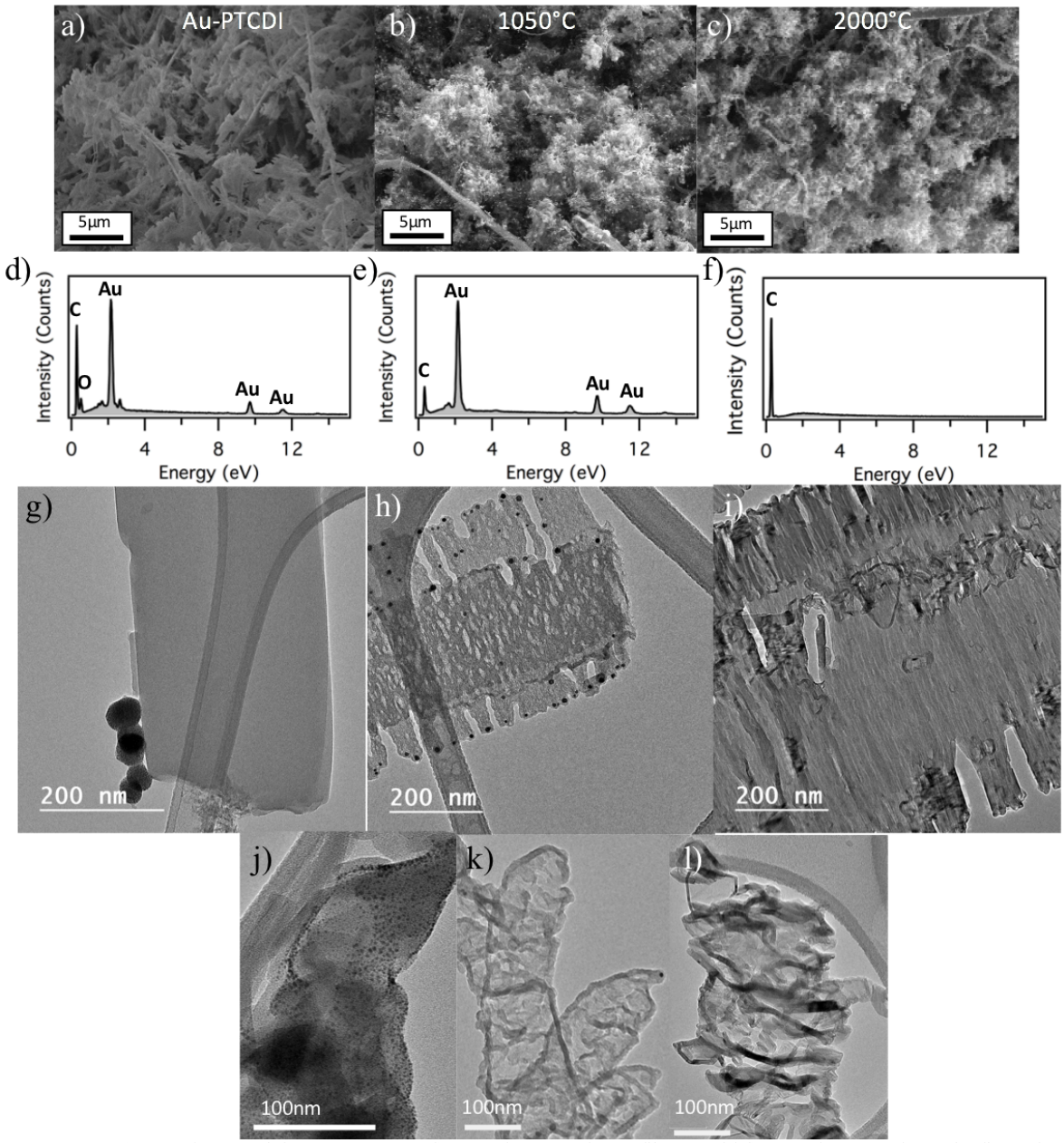

Figure 7.14 a-c) SEM images d-f) EDS spectra g-i) TEM images of nanofibers and j-l) TEM images of nanoleaflets of Au-PTCDI, Au-CNF 1050°C and Au-CNF 2000°C, respectively.

Treatment at 2000°C surpasses nickel's boiling point of 1450°C, allowing a highly crystalline and fully graphitic CNF aerogel to be synthesized with altered nanoscale morphology. SEM shows that the 2000°C Ni-CNF aerogel maintains the nanofiber morphology of its Ni-PTCDI and Ni-CNF 1050°C aerogel counterparts at the microscale. EDS confirms that all nickel has evaporated and none remains after treatment at 2000°C (**Figure 7.13g,h)**. Additionally, TEM reveals the starkly different nanoscale morphology as the result of the Ni-directed assembly. As opposed to platelet and accordion type morphologies formed in the absence of $NiCl_2$, Ni-CNF aerogels contain highly irregular stacking of the (002) lattice plane. At temperatures as high as 2000°C, carbon atoms can readily diffuse and dissolve in nickel and be redeposited into irregular structures as seen in **Figure 7.13i**. The large degree of disorder and nonuniform packing of (002)

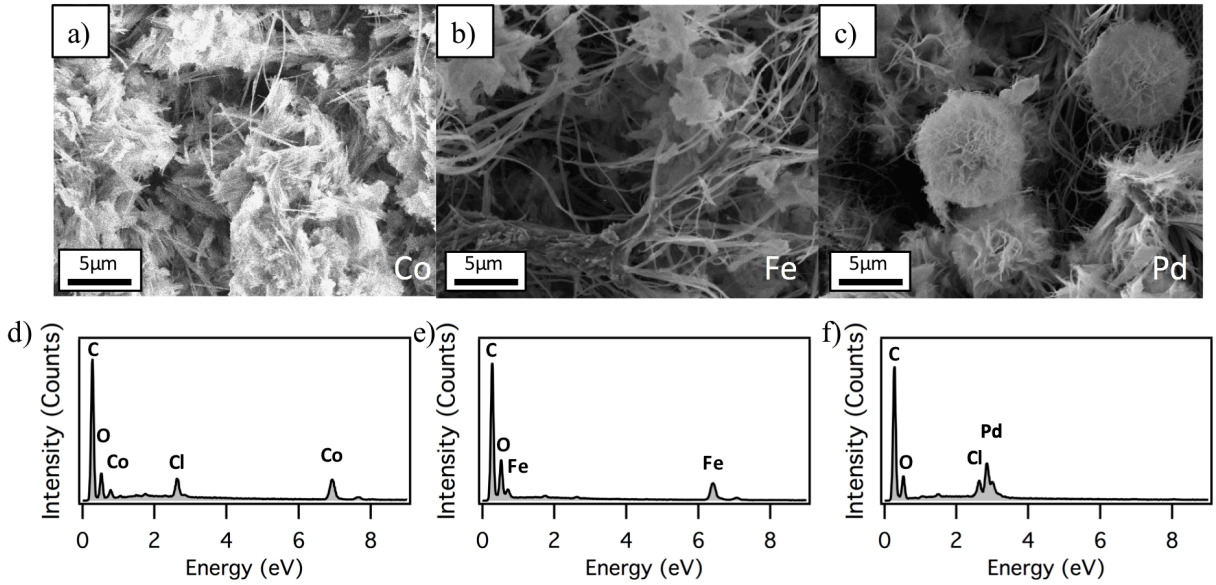

Figure 7.15 a-c) SEM images d-f) EDS spectra of Co-PTCDI, Fe-PTCDI, Pd-PTCDI aerogels, respectively.

domains leaves more vacant space in the CNF interior. This is significant because the irregularity results in an increased number of defects and can lead to additional active sites for catalysis[208,209]. This morphology also gives access to a larger accessible surface area for gas storage in the nanofibers, while the high crystallinity maintains the good stability of CNFs. As a result of this phenomenon, the surface area of Ni-CNF aerogels treated at 1050 °C and 2000 °C are 102 and 43 m^2/g, respectively; increased relative to self-assembly without metal at 1050 °C treatment and comparable with classical self-assembly at 2000 °C treatment.

Another example of metal directed assembly uses $HAuCl_4$ to synthesis Au-PTCDI aerogels as well as Au-CNF aerogels of both low crystallinity and high crystallinity. As seen in the SEM image of Au-PTCDI in **Figure 7.14a**, the resulting aerogel contains a mixture of wide diameter fibers as well as a nanoleaflet-type morphology. EDS confirms the presence of Au in the Au-PTCDI aerogel, and both nanofiber and nanoleaflet morphologies are observed in TEM (**Figure 7.14 d,g,j)**. Nanofibers have larger diameters than those made through classical self-assembly of PTCDI, and the nanoleaflets are approximately 150nm in some areas. Gold nanoparticles are formed following the addition of ammonium hydroxide, thus the Au-PTCDI aerogel contains gold nanoparticles assembled directly on the PTCDI (**Figure 7.14j**), as well as large spheres of agglomerated nanoparticles **(Figure 7.14g).**

Following treatment at 1050°C, the Au-CNF aerogel is still composed of nanofiber and nanoleaflet morphologies and EDS indicates the continued presence of gold in the carbonized aerogel (**Figure 7.14b,e)**. Under TEM, gold nanoparticles are found to assemble along the outer edges of the nanofiber, which are no longer smooth but contains spikes (**Figure 7.14h**). It is hypothesized that at these high temperatures, the nanoparticles act as catalysts for the growth of the spikes away from the center of the fiber. Upon cooling, the gold precipitates back into nanoparticles at the tips of the fibers. Additionally, the nanoleaflets in the aerogel are graphitized at the high temperature (**Figure 7.14k).**

Treatment at 2000°C results in a highly graphitic material made up of the nanofibers and nanoleaflets (**Figure 7.14c)**. The melting point for gold of 1064°C is surpassed and the resulting Au-CNF aerogel is fully composed of carbon with no trace of gold left in the EDS spectrum

(**Figure 7.14f).** A similar phenomenon is observed after 2000°C firing as in the other aerogels, where all nanostructures present are fully graphitic as marked by the lattice fringes throughout the nanofibers and nanoleaflets (**Figure 7.14 i,j)**.

While two examples are presented here of nickel and gold directed assembly, resulting in nanofibers of altered morphology as well as leaflets, other metal salts can also be used. As seen in **Figure 7.15,** other nanoscale morphologies are formed by cobalt, palladium and iron directed assembly including nanoflowers, nanoleaflets, and nanofibers of different widths, giving a broad range of aerogels based on graphitic nanoassemblies as well as composite aerogels, depending on annealing temperature.

7.5 Incorporating CNF Aerogels for Energy Storage and Future Directions

The large surface area and high conductivity of CNF aerogels make them promising materials for energy storage applications. Graphitic materials have been widely studied for supercapacitor electrodes, as well as lithium ion battery anode materials[97,210,211]. Future studies should explore the use of these aerogels as supercapacitor electrodes and battery anodes. The added benefit of incorporating aerogels into these applications is their mechanical stability making them capable of being freestanding electrodes not requiring a substrate for device assembly. Comprehensive study of the performance of aerogels in these application with different annealing temperatures will be useful for optimizing the electrode performance and active materials can be introduced into the aerogel by metal directed assembly.

PART III: Chemical Modification of Boron Nitride Nanomaterials

Chapter 8: Functionalization of Boron Nitride Nanomaterials for High Performance Polymer Composites

Nano Fun Fact: One nanometer is 10^{-9} m, the size of a person is about 1 m, and the sun is about 10^{9} m, meaning that the difference in the size of a human from the sun and a humane from the materials described in this thesis are the same order of magnitude.

8.1 Searching for an Ideal Filler

While the field of polymer science has made it possible to tailor-make high performance polymers, a number of properties are not currently achievable in pure, as-synthesized native polymers[212–214]. One important approach to improve polymer properties is the formation of polymer composites utilizing a filler material. A wide range of materials have been explored as potential filler materials including metals, ceramics, and fiberglass[215–217]. A filler possesses one or a number of desirable properties to impart into a polymer matrix. These properties can include thermal conductivity, excellent mechanical properties, neutron absorption, or resistance to oxidation. One of the leading materials for next generation polymer composites BN nanomaterials as nanofillers. This chapter will explore forming polyimide nanocomposites using 1D, 2D, and 3D BN nanofillers and some of the challenges faced during this process.

8.1.1 Boron Nitride Nanofillers

Bulk hexagonal boron nitride (h-BN) is a wide band gap material with excellent resistance to oxidation up to 800°C. It is chemically inert and has a large neutron absorption cross section. However, despite having strong sp^2 bonds in the *xy* plane, bulk h-BN possesses poor mechanical properties due to the Van Der Waals forces holding the layers together in the c direction. Importantly, the (002) plane of h-BN is among the strongest of any known insulator. This plane also possesses a high thermal conductivity of 400 W/mK with low thermal conductivity in the z direction of 2 W/mK due to phonon scattering between layers. In order to take advantage of the superior thermal and mechanical properties of the (002) plane, it must be maximally exposed by the formation of nanostructures. These nanostructures include:

1) 1D BN nanotubes (BNNTs) with high thermal conductivity and superior mechanical properties along the tube axis
2) 2D BN nanosheets (BNNSs) that possess excellent in-plane thermal and mechanical properties
3) 3D BN aerogels, a nanostructured 3-dimensional system consisting of crosslinked BNNSs resulting in a porous high surface area structure

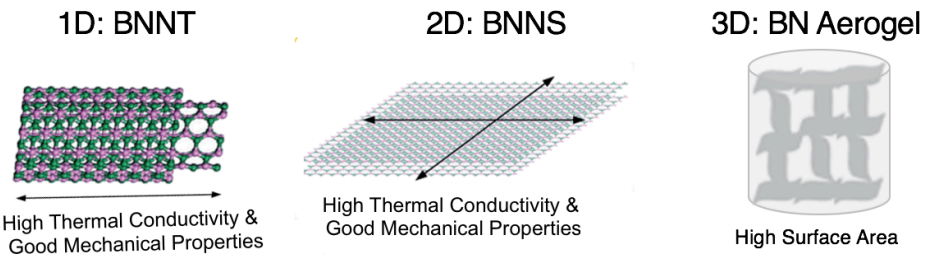

Figure 8.1 Structures of 1D BNNTs and 2D BNNSs which possess high thermal conductivities and excellent mechanical properties along the axis and in the plane, respectively. BN aerogels are crosslinked BNNSs with high surface areas and porosity.

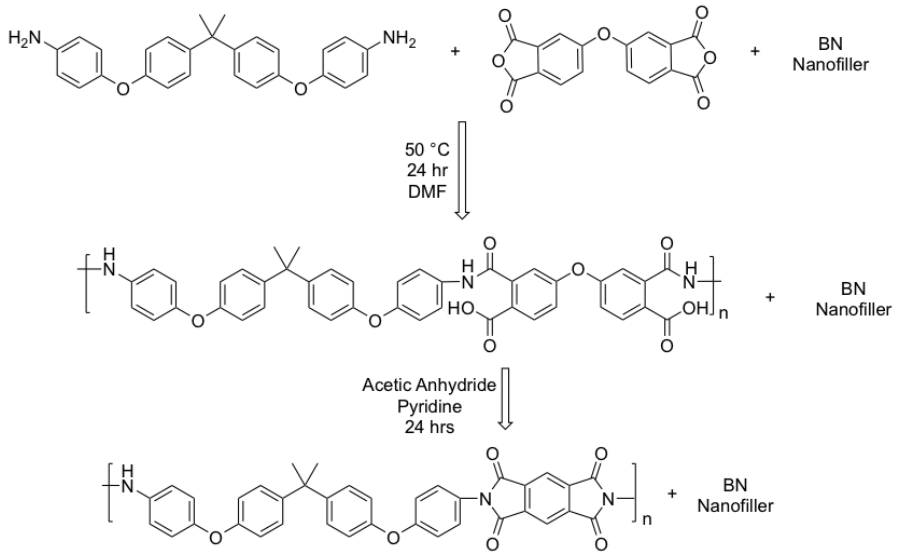

Figure 8.2 Two-step synthesis of polyimide BAPP and ODPA in the present of BN nanofiller yielding a polyamic acid which is chemically converted to polyimide.

These three BN nanomaterials are shown in **Figure 8.1**. Additionally, their large band gap makes it possible to load large contents of BN into the polymer without compromising the insulating character of most polymers or changing the color. Until recently, BN nanotubes were not readily available due to a lack of scalable syntheses. With recent progress in production of BN nanotubes, they have begun to be studied as fillers in nanomaterials and have been capable of improving their thermal and mechanical properties[218–222].

8.1.2 Beating the Heat in Polyimide

Polyimides are a class of polymers with a wide range of applications including in microelectronics, aerospace, and the military. They are known for their excellent mechanical properties and high temperature thermal stability, as well as solvent resistance and electrical insulation. These properties are beneficial for applications in extreme environments. However, polyimides have intrinsically low thermal conductivity, which is important for many applications including for heat dissipation in electronic packaging. This thermal conductivity problem could be solved by the incorporation of a filler into the polymer, forming a composite material. Polymer composites have the potential to enhance the thermal conductivity while maintaining or even enhancing polyimide's important intrinsic properties. As discussed in **Section 8.1.1**, BN nanofillers are excellent candidates for nanofillers and could improve the thermal conductivity of polyimides while maintaining their electrically insulating properties and even improving the mechanical properties and thermal stability.

8.2 Polyimide Composites with 1D, 2D, and 3D BN Nanofillers

Polyimide composites are synthesized using a two-step method in order to enhance the dispersion of BN nanofillers within the polymer. The composite morphology and interfacial

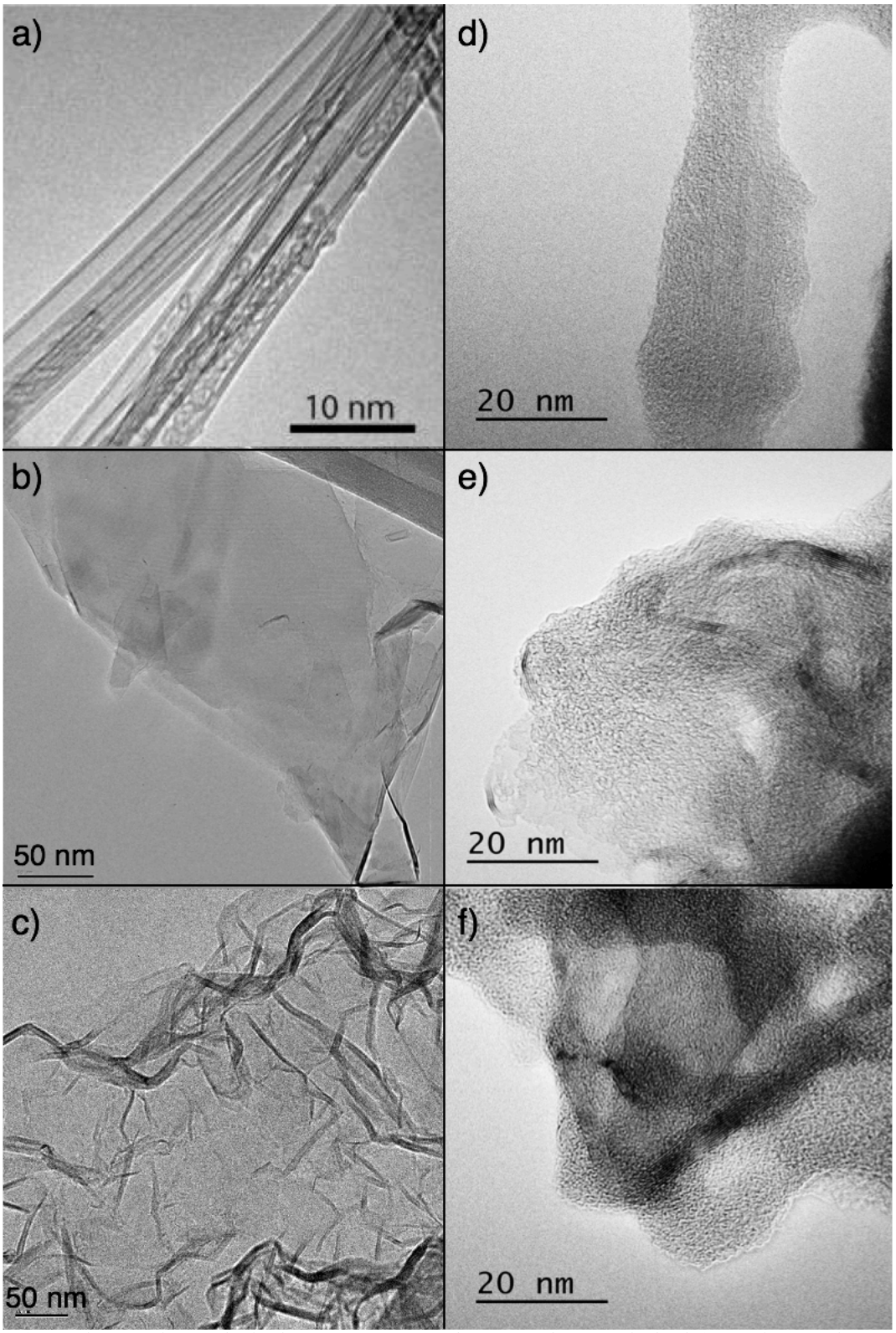

Figure 8.3 a-c) TEM images of as-synthesized BNNTs, BNNSs, and BN aerogels, respectively. d-e) TEM images of BNNTs, BNNSs, and BN aerogels in the polyimide composite indicating that there are interfacial interactions between the BN nanofiller and the polyimide. In collaboration with Thang Pham.

interactions between polyimide and BNNTs, BNNSs, and BNAGs at two different BN loading

contents are characterized and their changes in the glass transition temperature and oxidation temperature are studied.

8.2.1 Polyimide/BN Nanofiller Composite Synthesis

To form polyimide nanocomposites using BN nanofillers, a two-step *in-situ* polymerization is employed in the presence of the BN nanofiller (**Figure 8.2**). This allows for maximum dispersion of the BN nanofiller within the polymer. In the first step a diamine, 2,2-Bis[4-(4-aminophenoxy)phenyl]propane (BAPP), and a dianhydride, 4,4'-oxydiphthalic anhydride (ODPA), are reacted under inert conditions at 50°C for 24hrs using 18% solids. This yields a polyamic acid, which is dried under vacuum. In the second step, the polyamic acid is imidized using acetic anhydride and pyridine (4 equivalents of 1:1 acetic anhydride: pyridine per mole monomer) yielding the final polyimide BN nanofiller composite. Under these conditions, composites with 0.5wt% and 1wt% BN nanofiller are synthesized.

BNNTs are synthesized using an extended pressure inductively coupled plasma as previously published, and BNNSs and BN aerogels are synthesized by carbothermal conversion from a carbon precursor as described in **Chapter 2**. Graphite is used as a precursor for BNNSs and graphene aerogels are converted to BN aerogels.

8.2.2 Nanocomposite Morphology

The morphology of the composites are studied using transmission electron microscopy (TEM) and scanning electron microscopy (SEM). TEM can be used to study the interactions between the BN nanofiller and polyimide host matrix. The interactions between the filler and the

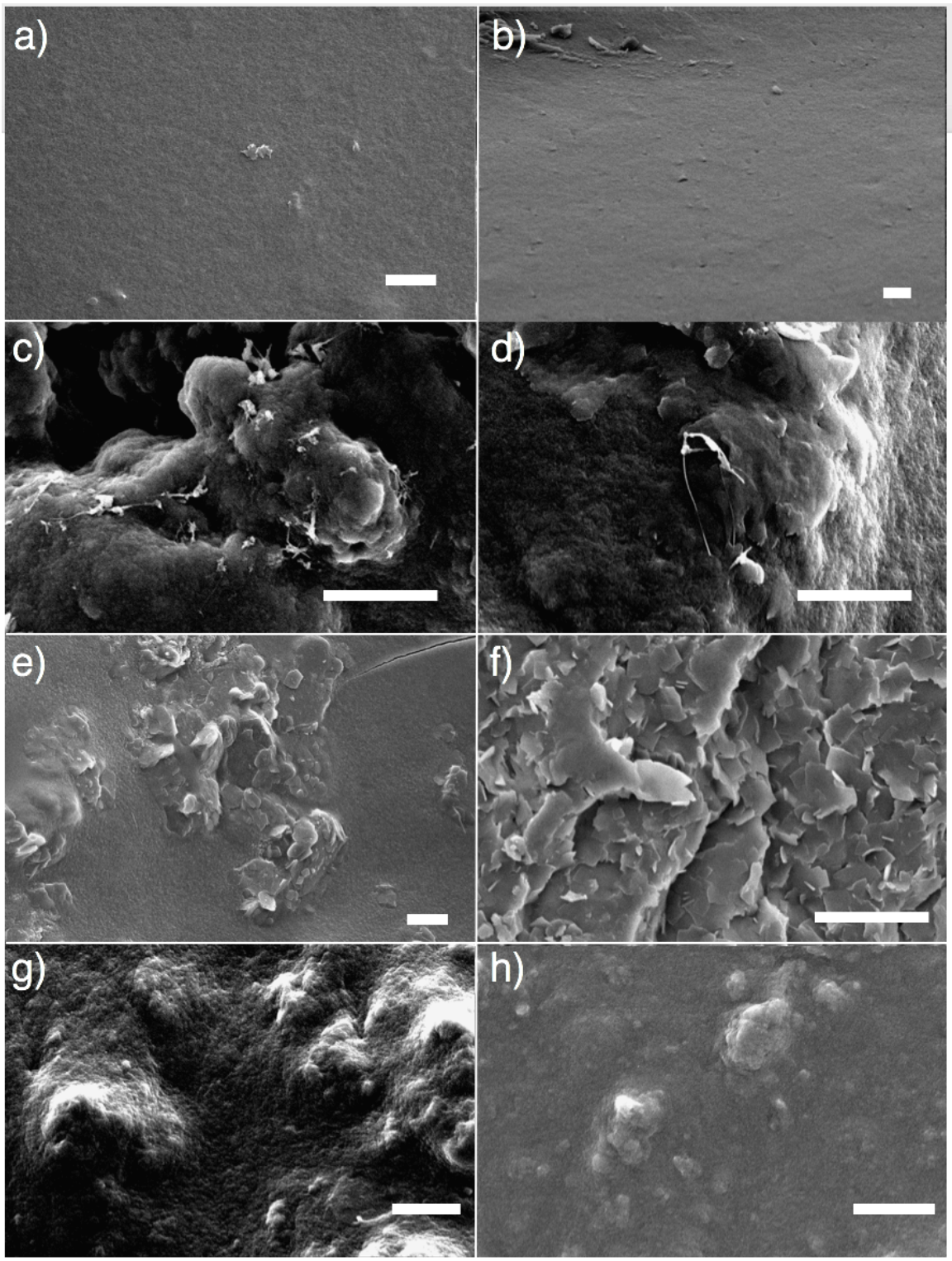

Figure 8.4 SEM images of a,b) native PI matrix with no nanofiller c,d) BNNT/PI composites e,f) BNNS/PI composites and g,h) BN aerogel composites with 0.5wt% and 1wt% nanofiller loading, respectively. Scale bar: 2μm.

matrix are vital to ensure that the filler is well dispersed within the matrix and does not simply form aggregates. Additionally, excellent nanofiller dispersion is necessary in order to impart its

properties to the host matrix. In this polyimide/BN nanofiller system π-π interactions between the aromatic rings in the polyimide and the π electron system of the BN filler are the predominant intermolecular interactions between the two materials. Additionally, Van Der Waal interactions between the BN nanofillers themselves can lead to agglomeration which is detrimental to the composite. **Figure 8.3a-c** shows the typical morphology of BNNTs, BNNSs, and BN aerogels when they are not dispersed within a polymer. After forming a nanocomposite, **Figure 8.3d-f** shows that there is a layer of polyimide approximately 15nm thick which surrounds BNNTs, BNNSs, and BN aerogels, respectively. This indicates that there is effective π-π stacking between the nanomaterial and the polymer.

SEM images in **Figure 8.4** reveal the composite morphology and distribution of the nanofiller within the polyimide matrix. Furthermore, it is possible to investigate the concentration dependent distribution of BNNTs, BNNSs, and BN aerogels within the matrix. The surface of native PI is shown in **Figure 8.4a,b** and is characterized by a highly smooth surface. Upon incorporation of 0.5 and 1wt% BNNTs, the surface becomes notably bumpier and inhomogeneous (**Figure 8.4c,d)**. Additionally, bundles of nanotubes are observed on the surface implying that weak interfacial interactions between the nanofiller and the polymer are present and insufficient to prevent agglomeration. Nanocomposites using a BNNS nanofiller result in a less bumpy surface at 0.5% than BNNTs, but increasing the concentration to 1wt% results in dramatic agglomeration of nanosheets within the matrix (**Figure 8.4e,f)**. Using BN aerogel nanofillers, a similar bumpy morphology is observed as was seen with BNNTs. In this case, clumps of BN aerogels are visible. BN aerogels are covalently crosslinked BNNSs with a large surface area to interact with the polymer (**Figure 8.4g,h)**. Agglomeration to the same degree and BNNTs and BNNSs is not possible due to the covalent crosslinking and the individual nanosheets will not bundle with one another, but instead maintain the aerogel morphology.

8.2.3 Thermal Properties of Nanocomposites

In order to study the oxidation resistance of the nanocomposites, thermogravimetric analysis (TGA) is performed in a 80% nitrogen, 20% oxygen environment. In this technique, the sample is heated at a constant rate and changes in the weight of the samples are monitored. Two important points on TGA plots are $T_{5\%}$, the temperature at which 5% of the mass is lost and $T_{75\%}$, where 75% of the mass is lost. The TGA plots are shown in **Figure 8.5a-c** and $T_{5\%}$ and $T_{75\%}$ are summarized in **Figure 8.5d-e**. The native polymer loses 5% mass at 480ºC and 75% mass at 777ºC. Nanocomposites with each nanofiller and concentration exhibit modest changes in the $T_{5\%}$ but the high temperature stability is clearly affected as noted by the dramatic increase in $T_{75\%}$ in each sample relative to the native polymer. The native polymer is fully decomposed by 900ºC, yet none of the nanocomposites are fully decomposed at 1000ºC, the maximum operating temperature of the TGA. There is also an evident trend between the nanofillers and loading concentrations. The $T_{75\%}$ of 0.5wt% BNNTs and BNNSs increase relative to the native polymer, from 777 ºC to 885 and over 1000ºC, respectively. Upon further BN loading at 1wt%, $T_{75\%}$ actually decreases indicating that additional mass is not beneficial. However, the thermal stability of the nanocomposite formed using BN aerogels increases with increased filler loading. This behavior is explained based on the difference in the dispersion of the nanofillers within the polyimide matrices. The high surface area and covalent crosslinking in BN aerogels prevents aggregation. Thus, at higher BN nanofiller loading, more PI is exposed to the BN aerogels whereas loading more BNNTs or BNNSs simply leads to increased agglomeration and is detrimental to the thermal stability.

Another property that effects the working temperature of polymers is the glass transition temperature (T_g). T_g is the temperature at which a polymer goes from a glassy solid to a viscoelastic

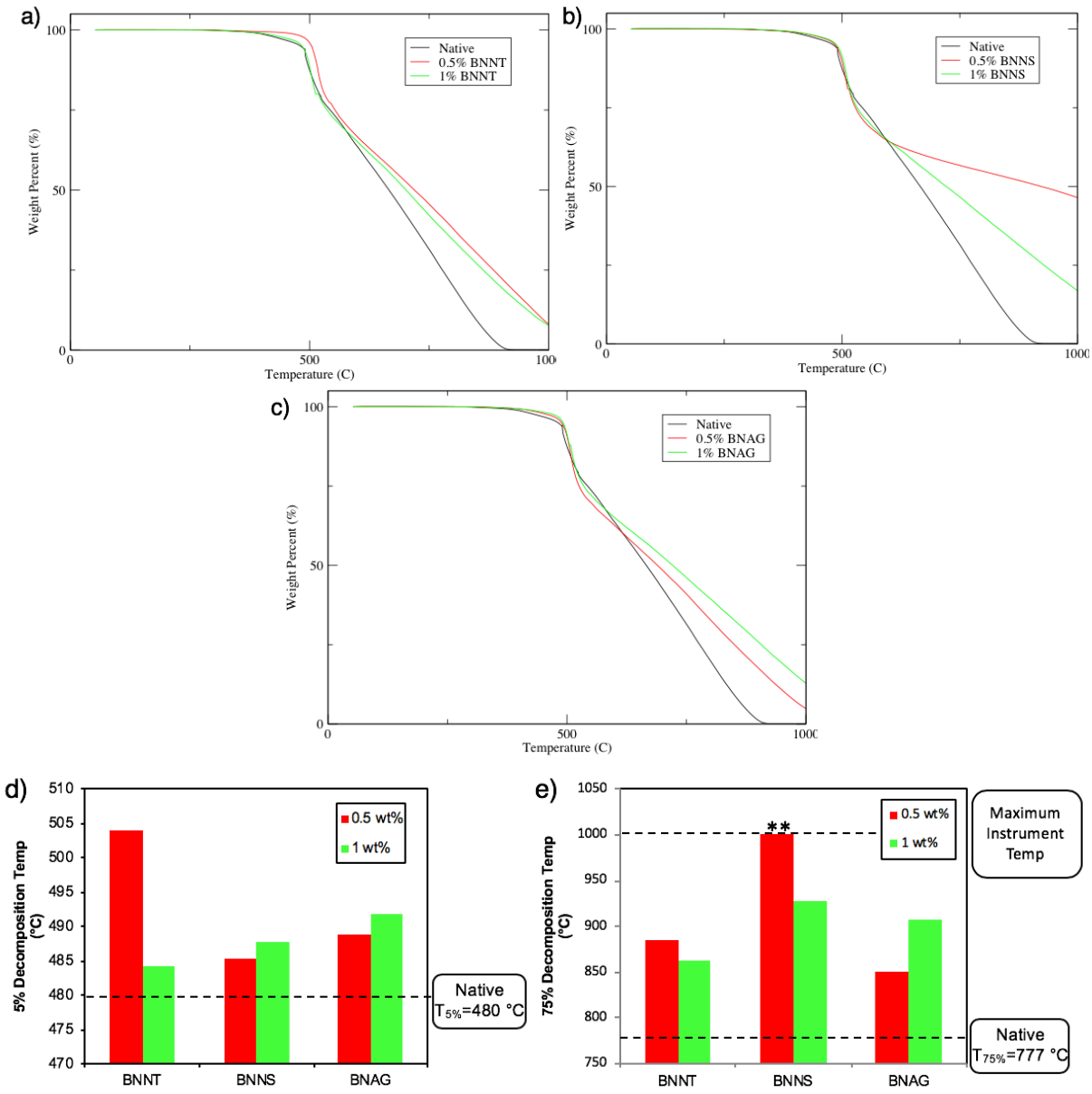

Figure 8.5 a-c) TGA plots of BNNTs, BNNSs, and BNAG polyimide composites. $T_{5\%}$ and $T_{75\%}$ are extracted and plotted in (d,e) to show changes with respective to the native polyimide represented by the dashed line.

fluid and increases when polymer chains are less mobile. Thus, introducing a mechanically strong BN nanofiller may restrict the mobility of the polymer chains and increase T_g thus allowing the polymer to function in higher temperature environments. Using differential scanning calorimetry (DSC) in collaboration with Ting Xu's group at UC Berkeley, T_g is measured. A typical DSC curve of native PI is shown in **Figure 8.6a**. The heat flow of the sample is measured as a function of temperature. At 172.3ºC there is a change in the heat flow behavior as a result of the heat capacity changing when the sample goes from a glassy solid to a viscoelastic fluid upon heating. The T_g's of BN nanocomposites are shown in **Figure 8.6b**. Compared to the native polymer, an increase in T_g is observed for all nanofillers and all concentrations indicating that the nanofiller is in fact restricting the mobility of the polymer chains in the composite. The same trend is observed in T_g as seen with $T_{75\%}$ where BNNTs and BNNSs have a larger T_g enhancement at 0.5 wt%

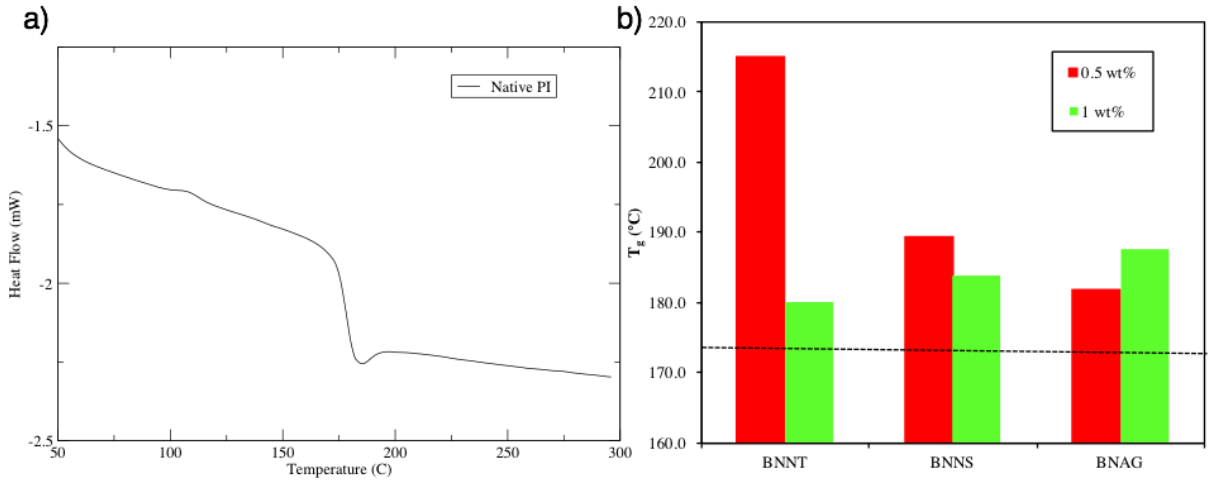

Figure 8.6 a) Representative DSC plot showing the glass transition temperature taking place at 173°C when the material goes from a solid to a viscoelastic fluid. B) T_g of BNNT, BNNS, and BN aerogel composites showing the change in T_g with BN nanofiller loading relative to the T_g of control PI (dashed line).

loading than at 1wt%. Conversely, BN aerogels have increased T_g with increased aerogel loading. Once again this is a consequence of the difference in dispersion between the two groups. Increased addition of BNNTs or BNNSs simply leads to large aggregates of BN nanofiller that less effectively restrict the mobility of the polymer chains, while BN aerogels are infiltrated with polymer as oppose to forming noninteracting aggregates.

The results of the thermal stability and T_g of BN/polyimide nanocomposites indicate that aggregation and lack of interfacial interactions between BN and polyimide hinder BN's ability to impart its thermal properties to those of the composite. This is the case most dramatically for BNNTs and BNNSs.

8.3 H_2O_2 Functionalization of BNNS, BNNT, BNAG

Morphological characterization and thermal studies described in **Section 8.2** indicate that the $\pi - \pi$ interactions between BN nanofillers and the polyimide matrix are insufficient for dispersion and the agglomeration is detrimental to the performance of the polymers. This effect is also seen when modelling mechanical reinforcement and thermal enhancement in polymer nanocomposites[223]. The strength of the composite can be modeled as shown in **Equation 8.1** and it is evident that the interaction strength, τ, is an important requisite for mechanical reinforcement.

$$\sigma_C = \left(\tau \times \frac{l}{D} - \sigma_m\right) V_f + \sigma_m \qquad \textbf{Equation 8.1}$$

Where σ_C is the strength of the composite, τ is the interaction strength, $\frac{l}{D}$ is the aspect ratio of the filler, V_f is the loading fraction of the filler and σ_m is the strength of the polymer matrix.

Additionally, thermal enhancement is modelled according to **Equation 8.2:**

$$k_c = k_f \times \emptyset_f + k_p \times \emptyset_p \qquad \textbf{Equation 8.2}$$

Where k_c, k_f, and k_p are the thermal conductivities of the composite, filler, and polymer, and $\emptyset_f$ and $\emptyset_p$ are the volume fractions of the filler and polymer, respectively.

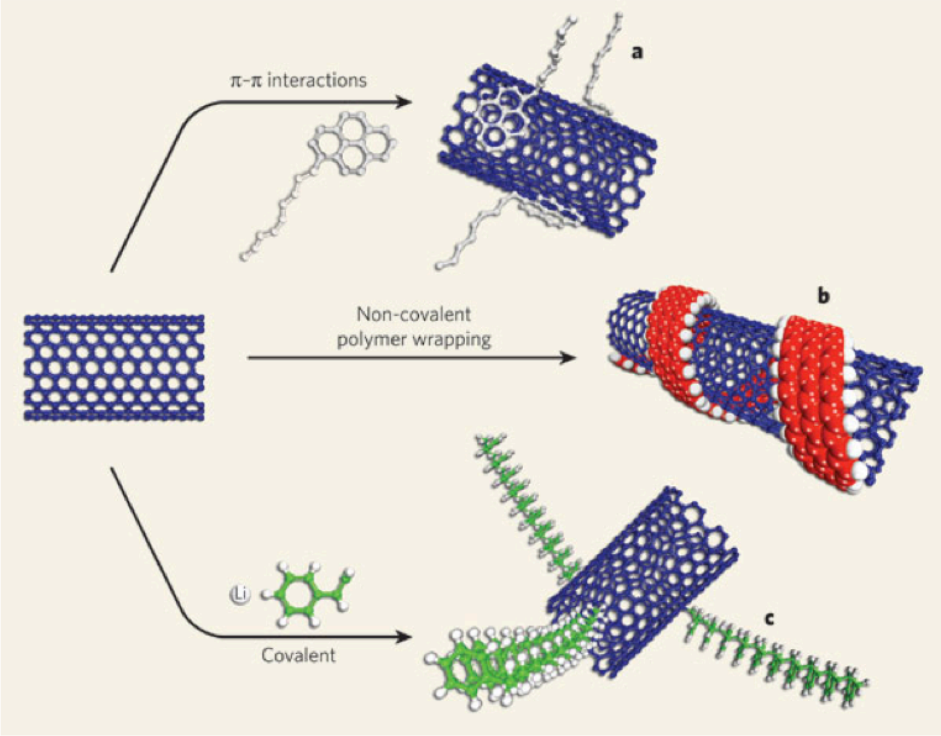

Figure 8.7 Three approaches to surface modifications of the surface of BN include non-covalent functionalization via π-π stacking, polymer wrapping, or covalent functionalization[261].

This thermal conductivity equation represents the maximum potential thermal conductivity due to the assumption that each filler particle is fully dispersed, thus agglomeration of filler particles will hinder the thermal enhancement.

From the glass transition and thermal stability trends as well as the relations for thermal and mechanical enhancement, it is evident that for optimal properties improved interfacial interactions and dispersion are necessary. This can be accomplished by modifying the BN nanofiller surface.

There are three approaches to modifying the surface which are shown in **Figure 8.7.** These include non-covalent functionalization by $\pi - \pi$ stacking using a molecule with an aromatic head group that can interact with BN and a tail group that will interact with the polymer, or polymer wrapping with a helical polymer via $\pi - \pi$ interactions. The third method is covalent functionalization of the surface of the BN. Covalent functionalization will result in a stronger interfacial interaction with polyimide and the functionalization can even be tailored such that it will covalently bond with polyimide and participate in the polymerization. Thus, covalent functionalization is selected as the route to modify the surface of BN nanofillers.

One of BN's remarkable properties is that it is chemically inert. While this is a beneficial property for many applications, it makes functionalization of BN extremely difficult and requires extreme environments. There have been few reports that functionalize BN nanomaterials using precursors that generate radical intermediates, or using ammonia plasmas[224–230]. However, there is no report of a functionalization that is successful on BNNTs, BNNSs, and BN aerogels. In fact, there is no publication of covalent functionalization of BN aerogels at all.

In order to covalently functionalize BNNTs, BNNSs, and BN aerogels with hydroxyl moieties, a hydrogen peroxide method is adopted as shown in **Figure 8.8a-c**. This synthesis was first developed by Zhi et al. using simply high temperatures. Kris Erickson further improved this

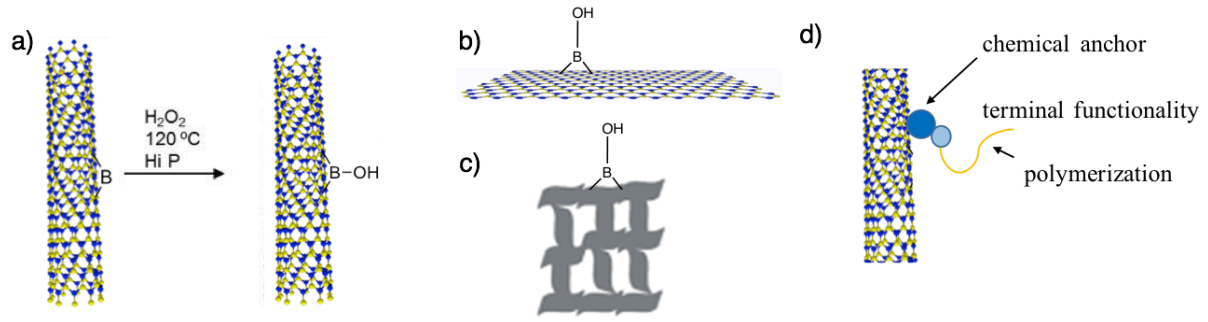

Figure 8.8 Hydrogen peroxide functionalization of a) BNNTs b) BNNSs and c) BN aerogels using high pressure and high temperature to hydroxylate a small portion of the BN surface d) Improved interfacial interactions between BN nanofiller and polymer by introducing a chemical anchor that is active for further derivatization and attached a terminal functionality which can participate in polymerization.

method using high pressure to functionalize BNNTs, and in this section the expansion of the functionalization method to include BNNSs and BN aerogels is accomplished[231,232].

A 10mL suspension of 20mg/mL BNNTs, BNNSs or BN aerogels are sonicated in isopropanol in order to debundle and disperse the BN nanomaterial in the solvent. The solution is loaded into a Teflon autoclave and isopropanol is evaporated at 50ºC under vacuum leaving behind a thin layer of BN nanomaterial stuck onto the walls of the Teflon beaker. Then 10mL of 15% hydrogen peroxide (H_2O_2) is added and the autoclave is sealed. Hydrogen peroxide will decompose into water and oxygen through hydroxyl radical intermediates which are vital for functionalization. This creates a high pressure environment which is thought to be important for functionalization but can also pose a safety concern. Thus, care must be taken that the pressure generated from hydrogen peroxide decomposition will not exceed the maximum operating pressure of the autoclave.

Once the BN nanomaterial is functionalized with hydroxyl functionalities, these sites are active for further derivatization and moieties that are important for interactions with the host polymer matrix can be incorporated. For example, a terminal amine can be used which can actually participate in polymerization during the synthesis of polyimide. This is one of the benefits of incorporating the BN nanofiller during the polymer synthesis. When a BN nanofiller with an amine

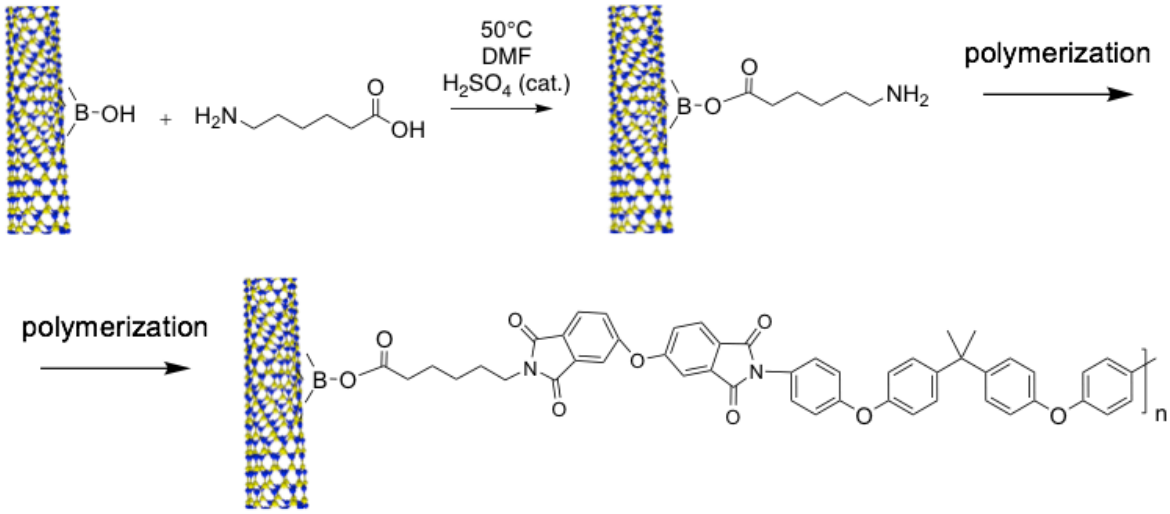

Figure 8.9 Fischer esterification between hydroxylated BN nanofiller and 4-aminocaproic acid yields a terminal amine which can participate in polymerization and covalently bond BN nanofiller to polymer.

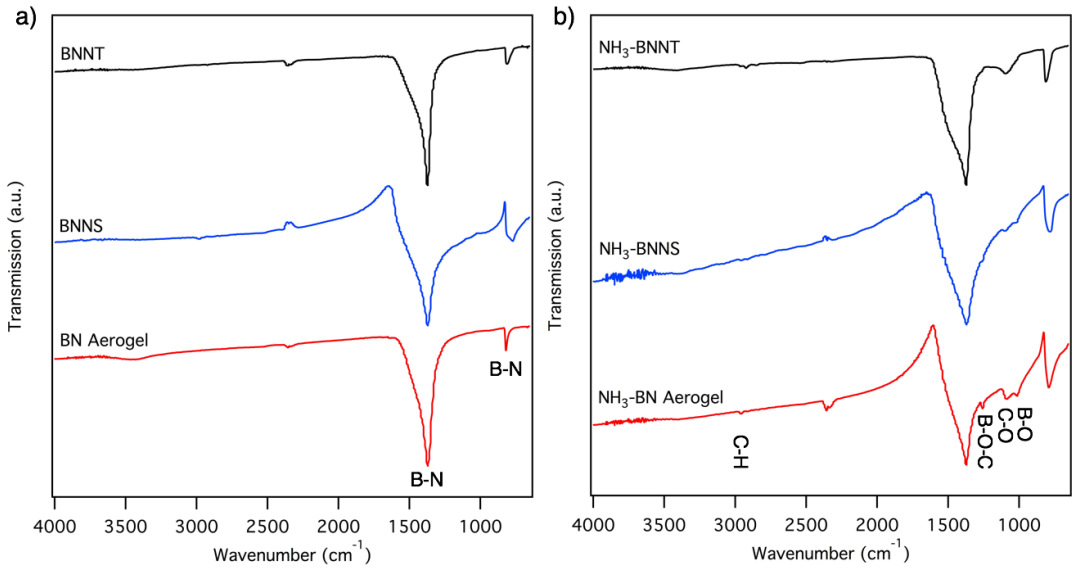

Figure 8.10 a) FTIR spectra of pristine BNNTs, BNNSs, and BN aerogels and b) FTIR spectra after covalent functionalization with a terminal amine functionality.

terminal functionality is added into the reaction with the diamine and dianhydride. It will react with the dianhydrides and forms a covalent bond between the nanofiller and the polyimide. This enables excellent interfacial interactions possible and maximizing dispersion of BN nanofiller within the polymer matrix.

This model can be incorporated into other polymeric systems as well as shown in **Figure 8.8d**. It relies on the chemical anchor which is the hydroxyl functionality, a terminal functionality which can participate in the polymerization, and a covalent bond to the polymer which forms during polymerization. A terminal amine is incorporated into the BN nanofiller using 6-amino hexanoic acid (**Figure 8.9)**. This Fischer esterification uses a sulfuric acid catalyst. Hydroxylated BN nanomaterial is much more readily suspendable in solvent and a 20mg/mL suspension in DMF is sonicated until full dispersion. 6-amino hexanoic acid is added with a catalytic amount of sulfuric acid and allowed to react for 24hrs at 50ºC with intermittent sonication. During the reaction, the carboxylic acid reacts with the hydroxyl group to form a boronate ester linkage and the terminal amine will participate in the polymerization during the growth of the polyimide.

The functionalization is confirmed using FTIR. **Figure 8.10a** shows the FTIR spectra of unfunctionalized BN nanomaterial and **Figure 8.10b** shows their spectra after functionalization. BN has two characteristic vibrations around 1370 cm^{-1} and 815cm^{-1} which are present prior to functionalization and persist after the reaction. A number of additional peaks emerge after the reaction which are indicative of covalent functionalization. Peaks at 1260, 1090 and 1080 cm^{-1} are present corresponding to B-O-C, C-O, and B-O stretching, respectively, indicating the formation of a boronate ester linkage. Additionally weak peaks at 2960 and 2930 cm^{-1} are observed due to C-H vibrations confirming the presents of alkyl groups on the surface. These results confirm the successful synthesis of amine terminated BNNTs, BNNSs, and BN aerogels which can be covalently incorporated into the polyimide matrix for maximal dispersion and interfacial interactions.

8.4 Drawbacks to H_2O_2 Functionalization

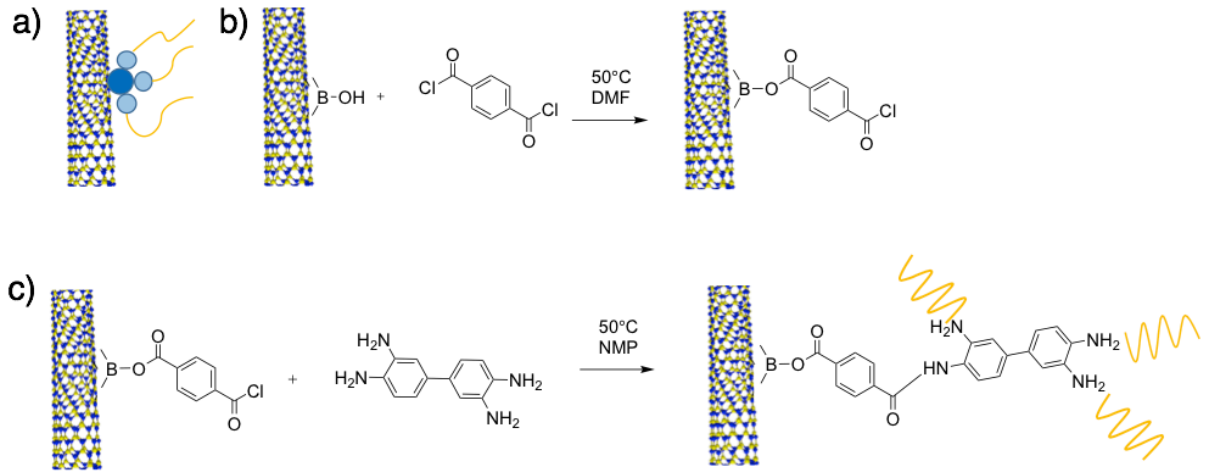

Figure 8.11 a) In order to preserve the intrinsic properties of the BN nanofiller, multiple terminal functionalities that participate in polymerization per chemical anchor can be incorporate. One example of this is b) Attachment of a terminal acyl chloride which will react with c) 4,4'-diaminobenzidine to for a nanofiller with three terminal amines to participate in polymerization per chemical anchor.

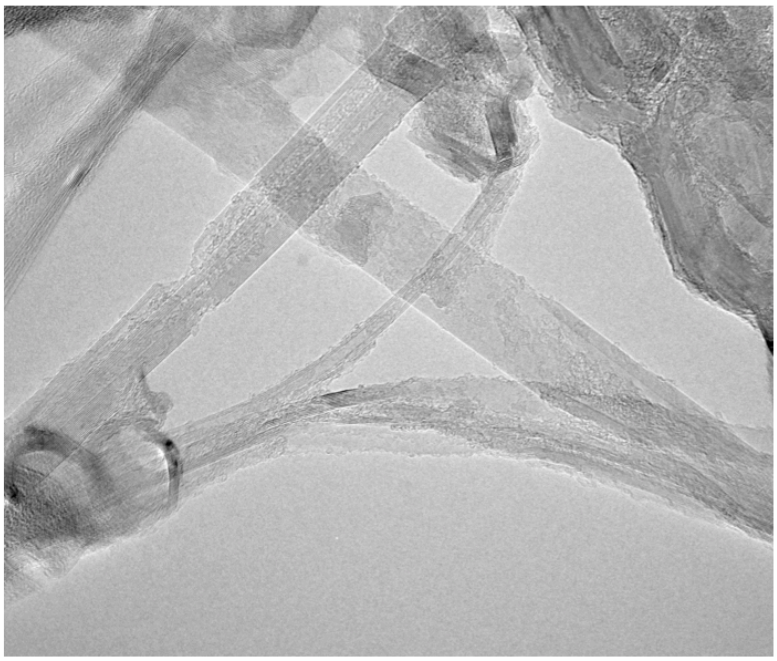

Figure 8.12 TEM image of BNNTs after H_2O_2 functionalization showing the enormous damage that occurs during the process. The nanotube walls are chewed up and one nanotube is completely unraveled into a nanooribbon. In collaboration with Brian Shevitki.

While covalent functionalization is the most attractive option for modifying the surface of BN, it is also important to take into account the impact that functionalization has on the intrinsic properties of the nanomaterial. BN nanomaterials have excellent mechanical properties due to the strong in-plane sp^2 bonds that make up the hexagonal structure. When a site is covalently functionalized, an sp^2 bond is broken and weaker sp^3 bonds are formed. This will potentially detrimentally affect the mechanical properties of the BN nanofiller. Additionally, the high thermal conductivity of BN nanomaterials is due to excellent conduction of phonons. The sp^3 bonds formed after covalent functionalization can serve as scattering sites of phonons and decrease the thermal conductivity. With this in mind, one approach to minimally impact the intrinsic properties of the

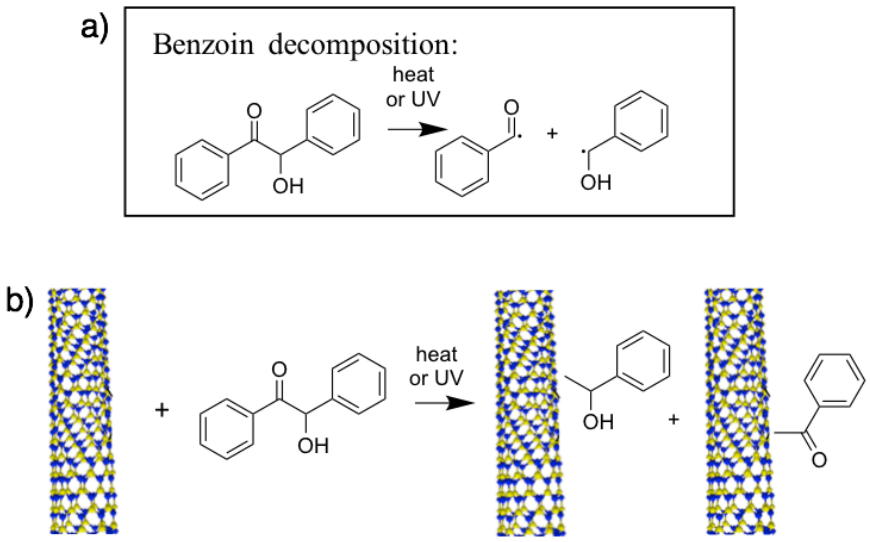

Figure 8.13 a) Benzoin decomposition to it corresponding radicals upon heating or exposure to UV light. This phenomenon is exploited by b) generating benzoin radicals in the present of BNNTs to functionalize the surface under mild conditions.

BN nanofiller due to functionalization is to maximize the number of contacts per functional group. As opposed to using the hydroxyl chemical anchor to attach one terminal functionality, one could attach a moiety with multiple terminal functionalities which can participate in polymerization (**Figure 8.11a).** For example, benzoyl chloride can be attached and the terminal acyl chloride can form an amide using 3,3'-diaminobenzidine leaving three terminal amine functionalities per sp^3 site (**Figure 8.11b)**. This allows minimal damage to the BN framework and maximizes the interfacial interactions with the polymer.

Another major drawback specifically to using hydrogen peroxide is the amount of damage that is done to the nanomaterial during the reaction. The high pressure and oxidative environment that is created in the autoclave not only functionalizes the surface, but also does tremendous damage. **Figure 8.12** shows a TEM image of a BNNT after H_2O_2 treatment and shows the damage that occurs as a result. The nanotube walls have been partially eaten away as a result of the treatment and some BNNTs are completely unraveled to form nanoribbon. In light of the damage that occurs, a more mild and gentler treatment which results in covalent functionalization is necessary.

8.5 Benzoin Functionalization

Methods which have proven successful in functionalizing BN nanomaterials have relied on radical intermediates which attack the unoccupied p orbital on boron. In order to pursue a gentler treatment, a compound which generates radicals under mild conditions is sought. In 2017, Cui et al. used the decomposition of benzoin into its corresponding radicals in the synthesis of copper nanowires[233]. This novel utilization of benzoin decomposition inspired the use of benzoin as a functionalization agent for BNNTs.

As shown in **Figure 8.13,** in an inert atmosphere and under heating or exposure to UV light, benzoin forms radicals. Radicals generated in the presence of BNNTs can proceed to functionalize the surface. A suspension of BNNTs and benzoin in anhydrous ethanol is prepared and refluxed at 80°C in an inert atmosphere to functionalize the surface. The IR spectrum of pristine BNNTs and functionalized BNNTs are shown in **Figure 8.14** and a number of peaks emerge after functionalization. Peaks at 2960, 2930, and 2850 cm^{-1} corresponding to C-H vibrations are observed. Additionally peaks at 1100 and 1020 cm^{-1} emerge which are due to B-C

and C-O vibrations, respectively. Peaks corresponding to BN are still present at 1340 and 787 cm^{-1}. These vibrations are shifted from their 1350 and 804 cm^{-1} positions in raw BNNTs, indicating a change in the vibrational properties as a result of functionalization. It is currently unclear which radical intermediate is involved in functionalization or if both functionalize the surface and further studies using XPS and NMR are necessary to fully characterize the system.

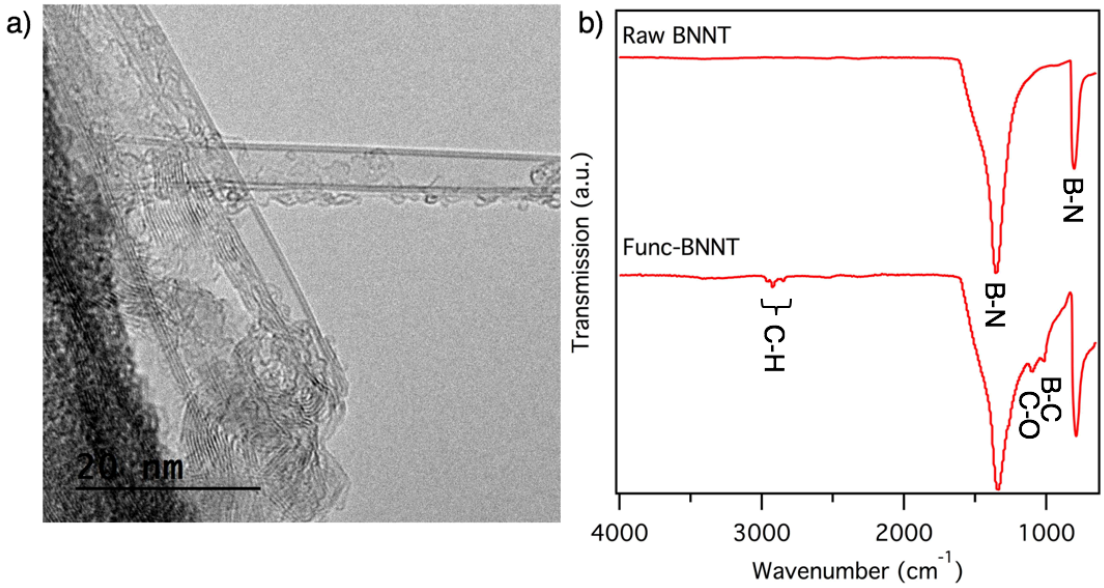

Figure 8.14 a) TEM image of benzoin functionalized BNNT that is intact and exemplifies the gentler functionalization treatment b) FTIR of raw BNNTs and benzoin functionalized BNNTs.

Using benzoin as a radical generating species, covalent functionalization of BNNTs is verified. Further studies will be necessary to verify this approach is capable of functionalizing BNNSs and BN aerogels. BNNTs are known to be more reactive than BNNSs due to the additional bond strain from the curvature. Despite this, no high temperatures, heavily oxidative conditions, or high pressures are necessary in this method making is an improved approach over harsh hydrogen peroxide treatment. These functionalized BNNTs can be further derivatized in order to incorporate multiple terminal amines per sp^3 bond and maintain the desirable properties of the BN nanofiller.

Chapter 9: Conclusion and Future Outlook

Throughout this dissertation a number of modifications to graphene and BN aerogels have been demonstrated which are capable of enhancing and tailoring their properties for targeted applications. A modification approach can be employed during the synthesis of graphene aerogels to alter the gelation chemistry and yield boron carbon nitride aerogels, which are predicted to have band gaps intermediate between graphene and BN (**Chapter 4)** and is also capable of physically modifying graphene and BN aerogels by tuning their densities and thus tuning their thermal and electrical properties (**Chapter 6)**. Additionally, post-synthetic chemical modification of aerogels is capable of introducing additional functionality into graphene aerogels by the formation of g-C_3N_4-graphene aerogel core-shell hybrid structures (**Chapter 5)**, as well as boron doped and defect-engineered graphene aerogels (**Chapter 3)**. Post-synthetic modification in the form of covalent functionalization of BN aerogels and related nanostructures was also demonstrated which is particularly useful for polymer composite applications (**Chapter 8)**. Furthermore, a new route to an important class of aerogels based on 1D nanomaterials is discovered which yields both semiconducting organic aerogels and conductive graphitic aerogels based on 1D nanofibers (**Chapter 7)**.

Through the research in this dissertation and the work of others, it is clear that huge benefits can occur through the coupling of graphene to other functional materials to form hybrid or composite materials[234,235]. The performance in a variety of applications is benefited from the synergistic effects between the two active materials and future work should be dedicated to developing new hybrid structures and exploration of their properties.

The field of nanomaterials is rapidly growing, with new classes of nanomaterials constantly being discovered. It is important that methods be explored to incorporate these new nanomaterials into high surface area aerogels in order to couple the intrinsic properties of the nanomaterial with the textural properties of the aerogel. This requires a deep understanding of the surface functionalities of the nanomaterials in order to induce gelation and chemical crosslinking.

One rapidly expanding new class of materials first synthesized in 2011 are the family of 2D transition metal carbides or nitrides called MXenes[236]. MXenes have been synthesized with a variety of compositions and have a general formula $M_{n-1}X_nT_x$ (n=1-3) where M is the transition metal, X is carbon or nitrogen, and T is the surface termination. These 2D nanomaterials are made by selective etching of their layered precursors resulting in -OH, and -F terminations. The most widely studied MXene is $Ti_3C_2T_x$, whose structure is shown in **Figure 9.1**. $Ti_3C_2T_x$ has a layered structure, exhibits metallic conductivity, and possesses a small band gap as well as excellent mechanical properties. One critical property of MXenes is the hydrophilicity of the material due to the abundance of surface functional groups making them suspendable in water, which is one of the key difficulties in other 2D materials. These properties have led MXenes to be integrated into a number of applications including batteries, supercapacitors, and sensors[237–243]. To date, most

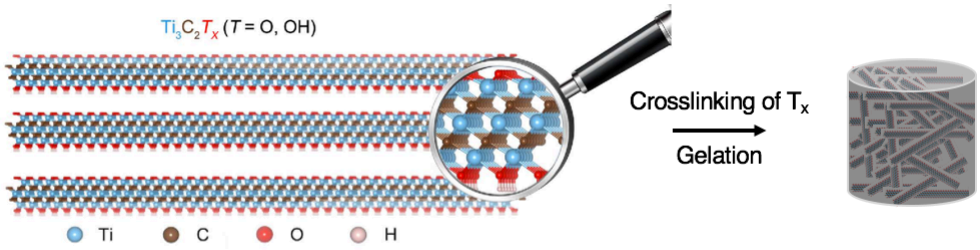

Figure 9.1 Layered structure of the MXene $Ti_3C_2T_x$ showing the basal plane which has metallic conductivity and surface terminations which make the material hydrophilic[245] .

studied have been performed on MXene films prepared by filtering colloidal suspensions of exfoliated MXenes and these materials have performed well. However, a high surface area and porous MXene aerogel material is expected to have improved performance due to enhanced mass diffusion and large area available for surface reactions and charge storage. Recently, MXene suspensions have been freeze-dried to yield porous 3D MXenes with low surface areas which are capable of capacitive water deionization and electromagnetic interference shielding[244,245]. However, to make a higher surface area and more mechanically robust MXene aerogel with more intimate electrical connections, chemical crosslinking is necessary. In the future, a method to chemically crosslink MXenes and undergo a sol-gel transition will likely play a pivotal role in optimizing MXene performance and will be useful in a number of applications. Additionally, interfacing MXenes and graphene into an aerogel morphology is a compelling route which is more readily accessible due to graphene's well understood sol-gel chemistry. As new classes of nanomaterials are synthesized and their extraordinary properties studied, it will continue to be of great importance to develop methods to induce gelation and integrate them into aerogel morphologies.

References

(1) Mermin, N. D. Crystalline Order in Two Dimensions. *Phys. Rev.* **1968**, *176* (1), 250–254.
(2) Wallace, P. R. The Band Theory of Graphite. *Phys. Rev.* **1947**, *71* (9), 622–634.
(3) Dresselhaus, M. S.; Dresselhaus, G. Intercalation Compounds of Graphite. *Adv. Phys.* **2002**, *51* (1), 1–186.
(4) Claire Berger, ; Zhimin Song; Tianbo Li; Xuebin Li; Asmerom Y. Ogbazghi; Rui Feng; Zhenting Dai; Alexei N. Marchenkov; Edward H. Conrad; Phillip N. First, and; et al. Ultrathin Epitaxial Graphite: 2D Electron Gas Properties and a Route toward Graphene-Based Nanoelectronics. **2004**.
(5) Gilbert, S. M.; Pham, T.; Dogan, M.; Oh, S.; Shevitski, B.; Schumm, G.; Liu, S.; Ercius, P.; Aloni, S.; Cohen, M. L.; et al. Alternative Stacking Sequences in Hexagonal Boron Nitride. **2019**.
(6) Novoselov, K. S.; Geim, A. K.; Morozov, S. V; Jiang, D.; Zhang, Y.; Dubonos, S. V; Grigorieva, I. V; Firsov, A. A. Electric Field Effect in Atomically Thin Carbon Films. *Science* **2004**, *306* (5696), 666–669.
(7) Novoselov, K. S.; Jiang, D.; Schedin, F.; Booth, T. J.; Khotkevich, V. V; Morozov, S. V; Geim, A. K. Two-Dimensional Atomic Crystals. *Proc. Natl. Acad. Sci. U. S. A.* **2005**, *102* (30), 10451–10453.
(8) Coleman, J. N.; Lotya, M.; O'neill, A.; Bergin, S. D.; King, P. J.; Khan, U.; Young, K.; Gaucher, A.; De, S.; Smith, R. J.; et al. *Two-Dimensional Nanosheets Produced by Liquid Exfoliation of Layered Materials*.
(9) Zhang, Y.; Zhang, L.; Zhou, C. Review of Chemical Vapor Deposition of Graphene and Related Applications. *Acc. Chem. Res.* **2013**, *46* (10), 2329–2339.
(10) Reina, A.; Jia, X.; Ho, J.; Nezich, D.; Son, H.; Bulovic, V.; Dresselhaus, M. S.; Kong, J. Large Area, Few-Layer Graphene Films on Arbitrary Substrates by Chemical Vapor Deposition. *Nano Lett.* **2009**, *9* (1), 30–35.
(11) Kim, K. K.; Hsu, A.; Jia, X.; Kim, S. M.; Shi, Y.; Hofmann, M.; Nezich, D.; Rodriguez-Nieva, J. F.; Dresselhaus, M.; Palacios, T.; et al. Synthesis of Monolayer Hexagonal Boron Nitride on Cu Foil Using Chemical Vapor Deposition. *Nano Lett.* **2012**, *12* (1), 161–166.
(12) Shi, Y.; Hamsen, C.; Jia, X.; Kim, K. K.; Reina, A.; Hofmann, M.; Hsu, A. L.; Zhang, K.; Li, H.; Juang, Z.-Y.; et al. Synthesis of Few-Layer Hexagonal Boron Nitride Thin Film by Chemical Vapor Deposition. *Nano Lett.* **2010**, *10* (10), 4134–4139.
(13) Blase, X.; Rubio, A.; Louie, S. G.; Cohen, M. L. *Stability and Band Gap Constancy of Boron Nitride Nanotubes*; 1994; Vol. 28.
(14) Novoselov, K. S.; Geim, A. K.; Morozov, S. V.; Jiang, D.; Katsnelson, M. I.; Grigorieva, I. V.; Dubonos, S. V.; Firsov, A. A. Two-Dimensional Gas of Massless Dirac Fermions in Graphene. *Nature* **2005**, *438* (7065), 197–200.
(15) Novoselov, K. S.; Geim, A. K.; Morozov, S. V; Jiang, D.; Zhang, Y.; Dubonos, S. V; Grigorieva, I. V; Firsov, A. A. Electric Field Effect in Atomically Thin Carbon Films. *Science* **2004**, *306* (5696), 666–669.
(16) Secor, E. B.; Lim, S.; Zhang, H.; Frisbie, C. D.; Francis, L. F.; Hersam, M. C. Gravure Printing of Graphene for Large-Area Flexible Electronics. *Adv. Mater.* **2014**, *26* (26), 4533–4538.
(17) El-Kady, M. F.; Strong, V.; Dubin, S.; Kaner, R. B. Laser Scribing of High-Performance and Flexible Graphene-Based Electrochemical Capacitors. *Science* **2012**, *335* (6074), 1326–1330.
(18) Georgiou, T.; Jalil, R.; Belle, B. D.; Britnell, L.; Gorbachev, R. V; Morozov, S. V; Kim, Y.-

J.; Gholinia, A.; Haigh, S. J.; Makarovsky, O.; et al. *Vertical Field Effect Transistor Based on Graphene-WS 2 Heterostructures for Flexible and Transparent Electronics*.
(19) Cui, Z.; Martinez, A. P.; Adamson, D. H. PMMA Functionalized Boron Nitride Sheets as Nanofillers. *Nanoscale* **2015**, *7* (22), 10193–10197.
(20) Tran, T. T.; Bray, K.; Ford, M. J.; Toth, M.; Aharonovich, I. *Quantum Emission From Hexagonal Boron Nitride Monolayers*; 2015.
(21) Oku, T.; Narita, I. Calculation of H2 Gas Storage for Boron Nitride and Carbon Nanotubes Studied from the Cluster Calculation. *Phys. B Condens. Matter* **2002**, *323* (1–4), 216–218.
(22) Chang, C. W.; Fennimore, A. M.; Afanasiev, A.; Okawa, D.; Ikuno, T.; Garcia, H.; Li, D.; Majumdar, A.; Zettl, A. Isotope Effect on the Thermal Conductivity of Boron Nitride Nanotubes. *Phys. Rev. Lett.* **2006**, *97* (8), 085901.
(23) Kroto, H. W.; Heath, J. R.; O'Brien, S. C.; Curl, R. F.; Smalley, R. E. C60: Buckminsterfullerene. *Nature* **1985**, *318* (6042), 162–163.
(24) Iijima, S. Helical Microtubules of Graphitic Carbon. *Nature* **1991**, *354* (6348), 56–58.
(25) Iijima, S.; Ichihashi, T. Single-Shell Carbon Nanotubes of 1-Nm Diameter. *Nature* **1993**, *363* (6430), 603–605.
(26) Saito, R.; Fujita, M.; Dresselhaus, G.; Dresselhaus, M. S. Electronic Structure of Graphene Tubules Based on C 60. *Phys. Rev. B* **1992**, *46* (3), 1804–1811.
(27) Saito, R.; Fujita, M.; Dresselhaus, G.; Dresselhaus, M. S. Electronic Structure of Chiral Graphene Tubules. *Appl. Phys. Lett.* **1992**, *60* (18), 2204–2206.
(28) Kosynkin, D. V.; Lu, W.; Sinitskii, A.; Pera, G.; Sun, Z.; Tour, J. M. Highly Conductive Graphene Nanoribbons by Longitudinal Splitting of Carbon Nanotubes Using Potassium Vapor. *ACS Nano* **2011**, *5* (2), 968–974.
(29) Cai, J.; Ruffieux, P.; Jaafar, R.; Bieri, M.; Braun, T.; Blankenburg, S.; Muoth, M.; Seitsonen, A. P.; Saleh, M.; Feng, X.; et al. Atomically Precise Bottom-up Fabrication of Graphene Nanoribbons. *Nature* **2010**, *466* (7305), 470–473.
(30) Rubio, A.; Corkill, J. L.; Cohen, M. L. Theory of Graphitic Boron Nitride Nanotubes. *Phys. Rev. B* **1994**, *49* (7), 5081–5084.
(31) Chopra, N. G.; Luyken, R. J.; Cherrey, K.; Crespi, V. H.; Cohen, M. L.; Louie, S. G.; Zettl, A. Boron Nitride Nanotubes. *Science (80-.).* **1995**, *269* (5226), 966–967.
(32) Fathalizadeh, A.; Pham, T.; Mickelson, W.; Zettl, A. Scaled Synthesis of Boron Nitride Nanotubes, Nanoribbons, and Nanococoons Using Direct Feedstock Injection into an Extended-Pressure, Inductively-Coupled Thermal Plasma. *Nano Lett.* **2014**, *14* (8), 4881–4886.
(33) Kim, K. S.; Kingston, C. T.; Hrdina, A.; Jakubinek, M. B.; Guan, J.; Plunkett, M.; Simard, B. Hydrogen-Catalyzed, Pilot-Scale Production of Small-Diameter Boron Nitride Nanotubes and Their Macroscopic Assemblies. *ACS Nano* **2014**, *8* (6), 6211–6220.
(34) Erickson, K. J.; Gibb, A. L.; Sinitskii, A.; Rousseas, M.; Alem, N.; Tour, J. M.; Zettl, A. K. Longitudinal Splitting of Boron Nitride Nanotubes for the Facile Synthesis of High Quality Boron Nitride Nanoribbons. *Nano Lett* **2011**, *11*, 3221–3226.
(35) Kistler, S. S. Coherent Expanded Aerogels and Jellies. *Nature* **1931**, *127* (3211), 741–741.
(36) Graham, G. A.; Grant, P. G.; Chater, R. J.; Westphal, A. J.; Kearsley, A. T.; Snead, C.; Domínguez, G.; Butterworth, A. L.; Mcphail, D. S.; Bench, G.; et al. Investigation of Ion Beam Techniques for the Analysis and Exposure of Particles Encapsulated by Silica Aerogel: Applicability for Stardust. *Meteorit. Planet. Sci.* **2004**, *39* (9), 1461–1473.
(37) Pekala, R. W. Organic Aerogels from the Polycondensation of Resorcinol with Formaldehyde. *J. Mater. Sci.* **1989**, *24* (9), 3221–3227.
(38) Guo, H.; Meador, M. A. B.; McCorkle, L.; Quade, D. J.; Guo, J.; Hamilton, B.; Cakmak,

M. Tailoring Properties of Cross-Linked Polyimide Aerogels for Better Moisture Resistance, Flexibility, and Strength. *ACS Appl. Mater. Interfaces* **2012**, *4* (10), 5422–5429.
(39) Benad, A.; Jürries, F.; Vetter, B.; Klemmed, B.; Hübner, R.; Leyens, C.; Eychmüller, A. Mechanical Properties of Metal Oxide Aerogels. *Chem. Mater.* **2018**, *30* (1), 145–152.
(40) Berestok, T.; Guardia, P.; Du, R.; Portals, J. B.; Colombo, M.; Estradé, S.; Peiró, F.; Brock, S. L.; Cabot, A. Metal Oxide Aerogels with Controlled Crystallinity and Faceting from the Epoxide-Driven Cross-Linking of Colloidal Nanocrystals. *ACS Appl. Mater. Interfaces* **2018**, *10* (18), 16041–16048.
(41) Jeffrey W. Long,; Michael S. Logan, ; Christopher P. Rhodes,; Everett E. Carpenter, ,; Rhonda M. Stroud, ‡ and; Debra R. Rolison*, †. Nanocrystalline Iron Oxide Aerogels as Mesoporous Magnetic Architectures. **2004**.
(42) Tang, Y.; Yeo, K. L.; Chen, Y.; Lim, A.; Yap, W.; Xiong, W.; Cheng, W. Ultralow-Density Copper Nanowire Aerogel Monoliths with Tunable Mechanical and Electrical Properties.
(43) and, I. U. A.; Brock*, S. L. Highly Luminescent Quantum-Dot Monoliths. **2007**.
(44) Nyström, G.; Fernández-Ronco, M. P.; Bolisetty, S.; Mazzotti, M.; Mezzenga, R. Amyloid Templated Gold Aerogels. *Adv. Mater.* **2016**, *28* (3), 472–478.
(45) Baumann, T. F.; Kucheyev, S. O.; Gash, A. E.; Satcher, J. H. Facile Synthesis of a Crystalline, High-Surface-Area SnO2 Aerogel. *Adv. Mater.* **2005**, *17* (12), 1546–1548.
(46) Meador, M. A. B.; Wright, S.; Sandberg, A.; Nguyen, B. N.; Van Keuls, F. W.; Mueller, C. H.; Rodríguez-Solís, R.; Miranda, F. A. Low Dielectric Polyimide Aerogels As Substrates for Lightweight Patch Antennas. *ACS Appl. Mater. Interfaces* **2012**, *4* (11), 6346–6353.
(47) Liu, W.; Herrmann, A.-K.; Bigall, N. C.; Rodriguez, P.; Wen, D.; Oezaslan, M.; Schmidt, T. J.; Gaponik, N.; Eychmüller, A. Noble Metal Aerogels—Synthesis, Characterization, and Application as Electrocatalysts. *Acc. Chem. Res.* **2015**, *48* (2), 154–162.
(48) Biener, J.; Stadermann, M.; Suss, M.; Worsley, M. A.; Biener, M. M.; Rose, K. A.; Baumann, T. F. Advanced Carbon Aerogels for Energy Applications. *Energy Environ. Sci.* **2011**, *4* (3), 656.
(49) Houria Kabbour, ; Theodore F. Baumann,; Joe H. Satcher, J.; Angelique Saulnier, and; Channing C. Ahn, . Toward New Candidates for Hydrogen Storage: High-Surface-Area Carbon Aerogels. **2006**.
(50) Cheng, W.; Rechberger, F.; Niederberger, M. Three-Dimensional Assembly of Yttrium Oxide Nanosheets into Luminescent Aerogel Monoliths with Outstanding Adsorption Properties. *ACS Nano* **2016**, *10* (2), 2467–2475.
(51) Chung, V.; Yip, M.-C.; Fang, W.; Chung, V. P. J. Resorcinol-Formaldehyde Aerogels for CMOS-MEMS Capacitive Humidity Sensor. *Artic. Sensors Actuators B Chem.* **2015**, *214*, 181–188.
(52) Biener, J.; Dasgupta, S.; Shao, L.; Wang, D.; Worsley, M. A.; Wittstock, A.; Lee, J. R. I.; Biener, M. M.; Orme, C. A.; Kucheyev, S. O.; et al. Macroscopic 3D Nanographene with Dynamically Tunable Bulk Properties. *Adv. Mater.* **2012**, *24* (37), 5083–5087.
(53) Worsley, M. A.; Olson, T. Y.; Lee, J. R. I.; Willey, T. M.; Nielsen, M. H.; Roberts, S. K.; Pauzauskie, P. J.; Biener, J.; Satcher, J. H.; Baumann, T. F. High Surface Area, Sp^2 -Cross-Linked Three-Dimensional Graphene Monoliths. *J. Phys. Chem. Lett.* **2011**, *2* (8), 921–925.
(54) Zhang, X.; Sui, Z.; Xu, B.; Yue, S.; Luo, Y.; Zhan, W.; Liu, B.; Lima, M. D.; Haque, M. H.; Gartstein, Y. N.; et al. Mechanically Strong and Highly Conductive Graphene Aerogel and Its Use as Electrodes for Electrochemical Power Sources. *J. Mater. Chem.* **2011**, *21* (18), 6494.
(55) Worsley, M. A.; Kucheyev, S. O.; Mason, H. E.; Merrill, M. D.; Mayer, B. P.; Lewicki, J.; Valdez, C. A.; Suss, M. E.; Stadermann, M.; Pauzauskie, P. J.; et al. Mechanically Robust

3D Graphene Macroassembly with High Surface Area. *Chem. Commun.* **2012**, *48* (67), 8428.
(56) Kris Erickson, B.; Erni, R.; Lee, Z.; Alem, N.; Gannett, W.; Zettl, A.; Erickson, K.; Alem, N.; Gannett, W.; Zettl, A.; et al. Determination of the Local Chemical Structure of Graphene Oxide and Reduced Graphene Oxide. **2010**.
(57) Worsley, M. A.; Charnvanichborikarn, S.; Montalvo, E.; Shin, S. J.; Tylski, E. D.; Lewicki, J. P.; Nelson, A. J.; Satcher, J. H.; Biener, J.; Baumann, T. F.; et al. Toward Macroscale, Isotropic Carbons with Graphene-Sheet-Like Electrical and Mechanical Properties. *Adv. Funct. Mater.* **2014**, *24* (27), 4259–4264.
(58) Worsley, M. A.; Pham, T. T.; Yan, A.; Shin, S. J.; Lee, J. R. I.; Bagge-Hansen, M.; Mickelson, W.; Zettl, A. Synthesis and Characterization of Highly Crystalline Graphene Aerogels. **1101**, *8* (10).
(59) Sing, K. S. W. Reporting Physisorption Data for Gas/Solid Systems with Special Reference to the Determination of Surface Area and Porosity (Recommendations 1984). *Pure Appl. Chem.* **1985**, *57* (4), 603–619.
(60) Brunauer, S.; Emmett, P. H.; Teller, E. Adsorption of Gases in Multimolecular Layers. *J. Am. Chem. Soc.* **1938**, *60* (2), 309–319.
(61) Hu, J.; Huang, Y.; Yao, Y.; Pan, G.; Sun, J.; Zeng, X.; Sun, R.; Xu, J.-B.; Song, B.; Wong, C.-P. Polymer Composite with Improved Thermal Conductivity by Constructing a Hierarchically Ordered Three-Dimensional Interconnected Network of BN. *ACS Appl. Mater. Interfaces* **2017**, *9* (15), 13544–13553.
(62) Pham, T.; Goldstein, A. P.; Lewicki, J. P.; Kucheyev, S. O.; Wang, C.; Russell, T. P.; Worsley, M. A.; Woo, L.; Mickelson, W.; Zettl, A. Nanoscale Structure and Superhydrophobicity of Sp 2-Bonded Boron Nitride Aerogels †. *Nanoscale* **2015**, *7*, 10449.
(63) Guo, H.; Zhang, W.; Lu, N.; Zhuo, Z.; Zeng, X. C.; Wu, X.; Yang, J. CO $_2$ Capture on *h* -BN Sheet with High Selectivity Controlled by External Electric Field. *J. Phys. Chem. C* **2015**, *119* (12), 6912–6917.
(64) Rousseas, M.; Goldstein, A.; Mickelson, W. Synthesis of Highly Crystalline Sp 2 -Bonded Boron Nitride Aerogels. *ACS Nano* **2013**, *7* (Suppl), 8540.
(65) Zhao, Y.; Yang, L.; Chen, S.; Wang, X.; Ma, Y.; Wu, Q.; Jiang, Y.; Qian, W.; Hu, Z. Can Boron and Nitrogen Co-Doping Improve Oxygen Reduction Reaction Activity of Carbon Nanotubes? *J. Am. Chem. Soc.* **2013**, *135* (4), 1201–1204.
(66) Gong, Y.; Fei, H.; Zou, X.; Zhou, W.; Yang, S.; Ye, G.; Liu, Z.; Peng, Z.; Lou, J.; Vajtai, R.; et al. Boron- and Nitrogen-Substituted Graphene Nanoribbons as Efficient Catalysts for Oxygen Reduction Reaction. *Chem. Mater.* **2015**, *27* (4), 1181–1186.
(67) Jiang, H. R.; Zhao, T. S.; Shi, L.; Tan, P.; An, L. First-Principles Study of Nitrogen-, Boron-Doped Graphene and Co-Doped Graphene as the Potential Catalysts in Nonaqueous Li–O $_2$ Batteries. *J. Phys. Chem. C* **2016**, *120* (12), 6612–6618.
(68) Panchakarla, L. S.; Subrahmanyam, K. S.; Saha, S. K.; Govindaraj, A.; Krishnamurthy, H. R.; Waghmare, U. V.; Rao, C. N. R. Synthesis, Structure, and Properties of Boron- and Nitrogen-Doped Graphene. *Adv. Mater.* **2009**, *21* (46), NA-NA.
(69) Qu, L.; Liu, Y.; Baek, J.-B.; Dai, L. Nitrogen-Doped Graphene as Efficient Metal-Free Electrocatalyst for Oxygen Reduction in Fuel Cells.
(70) Liu, Y.; Artyukhov, V. I.; Liu, M.; Harutyunyan, A. R.; Yakobson, B. I. Feasibility of Lithium Storage on Graphene and Its Derivatives. *J. Phys. Chem. Lett.* **2013**, *4* (10), 1737–1742.
(71) Ferrighi, L.; Datteo, M.; Di Valentin, C. Boosting Graphene Reactivity with Oxygen by Boron Doping: Density Functional Theory Modeling of the Reaction Path. *J. Phys. Chem.*

C **2014**, *118* (1), 223–230.
(72) Zhang, Y.-H.; Chen, Y.-B.; Zhou, K.-G.; Liu, C.-H.; Zeng, J.; Zhang, H.-L.; Peng, Y. Improving Gas Sensing Properties of Graphene by Introducing Dopants and Defects: A First-Principles Study. *Nanotechnology* **2009**, *20* (18), 185504.
(73) Zuo, Z.; Jiang, Z.; Manthiram, A. Porous B-Doped Graphene Inspired by Fried-Ice for Supercapacitors and Metal-Free Catalysts.
(74) Wang, Z.; Cao, X.; Ping, J.; Wang, Y.; Lin, T.; Huang, X.; Ma, Q.; Wang, F.; He, C.; Zhang, H.; et al. Electrochemical Doping of Three-Dimensional Graphene Networks Used as Efficient Electrocatalysts for Oxygen Reduction Reaction. *Nanoscale* **2015**, *7* (21), 9394–9398.
(75) Tai, J.; Hu, J.; Chen, Z.; Lu, H. Two-Step Synthesis of Boron and Nitrogen Co- Doped Graphene as a Synergistically Enhanced Catalyst for the Oxygen Reduction Reaction.
(76) Jin, J.; Pan, F.; Jiang, L.; Fu, X.; Liang, A.; Wei, Z.; Zhang, J.; Sun, G. Catalyst-Free Synthesis of Crumpled Boron and Nitrogen Co-Doped Graphite Layers with Tunable Bond Structure for Oxygen Reduction Reaction. *ACS Nano* **2014**, *8* (4), 3313–3321.
(77) Xie, Y.; Meng, Z.; Cai, T.; Han, W.-Q. Effect of Boron-Doping on the Graphene Aerogel Used as Cathode for the Lithium–Sulfur Battery. *ACS Appl. Mater. Interfaces* **2015**, *7* (45), 25202–25210.
(78) Zhang, H.; Lv, R. Defect Engineering of Two-Dimensional Materials for Efficient Electrocatalysis. *J. Mater.* **2018**, *4* (2), 95–107.
(79) Yadav, S.; Zhu, Z.; Singh, C. V. Defect Engineering of Graphene for Effective Hydrogen Storage. *Int. J. Hydrogen Energy* **2014**, *39* (10), 4981–4995.
(80) Schedin, F.; Geim, A. K.; Morozov, S. V.; Hill, E. W.; Blake, P.; Katsnelson, M. I.; Novoselov, K. S. Detection of Individual Gas Molecules Adsorbed on Graphene. *Nat. Mater.* **2007**, *6* (9), 652–655.
(81) T. O. Wehling,; K. S. Novoselov, ; S. V. Morozov, ; E. E. Vdovin, ; M. I. Katsnelson, ‖; A. K. Geim, and; Lichtenstein, A. I. Molecular Doping of Graphene. **2007**.
(82) Dai, J.; Yuan, J.; Giannozzi, P. Gas Adsorption on Graphene Doped with B, N, Al, and S: A Theoretical Study. *Appl. Phys. Lett.* **2009**, *95* (23), 232105.
(83) Liu, X.; Li, J.; Sun, J.; Zhang, X. 3D Fe $_3$ O $_4$ Nanoparticle/Graphene Aerogel for NO $_2$ Sensing at Room Temperature. *RSC Adv.* **2015**, *5* (90), 73699–73704.
(84) Long, H.; Harley-Trochimczyk, A.; Pham, T.; Tang, Z.; Shi, T.; Zettl, A.; Carraro, C.; Worsley, M. A.; Maboudian, R. High Surface Area MoS $_2$ /Graphene Hybrid Aerogel for Ultrasensitive NO $_2$ Detection. *Adv. Funct. Mater.* **2016**, *26* (28), 5158–5165.
(85) Turner, S.; Yan, W.; Long, H.; Nelson, A. J.; Baker, A.; Lee, J. R. I.; Carraro, C.; Worsley, M. A.; Maboudian, R.; Zettl, A. Boron Doping and Defect Engineering of Graphene Aerogels for Ultrasensitive NO $_2$ Detection. *J. Phys. Chem. C* **2018**, *122* (35), 20358–20365.
(86) Kim, Y. A.; Fujisawa, K.; Muramatsu, H.; Hayashi, T.; Endo, M.; Fujimori, T.; Kaneko, K.; Terrones, M.; Behrends, J.; Eckmann, A.; et al. Raman Spectroscopy of Boron-Doped Single-Layer Graphene. *ACS Nano* **2012**, *6* (7), 6293–6300.
(87) Yuge, K. Phase Stability of Boron Carbon Nitride in a Heterographene Structure: A First-Principles Study. *Phys. Rev. B* **2009**, *79* (14), 144109.
(88) Chen, J.; Shi, T.; Cai, T.; Xu, T.; Sun, L.; Wu, X.; Yu, D. Self Healing of Defected Graphene. *Appl. Phys. Lett. Raman Spectr. Graph. J. Chem. Phys.* **2013**, *102* (53), 103107–1126.
(89) Botari, T.; Paupitz, R.; Alves da Silva Autreto, P.; Galvao, D. S. Graphene Healing Mechanisms: A Theoretical Investigation. *Carbon N. Y.* **2016**, *99*, 302–309.
(90) McDougall, N. L.; Nicholls, R. J.; Partridge, J. G.; McCulloch, D. G. The Near Edge

Structure of Hexagonal Boron Nitride. *Microsc. Microanal.* **2014**, *20* (04), 1053–1059.
(91) Hanafusa, A.; Muramatsu, Y.; Kaburagi, Y.; Yoshida, A.; Hishiyama, Y.; Yang, W.; Denlinger, J. D.; Gullikson, E. M. Local Structure Analysis of Boron-Doped Graphite by Soft x-Ray Emission and Absorption Spectroscopy Using Synchrotron Radiation.
(92) Lv, R.; Chen, G.; Li, Q.; McCreary, A.; Botello-Méndez, A.; Morozov, S. V; Liang, L.; Declerck, X.; Perea-López, N.; Cullen, D. A.; et al. Ultrasensitive Gas Detection of Large-Area Boron-Doped Graphene. *Proc. Natl. Acad. Sci. U. S. A.* **2015**, *112* (47), 14527–14532.
(93) Epa, U.; of Air, O. *Air Quality Guide for Nitrogen Dioxide, EPA-456/F-11-003*.
(94) Harley-Trochimczyk, A.; Chang, J.; Zhou, Q.; Dong, J.; Pham, T.; Worsley, M. A.; Maboudian, R.; Zettl, A.; Mickelson, W. Catalytic Hydrogen Sensing Using Microheated Platinum Nanoparticle-Loaded Graphene Aerogel. *Sensors Actuators B Chem.* **2015**, *206*, 399–406.
(95) Dua, V.; Surwade, S. P.; Ammu, S.; Agnihotra, S. R.; Jain, S.; Roberts, K. E.; Park, S.; Ruoff, R. S.; Manohar, S. K. All-Organic Vapor Sensor Using Inkjet-Printed Reduced Graphene Oxide. *Angew. Chemie Int. Ed.* **2010**, *49* (12), 2154–2157.
(96) Paek, E.; Pak, A. J.; Kweon, K. E.; Hwang, G. S. On the Origin of the Enhanced Supercapacitor Performance of Nitrogen-Doped Graphene. *J. Phys. Chem. C* **2013**, *117* (11), 5610–5616.
(97) Simon, P.; Gogotsi, Y. Materials for Electrochemical Capacitors. **2008**.
(98) Simon, P.; Gogotsi, Y.; Dunn, B. Where Do Batteries End and Supercapacitors Begin? *Sci. Mag.* **2014**, *343*, 1210–1211.
(99) Ye, S.; Feng, J.; Wu, P. Deposition of Three-Dimensional Graphene Aerogel on Nickel Foam as a Binder-Free Supercapacitor Electrode. *ACS Appl. Mater. Interfaces* **2013**, *5* (15), 7122–7129.
(100) Jung, S. M.; Mafra, D. L.; Lin, C.-T.; Jung, H. Y.; Kong, J. Controlled Porous Structures of Graphene Aerogels and Their Effect on Supercapacitor Performance. *Nanoscale* **2015**, *7* (10), 4386–4393.
(101) Chen, Q.; Zhao, Y.; Huang, X.; Chen, N.; Qu, L. Three-Dimensional Graphitic Carbon Nitride Functionalized Graphene-Based High-Performance Supercapacitors. *J. Mater. Chem. A* **2015**, *3* (13), 6761–6766.
(102) Zhu, C.; Liu, T.; Qian, F.; Han, T. Y.-J.; Duoss, E. B.; Kuntz, J. D.; Spadaccini, C. M.; Worsley, M. A.; Li, Y. Supercapacitors Based on Three-Dimensional Hierarchical Graphene Aerogels with Periodic Macropores. *Nano Lett.* **2016**, *16* (6), 3448–3456.
(103) Wu, Z.-S.; Winter, A.; Chen, L.; Sun, Y.; Turchanin, A.; Feng, X.; Müllen, K. Three-Dimensional Nitrogen and Boron Co-Doped Graphene for High-Performance All-Solid-State Supercapacitors. *Adv. Mater.* **2012**, *24* (37), 5130–5135.
(104) Wu, Z.-S.; Sun, Y.; Tan, Y.-Z.; Yang, S.; Feng, X.; Müllen, K. Three-Dimensional Graphene-Based Macro- and Mesoporous Frameworks for High-Performance Electrochemical Capacitive Energy Storage. *J. Am. Chem. Soc.* **2012**, *134* (48), 19532–19535.
(105) Chmiola, J.; Yushin, G.; Gogotsi, Y.; Portet, C.; Simon, P.; Taberna, P. L. Anomalous Increase in Carbon Capacitance at Pore Sizes Less Than 1 Nanometer. *Science (80-.).* **2006**, *313* (5794), 1760–1763.
(106) Li, Y.; Li, Z.; Shen, P. K. Simultaneous Formation of Ultrahigh Surface Area and Three-Dimensional Hierarchical Porous Graphene-Like Networks for Fast and Highly Stable Supercapacitors. *Adv. Mater.* **2013**, *25* (17), 2474–2480.
(107) Liu, J. Charging Graphene for Energy. *Nat. Nanotechnol.* **2014**, *9* (10), 739–741.
(108) Ahn, J.-H.; Hee Hong, B. Things You Could Do with Graphene. *Nat. Publ. Gr.* **2014**, *9*.

(109) Gui, G.; Li, J.; Zhong, J. Band Structure Engineering of Graphene by Strain: First-Principles Calculations. *Phys. Rev. B* **2008**, *78* (7), 075435.
(110) Appelhans, D. J.; Lin, Z.; Lusk, M. T. Two-Dimensional Carbon Semiconductor: Density Functional Theory Calculations. *Phys. Rev. B* **2010**, *82* (7), 073410.
(111) Han, M. Y.; Özyilmaz, B.; Zhang, Y.; Kim, P. *Energy Band Gap Engineering of Graphene Nanoribbons*.
(112) Peng, Q.; De, S. *Tunable Band Gaps of Mono-Layer Hexagonal BNC Heterostructures*; 2012.
(113) Liu, A. Y.; Wentzcovitch, R. M.; Cohen, M. L. *Atomic Arrangement and Electronic Structure of BC2N*; Vol. 39.
(114) da Rocha Martins, J.; Chacham, H. Disorder and Segregation in B−C−N Graphene-Type Layers and Nanotubes: Tuning the Band Gap. *ACS Nano* **2011**, *5* (1), 385–393.
(115) Yuge, K. Phase Stability of Boron Carbon Nitride in a Heterographene Structure: A First-Principles Study. *Phys. Rev. B* **2009**, *79* (14), 144109.
(116) Muchharla, B.; Pathak, A.; Liu, Z.; Song, L.; Jayasekera, T.; Kar, S.; Vajtai, R.; Balicas, L.; Ajayan, P. M.; Talapatra, S.; et al. Tunable Electronics in Large-Area Atomic Layers of Boron–Nitrogen–Carbon. *Nano Lett.* **2013**, *13* (8), 3476–3481.
(117) Song, L.; Balicas, L.; Mowbray, D. J.; Capaz, R. B.; Storr, K.; Ci, L.; Jariwala, D.; Kurth, S.; Louie, S. G.; Rubio, A.; et al. Anomalous Insulator-Metal Transition in Boron Nitride-Graphene Hybrid Atomic Layers. *Phys. Rev. B* **2012**, *86* (7), 075429.
(118) Watanabe, M. O.; Itoh, S.; Mizushima, K.; Sasaki, T. Electrical Properties of BC 2 N Thin Films Prepared by Chemical Vapor Deposition ARTICLES YOU MAY BE INTERESTED IN. *J. Appl. Phys.* **1995**, *78*, 2880.
(119) Komatsu, T. Bulk Synthesis and Characterization of Graphite-like B–C–N and B–C–N Heterodiamond Compounds. *J. Mater. Chem.* **2004**, *14* (2), 221–227.
(120) Ma, F.; Wang, M.; Shao, Y.; Wang, L.; Wu, Y.; Wang, Z.; Hao, X. "Thermal Substitution" for Preparing Ternary BCN Nanosheets with Enhanced and Controllable Nonlinear Optical Performance †. *J. Mater. Chem. C* **2017**, *5*, 2559.
(121) Sun, C.; Ma, F.; Cai, L.; Wang, A.; Wu, Y.; Zhao, M.; Yan, W.; Hao, X. Metal-Free Ternary BCN Nanosheets with Synergetic Effect of Band Gap Engineering and Magnetic Properties OPEN. **2017**.
(122) Lei, W.; Portehault, D.; Dimova, R.; Antonietti, M. Boron Carbon Nitride Nanostructures from Salt Melts: Tunable Water-Soluble Phosphors. *J. Am. Chem. Soc* **2011**, *133*, 7121–7127.
(123) Jalaly, M.; Gotor, F. J.; Semnan, M.; María, &; Sayagués, J. A Novel, Simple and Rapid Route to the Synthesis of Boron Cabonitride Nanosheets: Combustive Gaseous Unfolding OPEN.
(124) Beniwal, S.; Hooper, J.; Miller, D. P.; Costa, P. S.; Chen, G.; Liu, S.-Y.; Dowben, P. A.; Sykes, E. C. H.; Zurek, E.; Enders, A. Graphene-like Boron–Carbon–Nitrogen Monolayers. *ACS Nano* **2017**, *11* (3), 2486–2493.
(125) Zheng, Y.; Jiao, Y.; Ge, L.; Jaroniec, M.; Zhang, S.; Communications, Q. * A. Angewandte Chemie Oxygen Reduction Two-Step Boron and Nitrogen Doping in Graphene for Enhanced Synergistic Catalysis**. *Angew. Chem. Int. Ed* **2013**, *52*, 3110–3116.
(126) Wang, S.; Zhang, L.; Xia, Z.; Roy, A.; Chang, D. W.; Baek, J.-B.; Dai, L. BCN Graphene as Efficient Metal-Free Electrocatalyst for the Oxygen Reduction Reaction. *Angew. Chemie Int. Ed.* **2012**, *51* (17), 4209–4212.
(127) Ma, F.; Wang, M.; Shao, Y.; Wang, L.; Wu, Y.; Wang, Z.; Hao, X. 'Thermal Substitution' for Preparing Ternary BCN Nanosheets with Enhanced and Controllable Nonlinear Optical

Performance. *J. Mater. Chem. C* **2017**, *5* (10), 2559–2565.
(128) Portehault, D.; Giordano, C.; Gervais, C.; Senkovska, I.; Kaskel, S.; Sanchez, C.; Antonietti, M. High-Surface-Area Nanoporous Boron Carbon Nitrides for Hydrogen Storage. *Adv. Funct. Mater.* **2010**, *20* (11), 1827–1833.
(129) Peng, D.; Jiang, W.; Li, F.-F.; Zhang, L.; Liang, R.-P.; Qiu, J.-D. One-Pot Synthesis of Boron Carbon Nitride Nanosheets for Facile and Efficient Heavy Metal Ions Removal. *ACS Sustain. Chem. Eng.* **2018**, *6* (9), 11685–11694.
(130) Jalaly, M.; José Gotor, F.; Semnan, M.; Jesús Sayagués, M. A Novel, Simple and Rapid Route to the Synthesis of Boron Cabonitride Nanosheets: Combustive Gaseous Unfolding. *Sci. Rep.* **2017**, *7* (1), 3453.
(131) Li, Z. Q.; Lu, C. J.; Xia, Z. P.; Zhou, Y.; Luo, Z. X-Ray Diffraction Patterns of Graphite and Turbostratic Carbon. **2007**.
(132) Yoon, S.-H.; Lim, S.; Song, Y.; Ota, Y.; Qiao, W.; Tanaka, A.; Mochida, I. KOH Activation of Carbon Nanofibers.
(133) Chen, Y.; Liu, Q.; Wang, J. Carbon Dioxide Activated Carbon Nanofibers with Hierarchical Micro-/Mesoporosity towards Electrocatalytic Oxygen Reduction †. **2016**.
(134) Wang, X.; Maeda, K.; Thomas, A.; Takanabe, K.; Xin, G.; Carlsson, J. M.; Domen, K.; Antonietti, M. A Metal-Free Polymeric Photocatalyst for Hydrogen Production from Water under Visible Light. *Nat. Mater.* **2009**, *8* (1), 76–80.
(135) Zhang, G.; Zhang, J.; Zhang, M.; Wang, X. Polycondensation of Thiourea into Carbon Nitride Semiconductors as Visible Light Photocatalysts. *J. Mater. Chem.* **2012**, *22* (16), 8083.
(136) Dong, G.; Zhang, L. Porous Structure Dependent Photoreactivity of Graphitic Carbon Nitride under Visible Light. *J. Mater. Chem.* **2012**, *22* (3), 1160–1166.
(137) Mao, J.; Peng, T.; Zhang, X.; Li, K.; Ye, L.; Zan, L. Effect of Graphitic Carbon Nitride Microstructures on the Activity and Selectivity of Photocatalytic CO2 Reduction under Visible Light. *Catal. Sci. Technol.* **2013**, *3* (5), 1253.
(138) Goettmann, F.; Fischer, A.; Antonietti, M.; Thomas, A. Metal-Free Catalysis of Sustainable Friedel–Crafts Reactions: Direct Activation of Benzene by Carbon Nitrides to Avoid the Use of Metal Chlorides and Halogenated Compounds. *Chem. Commun.* **2006**, *0* (43), 4530–4532.
(139) Goettmann, F.; Fischer, A.; Antonietti, M.; Thomas, A. Chemical Synthesis of Mesoporous Carbon Nitrides Using Hard Templates and Their Use as a Metal-Free Catalyst for Friedel–Crafts Reaction of Benzene. *Angew. Chemie Int. Ed.* **2006**, *45* (27), 4467–4471.
(140) Yan, S. C.; Li, Z. S.; Zou, Z. G. Photodegradation Performance of G-C $_3$ N $_4$ Fabricated by Directly Heating Melamine. *Langmuir* **2009**, *25* (17), 10397–10401.
(141) Wang, W.; Yu, J. C.; Xia, D.; Wong, P. K.; Li, Y. Graphene and G-C $_3$ N $_4$ Nanosheets Cowrapped Elemental α-Sulfur As a Novel Metal-Free Heterojunction Photocatalyst for Bacterial Inactivation under Visible-Light. *Environ. Sci. Technol.* **2013**, *47* (15), 8724–8732.
(142) Yang, S.; Gong, Y.; Zhang, J.; Zhan, L.; Ma, L.; Fang, Z.; Vajtai, R.; Wang, X.; Ajayan, P. M. Exfoliated Graphitic Carbon Nitride Nanosheets as Efficient Catalysts for Hydrogen Evolution under Visible Light. *Adv. Mater.* **2013**, *25* (17), 2452–2456.
(143) Cao, S.; Low, J.; Yu, J.; Jaroniec, M. Polymeric Photocatalysts Based on Graphitic Carbon Nitride. *Adv. Mater.* **2015**, *27* (13), 2150–2176.
(144) Lee, R.-L.; Tran, P. D.; Pramana, S. S.; Chiam, S. Y.; Ren, Y.; Meng, S.; Wong, L. H.; Barber, J. Assembling Graphitic-Carbon-Nitride with Cobalt-Oxide-Phosphate to Construct an Efficient Hybrid Photocatalyst for Water Splitting Application. *Catal. Sci. Technol.*

2013, *3* (7), 1694.
(145) Wang, Y.; Li, H.; Yao, J.; Wang, X.; Antonietti, M. Synthesis of Boron Doped Polymeric Carbon Nitride Solids and Their Use as Metal-Free Catalysts for Aliphatic C–H Bond Oxidation. *Chem. Sci.* **2011**, *2* (3), 446–450.
(146) Hu, S.; Li, F.; Fan, Z.; Wang, F.; Zhao, Y.; Lv, Z. Band Gap-Tunable Potassium Doped Graphitic Carbon Nitride with Enhanced Mineralization Ability. *Dalton Trans.* **2015**, *44* (3), 1084–1092.
(147) Zhang, J.; Chen , X.; Takanabe, K.; Maeda, K.; Domen, K.; Epping, J. D.; Fu, X.; Antonietti, M.; Wang , X. Synthesis of a Carbon Nitride Structure for Visible-Light Catalysis by Copolymerization. *Angew. Chemie Int. Ed.* **2010**, *49* (2), 441–444.
(148) Tong, Z.; Yang, D.; Xiao, T.; Tian, Y.; Jiang, Z. Biomimetic Fabrication of G-C3N4/TiO2 Nanosheets with Enhanced Photocatalytic Activity toward Organic Pollutant Degradation. *Chem. Eng. J.* **2015**, *260*, 117–125.
(149) Kumar, S.; Baruah, A.; Tonda, S.; Kumar, B.; Shanker, V.; Sreedhar, B. Cost-Effective and Eco-Friendly Synthesis of Novel and Stable N-Doped ZnO/g-C3N4 Core–Shell Nanoplates with Excellent Visible-Light Responsive Photocatalysis. *Nanoscale* **2014**, *6* (9), 4830.
(150) Huang, H.; Yang, S.; Vajtai, R.; Wang, X.; Ajayan, P. M. Pt-Decorated 3D Architectures Built from Graphene and Graphitic Carbon Nitride Nanosheets as Efficient Methanol Oxidation Catalysts. *Adv. Mater.* **2014**, *26* (30), 5160–5165.
(151) Yang, S.; Feng, X.; Wang, X.; Müllen, K. Graphene-Based Carbon Nitride Nanosheets as Efficient Metal-Free Electrocatalysts for Oxygen Reduction Reactions. *Angew. Chem. Int. Ed. Engl.* **2011**, *50* (23), 5339–5343.
(152) Tong, Z.; Yang, D.; Shi, J.; Nan, Y.; Sun, Y.; Jiang, Z. Three-Dimensional Porous Aerogel Constructed by g-C3N4 and Graphene Oxide Nanosheets with Excellent Visible-Light Photocatalytic Performance. *ACS Appl. Mater. Interfaces* **2015**, *7* (46), 25693–25701.
(153) Han, Q.; Cheng, Z.; Gao, J.; Zhao, Y.; Zhang, Z.; Dai, L.; Qu, L. Mesh-on-Mesh Graphitic-C $_3$ N $_4$ @Graphene for Highly Efficient Hydrogen Evolution. *Adv. Funct. Mater.* **2017**, *27* (15), 1606352.
(154) Zhu, J.; Xiao, P.; Li, H.; Carabineiro, S. A. C. Graphitic Carbon Nitride: Synthesis, Properties, and Applications in Catalysis. *ACS Appl. Mater. Interfaces* **2014**, *6* (19), 16449–16465.
(155) Peer, M.; Lusardi, M.; Jensen, K. F. Facile Soft-Templated Synthesis of High-Surface Area and Highly Porous Carbon Nitrides. *Chem. Mater.* **2017**, *29* (4), 1496–1506.
(156) Zhao, Y.; Liu, Z.; Chu, W.; Song, L.; Zhang, Z.; Yu, D.; Tian, Y.; Xie, S.; Sun, L. Large-Scale Synthesis of Nitrogen-Rich Carbon Nitride Microfibers by Using Graphitic Carbon Nitride as Precursor. *Adv. Mater.* **2008**, *20* (9), 1777–1781.
(157) Feng, D.; Cheng, Y.; He, J.; Zheng, L.; Shao, D.; Wang, W.; Wang, W.; Lu, F.; Dong, H.; Liu, H.; et al. Enhanced Photocatalytic Activities of G-C3N4 with Large Specific Surface Area via a Facile One-Step Synthesis Process. *Carbon N. Y.* **2017**, *125*, 454–463.
(158) Dong, G.; Zhang, Y.; Pan, Q.; Qiu, J. A Fantastic Graphitic Carbon Nitride (g-C3N4) Material: Electronic Structure, Photocatalytic and Photoelectronic Properties. *J. Photochem. Photobiol. C Photochem. Rev.* **2014**, *20*, 33–50.
(159) Xiang, Q.; Yu, J.; Jaroniec, M. Preparation and Enhanced Visible-Light Photocatalytic H 2-Production Activity of Graphene/C 3 N 4 Composites. *J. Phys. Chem. C* **2011**, *115*, 7355–7363.
(160) Turner, S.; Long, H.; Shevitski, B.; Pham, T.; Lorenzo, M.; Kennedy, E.; Aloni, S.; Worsley, M.; Zettl, A. Density Tunable Graphene Aerogels Using a Sacrificial Polycyclic Aromatic Hydrocarbon. *Phys. status solidi* **2017**, *254* (11), 1700203.

(161) Hu, H.; Zhao, Z.; Wan, W.; Gogotsi, Y.; Qiu, J. Ultralight and Highly Compressible Graphene Aerogels. *Adv. Mater.* **2013**, *25* (15), 2219–2223.
(162) Worsley, M. A.; Pauzauskie, P. J.; Olson, T. Y.; Biener, J.; Satcher, J. H.; Baumann, T. F. Synthesis of Graphene Aerogel with High Electrical Conductivity. *J. Am. Chem. Soc.* **2010**, *132* (40), 14067–14069.
(163) Lu, X.; Arduini-Schuster, M. C.; Kuhn, J.; Nilsson, O.; Fricke, J.; Pekala, R. W. Thermal Conductivity of Monolithic Organic Aerogels. *Science* **1992**, *255* (5047), 971–972.
(164) Lu, X.; Nilsson, O.; Fricke, J.; Pekala, R. W. Thermal and Electrical Conductivity of Monolithic Carbon Aerogels. *J. Appl. Phys.* **1993**, *73* (2), 581–584.
(165) ElKhatat, A. M.; Al-Muhtaseb, S. A. Advances in Tailoring Resorcinol-Formaldehyde Organic and Carbon Gels. *Adv. Mater.* **2011**, *23* (26), 2887–2903.
(166) Temirov, R.; Soubatch, S.; Luican, A.; Tautz, F. S. Free-Electron-like Dispersion in an Organic Monolayer Film on a Metal Substrate. *Nature* **2006**, *444* (7117), 350–353.
(167) Kaushik Balakrishnan, †; Aniket Datar, †; Randy Oitker, †; Hao Chen, ‡; Jianmin Zuo, ‡ and; Ling Zang*, †. Nanobelt Self-Assembly from an Organic n-Type Semiconductor: Propoxyethyl-PTCDI. **2005**.
(168) Kim, B. J.; Yu, H.; Oh, J. H.; Kang, M. S.; Cho, J. H. Electrical Transport through Single Nanowires of Dialkyl Perylene Diimide. *J. Phys. Chem. C* **2013**, *117* (20), 10743–10749.
(169) Goldstein, A. P.; Mickelson, W.; Machness, A.; Lee, G.; Worsley, M. A.; Woo, L.; Zettl, A. Simultaneous Sheet Cross-Linking and Deoxygenation in the Graphene Oxide Sol − Gel Transition. *J. Phys. Chem. C* **2014**, *118* (49), 28855–28860.
(170) Chou, Y.-H.; Lee, W.-Y.; Chen, W.-C. Self-Assembled Nanowires of Organic n-Type Semiconductor for Nonvolatile Transistor Memory Devices. *Adv. Funct. Mater.* **2012**, *22* (20), 4352–4359.
(171) Yang, B.; Wang, F.-X.; Wang, K.-K.; Yan, J.-H.; Liu, Y.-Q.; Pan, G.-B. One-Step Fabrication of Ultralong Nanobelts of PI-PTCDI and Their Optoelectronic Properties. *Phys. Chem. Chem. Phys.* **2014**, *16* (46), 25251–25254.
(172) Zang, L.; Che, Y.; Moore, J. S. One-Dimensional Self-Assembly of Planar π-Conjugated Molecules: Adaptable Building Blocks for Organic Nanodevices. *Acc. Chem. Res.* **2008**, *41* (12), 1596–1608.
(173) Worsley, M. A.; Livermore, L.; Kucheyev, S. O.; David Kuntz, J.; Lewicki, J. P. Stiff and Electrically Conductive Composites of Carbon Nanotubes and Polymers Membrane Characterization Test View Project Direct Metal Writing Additive Manufacturing View Project. **2012**.
(174) Lewicki, J. P.; Worsley, M. A.; Albo, R. L. F.; Finnie, J. A.; Ashmore, M.; Mason, H. E.; Baumann, T. F.; Maxwell, R. S. The Effects of Highly Structured Low Density Carbon Nanotube Networks on the Thermal Degradation Behaviour of Polysiloxanes. *Polym. Degrad. Stab.* **2014**, *102*, 25–32.
(175) Worsley, M. A.; Kuntz, J. D.; Kucheyev, S.; Hamza, A. V; Satcher, J. H.; Baumann, T. F. Electrically Conductive Composites via Infiltration of Single-Walled Carbon Nanotube-Based Aerogels. *MRS Proc.* **2010**, *1258*, 1258-R05-31.
(176) Sari, F. N. I.; Ting, J.-M. Direct Growth of MoS2 Nanowalls on Carbon Nanofibers for Use in Supercapacitor. *Sci. Rep.* **2017**, *7* (1), 5999.
(177) Hu, H.; Zhao, Z.; Zhang, R.; Bin, Y.; Qiu, J. Polymer Casting of Ultralight Graphene Aerogels for the Production of Conductive Nanocomposites with Low Filling Content. *J. Mater. Chem. A* **2014**, *2* (11), 3756–3760.
(178) Yang, D.-J.; Kamienchick, I.; Youn, D. Y.; Rothschild, A.; Kim, I.-D. Ultrasensitive and Highly Selective Gas Sensors Based on Electrospun SnO2 Nanofibers Modified by Pd

Loading. *Adv. Funct. Mater.* **2010**, *20* (24), 4258–4264.
(179) Tan, C.; Qi, X.; Liu, Z.; Zhao, F.; Li, H.; Huang, X.; Shi, L.; Zheng, B.; Zhang, X.; Xie, L.; et al. Self-Assembled Chiral Nanofibers from Ultrathin Low-Dimensional Nanomaterials. *J. Am. Chem. Soc.* **2015**, *137* (4), 1565–1571.
(180) Martin-Gullon, I.; Vera, J.; Conesa, J. A.; González, J. L.; Merino, C. Differences between Carbon Nanofibers Produced Using Fe and Ni Catalysts in a Floating Catalyst Reactor. **2006**.
(181) Murthy, A. A.; Li, Y.; Palacios, E.; Li, Q.; Hao, S.; Distefano, J. G.; Wolverton, C.; Aydin, K.; Chen, X.; Dravid, V. P. Optically Active 1D MoS 2 Nanobelts. **2018**.
(182) Chacko, D. K.; Madhavan, A. A.; Arun, T. A.; Thomas, S.; Anjusree, G. S.; Deepak, T. G.; Balakrishnan, A.; Subramanian, K. R. V.; Sivakumar, N.; Nair, S. V.; et al. Ultrafine TiO2 Nanofibers for Photocatalysis. *RSC Adv.* **2013**, *3* (47), 24858.
(183) Shin, J.; Choi, S.-J.; Lee, I.; Youn, D.-Y.; Park, C. O.; Lee, J.-H.; Tuller, H. L.; Kim, I.-D. Thin-Wall Assembled SnO $_2$ Fibers Functionalized by Catalytic Pt Nanoparticles and Their Superior Exhaled-Breath-Sensing Properties for the Diagnosis of Diabetes. *Adv. Funct. Mater.* **2013**, *23* (19), 2357–2367.
(184) Chambers, C. Manufacture of Carbon Filaments. 405,480, August 30, 1889.
(185) Oberun, A.; Endo, M.; Koyama, T. *FILAMENTOUS GROWTH OF CARBON THROUGH BENZENE DECOMPOSITION*; 1976; Vol. 32.
(186) Rodriguez, N. M. A Review of Catalytically Grown Carbon Nanofibers. *J. Mater. Res.* **1993**, *8* (12), 3233–3250.
(187) Rodriguez, N. M.; Chambers, A.; Terry, R.; Baker, K. *Catalytic Engineering of Carbon Nanostructures*; 1995; Vol. 11.
(188) Nan, D.; Huang, Z.-H.; Lv, R.; Yang, L.; Wang, J.-G.; Shen, W.; Lin, Y.; Yu, X.; Ye, L.; Sun, H.; et al. Nitrogen-Enriched Electrospun Porous Carbon Nanofiber Networks as High-Performance Free-Standing Electrode Materials. *J. Mater. Chem. A* **2014**, *2* (46), 19678–19684.
(189) McDonough, J. R.; Choi, J. W.; Yang, Y.; La Mantia, F.; Zhang, Y.; Cui, Y. Carbon Nanofiber Supercapacitors with Large Areal Capacitances. *Appl. Phys. Lett.* **2009**, *95* (24), 243109.
(190) Sebastián, D.; Suelves, I.; Moliner, R.; Lázaro, J.; Stassi, A.; Baglio, V.; Aricò, A. S. Optimizing the Synthesis of Carbon Nanofiber Based Electrocatalysts for Fuel Cells. *"Applied Catal. B, Environ.* **2013**, *132–133*, 22–27.
(191) Zhang, G.; Wu, H. Bin; Hoster, H. E.; Lou, X. W. (David). Strongly Coupled Carbon Nanofiber–Metal Oxide Coaxial Nanocables with Enhanced Lithium Storage Properties. *Energy Environ. Sci.* **2014**, *7* (1), 302–305.
(192) Delgado, M. C. R.; Kim, E.-G.; Filho, D. A. da S.; Bredas, J.-L. Tuning the Charge-Transport Parameters of Perylene Diimide Single Crystals via End and/or Core Functionalization: A Density Functional Theory Investigation. *J. Am. Chem. Soc.* **2010**, *132* (10), 3375–3387.
(193) Kaushik Balakrishnan, †; Aniket Datar, †; Randy Oitker, †; Hao Chen, ‡; Jianmin Zuo, ‡ and; Ling Zang*, †. Nanobelt Self-Assembly from an Organic n-Type Semiconductor: Propoxyethyl-PTCDI. **2005**.
(194) Zang, L. Interfacial Donor–Acceptor Engineering of Nanofiber Materials To Achieve Photoconductivity and Applications. *Acc. Chem. Res.* **2015**, *48* (10), 2705–2714.
(195) Wu, N.; Zhang, Y.; Wang, C.; Slattum, P. M.; Yang, X.; Zang, L. Thermoactivated Electrical Conductivity in Perylene Diimide Nanofiber Materials. *J. Phys. Chem. Lett.* **2017**, *8* (1), 292–298.

(196) Li, L.; Cai, Z. Structure Control and Photocatalytic Performance of Porous Conjugated Polymers Based on Perylene Diimide. *Polym. Chem.* **2016**, *7* (30), 4937–4943.
(197) Schon, T. B.; Tilley, A. J.; Kynaston, E. L.; Seferos, D. S. Three-Dimensional Arylene Diimide Frameworks for Highly Stable Lithium Ion Batteries. *ACS Appl. Mater. Interfaces* **2017**, *9* (18), 15631–15637.
(198) Zhang, L.; Zhong, X.; Pavlica, E.; Li, S.; Klekachev, A.; Bratina, G.; Ebbesen, T. W.; Orgiu, E.; Samorì, P. A Nanomesh Scaffold for Supramolecular Nanowire Optoelectronic Devices. *Nat. Nanotechnol.* **2016**, *11* (10), 900–906.
(199) Fu, X.; Choi, J.-Y.; Zamani, P.; Jiang, G.; Ariful Hoque, M.; Mohamed Hassan, F.; Chen, Z. Co−N Decorated Hierarchically Porous Graphene Aerogel for Efficient Oxygen Reduction Reaction in Acid. **2016**.
(200) Sui, Z.; Meng, Q.; Zhang, X.; Ma, R.; Cao, B. Green Synthesis of Carbon Nanotube–Graphene Hybrid Aerogels and Their Use as Versatile Agents for Water Purification. *J. Mater. Chem.* **2012**, *22* (18), 8767.
(201) Deng, W.; Shen, Y.; Qian, J.; Cao, Y.; Yang, H. A Perylene Diimide Crystal with High Capacity and Stable Cyclability for Na-Ion Batteries. *ACS Appl. Mater. Interfaces* **2015**, *7* (38), 21095–21099.
(202) Mohanan, J. L.; Arachchige, I. U.; Brock, S. L. Porous Semiconductor Chalcogenide Aerogels. *Science* **2005**, *307* (5708), 397–400.
(203) Ferrari, A. C.; Meyer, J. C.; Scardaci, V.; Casiraghi, C.; Lazzeri, M.; Mauri, F.; Piscanec, S.; Jiang, D.; Novoselov, K. S.; Roth, S.; et al. Raman Spectrum of Graphene and Graphene Layers. *Phys. Rev. Lett.* **2006**, *97* (18), 187401.
(204) Yang, D.; Velamakanni, A.; Lay Bozoklu, G.; Park, S.; Stoller, M.; Piner, R. D.; Stankovich, S.; Jung, I.; Field, D. A.; Ventrice, C. A.; et al. Chemical Analysis of Graphene Oxide Films after Heat and Chemical Treatments by X-Ray Photoelectron and Micro-Raman Spectroscopy. **2008**.
(205) Holzwarth, U.; Gibson, N. The Scherrer Equation versus the "Debye-Scherrer Equation." *Nat. Nanotechnol.* **2011**, *6* (9), 534–534.
(206) Yoon, S.-H.; Lim, S.; Hong, S.; Mochida, I.; An, B.; Yokogawa, K. Carbon Nano-Rod as a Structural Unit of Carbon Nanofibers. *Carbon N. Y.* **2004**, *42* (15), 3087–3095.
(207) Xia, B.; Lenggoro, I. W.; Okuyama, K. Preparation of Ni Particles by Ultrasonic Spray Pyrolysis of NiCl2·6H2O Precursor Containing Ammonia. *J. Mater. Sci.* **2001**, *36* (7), 1701–1705.
(208) Ortiz-Medina, J.; Wang, Z.; Cruz-Silva, R.; Morelos-Gomez, A.; Wang, F.; Yao, X.; Terrones, M.; Endo, M. Defect Engineering and Surface Functionalization of Nanocarbons for Metal-Free Catalysis. *Adv. Mater.* **2019**, 1805717.
(209) Jiang, Y.; Yang, L.; Sun, T.; Zhao, J.; Lyu, Z.; Zhuo, O.; Wang, X.; Wu, Q.; Ma, J.; Hu, Z. Significant Contribution of Intrinsic Carbon Defects to Oxygen Reduction Activity. **2015**.
(210) Zhu, Y.; Murali, S.; Stoller, M. D.; Ganesh, K. J.; Cai, W.; Ferreira, P. J.; Pirkle, A.; Wallace, R. M.; Cychosz, K. A.; Thommes, M.; et al. Carbon-Based Supercapacitors Produced by Activation of Graphene. *Science (80-.).* **2011**, *332* (6037), 1537–1541.
(211) Xiao, J.; Mei, D.; Li, X.; Xu, W.; Wang, D.; Graff, G. L.; Bennett, W. D.; Nie, Z.; Saraf, L. V.; Aksay, I. A.; et al. Hierarchically Porous Graphene as a Lithium–Air Battery Electrode. *Nano Lett.* **2011**, *11* (11), 5071–5078.
(212) Xiong, M.; Schneiderman, D. K.; Bates, F. S.; Hillmyer, M. A.; Zhang, K. Scalable Production of Mechanically Tunable Block Polymers from Sugar.
(213) Bin Liu, †; Wang-Lin Yu, †; Yee-Hing Lai, *,‡ and; Wei Huang*, †. Blue-Light-Emitting Fluorene-Based Polymers with Tunable Electronic Properties. **2001**.

(214) Liu, J.; Yang, R. Tuning the Thermal Conductivity of Polymers with Mechanical Strains Laser Irradiation Induced Melting and Reduction Reaction for the Formation of Pt-Based Bimetallic Alloy Particles in Liquids View Project Tuning the Thermal Conductivity of Polymers with Mechanical Strains.
(215) Croce, F.; Persi, L.; Scrosati, B.; Serraino-Fiory, F.; Plichta, E.; Hendrickson, M. A. *Role of the Ceramic Fillers in Enhancing the Transport Properties of Composite Polymer Electrolytes*; 2001; Vol. 46.
(216) Stefanescu, E. A.; Tan, X.; Lin, Z.; Bowler, N.; Kessler, M. R. Multifunctional Fiberglass-Reinforced PMMA-BaTiO 3 Structural/Dielectric Composites. *Polymer (Guildf).* **2011**, *52*, 2016–2024.
(217) Mamunya, Y. P.; Davydenko, V. V; Pissis, P.; Lebedev, E. V. *Electrical and Thermal Conductivity of Polymers Filled with Metal Powders*.
(218) Zhi, C. Y.; Bando, Y.; Tang, C. C.; Huang, Q.; Golberg, D. Boron Nitride Nanotubes: Functionalization and Composites. *J. Mater. Chem.* **2008**, *18* (33), 3900.
(219) Zhou, S.-J.; Ma, C.-Y.; Meng, Y.-Y.; Su, H.-F.; Zhu, Z.; Deng, S.-L.; Xie, S.-Y. Activation of Boron Nitride Nanotubes and Their Polymer Composites for Improving Mechanical Performance. *Nanotechnology* **2012**, *23* (5), 055708.
(220) Zeng, X.; Ye, L.; Yu, S.; Li, H.; Sun, R.; Xu, J.; Wong, C.-P. Artificial Nacre-like Papers Based on Noncovalent Functionalized Boron Nitride Nanosheets with Excellent Mechanical and Thermally Conductive Properties. *Nanoscale* **2015**, *7* (15), 6774–6781.
(221) Song, W.-L.; Wang, P.; Cao, L.; Anderson, A.; Meziani, M. J.; Farr, A. J.; Sun, Y.-P. Polymer/Boron Nitride Nanocomposite Materials for Superior Thermal Transport Performance. *Angew. Chem. Int. Ed. Engl.* **2012**, *51* (26), 6498–6501.
(222) Nasrabadi, A. T.; Foroutan, M. Interactions between Polymers and Single-Walled Boron Nitride Nanotubes: A Molecular Dynamics Simulation Approach. *J. Phys. Chem. B* **2010**, *114* (47), 15429–15436.
(223) Coleman, J. N.; Khan, U.; Blau, W. J.; Gun'ko, Y. K. Small but Strong: A Review of the Mechanical Properties of Carbon Nanotube-Polymer Composites.
(224) Sainsbury, T.; O'Neill, A.; Passarelli, M. K.; Seraffon, M.; Gohil, D.; Gnaniah, S.; Spencer, S. J.; Rae, A.; Coleman, J. N. Dibromocarbene Functionalization of Boron Nitride Nanosheets: Toward Band Gap Manipulation and Nanocomposite Applications. *Chem. Mater.* **2014**, 141208064817004.
(225) Sainsbury, T.; Satti, A.; May, P.; Wang, Z.; McGovern, I.; Gun'ko, Y. K.; Coleman, J. Oxygen Radical Functionalization of Boron Nitride Nanosheets. *J. Am. Chem. Soc.* **2012**, *134* (45), 18758–18771.
(226) Ikuno, T.; Sainsbury, T.; Okawa, D.; Fréchet, J. M. J.; Zettl, A. Amine-Functionalized Boron Nitride Nanotubes. *Solid State Commun.* **2007**, *142* (11), 643–646.
(227) Sainsbury, T.; Satti, A.; May, P.; O'Neill, A.; Nicolosi, V.; Gun'Ko, Y. K.; Coleman, J. N. Covalently Functionalized Hexagonal Boron Nitride Nanosheets by Nitrene Addition. *Chem. - A Eur. J.* **2012**, *18*, 10808–10812.
(228) Xie, S.-Y.; Wang, W.; Fernando, K. A. S.; Wang, X.; Lin, Y.; Sun, Y.-P. Solubilization of Boron Nitride Nanotubes. *Chem. Commun. (Camb).* **2005**, No. 29, 3670–3672.
(229) Pal, S.; Vivekchand, S. R. C.; Govindaraj, A.; Rao, C. N. R. Functionalization and Solubilization of BN Nanotubes by Interaction with Lewis Bases. *J. Mater. Chem.* **2007**, *17* (5), 450–452.
(230) Shin, H.; Guan, J.; Zgierski, M. Z.; Kim, K. S.; Kingston, C. T.; Simard, B. Covalent Functionalization of Boron Nitride Nanotubes via Reduction Chemistry. *ACS Nano* **2015**, *9* (12), 12573–12582.

(231) Zhi, C. Y.; Bando, Y.; Terao, T.; Tang, C. C.; Kuwahara, H.; Golberg, D. Chemically Activated Boron Nitride Nanotubes. *Chem. - An Asian J.* **2009**, *4* (10), 1536–1540.
(232) Erickson, K. Synthesis and Functionalization of Carbon and Boron Nitride Nanomaterials and Their Applications, 2012.
(233) Cui, F.; Dou, L.; Yang, Q.; Yu, Y.; Niu, Z.; Sun, Y.; Liu, H.; Dehestani, A.; Schierle-Arndt, K.; Yang, P. Benzoin Radicals as Reducing Agent for Synthesizing Ultrathin Copper Nanowires. *J. Am. Chem. Soc.* **2017**, *139* (8), 3027–3032.
(234) Worsley, M. A.; Shin, S. J.; Merrill, M. D.; Lenhardt, J.; Nelson, A. J.; Woo, L. Y.; Gash, A. E.; Baumann, T. F.; Orme, C. A. Ultralow Density, Monolithic WS_2, MoS_2, and MoS_2/Graphene Aerogels. *ACS Nano* **2015**, *9* (5), 4698–4705.
(235) Lv, P.; Tang, X.; Wei, W. Graphene/MnO 2 Aerogel with Both High Compression-Tolerance Ability and High Capacitance, for Compressible All-Solid-State Supercapacitors †. **2017**.
(236) Naguib, M.; Kurtoglu, M.; Presser, V.; Lu, J.; Niu, J.; Heon, M.; Hultman, L.; Gogotsi, Y.; Barsoum, M. W. Two-Dimensional Nanocrystals Produced by Exfoliation of Ti3AlC2. *Adv. Mater.* **2011**, *23* (37), 4248–4253.
(237) Xie, Y.; Dall'Agnese, Y.; Naguib, M.; Gogotsi, Y.; Barsoum, M. W.; Zhuang, H. L.; Kent, P. R. C. Prediction and Characterization of MXene Nanosheet Anodes for Non-Lithium-Ion Batteries. *ACS Nano* **2014**, *8* (9), 9606–9615.
(238) Liang, X.; Garsuch, A.; Nazar, L. F. Sulfur Cathodes Based on Conductive MXene Nanosheets for High-Performance Lithium-Sulfur Batteries. *Angew. Chemie Int. Ed.* **2015**, *54* (13), 3907–3911.
(239) Naguib, M.; Come, J.; Dyatkin, B.; Presser, V.; Taberna, P.-L.; Simon, P.; Barsoum, M. W.; Gogotsi, Y. MXene: A Promising Transition Metal Carbide Anode for Lithium-Ion Batteries. *Electrochem. commun.* **2012**, *16* (1), 61–64.
(240) Ghidiu, M.; Lukatskaya, M. R.; Zhao, M.-Q.; Gogotsi, Y.; Barsoum, M. W. Conductive Two-Dimensional Titanium Carbide 'Clay' with High Volumetric Capacitance. *Nature* **2014**, *516* (7529), 78–81.
(241) Hu, M.; Li, Z.; Zhang, H.; Hu, T.; Zhang, C.; Wu, Z.; Wang, X. Self-Assembled $Ti_3C_2T_x$ MXene Film with High Gravimetric Capacitance. *Chem. Commun.* **2015**, *51* (70), 13531–13533.
(242) Kim, S. J.; Koh, H.-J.; Ren, C. E.; Kwon, O.; Maleski, K.; Cho, S.-Y.; Anasori, B.; Kim, C.-K.; Choi, Y.-K.; Kim, J.; et al. Metallic $Ti_3C_2T_x$ MXene Gas Sensors with Ultrahigh Signal-to-Noise Ratio. *ACS Nano* **2018**, *12* (2), 986–993.
(243) Guo, Y.; Zhong, M.; Fang, Z.; Wan, P.; Yu, G. A Wearable Transient Pressure Sensor Made with MXene Nanosheets for Sensitive Broad-Range Human–Machine Interfacing. *Nano Lett.* **2019**, *19* (2), 1143–1150.
(244) Bao, W.; Tang, X.; Guo, X.; Choi, S.; Wang, C.; Gogotsi, Y.; Wang, G. Porous Cryo-Dried MXene for Efficient Capacitive Deionization. *Joule* **2018**, *2* (4), 778–787.
(245) Bian, R.; He, G.; Zhi, W.; Xiang, S.; Wang, T.; Cai, D. Ultralight MXene-Based Aerogels with High Electromagnetic Interference Shielding Performance. *J. Mater. Chem. C* **2019**, *7* (3), 474–478.
(246) Geim, A. K.; Novoselov, K. S. The Rise of Graphene. *Nat. Mater.* **2007**, *6* (3), 183–191.
(247) Balandin, A. A.; Ghosh, S.; Bao, W.; Calizo, I.; Teweldebrhan, D.; Miao, F.; Lau, C. N. Superior Thermal Conductivity of Single-Layer Graphene. *Nano Lett.* **2008**, *8* (3), 902–907.
(248) Liu, L.; Ryu, S.; Tomasik, M. R.; Stolyarova, E.; Jung, N.; Hybertsen, M. S.; Steigerwald, M. L.; Brus, L. E.; Flynn, G. W. Graphene Oxidation: Thickness-Dependent Etching and Strong Chemical Doping. *Nano Lett.* **2008**, *8* (7), 1965–1970.

(249) Falin, A.; Cai, Q.; Santos, E. J. G.; Scullion, D.; Qian, D.; Zhang, R.; Yang, Z.; Huang, S.; Watanabe, K.; Taniguchi, T.; et al. Mechanical Properties of Atomically Thin Boron Nitride and the Role of Interlayer Interactions. *Nat. Commun.* **2017**, *8*, 15815.
(250) *Graphene and Boron Nitride Single Layers*; 2018.
(251) Rasool, H. I.; Ophus, C.; Zhang, Z.; Crommie, M. F.; Yakobson, B. I.; Zettl, A. Conserved Atomic Bonding Sequences and Strain Organization of Graphene Grain Boundaries. **2014**.
(252) Gibb, A. L.; Alem, N.; Chen, J.-H.; Erickson, K. J.; Ciston, J.; Gautam, A.; Linck, M.; Zettl, A. Atomic Resolution Imaging of Grain Boundary Defects in Monolayer Chemical Vapor Deposition-Grown Hexagonal Boron Nitride. **2013**.
(253) Gibb, A. L. *Single Layer Nanomaterials: The Chemical Vapor Deposition Synthesis and Atomic Scale Characterization of Hexagonal Boron Nitride and Graphene*; 2015.
(254) Barty, A.; Marchesini, S.; Chapman, H. N.; Cui, C.; Howells, M. R.; Shapiro, D. A.; Minor, A. M.; Spence, J. C. H.; Weierstall, U.; Ilavsky, J.; et al. Three-Dimensional Coherent X-Ray Diffraction Imaging of a Ceramic Nanofoam: Determination of Structural Deformation Mechanisms. *Phys. Rev. Lett.* **2008**, *101* (5), 055501.
(255) He, X.; Zhang, L.; Meng, D.; Wu, J. From Hydrogel to Aerogel: A Green Fabrication of Multifunctional Polyimide Absorbents. *Eur. Polym. J.* **2017**, *89*, 461–467.
(256) Sun, H.; Xu, Z.; Gao, C. Multifunctional, Ultra-Flyweight, Synergistically Assembled Carbon Aerogels. *Adv. Mater.* **2013**, *25* (18), 2554–2560.
(257) Karan, S. Shape Based Characterization of Nanoparticles – A Fuzzy Mathematical Approach. *Proc. Indian Natl. Sci. Acad.* **2015**, *81* (5).
(258) Lei, W.; Mochalin, V. N.; Liu, D.; Qin, S.; Gogotsi, Y.; Chen, Y. Boron Nitride Colloidal Solutions, Ultralight Aerogels and Freestanding Membranes through One-Step Exfoliation and Functionalization. *Nat. Commun.* **2015**, *6* (1), 8849.
(259) Song, L.; Liu, Z.; Reddy, A. L. M.; Narayanan, N. T.; Taha-Tijerina, J.; Peng, J.; Gao, G.; Lou, J.; Vajtai, R.; Ajayan, P. M. Binary and Ternary Atomic Layers Built from Carbon, Boron, and Nitrogen. *Adv. Mater.* **2012**, *24* (36), 4878–4895.
(260) Cox, P. A.; Reid, M.; Leach, A. G.; Campbell, A. D.; King, E. J.; Lloyd-Jones, G. C. Base-Catalyzed Aryl-B(OH) 2 Protodeboronation Revisited: From Concerted Proton Transfer to Liberation of a Transient Aryl Anion. **2017**.
(261) Ajayan, P. M.; Tour, J. M. Materials Science: Nanotube Composites. *Nature* **2007**, *447* (7148), 1066–1068.